An integrated approach to assess slope instability offshore Espírito Santo, SE Brazil

Aldina Maria Martins Piedade

Submitted in partial fulfilment of the requirements for the degree of Ph.D.

Cardiff University

February 2016

An integrated approach to assess slope instability offshore Espírito Santo, SE Brazil

Aldina Maria Martins Piedade

FCT Fundação para a Ciência e a Tecnologia
MINISTÉRIO DA CIÊNCIA, TECNOLOGIA E ENSINO SUPERIOR

Declaration

This work has not been submitted in substance for any other degree or award at this or any other university or place of learning, nor is being submitted concurrently in candidature for any degree or other award.

Signed _____ (Candidate)

Date _____

Statement 1

This thesis is being submitted in partial fulfilment of the requirements for the degree of PhD.

Signed _____ (Candidate)

Date _____

Statement 2

This thesis is the result of my own independent work/investigation, except where otherwise stated. Other sources are acknowledged by explicit references. The views expressed are my own.

Signed _____ (Candidate)

Date _____

Statement 3

I hereby give consent for my thesis, if accepted, to be available online in the University's Open Access repository and for inter-library loan, and for the title and summary to be made available to outside organisations.

Signed _____ (Candidate)

Date _____

Table of Contents

Table of Figures

List of Tables

List of Equations

Acknowledgements

My first acknowledgement goes to the School of Earth and Ocean Earth Sciences and Cardiff University in general for the use of the facilities and opportunities granted for the completion of this thesis.

I would like to thank my main project supervisor at Cardiff University, Dr. Tiago Alves, for his support on the PhD matters and for the encouraging and supportive way with which he welcomed a Geographer into this PhD project. I would also like to thank him for his scientific inputs, English corrections and lots of positivism during this project.

Thank you to my second project supervisor, Prof. Dr. José Luís Zêzere, for his partial supervision of this project, and for his support and friendship in both professional and personal matters. Thank you for inspiring my enthusiasm about landslides. And finally, thank you for always making me feel welcome at University of Lisbon. I cannot thank him enough for all the opportunities I had since I became his student back in 2008.

Thank you to Fundação para a Ciência e Tecnologia (FCT-Portugal) for the PhD scholarship SFRH/BD/79052/2011 which allowed me to undertake this project. I thank CGGVeritas for the permission to use the seismic volume in this thesis, and Schlumberger for provision Petrel for seismic interpretation. Exprodat GIS for Petroleum is thanked to provide to the 3D Lab a licence of *Data Assistant software* which was a great support during this project. A special thanks to Dr. Chris Jepps who was always very kind and available to help. I must thank British Society for Geomorphology, International Association of Sedimentologists and European Geosciences Union for conferences attendance support. Also I thank Riskam group for support my hotel expenses in Paris during conference attendance. Thank you to InterRidge – International Cooperation in Ridge-Crest Studies for the Award Cruise Bursary to participate in Oceonograflu expedition. I would also like to thank all the scientists and crew on board of L´Atalante, who made this expedition one of the best experiences during my PhD. Thank you to Tectonic Studies Group from Geologic Society of London for the financial support to the field trip to the Carboneras Fault and Sorbas Basin, SE Spain.

Gwen Pettigrew is thanked for her IT support for the 3D Lab and for being always supportive and keeping the good humour. Thank you as well for letting me take home the chair and the screen during the last months of writing up. Alun Roger is thanked for all the IT support. I specially thank Dr. Jenny Pike, as my pastoral supervisor for always being available to chat, and to give her opinion and support.

I would like to thank my officemates in the room 1.59 for all the moments we spent sharing our feelings, expectations, daily problems and our small achievements. They are Ben, Usman, Ana, Davide, Olu, Tuvie, Hammod, Dan, Chris Wild, Nathalia, Tao Ze, Nick, Marco and Qin. A very special thanks to Duarte (and his wife Huiyu), Martino (and his wife Katinha), Iqbal, Kamal and Chris Kirkham for all the support, help and for becoming

Abstract

This thesis uses a three-dimensional (3D) seismic reflection data from the continental slope of the Espírito Santo Basin (SE Brazil) to investigate, at first, the prolonged halokinesis on raft tectonics and its effect on the surrounding structures and how these can affect the post-raft overburden units. Secondly, the high-quality 3D seismic dataset was the source of information to characterise, describe and model a set of mass-transport deposits (MTDs). Their morphology and kinematic factors are described using a geomorphological approach.

The main research hypothesis for this thesis are i) how the salt and raft tectonic are acting on the continental slope of Espírito Santo Basin and how is their influence in the post raft overburden? ii) which are the most common typology of MTDs in the study area and is it possible to related their morphometric and kinematic attributes with the slope geomorphology where the MTDs occurred?, and iii) is it possible applying a bivariate statistic method, already tested on onshore slope instability, to understand the natural conditions for the occurrence of MTD in the study area?

The Espírito Santo Basin is characterised by halokinesis where the Aptian salt has been withdraw into salt structures through time (e.g. diapirs, rollers and pillows). This process leads to complex raft deformation, which occurs in different forms as documented in this thesis. The salt and raft tectonics triggered faults that strongly influenced the post-raft overburden units and later induced the remobilisation of sediment near the seafloor.

The second analysis in this thesis is focused on the characterisation of MTDs. The 3D seismic data were the main source of information integrated into Geographic Information Systems (GIS) in order to compute a set of morphometric attributes to characterise the MTDs and the depositional surface which underlie them. At first, two different MTDs were identified and described; Confined and Unconfined. The inclusion of local topography in the studies to the occurrence of MTDs, as investigated in this part, is a new approach in submarine slope instability studies, and local topography was found to constrain the run-out distance of the MTDs.

Finally, the thesis aimed to understand the natural conditions favourable to the occurrence of MTDs in the study area. Seven predisposing factors were computed from the topographic layer, or depositional surface as named in this thesis. The spatial integration of the predisposing factors with the inventory was based on a statistical bivariate method (Informative Value). The results were validated and the predisposing factors were ranked according to their contribution to MTDs' spatial distribution, allowing for the computation of a sensitivity analysis. The best Area Under the Curve (AUC) was recorded by model 3 (AUC = 0.862).

The results of this thesis are important for both hydrocarbon exploration and academia. From the exploration point of view, the information given in the first data chapter contributes to the understanding of raft and salt tectonics as a trigger of reservoir compartmentalisation. The second analysis provides valuable techniques and methodologies that combine seismic datasets and GIS, used in the last section to calculate favourability scores as a further step for offshore hazard assessments. From an academic point of view, this thesis comprises a timely test of how methods and techniques applied in onshore analysis apply to offshore environments.

3

INTRODUCTION AND LITERATURE REVIEW

Chapter One

1.1. **Project rational and objectives**

1.1.1. **Rationale**

Deepwater continental slopes have been studied for many years, mostly related to hydrocarbon exploration, which has contributed to significantly improving the available tools and techniques for their analysis such as 3D seismic data. These forms of analysis can be applied not only to exploration but can also contribute greatly to improving knowledge within academia within which the information can be input in different approaches. The higher resolution of new datasets has allowed the use of that information to lead the application of new tools and methods related to submarine slope instability (e.g. McAdoo et al., 2000, Chang and Park, 2004, Nadim, 2006, Hough et al., 2011, Moscardelli and Wood, 2015).

Salt basins are frequently the focus of research studies due their major hydrocarbon potential (Fort et al., 2004, Jean-Pierre Brun, 2011, Mohriak et al., 2012). However, margins affected by salt tectonics are very interesting from a structural perspective, driven by the combination of gravity gliding and its effects on shaping basins, generally affecting younger stratigraphic units. The most extreme deformation of salt tectonics occurs during down slope translation of large blocks of strata with no significant rotation and are termed raft tectonics (Gaullier et al., 1993). Salt withdraw and consequent raft deformation can trigger the evolution of the growth fault/raft system due to regional extension, which in practice affects the structures (e.g. Duval et al., 1992, Gaullier et al., 1993, Penge et al., 1999, Rowan et al., 1999, Rouby et al., 2002, Brun and Mauduit, 2008, Alves, 2012) and stratigraphic units above (overburden) (Alves et al., 2009, Alves, 2012, Omosanya and Alves, 2013).

Mass-wasting features are common place within continental slopes, whereby the combined actions of local and regional tectonics, sediment input and gravitational instability can result in the formation of complex structures (Mienert et al., 2003, Bryn et al., 2005, Kvalstad et al., 2005, Masson et al., 2006, Gee et al., 2006, Talling et al., 2007, Garziglia et al., 2008, Gamboa et al., 2010). Mass-wasting occurs when downslope directed shear stress exceeds the shear strength of the seafloor (Varnes, 1978), resulting

in mass movement events that can be classified as mass-transport deposits (MTDs) or mass-transport complexes (MTC) when they are composed of multiple failure events (Moscardelli et al., 2006).

Classifying MTDs can be a complicated and sometimes challenging task due to significant variability in their character (e.g. volume, thickness, provenance, lithology, kinematic features, etc.). Nevertheless, following the first mass failure, MTDs always involve the transport of sediments over a detachment surface termed the basal shear surface. During this process, depending on their origin, predisposing and triggering factors can result in variability in the final dimensions and size of MTDs (volume, area, length, width) (Hampton et al., 1996, Mosher et al., 2010, Moscardelli and Wood, 2015), associated kinematic features (Bull et al., 2009) and different forms of slope accommodation (Frey-Martínez et al., 2006). Their classification, however, is primarily based on the movements themselves and in their geomorphologic expression.

Despite all the published data about submarine slope movements in general and MTDs, there is still the need for further study of each of the parameters that are involved during their failure. Many studies apply to onshore analogues (Carrara et al., 1999, Guzzetti, 2005, Guzzetti et al., 2006, Zêzere et al., 2009, Corominas et al., 2013). This conceptual model is part of the methodology that has been used for slope instability, hazard and risk assessment (van Westen et al., 2006, van Westen et al., 2008). It assumed that the answer for the past can be found by understanding the present, which may be the key to preventing future slope instability and associated events (Varnes, 1978).

In this thesis, the three-dimensional (3D) seismic volume BES 100 from the salt-rich continental margin of the Espírito Santo Basin will be used to test the following general assumption:

i)   Raft tectonics are the last stage of salt tectonics deformation. Theoretically, areas of raft tectonics are the result of gliding downslope of the overburden on top of a viscous layer of salt, until salt has been completely withdrawn and rafts will be welded onto pre-salt units. During this process, rafts tectonics accommodate themselves into the salt layer and post-raft stratigraphic units will adjust to accommodate the space left by the movement of the rafts. In the meantime, salt accumulates into diverse forms (e.g. pillows, roller,

tongues and diapirs) and rafts will deform and compartmentalise in different styles, in order to accommodate salt withdrawal. The tectonics briefly described trigger a set of fault and regional adjustments in the post-raft stratigraphy and at basin scale. It is, therefore possible to describe the deformation styles of raft tectonics and establish their influence in the post-raft overburden. The study area is shown to comprise an essential piece of information to understand the later stages of raft tectonics on continental margins which, in this case-study, shows little effect of overburden thickness on raft segmentation.

ii)   Mass-transport deposits are recognised in all margins and are well described in the literature based on their size, shape, accumulation and gliding patterns, stratigraphy and kinematic features. Essentially, the studies focus on the geomorphology of the movement itself. Although the movement of MTDs over any surface is generally erosive it is believed that the local topography and morphology within a region prior to mass movement have a significant influence on the final dimensions and location of MTDs during gliding. In order to fill the gap within literature, the relationship between these factors will be computed using a combination of 3D seismic data and Geographic Information Systems (GIS) slope morphometric tools. The primary focus will be on the surface beneath the MTDs, the depositional surface.

iii)   Submarine mass-movements are one of the most dangerous and destructive natural hazards that can affect offshore explorations and/or coastal populations and infrastructure. Identifying and understanding all of the natural factors that are involved in their failure parameters and processes is challenging. However, developed seismic databases can provide details which allow the application of methodologies from onshore risk assessment to offshore test areas. The uncertainties of this methodology must be taking into consideration, however, it is considered valid for the rationale framework for estimating the probability of slope failure to be applied to

submarine mass-movements in general. The MTDs presented within this study will be integrated together with a set of predisposing factors into a statistical bivariate method to understand the geomorphologic parameters contributing to submarine slope failure, in a given area, offshore Espírito Santo Basin.

These assumptions are important because contribute are the base for further investigations, using a new detailed image of the structural deformation of salt tectonics areas, specifically raft tectonics. It will be connected to the MTD failure in the overlying stratigraphic units and ultimately used to produce a model and a methodology for the early stages of risk assessment offshore. The results presented here are important as an academic exercise and also relevant to industry and offshore geohazards assessment.

1.1.2. **Objectives**

This work presents an investigation of salt tectonic areas, specifically raft tectonic deformation styles and their influence on post-raft stratigraphic units where MTD are located. Using a high-quality 3D seismic data from the Espírito Santo Basin has allowed for the use of information for the early stages of offshore risk assessment using statistics bivariate methods. The aims of this research are expecting to fill and document the assumption pointed out following the objectives:

- To image raft tectonics using high resolution seismic data from Espírito Santo Basin.
- To document the spatial distribution and structural deformation of raft tectonics on the continental slope offshore Espírito Santo Basin (SE Brazil).
- To relate raft tectonics with the post-raft thickness and fault set that also affect overburden stratigraphic units.

- To document different MTD types at the same stratigraphic level considering the local topography of their location.
- To calculate morphometric attributes and their spatial distribution providing information about the study area and computed-generated geomorphometric maps.

- To use a set of geomorphometric maps as a predisposing factor to understand the natural condition that were present when MTDs occurred.

- To apply a bivariate statistic method in order to achieve favourability scores to MTD occurrence in the Espírito Santo basin.

In the next section is given a summary of the literature review of salt and raft tectonics in the Espírito Santo Basin. This is followed by an overview of the main points focused on MTDs and statistics bivariate methods, and respective models validations, in order to provide the key background information into the three results chapters.

1.2. **Salt tectonics margins**

The prime interest in salt tectonics comes from the oil industry, due to important hydrocarbon provinces in salt basins (e.g. North Sea, Gulf of Mexico, Campos and Espírito Santo Basin, Levant Basin etc.). The interest of the oil industry has resulted in the provision of high resolution datasets, which has aided in the advancement of our understand of salt tectonics areas (Rowan et al., 1998, Penge et al., 1999, Rouby et al., 2002, Fort et al., 2004). Salt is unique in its geologic deformation style, which can result in a massive deformation overprint on some passive margins making salt tectonics an important component of many sedimentary basins. Passive margins are, therefore, perfect natural laboratories to study the dynamics of salt tectonics, in the lack of crustal-scale tectonics (Jean-Pierre Brun, 2011). Furthermore, salt layers can play a significant role in the creation of structural traps and can have an enormous influence in reservoir distribution. Salt itself is an important seal to fluid migration.

1.2.1. **Salt flow – Mechanisms**

Regions of salt tectonics are well known by their deformation, which involves the flow of the salt as a viscous layer (Jackson and Talbot, 1991, Brun and Fort, 2011). Differential loading is considered to be one the dominant forces that drives salt flow. The capacity of salt to flow can be impeded by both boundary friction within the salt layer and the strength of the overburden. Salt can remain static for tens or hundreds of millions years,

until the driving forces are sufficient to overcome the resisting forces (Hudec and Jackson, 2007). There are three main mechanism of salt flow:

(i) Differential loading; the geometry of the salt body, geologic setting, depth and thermal conditions of the salt defines where the salt flows and is driving by gravitational loading (Figure 1.1), displacement loading (Figure 1.2) and thermal loading (Hudec and Jackson, 2007).

(ii) Vertical salt flow (halokinesis) divides in three main processes 1) reactive stage, producing salt mounds and pillows, 2) active stage comprises the period during which the salt flows upward and arrives near or at the surface of seafloor and 3) the passive stage which forms apparent diapirism and the salt does not deform the sediments of the overburden sedimentary units (Vendeville and Jackson, 1992a, Hudec and Jackson, 2007) (Figure 1.3).

(iii) Boundary friction within the salt layer and the strength of the overburden, where both the shear and friction strength increase with depth of burial and confined pressure (Hudec and Jackson, 2007).

Gravitational loading
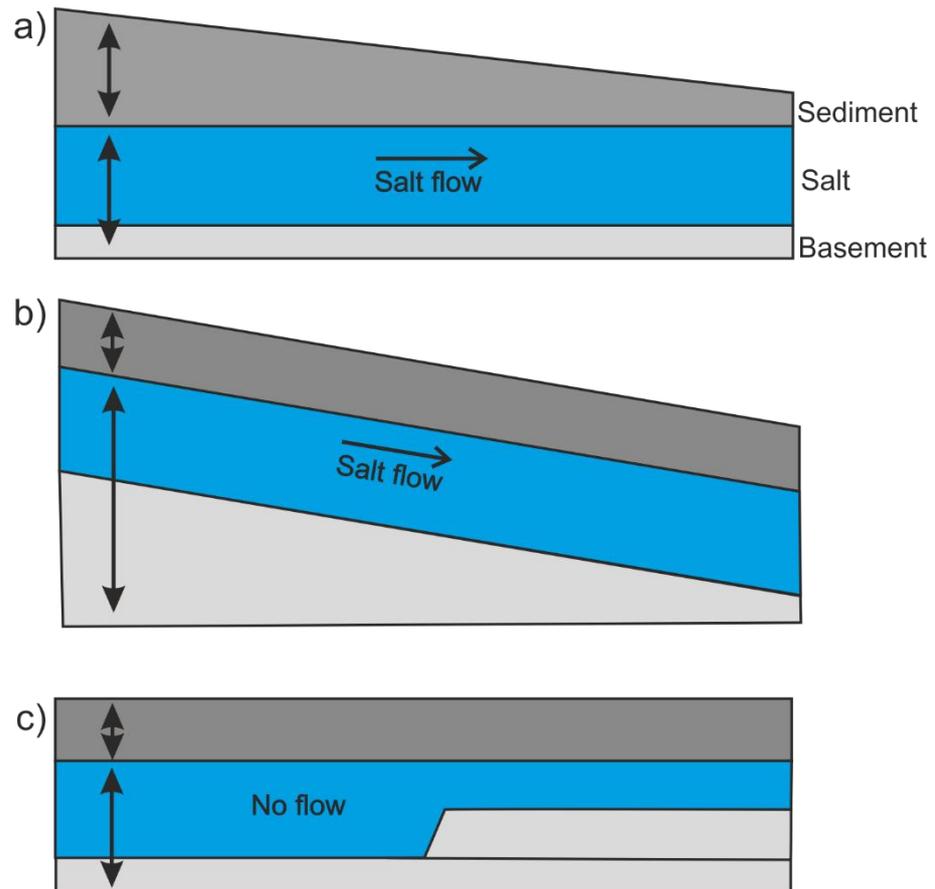
Figure 1.1 – Gravitational loading; (a) A laterally varying overburden thickness above a horizontal head gradient. Salt will flow from left to right along the pressure head gradient. (b) A uniform overburden thickness above an inclined, tabular salt layer produces an elevation head gradient. Salt will flow from left to right down the elevation head gradient. (c) A uniform overburden thickness above a flat-lying salt layer produces neither elevation nor head gradients, even though the salt thickness varies. (Hudec and Jackson, 2007).

Displacement loading
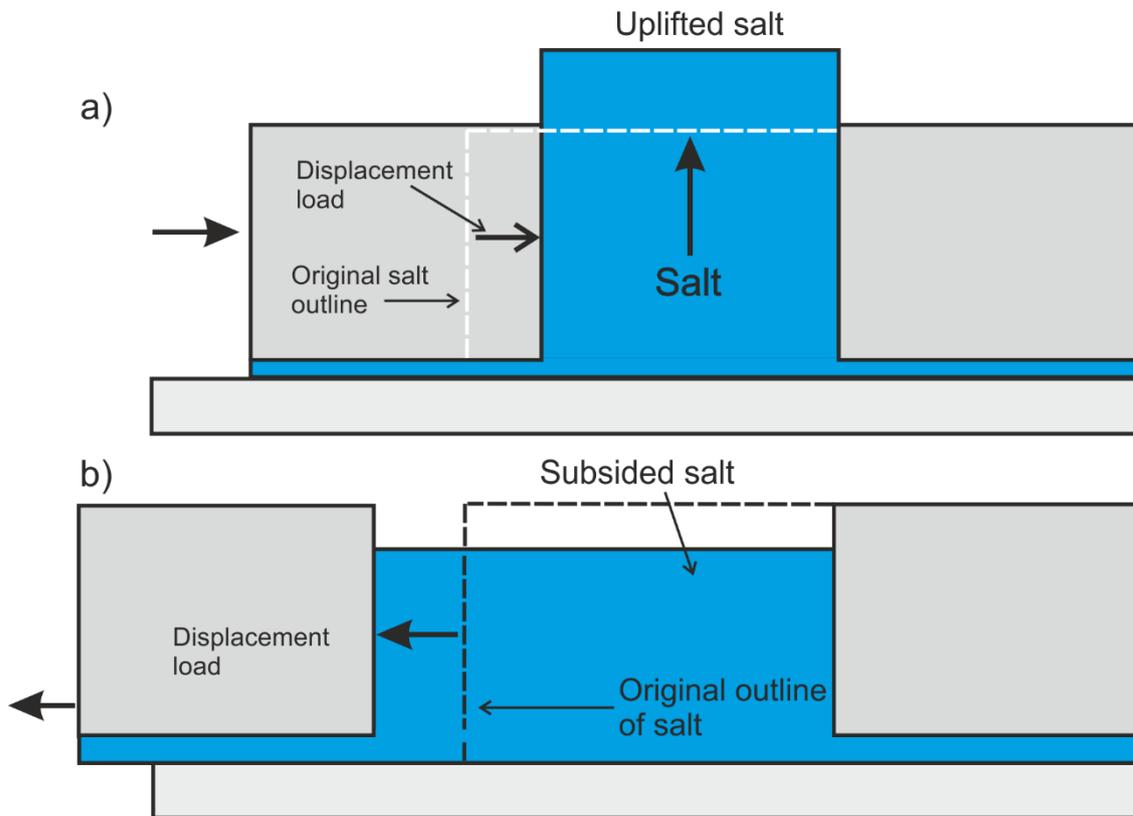
Figure 1.2 – The effects of displacement loading on salt structures; a) In shortening, salt is loaded horizontally by inward movement of one or both sidewalls where the horizontal displacement load exceeds the vertical gravitational load, forcing salt to rise. (b) During extension, the salt is unloaded horizontally by movements of one or both sidewalls. The vertical gravitational load then exceeds the horizontal displacement load, so salt subsides (Modified after Hudec and Jackson, 2007).

VERTICAL SALT FLOW

Reactive diapirism

Active diapirism

Overburden load
pressurise salt

Passive diapirism

Mass column
of salt

Mass column
of sediments

Allochthonous sheet advance
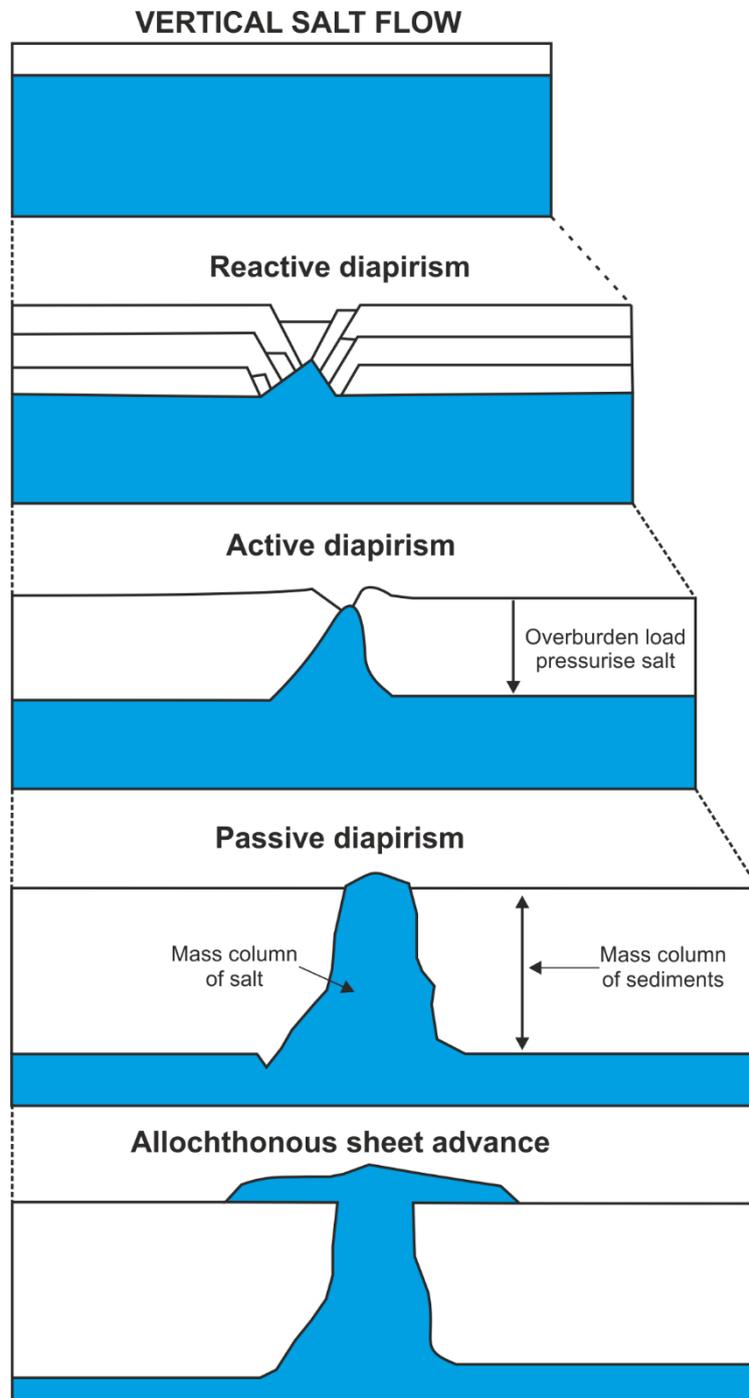
Figure 1.3 – Vertical salt flow. The mature of a given structure depends on availability of salt, extension rate and sedimentation. Vertical salt flow does not necessarily follow through all these stages. Modified after Vendeville and Jackson (1992b), Hudec and Jackson (2007), .
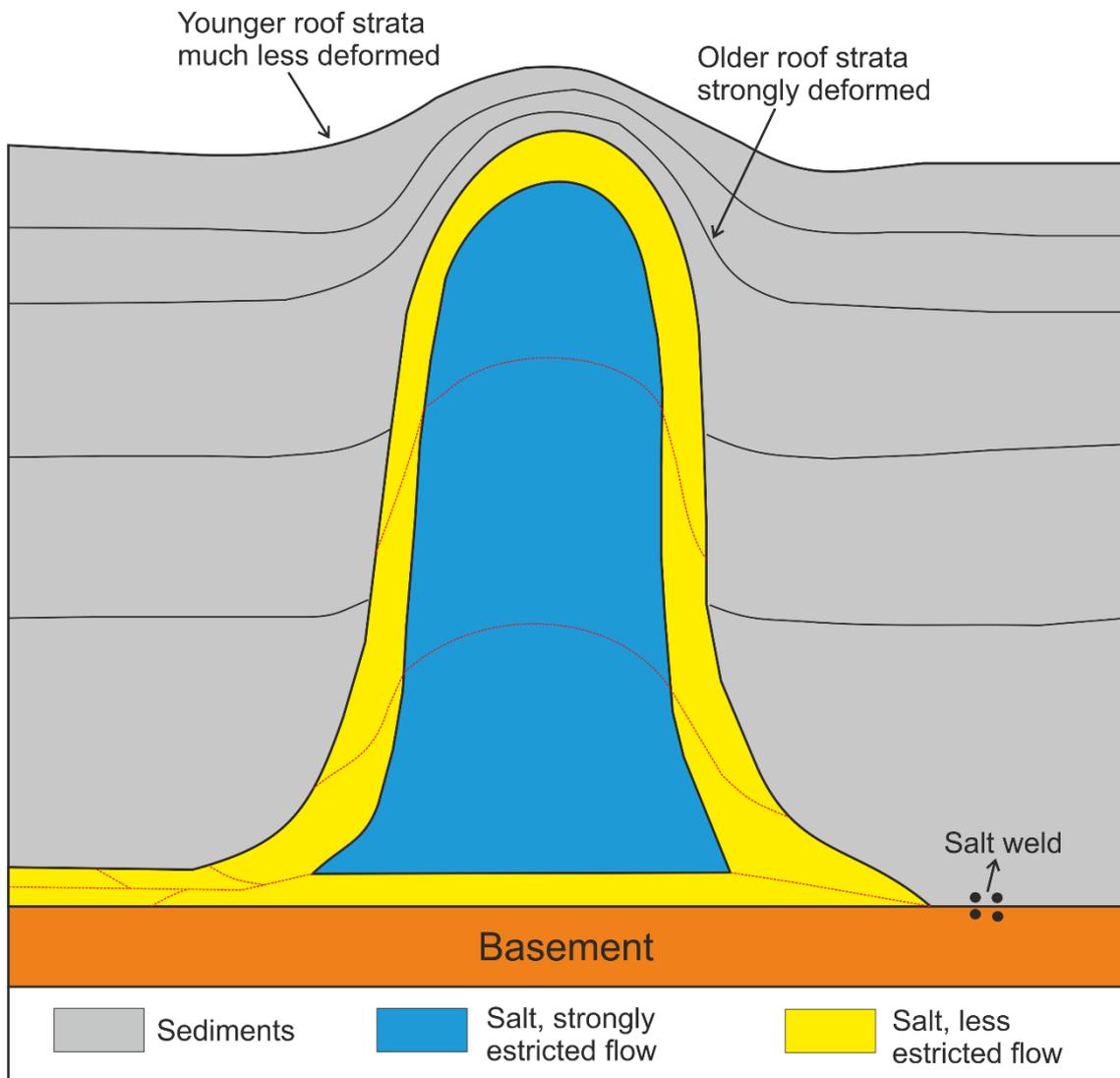
Figure 1.4 - Factors resisting salt flow, where first diapir required deformation of the overlying roof. Salt deformation is accomplished if the roof is thin and weak but becomes progressively more difficult as roof thickness increases. Secondly, salt is strongly sheared near the edges of salt bodies during flow, a phenomenon causing resistance to deformation. The salt flow is inhibited when the salt layers becomes too thin. Dashed red line represents the different phases of diapir grow. Red dashed-line represents the (Modified after Hudec and Jackson, 2007).

1.2.2. **Structural style in salt-rich passive continental margins**

Salt tectonics within passive margins is currently interpreted as a gravity-driven over a décollement surface, such as evaporites or shales (Fort et al., 2004, Rowan et al., 2012), where the evaporites are considered a viscous material. Brun and Fort (2011) proposed dividing this process into two different types of models: i) pure spreading only driven by differential sedimentary loading and ii) dominant gliding primarily due to margin.

The upper slope of salt-rich continental margins are generally dominated by an extensional domain and processes, where salt pillow and rollers are attached to large faults (Rowan et al., 1999, Alves, 2012). In mid-continental lower-slope domains the salt structures grow into diapir and salt walls, essentially making a transition between extensional upper-slope and lower-slope domains. These compressive zones are dominated by salt ridges, thrust, allochthonous salt sheets and canopies (Fort et al., 2004, Omosanya, 2014).

1.2.3. **Raft tectonics**

The most extreme deformation associated with salt tectonics occurs with the down slope translation of large blocks of strata with no significant rotation and is termed raft tectonics (Gaullier et al., 1993). Raft tectonics is a major form of thin-skinned extension (Duval et al., 1992, Gaullier et al., 1993, Mauduit et al., 1997), in areas where the overburden stretches to two or three times its original length (Figure 1.5). When the allochthonous fault blocks are sufficiently displaced for them to no longer be in mutual contact, they are termed rafts. With less extension, if fault blocks are still in contact, they can be termed pre-rafts. Exceptional extension of the overburden over a non-deforming basement is enabled by an intervening ductile, weak, décollement layer, typically consisting of thin evaporates or shale. In the widening gaps between the gliding rafts, younger sediments accumulate as trough-like depocentres (Duval et al., 1992). The geometry and the dynamics of the resulting extensional structures are strongly controlled by the slope orientation. The fault system is crucial to understand the

complex geometries of structures developed during rafting which, in turn, is important for efficient hydrocarbon exploration (Gaullier et al., 1993).
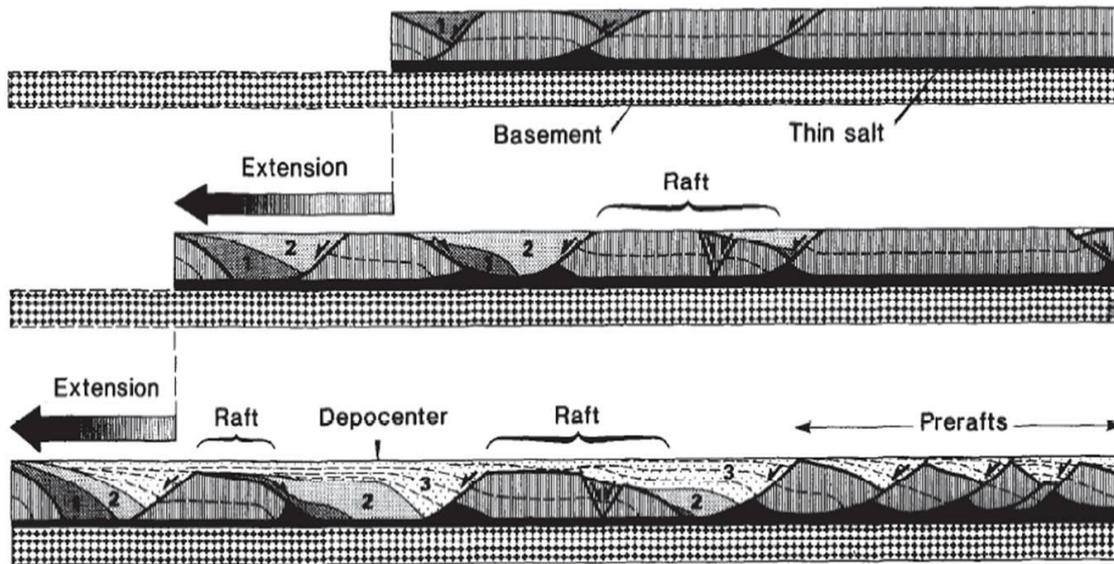
Figure 1.5 – Raft tectonics formation during thin-skinned extension. Pre-rafts remain in mutual contact and hanging walls on their original footwall after faulting. In contrast, rafts separate so far that they are no longer in contact, and salt acts a décollement layer (Duval et al., 1992).

Within documented literature some factors and parameters affecting raft geometry and gliding have been referred to. Mauduit et al. (1997) highlight some of these which were observed in the Gulf of Guinea. Three examples illustrate the possible role of the basal slope angle and sedimentation rate on syn-sedimentary deformation during gravity gliding. If the slope angle is low, deformation is restricted to a few fault sites on the seaward (downslope) side. If the slope angle is higher the number of faults increases, indicating distributed deformation and displacement (Mauduit et al., 1997). In this case the sediment supply is low, however, if sediment supply is high during gliding, displacement rate seems to increase with time. To summarize, the author separated based on two clear factors that influence the geometry of the raft in the Gulf of Guinea: 1) the effect of basal slope angle which resulted in the identification of three different deformation areas and; 2) Low basal slope angles (0 to 1°) by a single downslope deformed zone with tilted blocks and associated asymmetric depocentres. Block tilting is controlled by planar of listric synthetic normal faults. Antithetic normal faults are only active during the early stages of deformation. For higher basal slope angles, the

deformation zone develops upslope. A central raft translates without deformation of the overburden and separates the two deformation zones (Mauduit et al., 1997).

In order to understand the potential effects of sedimentation on deformation, Mauduit et al. (1997) tested, two rates of sedimentation were tested, low and high. Both types of experiments yielded a downslope deformation zone with tilted blocks delimited by synthetic normal faults and rafted block. As was observed before, the first structures to develop correspond to symmetric grabens, regardless of the sedimentation rate. As sedimentation rate increases, the number of rafts or tilted blocks also increases. The study presented by (Mauduit et al., 1997), demonstrates that an increment in sedimentation rate enhances the displacement rate.

Recently, new high resolution seismic data from hydrocarbon exploration allows a different approach about raft tectonic gliding and some new factors that control or condition the raft tectonic gliding are coming to light. Based on 3D seismic-reflection data from SE Brazil, new approaches have been discuss, for instance, Alves (2012), highlighted normal faults reactivated during the gravitational gliding of Albian rafts.

1.2.4. **Salt-related faults**

Faults that are salt-related have been documented in many areas such as as SE Brazil (Baudon and Cartwright, 2008, Alves et al., 2009, Alves, 2012) and the Gulf of Mexico (Rowan et al., 1998, Rowan et al., 1999, Brun and Mauduit, 2008). The classification used in this thesis follows that from this published literature and gives a classification that is strictly geometric without reference to kinematics, dynamics, or genesis. The faults observed are grouped into fault families by Rowan et al. (1999) (Figure 1.6), where each fault family comprises a range of faults that display similar three-dimensional form and geometric relationships with deformed strata and associated salt (Rowan et al., 1999). The faults identified form in response to the adaptation of salt tectonics in vertical movement (caused by downward salt withdrawal or upward diapirism) and to lateral translation above salt (Rowan et al., 1999) (Figure 1.7).
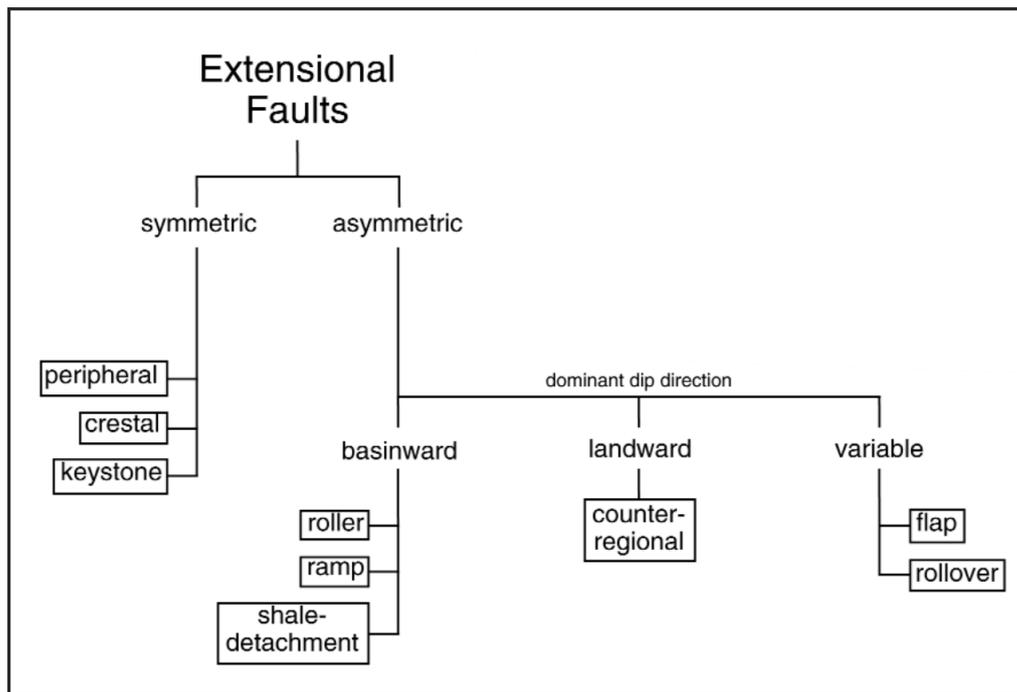
Figure 1.6 - Classification system for fault families observed in the northern Gulf of Mexico. (Modified from Rowan et al., 1999). This classification is also observed in the Espírito Santo Basin and is used in this thesis to classify some of the faults observed related to salt and raft tectonics.
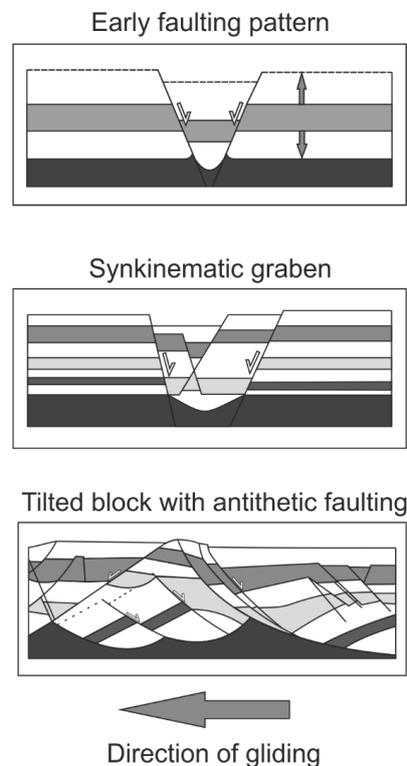
Figure 1.7 - Development of typical structural faults patterns following the work of (Mauduit et al., 1997). (Synkinematic grabens formed at the initial phases of rafting give rise to synthetic and antithetic faults when stretching reaches its paroxysm, and rafts become individual structures moving downslope due to extension.

1.3. **Mass-transport deposits**

The terminology mass-transport deposit (MTD) encompasses all types of submarine mass movement, comprising sediment packages emplaced during a single event of slope failure. It differs from mass-transport complex in the way that considered multiple slope failure when coalesced into a large unit or package (Varnes, 1978, Hampton et al., 1996, Masson et al., 2006, Moscardelli and Wood, 2008). Mass-transport deposits can be observed in all margins and different geological settings, occurring at all water depths where soft sediments are present and the natural conditions are favourable to their occurrence (McAdoo et al., 2000, Hühnerbach and Masson, 2004, Gamboa et al., 2010, Omeru and Cartwright, 2015).

Mass-transport deposits can covers very large areas of tens to hundreds of kilometres, depending if they are formed in the shelf break or mid-slope. Smaller MTDs are normally formed at flanks of diapirs or by the collapse of canyons walls (Hampton et al., 1996, Masson et al., 2006, Omosanya, 2014). MTDs play a large role in the stratigraphic fill of worldwide basins (Moscardelli and Wood, 2008), transporting and remobilising a large amount of sediment in offshore areas, which comprise 10% to 27% of the continental slope strata (Hühnerbach and Masson, 2004). This fact has important implications on hydrocarbon reservoirs (Welbon et al., 2007) and geohazards, both in coastal areas or in exploration infrastructures (Ioualalen et al., 2010).

1.3.1. **Classification of mass-transport deposits**

Mass-transport deposit is a general term used for the failure and downslope movement of sediment under the influence of gravity forces. In recent years, the literature has been outlining different classification schemes. Nevertheless, a scale-consistent and common classification that focuses on the descriptive and morphological factors needed to be defined for all the MTDs (Posamentier et al., 2011). Moscardelli and Wood (2008) compiled a classification that has been also defined by Masson et al. (2006) based on the transport mechanism and sedimentary structures (Figure 1.8) which are: i)slides, involving movement of a coherent mass of sediment along a planar glide plans; ii) slump, a coherent mass of sediment that moves on a concave-up glide plane and

undergoes rotational movements causing internal deformation; iii) debris flow, involving flow with plastic rheology, cohesive flow of clasts in a fine-grained matrix; and iv) turbidite, included gravity flows and turbulent state in which sediment grains are in suspension by fluid turbulence (Figure 1.8).

GRAVITY INDUCED DEPOSITS			Genetic Classification Transport Mechanism	Descriptive Classification Sedimentary Structures	Seismically Recognized Features (Moscardelli et al., 2006)
Mass Transport Complex	Slide		Shear failure along discrete shear planes with little or no internal deformation or rotation.	Essentially undeformed, continuous bedding.	Continuous blocks without apparent internal deformation. High-amplitude, continuous reflections.
	Slump		Shear failure accompanied by rotation along discrete shear surfaces with various degrees of internal deformation.	Plastic deformation particularly at the toe or base. Plow structures, folds, tension faults, joints, slickensides, grooves, rotational blocks.	Compressional ridges, imbricate slides, irregular upper bedding contacts, duplex structures, contorted layers. Low-and-high-amplitude reflections geometrically arranged as though deformed through compressive stresses.
	Debris Flow		Shear distributed throughout the sediment mass. Strength is principally from cohesion due to clay content. Additional matrix support may come from buoyancy. Plastic rheology and laminar state.	Matrix supported, random fabric, clast size variable, matrix variable. Rip ups, rafts, inverse grading and flow structures possible.	Mega rafted and/or detached blocks, irregular upper bedding contacts, lateral pinch-out geometries, oriented ridges and scours. Low-amplitude, semitransparent chaotic reflections.
Turbidity Current	Turbidite		Supported by fluid turbulence (Newtonian rheology).	Normal size grading, sharp basal contacts, gradational upper contacts.	Lobate features. Laterally continuous.
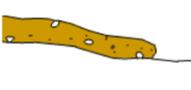
Figure 1.8 – Classification of gravity- induced deposits Moscardelli and Wood (2008)

1.3.2. **Morphologic classification of mass-transport deposits**

In addition, multiple transport processes may have occurred within a single MTD, it is incorrect to characterise an entire deposit on seismic based on localised observation. MTD itself can have different features and can show a large range of internal deformation geometries.

MTDs often present three important domains, the extensional headwall domain, translational domain and compressional toe domain (Figure 1.9). Nevertheless, not so well conserved MTD or poor documented can show absence of some of the domains. In these cases, that is possible identified the geological structures or features which records information related to the type and indication of motion at the time of emplacement are a great contribution to the understanding of the initiation, dynamic

and cessation of slope failures, and it is designated as kinematic indicators by Bull et al. (2009) (Figure 1.10).

The frontal emplacement of MTDs are also geomorphologic features highlighted by Frey-Martínez et al. (2006) in the continental margin offshore Israel (Eastern Mediterranean), which have been used to analyse the compressional structures within the toe regions of two major buried submarine landslides. Using high spatial resolution data allowed a detailed analysis of the geometries and deformational structures within the toe regions of the two landslides, and this has been used to develop a mechanical model for their development. Importantly, it has been recognised that submarine landslides may be divided into two main types according to their form of frontal emplacement: *frontally confined*: the landslide undergoes a restricted downslope translation and does not overrun the undeformed downslope strata and; *frontally emergent,* much larger downslope translation occurs because the landslide is able to ramp up from its original basal shear surface and translate in an unconfined manner over the seafloor (Figure 1.11) (Frey-Martínez et al., 2006).
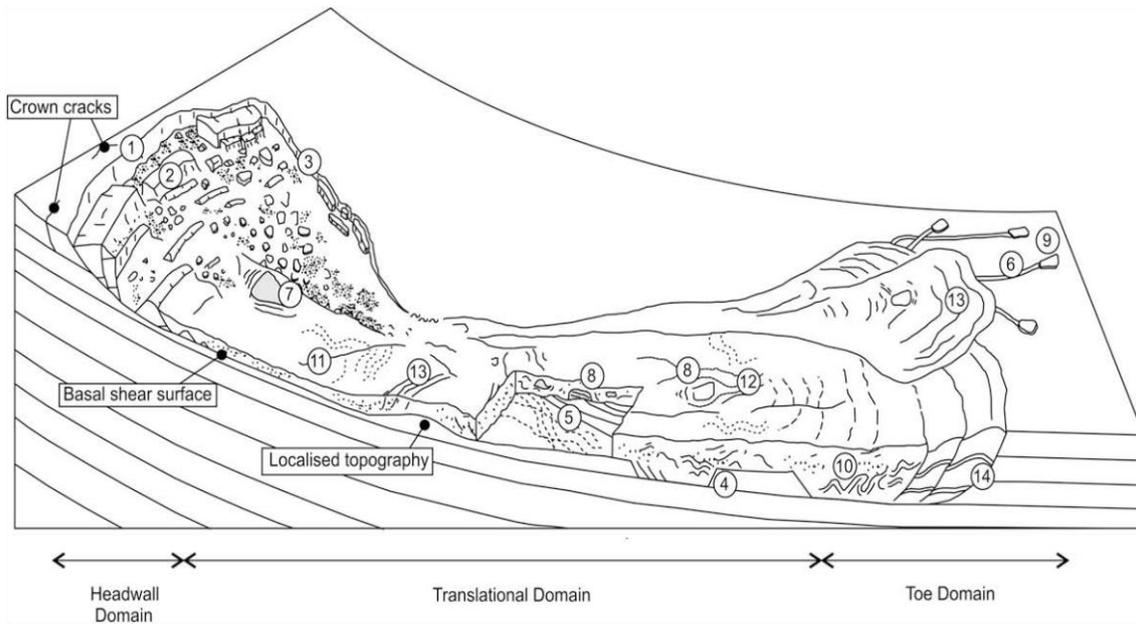
Figure 1.9 - Schematic representation of a typical MTD tripartite morphology: (1) Headwall scarp; (2) Extensional ridges and blocks; (3) Lateral margins; (4) Basal shear surface ramps and flats; (5) Basal shear surface grooves; (6) Basal shear surface striations; (7) Remnant blocks; (8) Translated blocks; (9) Outrunner blocks; (10) Folds; (11) Longitudinal shears/first order flow fabric; (12) Second order flow fabric; (13) Pressure ridges; (14) Fold and thrust systems (Prior et al., 1984, Bull et al., 2009).
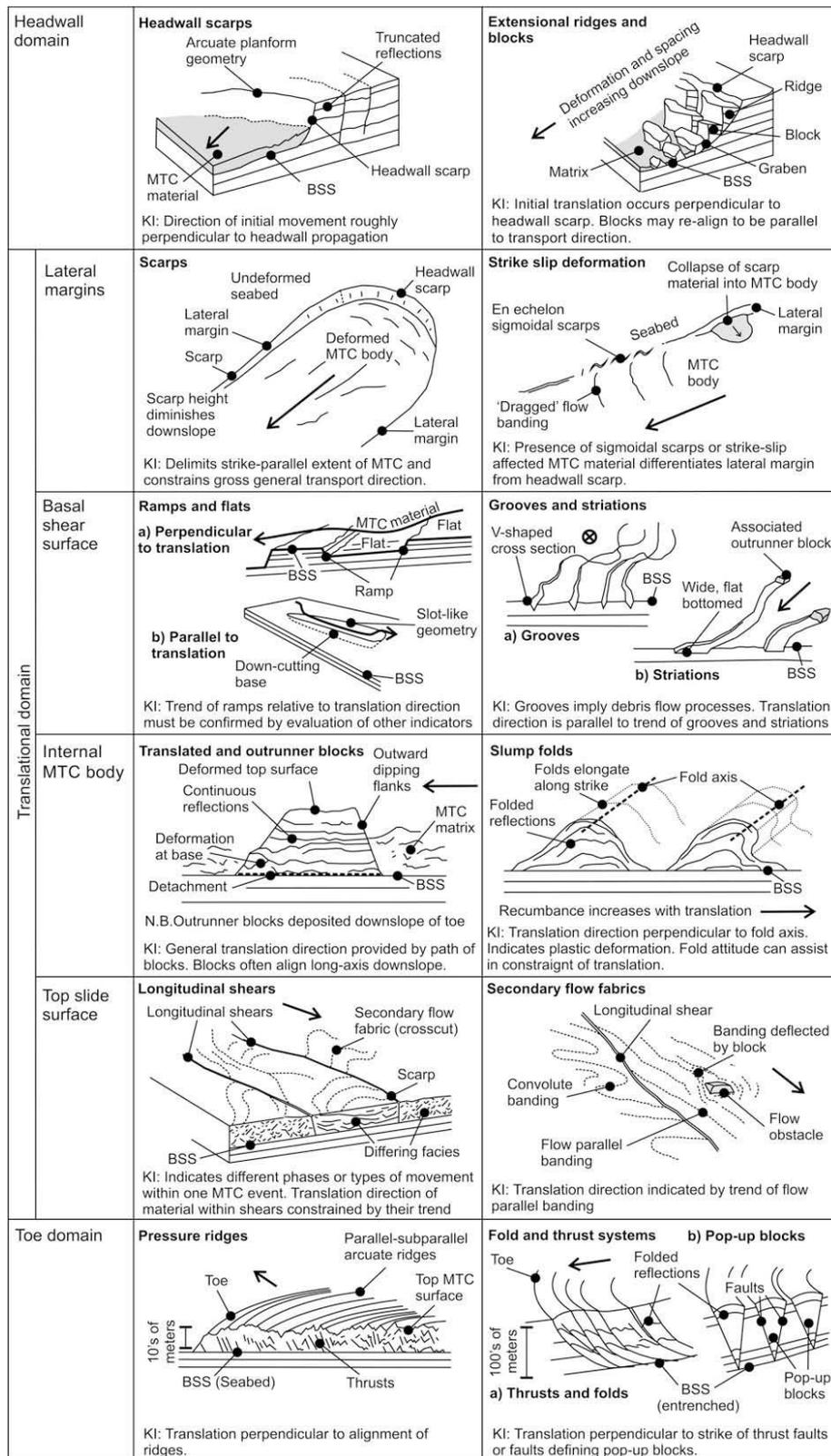
Figure 1.10 – Summary diagram showing key geometrical and geological criteria for the recognition of all kinematic indicator types. (Bull et al., 2009).

22
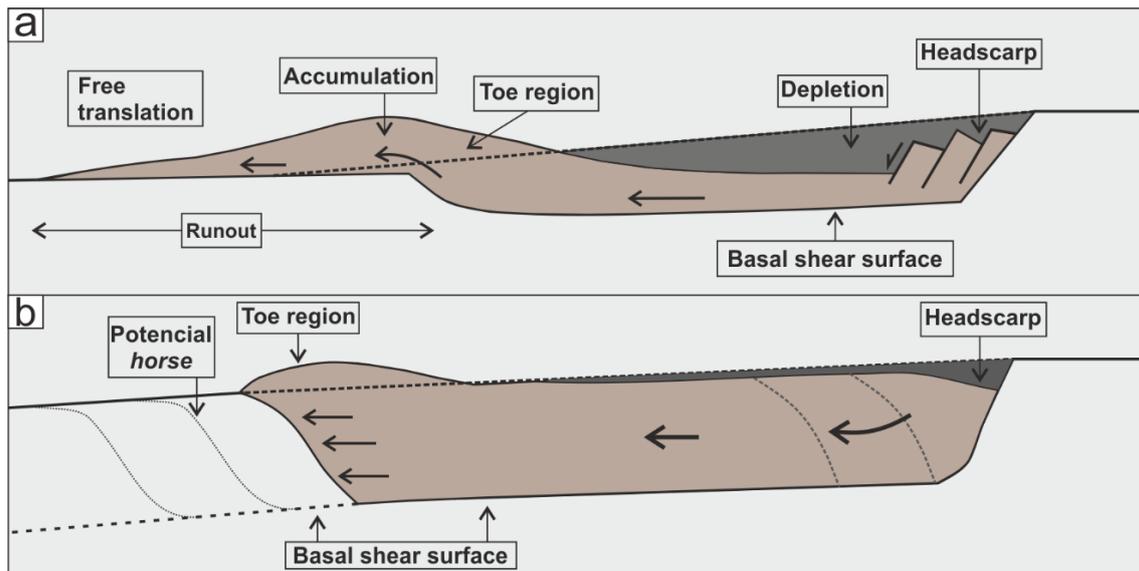
Figure 1.11 - Two main types of mass-transport deposits according to their frontal emplacement: (a) Frontally emergent, where the material ramps out the basal shear surface onto the seabed and is free to travel considerable distances over the undeformed slope position. (b) Frontally confined, the mass is buttressed against the frontal ramp and does not abandon the original basal shear surface (Modified from Frey-Martínez et al., 2006)

1.3.3. **Predisposing factors for the occurrence slope instabilities**

Predisposing factors (or preconditions) are static, inherent of slope environment, and not only influence the margin of stability, but more importantly in this context act as pre-disposing to allow other dynamic destabilising factors to operate more effectively (e.g. triggers). For instances, slope materials that lose strength more readily than others in the presence of water predispose the slope to failure during a rainstorm in onshore examples (Glade and Crozier, 2005). The predisposing factors are often considered as environmental factors which are constituted by terrain and topography attributes, whereby the Model Digital Terrain (MDT) is often the main source to produce very significant layers of predisposing factors. These factors include slope gradient, slope direction, slope shape, flow direction, flow accumulation, internet relief, rock types etc. (Remondo et al., 2003, van Westen et al., 2008). Usually, the predisposing factors that are used for modelling depend on the type of slope movement, the type of terrain and the availability of data sources (Zêzere et al., 2004, van Westen et al., 2008, Pereira et al., 2012).

1.3.4. **Triggering factors**

Triggering factors are the ones responsible for the initiation of the movement. These factors shift the slope from a 'marginally stable' to an 'actively unstable' state (Glade and Crozier, 2005). The common triggering factors are usually external forces that affect the slope and initiate the movement (Figure 1.12). In fact, depending on the slope, the actual trigger has little influence on the slope if the predisposing factors govern the stability of the slope (Rodríguez-Ochoa et al., 2015).

Based on the literature (Hampton et al., 1996, e.g. Locat and Lee, 2002, Hance, 2003, Masson et al., 2006, Rodríguez-Ochoa et al., 2015) the most common triggering factors for submarine slope movements are mechanisms such as: earthquakes, gas hydrates, groundwater seepage, over steepening, high sedimentation rate/underconsolidation, magma and mud volcanoes, and salt diapirism.

1.3.4.1. Factor of safety (F)

Independent of the triggering mechanism responsible for the slope movements, the factor of safety (F) is the responsible for their occurrence (Hampton et al., 1996, Locat and Lee, 2002). A general definition of the factor of safety (F) of a slope results from the comparison the downslope shear stress with the shear strength of the slope, along as assumed rupture surface. The factor of safety, represents mathematically the equilibrium conditions between the factors that are favourable for the slope failure and those that prevent it (Figure 1.12). When F > 1 the slope is thought to be stable, unstable when F < 1, and relatively unpredictable if F = 1 (Figure 1.12). the transition between stability and instability may be predict mathematically as a decrease in the factor of safety to values below unity (De Blasio, 2011). The factor of safety is calculated by the equation:

Equation 1.1

$$F = \frac{\sum ResistingForces}{\sum GravitationalForces}$$
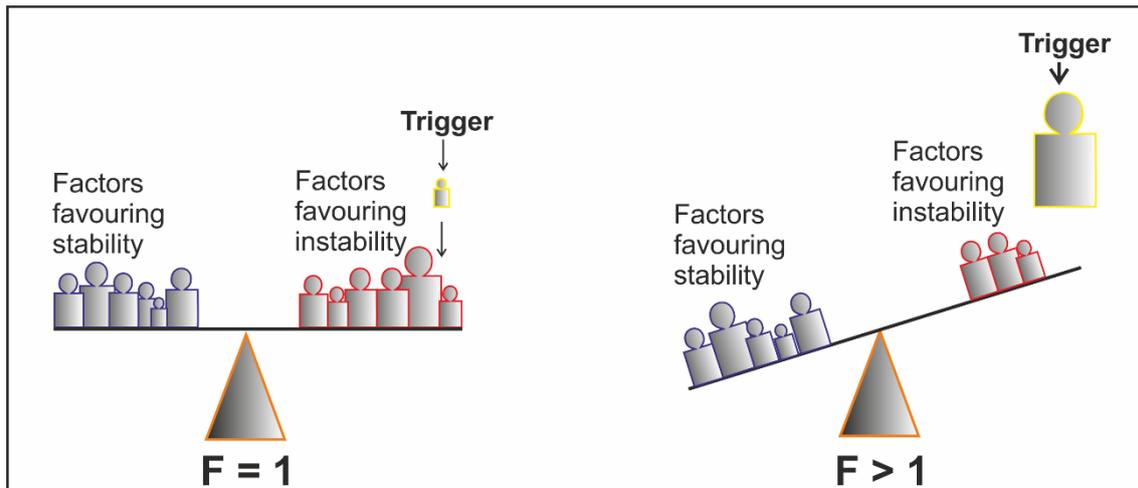
Figure 1.12 – The factor of safety (F) reflects the equilibrium conditions between predisposing factors and triggering factors mechanisms. The factors favouring stability of the slope are shown in blue and the factors triggering failure are red. The slope fails when FS is <1. Modified after Camerlenghi (2013) in Omosanya (2014).

1.4. **Workflow to for and risk assessment**

The methodology for risk assessment for onshore slope movements is well known with a vast range of methods (Thiery et al., 2007, Cees J. van Westen, 2008, van Westen et al., 2008). The total risk is a result of an equation where the hazard and the elements at risk are considered. Varnes (1978) has proposed the most widely adopted definition of hazard as the probability of occurrence of a potentially damaging phenomenon within a given area and a given period of time. Legros (2002), pointed out that this definition requires the definition of the location (where?), time recurrence (when?) and the magnitude (how powerful?) of the phenomena. The susceptibility analysis tries to answer the question "where" and is done by following the methodology in the Figure 1.13.

In offshore studies is harder to assess the risk. In this thesis presents the first steps to contribute for it, by the computation of the favourability scores for the occurrence of MTDs, following the methodology proposed in the Figure 1.13.
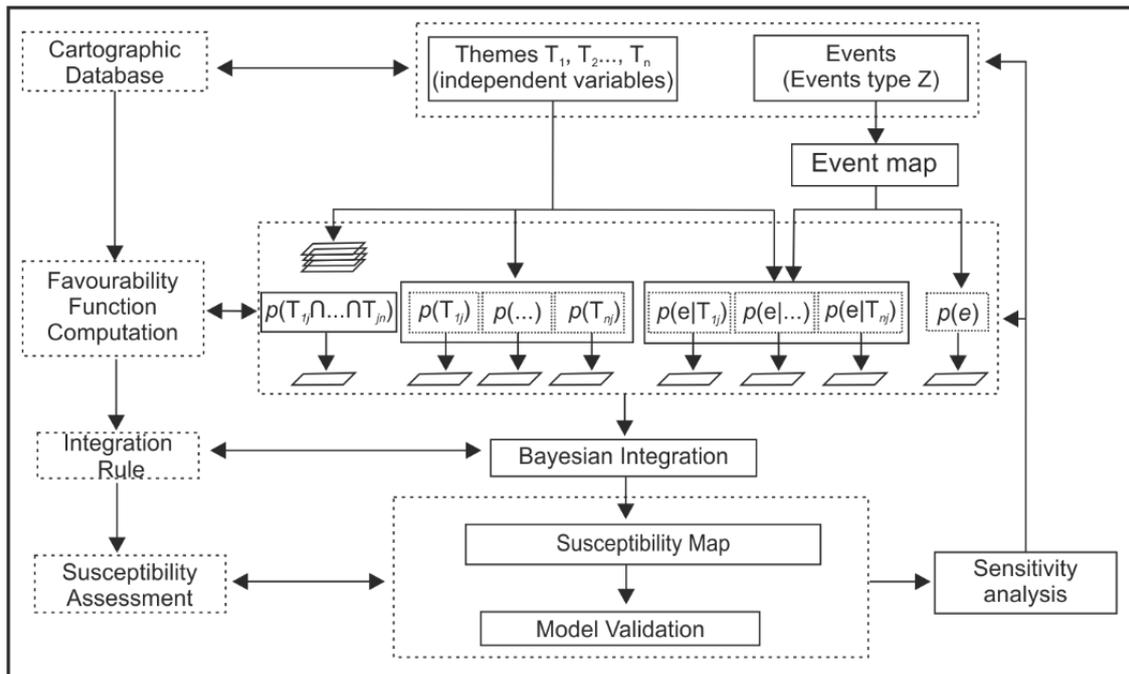
Figure 1.13 – Methodology for landslide susceptibility assessment and validation (Zêzere et al., 2004)

1.4.1. **Different types of models**

The first step in assessing slope instabilities is defining the susceptibility (LS), i.e., the spatial probability of slope instability occurrence. The most used methods for LS zonation can be synthetically divided into three main groups (van Westen et al., 1997, Carrara et al., 1999, Clerici et al., 2010):

i) Heuristic methods: These can be separated into qualitative and semiquantitative methods. The weight of the factors that produce instability is evaluated by the operator based on their own knowledge and experience, which lends this method substantial subjectivity. The Heuristic qualitative approach uses direct and semi-direct mapping methodologies which means that during the inventory a direct relationship is made between the events and terrain parameters. Heuristic methods are suitable for small-scales and regional surveys.

ii) Deterministic methods: This kind of method is based on engineering, geotechnical, or process-based approaches and requires a collection of

geotechnical parameters (e.g. normal stress, angle of internal friction, pore water pressure, etc). Deterministic methods due to their extreme variability of geotechnical characteristics are more effective only at single-slope scales, and are the most appropriate to use by engineers in the design of infrastructure or corrective works.

iii)   Statistics methods: This method can be divided into bivariate and multivariate.

Bivariate and multivariate methods are GIS-based and despite the methodological and operational differences, when applied to LS studies are based on the common assumption that slope failure in the future will be more likely to occur under the same conditions that led to past and present instabilities events (Zêzere et al., 2004, van Westen et al., 2006). It is assumed for LS analyses that the futures instability events can be predict by statistical relationships between past events and spatial information of the predisposing factors. In other words, these methods are carried out by evaluating the similarity between the conditions in such areas and the conditions that led to slope instabilities in the past (van Westen et al., 2006), using algorithms based on statistical/probabilistic analysis (Bayesian model) over a unique-condition of terrain units in a raster basis (Zêzere et al., 2004). The conceptual model focuses mainly on the following steps: (1) the mapping of the slope movements; (2) the mapping of a set of predisposing or precondition factors that are considered to be directly or indirectly connected with the slope instabilities and (3) the classification of the final predictive maps on the basis of the final statistical relationships.

1.4.1.1. Bivariate statistic methods

The technical principle of bivariate statistic methods is that all possible causative terrain parameters are entered into a GIS and crossed for their analysis with a slope instabilities distribution map. By the use of bivariate statistical methods, the role of individual or a combinations of parameters with regard to slope failures is statistically evaluated. Many statistical methods exist to determine the contribution of a certain parameter class to the occurrence of a slope movement. In this thesis the Informative Value (IV) method is used (Yan, 1988, Yin and Yan, 1988).

Yin and Yan (1988) define an information value to calculate the susceptibility for the occurrence of a slide, which is a logarithm of the ratio between the density of landslides in a class and the density of landslides for the whole study area. Chung and Fabbri (1993) developed statistical procedures under the name of predictive modelling, applying favourability functions on individual parameters. Using these statistical and probabilistic methods, terrain units or grid cells are transformed to new values representing the degree of probability, certainty, belief or favourability that the terrain units or grid cells may contain or be subject to a particular type of slope movement. The bivariate statistical methods give a satisfactory combination of the (subjective) professionally geared direct mapping (e.g. slope movement inventory, mapping predisposing factors) and the (objective) data-driven analysis capabilities from the use of GIS (van Westen et al., 1997).

Recent developments in GIS software and computer power permit an increased number of independent variables for data-driven slope movement susceptibility models. Recent studies involve over a dozen variables considered as predisposing factors of slope instability (e.g. Den Eeckhaut et al., 2010, Sterlacchini et al., 2011). The inventory of slope movements is considered the dependent variable in the models.

The drawback related to bivariate statistical methods is that it considers the assumption of conditional independence. Which in practice means that all the predisposing factors considered are independent with respect to the probability for the given type of slope movement, which in most of the cases are not valid. This drawback can be avoided or minimised by the user by making an evaluation and making a new parameter map by combining the dependent ones (van Westen et al., 1997).

1.4.1.2. Data integration

Data integration can be defined as the transformation of our experience of the real work into the computation domain, which can comply with models and rules with the aim to provide useful information (Chung and Fabbri, 1993). Quantitative representation of spatially distributed map patterns or phenomena plays a crucial role in data integration. It also defines the types of combination rules applied to them.

Maps are the representation of observations and interpretation of nature and can also include the interference of humans with nature, which is a basic and well-known concept still valid though time. Constructing thematic layers requires special care related to decisions and processes when selecting attributes, mainly accuracy and confidence (Chung and Moon, 1991, Chung and Fabbri, 1993).

Following Chung and Fabbri (1993), maps can present different types of information, such as: 1) continuous measurements; 2) discrete samples (e.g. sediment data); 3) distinct geometric objects (polygons, point and lines) for example landslides or mineral occurrences as implied by the authors and 4) complete polygonisation of map space. In some cases it is necessary to construct special-propose thematic maps where different aspects of complex associations of mapable features on phenomena are represented and grouped into classes for human use, such as assessment of natural hazards and environmental impacts, for instances. To fulfil this the first step is to define the purpose of the information integration and the second is to represent the map information in a standard way according to the defined purpose.

The data acquisition for modelling spatial data is nowadays mostly done by computer, where a set of attributes can be incorporated and used in the modelling. The data is characterised by high spatial variation (e.g. geologic layers, remotely sensed images and digital elevation) and the satisfactory representation is by using a "raster format". Raster files can contain a rectangle or matrix of numbers in each element, called a pixel (p). The value of a pixel may represent a terrain unit of the phenomena represented in the map (Chung and Fabbri, 1993). For spatial data integration studies, it is important that all the different sources of information are represented in the same format and use the same single data model format (e.g. pixel size). Using a raster model seems to be the most practical and coherent representation for statistical analysis and interpretation. (Chung and Fabbri, 1993). The raster format is, therefore, the format representation that will be used in this thesis (chapter 5 and 6).

Spatial integration is key for statistical modelling, whereby the rules work with different maps that can represent the phenomena to model. The representation of the Favourability Function considers a number (*n)* of layers of map data each containing a set of map units (in a single theme) for a given area (A) where a specific phenomenon

(e.g. slope movement) for a specific theme (D) is sought. Consider a pixel *p* in A and a proposition: T*p*: "*p* contains a phenomenon of type D" (Chung and Fabbri, 1993). The integration (or combination) rules for the data are determined by the method used, which in this thesis is the Bivariate Informative Value (IV) in the chapter 6.

1.4.2. Model validation (success and predictive rates)

An important and absolutely essential component is to carry out a validation of the prediction results. Validation of a model is essential in order for predictive models to be considered accurate (Chung and Fabbri, 2003). A predictive map can be validated using the data inventory data partition via 3 different procedures: i) temporal partition, which uses an inventory from two different dates; ii) spatial partition, whereby the inventory is divided between two different areas; and iii) random, where the inventory of past slope movements are randomly divided into groups, instead on two periods of time or two areas. (Chung and Fabbri, 2003).

1.4.2.1. Success-rate curves

Success-rate curves (SRCs) (Chung and Fabbri, 1999) are used to assess the performances of the models since success curves are computed using the same slope instability inventory training group that was used to compute the model. SRCs are made by plotting the cumulative percentage of susceptible areas (starting from the highest probability values to the lowest ones) on the X axis and the cumulative percentage of corresponding training points on the Y axis (Figure 1.14). The steeper the curve the better the capability of the model to describe the distribution of the slope movements considered in the model, which is also dependent of the slope instability distribution in the area.

1.4.2.2. Prediction rate curves

The predictive power of the maps is assessed using prediction-rate curves — PRCs (Chung and Fabbri, 2003). The methodology to calculate predictive-rate curves is the same as success-rate curves. Nevertheless, instead of the same training group, a prediction training group is used (that were not used in training the model), based in

one of the partition methods above mentioned. The predictive power of the three spatially divided inventories can be analysed by cross-validation.

The model should be computed using an older slope movement inventory, and more recent ones should be used for the evaluation of the prediction, as applied by (Guzzetti et al., 2006, Zêzere et al., 2008, Blahut et al., 2010).

Finally, the Area under the Curve (AUC) can be calculated. This area is expressed as a percentage of the graph that lies under the curve (Figure 1.14) and allows an easy comparison between success-rate curves and predictive-rate curves. Evaluation of the prediction power of the models remains a difficult task and for all approaches the quality of the predictive variable and inventory are essential to obtain high predictive models rates (Blahut et al., 2010). At closer to 1, the better AUC is for the predictive capability of the model for slope movement. A casual predictive rate will be manifested by 0.5 AUC (line in red). AUCs below 0.5 show models with a predictive power that is worse than a random one and should not be considered (Figure 1.14).

1.4.2.3. Sensitivity analysis

The sensitivity analysis is the last step to better understand the predictive models. The predictive capacity of the models does not automatically increase with the increasing number of variables assumed to be slope movements predisposing factors (Zêzere et al., 2008). Undertaking a sensitivity analysis attempts to discriminate the relevance of each predisposing factor for the predictive model, by crossing each one individual with the inventory of slope movements and calculating the AUC for each individual model (Pereira et al., 2012). This step, allows the understanding of which predisposing factors are most important for the slope instability in a given area, but also defines the best variable combination by computing the corresponding success and predictive rates (Guzzetti et al., 2006, Zêzere et al., 2008).
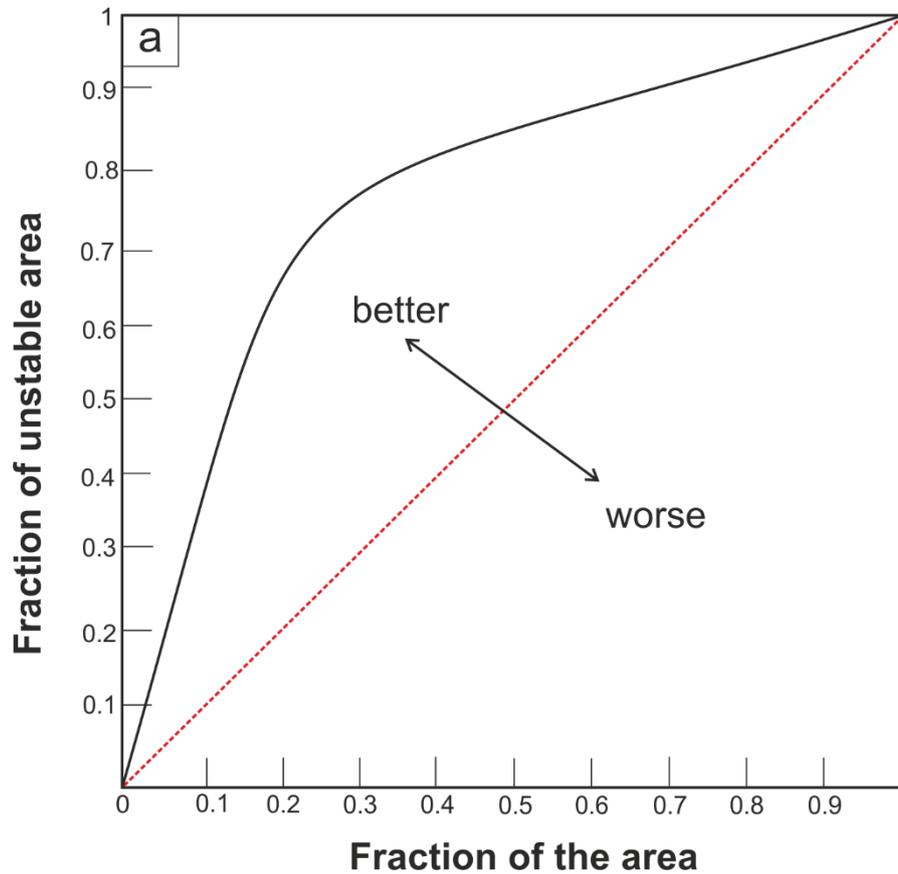
Figure 1.14 – Graphic definition of the Success and Predictive rata. The red dashed line shows an AUC of 0.50, random calculated.

1.5. **Structure or layout of the thesis**

This thesis is divided into seven chapters. This chapter contains the introduction, which highlights the rationale, research hypothesis and the literature review for the focus of this thesis. Chapter 2 presents an overview of the geological context of the Espírito Santo basin, emphasizing the key geological features that are the focus of this PhD thesis. Chapter 3 describes the methods used within this study, describes the seismic interpretation techniques and tools used. There is also a focus on the statistical methods and Geographic Information Systems integration for modelling presented in chapters 4, 5, and 6, which are the core results chapters of this thesis. Chapter 4 presents an analysis of salt tectonics and raft tectonics deformation within the Espírito Santo basin. Chapter 5 introduces the palaeo-topography and barriers on the gliding surface for two MDTs considered. Chapter 6 introduces a new approach to favourability score analyses for the

occurrence of MTDs, considering a set of predisposing factors. The general discussion and conclusions of the major findings of this PhD thesis are included into chapter 7. The appendices includes a brief summary of the processing algorithm, and calculation of the Informative Value method used in chapter 6.

Important contributions to knowledge from this research are:

iv)   The characterisation of the last stage of salt tectonics deformation, the raft tectonics, their forms of deformation and relationship with post-raft overburden and underneath salt layers.

v)   The geomorphologic characterisation of a topographic surface and its relationship with the MTDs.

vi)   The use of high resolution 3D seismic information as a source of data to compute morphometric attributes into a GIS environment.

vii) The use of statistics methods (bivariate) for the computation of favourability scores to the occurrence of MTDs.

GEOLOGICAL SETTING OF THE ESPÍRITO SANTO BASIN, SE BRAZIL

Chapter Two

2.1. **Introduction**

The aim of this chapter is to describe the regional geological and tectonic stratigraphy settings of Espírito Santo Basin and regional aspects of SE Brazilian Margin. The information presented within this section is important as a way to provide a coherent geological context for the remaining chapters of the thesis. It is also describes the seismic stratigraphy of the study area.

2.2. **Location of the study area**

The Espírito Santo Basin (ESB) is located along the SE continental margin of Brazil, specifically in the central and northern parts of the Espírito Santo state (Figure 2.1). It covers an area of about 125 000 km^2, the most part of which is offshore (107 000 km^2). The basin is delimited by the Campos Basin to the south (Fiduk et al., 2004), and the Abrolhos Plateau to the north (Figure 2.1). The Abrolhos Plateau is a volcanic structure generated in the Palaeogene (Mohriak, 2005) and limiting the Espírito Santo Basin at North.
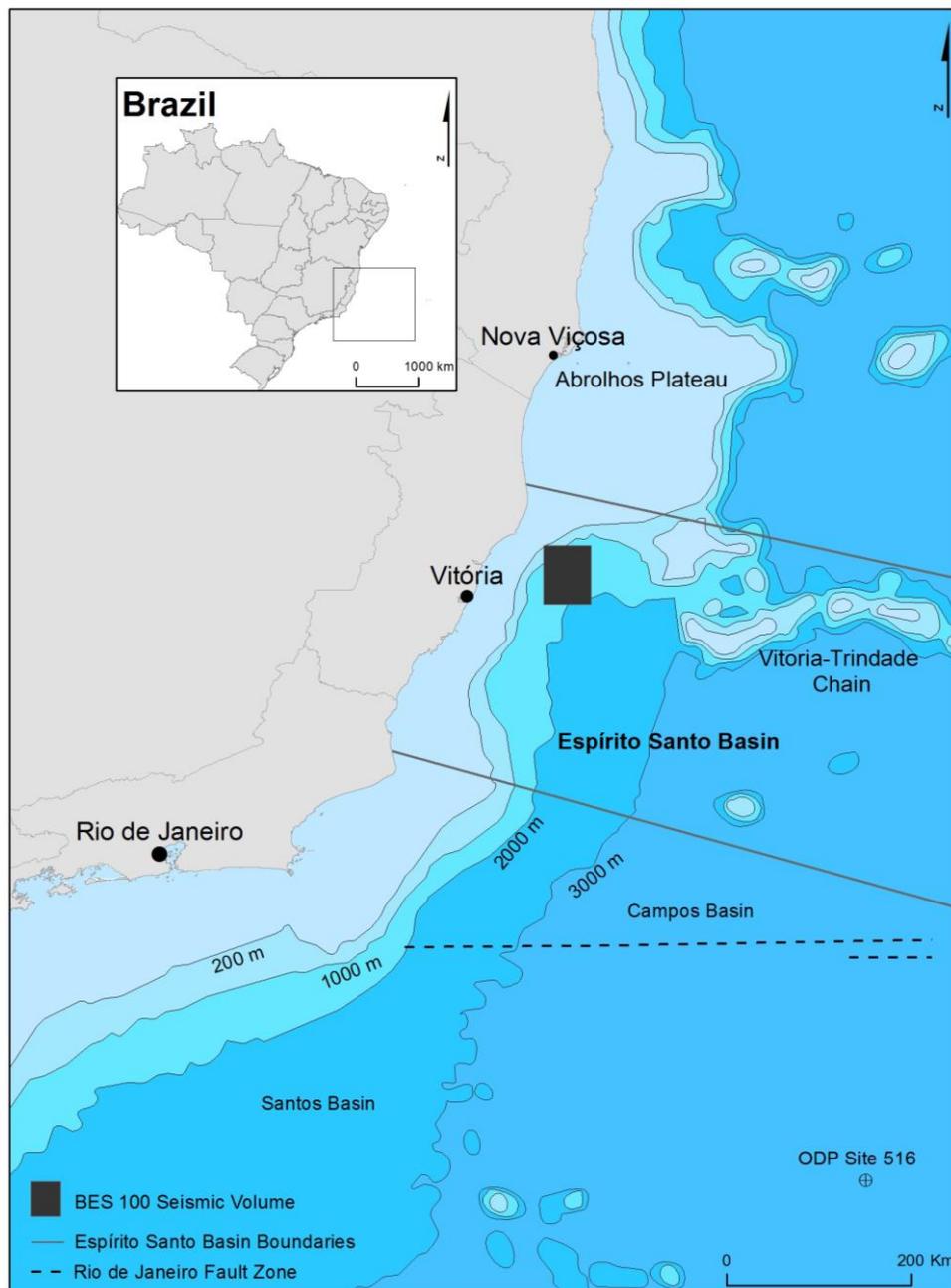
Figure 2.1 - Location and geographic limits of the Espírito Santo Basin, SE Brazilian Margin. The figure shows the location of the BES-100 seismic volume used in this thesis, roughly represented by the black rectangle. ODP Site 516 is indicated in the figure.

2.3. **Andean tectonic phases and their effect on SE Brazil**

The SE Brazilian margin is well known to have been affected by important tectonic episodes (França et al., 2007), some of which can be correlated to deformation pulses in the Central Andes (Mégard, 1984, Mégard et al., 1984, Gregory-Wodzicki, 2000).

These deformation pulses are chiefly materialised in the Espírito Santo by regional unconformities (França et al., 2007) (Figure 2.2).

In South America, the Andean Orogeny was triggered in the Late Albian, during an event named Mochica phase (Mégard, 1984, Mégard et al., 1984). The following tectonic event, the Peruvian phase (90-80 Ma; Scheuber et al., 1994) resulted in the deposition of extensive submarine channels, sands and finer-grained turbidites in the region where the study area is located.

A major reconfiguration of SE-Pacific oceanic plates occurred at 49 Ma, during the Eocene Incaic phase (Mégard, 1984, Isacks, 1988). The last Andean compressive events are divided into three distinct phases: the Quechua 1, 2 and 3 (Mckee and Noble, 1982, Mégard et al., 1984). The Quechua 1 phase occurred between ~20 and 12.5 Ma (Early to Midle Miocene; Mégard, 1984), affecting the western Cordillera, where it reactivated the Incaic structures, the Altiplano and probably the eastern Cordillera when crustal shortening during this phase was northeast-southwest trending. Extensive uplift followed this phase and subsequent erosion carved the main Puna erosions surface (Mégard, 1984). The Quechua 2 phase 9.5-8.5 Ma in the Ayacucho basin of central Peru (Mégard, 1984), was marked by important strike-slip movements many longitudinal NW-SE trending faults analysis of brittle tectonics indicates that this motion was N-S oriented. Shortening in a nearly E-W direction occurred during Quechua 3 (at ~6 Ma) in Ayacucho but is considered to be Pliocene in age in the sub-Andrean zone where it gave rise to the sub-Andean trust and fold belt (STFB) (Mégard, 1984). It fix a setting that contrasts with the N-S compression recorded at present in the eastern part of South America (Lima, 2003).
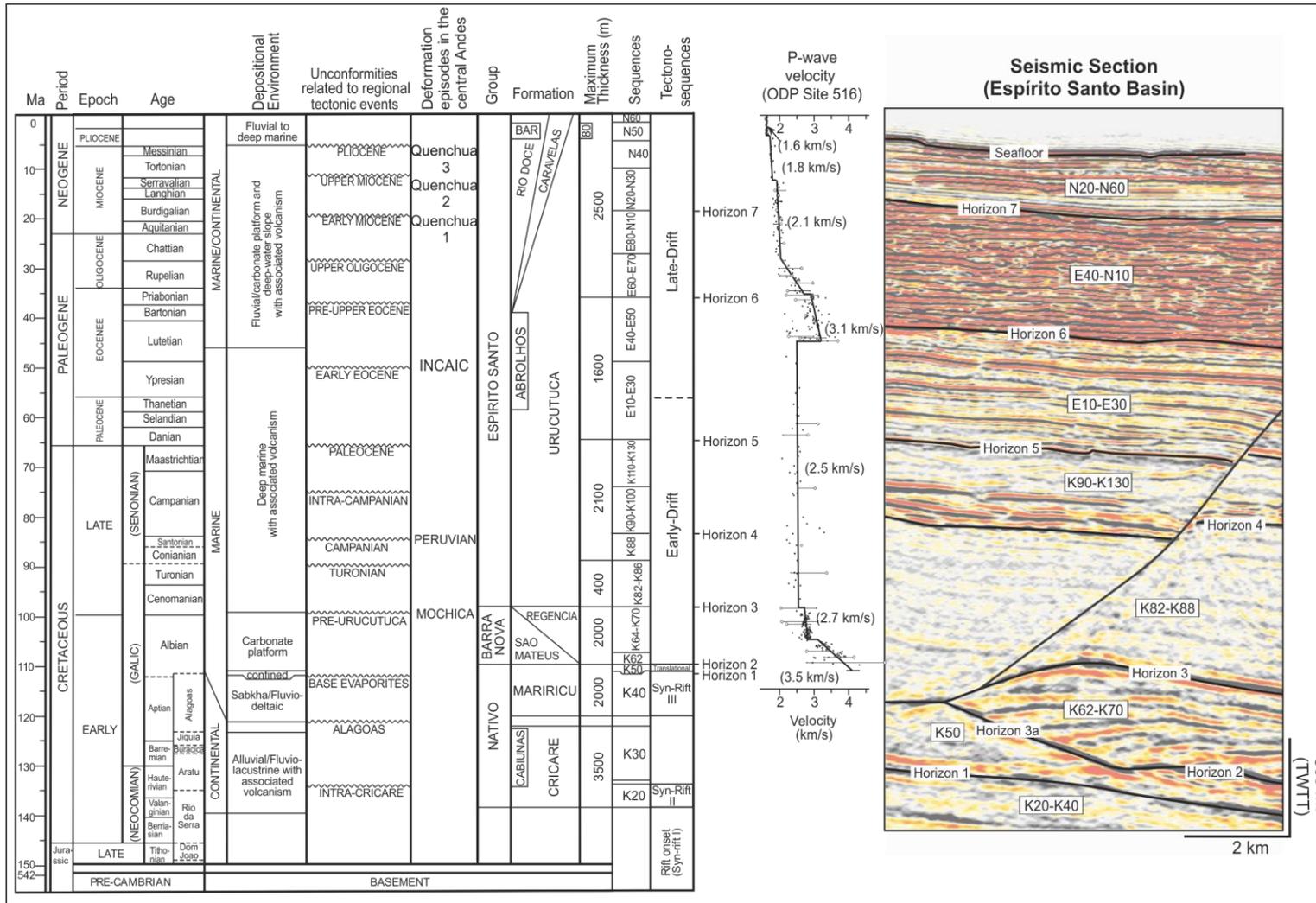
Figure 2.2 – Correlation panel between the interpreted seismic units and stratigraphic information from Espírito Santo Basin based on (França et al., 2007). Velocity data for ODP Site 516 (Barker et al., 1993).

2.4. **Tectonic and stratigraphic regional settings**

The Espírito Santo Basin is a typical rifted passive margin. It shares identical deformation histories with other basins of the SE Brazilian margin, in particular with the Santos and Campos Basins, two of the most well-known basins in the South Atlantic region (Figure 2.1).

The Espírito Santo Basin comprises a series of rift basins of Late Jurassic-Cretaceous age, which are located between the Victoria-Trindade High and Abrolhos Plateau. Its tectonic evolution records four distinct stages: pre-rift, syn-rift, transition and drift phase (Chang et al., 1992, Alves, 2012, Gamboa et al., 2012, Fiduk et al., 2004), which are materialised by five megasequences (Fiduk et al., 2004).

The initial **pre-rift stage** occurred from the Late Jurassic to earliest Cretaceous (Berriasian) (Figure 2.3). This stage included the events that preceded continental rifting, and is associated with the crustal uplift and development of a peripheral depression (Ojeda, 1982).

The **syn-rift stage**, dated from the late Berriasian/Valanginian to the early Aptian, is marked by significant tectonic activity that led to formation of rift basins (Ojeda, 1982, Demercian et al., 1993, Mohriak, 2005, França et al., 2007, Gamboa et al., 2011) during the divergent movement of the South American and African plates (França et al., 2007) (Figure 2.3). During this stage basic structural-stratigraphic framework of the Brazilian marginal basins was formed (Ojeda, 1982): i) a central graben along the intumescence axis of the rifting; and ii) asymmetric rift valleys, which were located between the central graben and the stable craton. This stage denotes the accumulation of lacustrine sediments in fault-controlled basins, followed by carbonate deposition at the beginning of the Aptian. The sediments recorded in this stage consist mostly of non-marine, fluvial, clastic, deltaic and deep-water basin deposits. The dominant lithologies are coarse to fine sandstones, silts and shales (Ojeda, 1982). Principal megasequences include the Cricaré and Marirícu Formations, which are composed of fluvial sandstones and syn-tectonic conglomerates intercalated with magmatic extrusive marking the igneous

activity in the Espírito Santo Basin (Ojeda, 1982, Chang et al., 1992, Mohriak, 2003, Fiduk et al., 2004).

The **transitional stage**, occurs between the Aptian and the Early Albian. It records widespread tectonic quiescence and the cessation of basement fault activity (Gamboa et al., 2011). Stratigraphically, this stage is marked by a transition from essentially continental syn-rift strata to marine drift units. These latter units mark the first marine incursions into the central graben of the southeast Brazilian rift basins (e.g. Dias, 2005). The transitional stage in SE Brazil records the deposition of more than 3000 m of evaporites, mainly halite and anhydrite resulting from extreme marine evaporation in arid climate conditions (Mohriak, 2003, França et al., 2007, Mohriak et al., 2008) under a relative tectonic stability. Ojeda (1982) identified two different episodes during the Aptian; the Paripueira cycle deposited during the early Aptian and the Ibura cycle during the late Aptian (Figure 2.3).

The **drift stage** is marked by continued spreading between the South American and African plates. The stage is dominated by open marine environments. It is divided into two main periods: Albian-Cenomanian (transgressive) and Turonian-Holocene (regressive) (Ojeda, 1982). In the first transgressive period, the major geologic events affecting the study area were: i) the development of shelf and slope physiographic features; (ii) the generalized deposition of a thick carbonate sequence as slope calcilutites and clastic fan-delta depositional system; (iii) local syntectonic conglomerate deposition; (iv) diapirism of salt and shale; and (v) the development of growth faults with salt displacement (Ojeda, 1982). During the second (regressive) period are recorded: (i) a pronounced migration of the South American plates; (ii) accentuated subsidence of the oceanic crust; and (iii) accumulation of a thick wedge of sediments during a transgressive sequence. The late Albian limit coincides with the top of the first (transgressive) sequence and is associated with erosion of the Regência and Fazenda Cedro palaeocanyons onshore and on the continental shelf. The basal deposits in the transgressive sequence consist of dark mudstones, turbiditic sandstones and local carbonates derived from the erosion of Albian carbonate
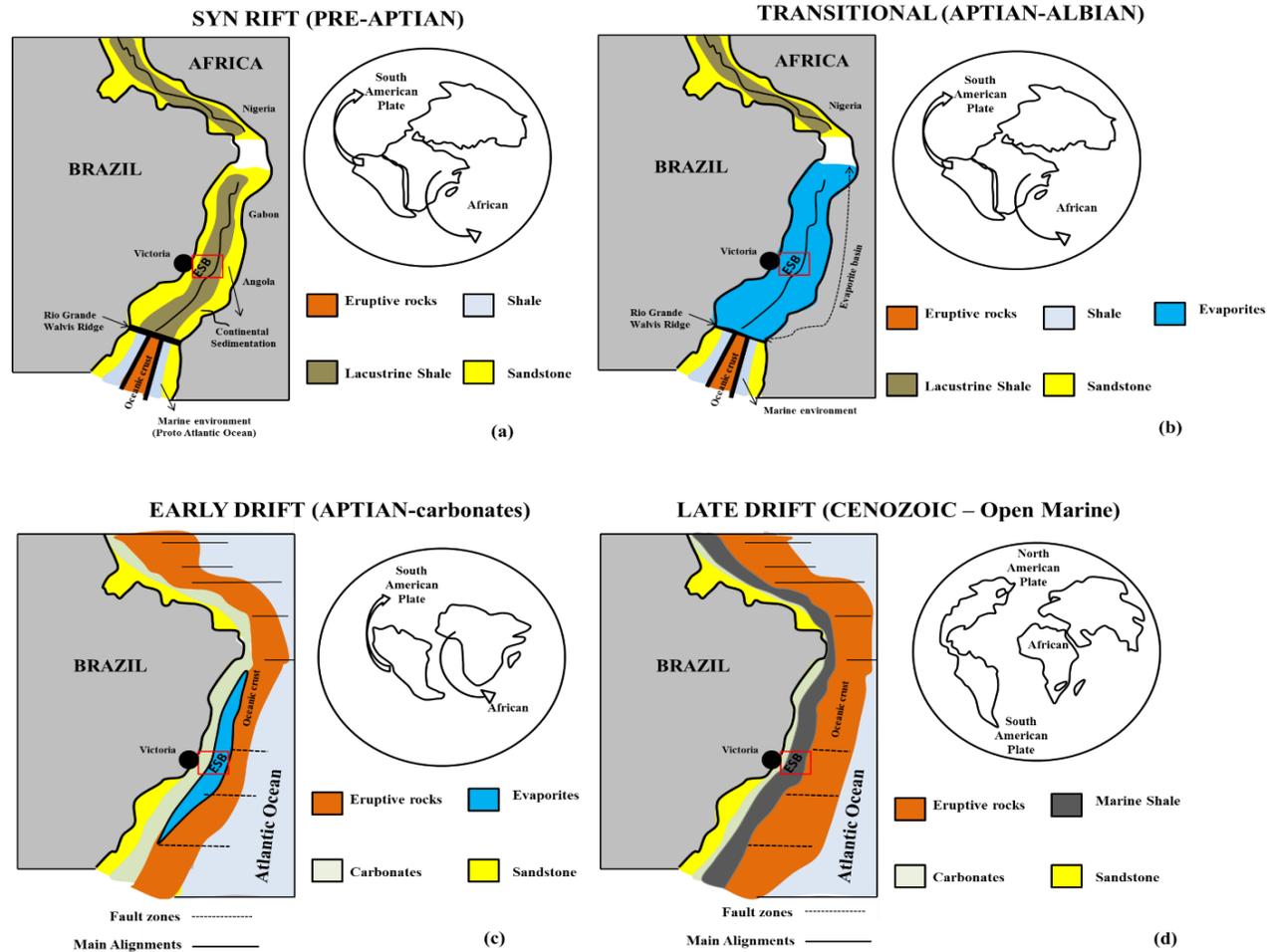
Figure 2.3 – Paleogeography and plate reconstruction of the Espírito Santo Basin during opening of the South Atlantic, from Aptian to Holocene. The red box highlights the relative position of the Espírito Santo Basin through time (Omosanya, 2014).

The regressive sequence suggests important tectonic activity marked by the reactivation of ancient rift structures and uplift of hinterland mountain chains. This resulted in a generalised sea-level drop and creation of a regional unconformity (Meisling et al., 2001, França et al., 2007).

The drift stage in the Espírito Santo Basin post-rift is, therefore, dominated by continental-slope embankment, incision of a submarine channel system and significant mass-gravitational processes, with salt tectonics playing a significant role in upper-crust deformation (Davison, 2007). Furthermore, it shows significant Late Cretaceous-Cenozoic halokinesis controlled by thin-skinned gravitational gliding of post-salt strata over Aptian evaporites (Demercian et al., 1993).

2.5. **Halokinesis in the Espírito Santo Basin**

Evaporites were accumulated in the Espírito Santo Basin during the Late Aptian to Early Albian transitional stage and are widespread along both the Brazilian and West African margins. As a result, the Late Cretaceous and Cenozoic evolution of the Espírito Santo Basin are mainly controlled by thin-skinned gravitational gliding, differential loading and gravity spreading above Aptian evaporites (Demercian et al., 1993, Fiduk et al., 2004). Deformation in the basin occurs in three (3) distinct tectonic domains: (i) extensional, which is located in the tilted margin; (ii) transitional, which is located in the mid-slope where salt are accumulated into diapirs (Figure 2.4); and (iii) compressional domain on the distal slope, where is observed allochthonous salt canopies (Demercian et al., 1993, Fiduk et al., 2004, Davison, 2007). In the study area are structures such as salt rollers, vertical salt diapirs, allochthonous salt tongues, shallow canopies coalescing from the combination of two distinct tongues, deep salt canopies, and trusted salt nappes (Fiduk et al., 2004, Omosanya and Alves, 2013). This salt is dated as late Aptian and corresponds mainly to halite with intercalations of less soluble salt (anhydrite) and more soluble K-rich salts, such as sylvite, carnalite and tachydrite (Mohriak et al., 2008). The modern seafloor is deformed by several diapirs and salt canopies developed through the entire Cenozoic as a result of high sediment-input rates on the continental
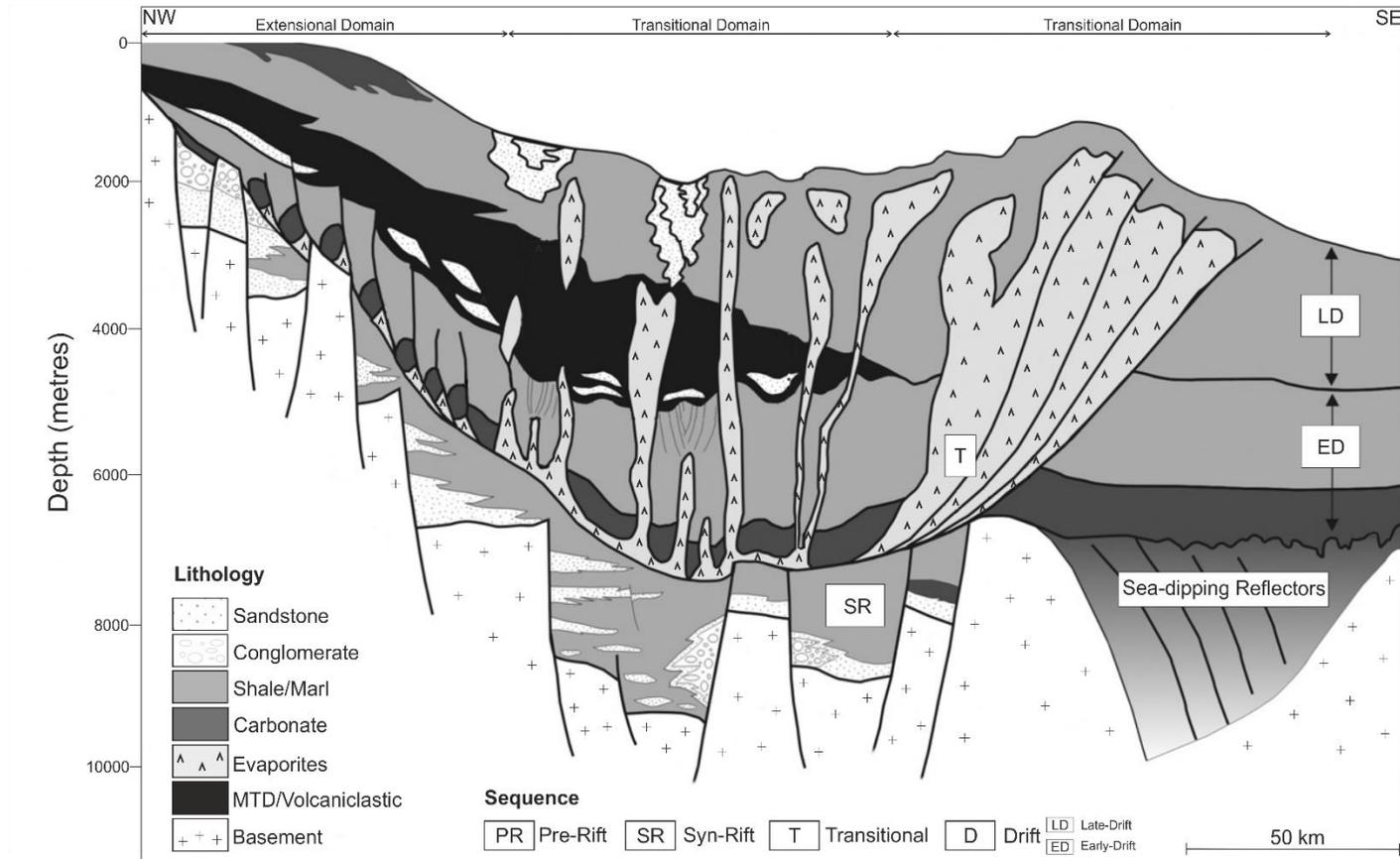
Figure 2.4 - Sketch showing the relative location of the study area on the continental slope of Espírito Santo. Modified from Fiduk et al., (2004); Gamboa et al., (2010) and Omosanya and Alves (2013). SR – Syn-Rift sequence, T – Transitional sequence, ED – Early Drift sequence, LD – Late Drift sequence. Dashed line indicates the relative position of the interpreted seismic volume.

slope (Lima, 2003, Fiduk et al., 2004, Gamboa, 2011). The emplacement of the Abrolhos Plateau is also considered to have controlled salt deformation by inducing tectonic movements on the margin, thus accelerating gravitational gliding processes and the subsequent deformation of salt structures during the Early Cenozoic (Fiduk et al., 2004, Gamboa, 2011). The deformation of the Aptian salt layer into growing salt structures resulted in multiple stages of faulting (Baudon and Cartwright, 2008, Alves et al., 2009) (Figure 2.5). The fragmentation of post-salt strata generated isolated blocks of Albian carbonates, named 'tectonic rafts' (Alves, 2012). Large roller and keystone faults propagated from these rafts into the post-raft overburden in the Late Cretaceous and Palaeocene. These faults are truncated by the Early/Mid-Eocene unconformity (Gamboa, 2011). In Late Eocene to Holocene strata faulting is less significant, but there is reactivation of the older faults due to the collapse of salt structures - with very little to insignificant expression on the actual seafloor (Baudon and Cartwright, 2008, Alves, 2012).

Halokinetic movements thus play an important part in the Espírito Santo Basin evolution. Since its early deformation stages, halokinesis is closely associated with the triggering of expressive and important fault systems at depth (Figure 2.5). The resulting stratigraphic units deposited in the Espírito Santo Basin were mainly deposited during the transgressive and high stand episodes during the Cenozoic, followed by regressive episodes recording widespread submarine canyon incision (Fiduk et al., 2004). Consequently, the very thick Tertiary sequence in the Espírito Santo Basin continental slopes is composed of a mixture of carbonate and clastic sediment. In such a context, mass-wasting events offshore Espírito are a result of regional tectonic movements (Mohriak et al., 2008) and slope instability related to halokinesis (Fiduk et al., 2004).
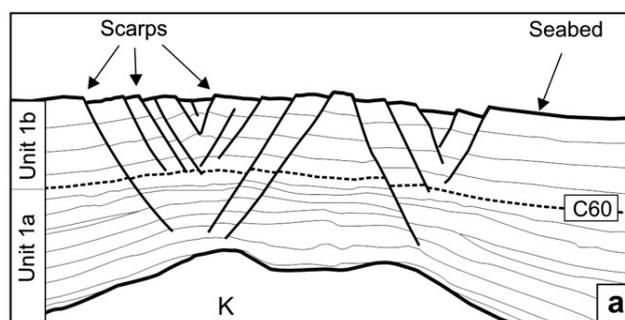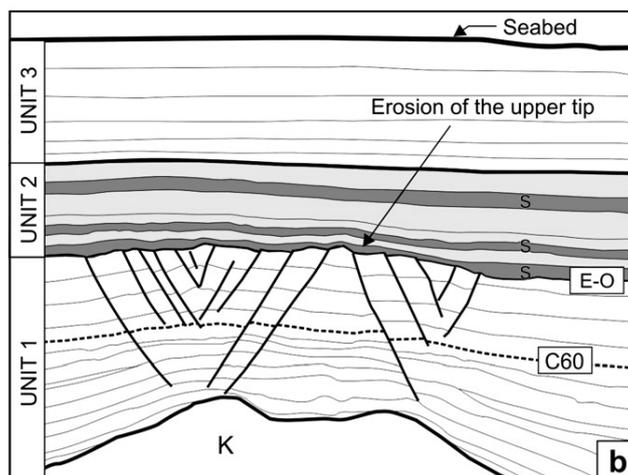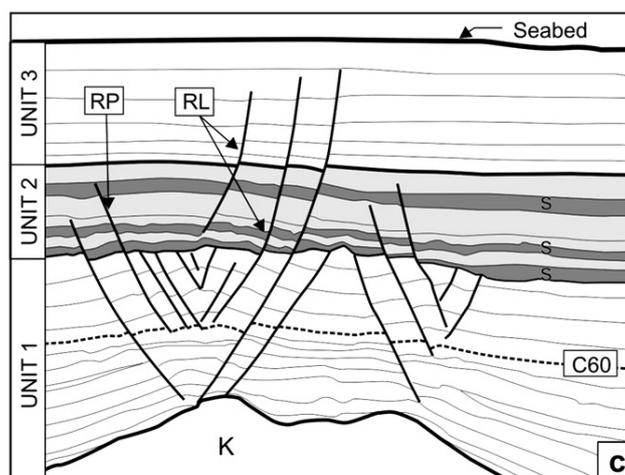
Figure 2.5 - A three-step evolutionary model for the crestal graben faults from Espírito Santo Basin. (a) First phase of faulting occurred between the early Cenozoic (time of formation of major anticlines) and the late Eocene (time of deposition of the sediments in the upper part of Unit 1b). Most of the uplift of the Cretaceous sequence (K) was contemporaneous with the deposition of sediments that compose Unit 1a. The faults offsetting Unit 1 were active at the deposition of the upper part of Unit 1b. (b) Period of quiescence during deposition of Units 2 and 3. (c) Phase of faulting 2 by blind propagation of post sedimentary faults resulting in the reactivation of faults situated in Unit 1 by upward post-sedimentary propagation (RP) into Units 2 and 3 or reactivation by linkage (RL) of a fault that initiated in Units 2 and 3 and propagated downwards to link with faults in Unit 1. Dark shaded areas represent the slump deposit intervals. (Baudon and Cartwright, 2008)

2.6. **Structural setting of the Espírito Santo Basin**

Continental rifting, and subsequent break-up associated with the opening of Southern Atlantic Ocean, contributed to shape the structural framework of Espírito Santo Basin. Structures generated at this time include antithetic step-fault blocks, synthetic step-faults, hinges with compensation grabens, structural inversion axes, homoclinal structures, growth faults with rollovers, salt and shale and also some structural features related to igneous activity (Ojeda, 1982, Fiduk et al., 2004, Mohriak, 2003).

In detail, the study area crosses a region of salt structures, on the mid-continental slope, comprising a series of horsts, grabens and salt-related faults (Figure 2.4). As a result, three main phases of fault growth are observed in the study area, including faulting of overburden strata on salt crests linked to the development and later withdrawal of salt from diapirs (Alves et al., 2009, Alves, 2012, Omosanya and Alves, 2014, Omosanya, 2014). Omosanya (2014), pointed out three different stages of faulting on the Espírito Santo continental slope:

(i)   Early Paleocene to late Eocene, in which halokinesis triggered the growth of extensional faults set on the crest of rising salt anticlines. These faults propagated through the Late Cretaceous and Eocene strata and were mostly truncated by the mid-Eocene unconformity;

(ii)   These latter fault sets were then eroded during the deposition of mass-transport complexes (MTCs) and submarine channels in late Eocene to Oligocene times during a period of tectonic inactivity;

(iii)   Reactivation of older faults sets by vertical propagation and dip linkages in late Cenozoic were dependent on movements of Albian rafts and cessation of tectonic slope tilting (Alves, 2012). Faulting of Late Eocene to Holocene strata is less expressive, reactivated faults have poor or no expression on the modern seafloor (Alves, 2012).

In parallel, the structural inversion of the East Brazilian Rift System (EBRIS) is recorded in the study area and was influenced by plate-wide horizontal compression associated with the Andean Orogeny (Cobbold, et al., 2010). This resulted in the reactivation of multiple faults reactivation in the study area and throughout the Southeast Brazilian margin. During the

Cretaceous and Cenozoic, Early Cretaceous and older structures on rifted margins of SE Brazil were reactivated as a result of far-field stresses and hotspot activity. That reactivation occurred as a right-lateral mode during three main phases (Late Cretaceous, Eocene and Neogene), which correlate with changing conditions of convergence at the Andean margin of South America (Cobbold et al., 2001).

2.7. **Seismic Stratigraphy**

The seismic stratigraphy of the Espírito Santo Basin is correlated here with lithostratigraphic information in França et al. (2007), Alves and Cartwright (2009) and Alves (2012). Figure 2.2 includes a seismic section showing the horizons interpreted and mapped in this work: a) base (horizon 3a) and top rafts (horizon 3), b) base Santonian (horizon 4) and c) seafloor, which mainly divided the stratigraphic packages considered in this work. For further detail, the interpreted seismic-stratigraphic units are summarised in Table 2.1.

Despite the description of all stratigraphic packages that are observed in the Espírito Santo Basin, which are all affected by the processed described in this thesis. The focus are in the Aptian salt (K50), mainly constituted by halite intercalated with carbonate intervals and anhydrite. The Albian package (K62-K70) consists mainly of sand, silts, ooliticlimestones and marls, which are basically the material of the Albian rafts. These two stratigraphic packages are focused in the chapter 4, while the chapter 5 and 6 are focused on the sequence N20 – N60 constituted by sandstones, calcarenites and marls. As the study are located at continental slope is expected a sedimentary package marked by high percentage of sandy materials.

2.7.1. **K20 to K40 sequence (Earliest Cretaceous to Early/Mid Aptian)**

The K20-K40 sequences comprise syn-rift and early post-rift strata below the imaged tectonic rafts (Figure 2.2 and Table 2.1). The lower boundary of K20 is marked by a surface of moderate-amplitude, locally diffractive reflections which marks the top of basement rocks. The contact between K20 and K30 is hardly observed, as sequences comprise moderate to high amplitude, low frequency reflections. K40 has higher amplitude and is more continuous than K20 and K30.

The boundaries between K20, K30 and K40 are difficult to distinguish on the interpreted seismic volume partly because all sequences comprise moderate to high amplitude, low frequency reflections (Figure 2.2). Nevertheless, K40 shows higher amplitude reflections, more laterally continuous, than K20 and K30.

K20 comprises the oldest units in the study area (dated as belonging to the Valanginian) and forms the base of the Nativo Group (Cricaré Formation). Heterolithic conglomerates and coarse sandstones, observed in proximal regions of Espírito Santo, grade into fine-grained mudstones towards distal areas (França et al., 2007). The K30 sequence comprises volcanic and volcaniclastic rocks intercalated in sandstones and conglomerates (Jaguaré Member), changing into shales, marls and carbonate units towards more distal regions (França et al., 2007). The basal post-rift Sequence K40 comprises conglomerates and sandstones grading into fine sandstones and shales deposited in lacustrine and sabkha environments (Membro Mucurí, França et al., 2007).

2.7.2. **K50 sequence (Aptian)**

The K50 sequence comprises the core of salt pillows and diapirs in the study area. It shows chaotic to low amplitude reflections in its interior (Figure 2.2 and Table 2.1). Its lower boundary consists of an irregular reflection with moderate to high amplitude, below which high amplitude strata are observed. Its top boundary coincides with the first continuous strata above the imaged salt structures. In the data interpreted in this work, the K50 sequence is only preserved within triangular salt anticlines (rollers) formed between displaced rafts (Figure 2.2).

The K50 Sequence was deposited in a series of confined basins in conditions of high evaporation (França et al., 2007). Carbonate and anhydrite intervals predominate in shallow marginal areas of Espírito Santo, whereas halite is more abundant in the central and distal parts of the basin (Table 2.1).

2.7.3. **K62 to K70 sequences (Albian)**

The K62 to K70 sequences comprise high-amplitude internal reflections deposited above K50 and the basal K20 to K40 sequences. The lower boundary of K62-K70 is coincident with

Horizon 2. The top (Horizon 3) comprises an angular unconformity in the study area (França et al., 2007).

The thickness of K62-K70 reaches 600 ms two-way travel time (TWTT) in the interpreted seismic volume (Table 2.1). The sequences include marine strata, mainly sands, silt, shales and oolitic limestones and marls, which are partly time equivalent to Unit 7 at DSDP Site 356 (Kumar et al., 1977) and to the onshore Regência Formation (Bruhn and Walker, 1997, Fiduk et al., 2004, França et al., 2007). The top of K62-K70 is an angular unconformity in the proximal regions of the Espírito Santo Basin, and changes into a paraconformity in deeper waters (França et al., 2007).

2.7.4. **K82 to K88 sequences (Late Albian to Santonian)**

The K82 to K88 sequences comprise continuous, low-amplitude reflections deposited above Albian-Aptian rafts and salt structures. The lower boundary of K82-K88 is sharp, and marked by growth onto major faults above Horizons 2 and 3. The upper boundary of Late Albian-Santonian strata is an irregular high-amplitude reflection representing an unconformity (Horizon 4) of Santonian age (França et al., 2007).

In the K82-K88 sequences are included shales and turbidite sands (França et al., 2007). Locally, the lower boundary of K82 contains carbonate breccias derived from eroded Albian carbonate platforms. The K82-K88 sequences belong to the lower Urucutuca Formation.

2.7.5. **K90-K130 sequence (Late Santonian to Maastrichtian)**

A major unconformity related to the incision of a Late Santonian to Maastrichtian channel system is observed in the study area above low-amplitude strata of K82-K88 (Golfinho Field, Vieira et al., 2007). This same boundary (Horizon 4) is marked by high-amplitude reflections above a faulted succession (Figure 2.2). Growth of strata onto roller faults is observed below the unconformity. A regional unconformity of Late Maastrichtian age (Vieira et al., 2007) marks the upper boundary of K90-K130.

K90-K130 comprises the middle part of the Urucutuca Formation (Fiduk et al., 2004; França et al., 2007). The main lithologies in the sequence are turbidites and shales, changing into marly successions towards more distal parts of the Espírito Santo Basin (França et al., 2007).

2.7.6. **E10-E30 sequence (Paleocene to Early Eocene)**

The E10-E30 sequence comprises high-amplitude seismic reflections intersected by closely-spaced normal faults. Its lower boundary coincides with the Maastrichtian unconformity. The upper boundary of the sequence is marked by Horizon 6, a regional unconformity above which moderately faulted high-amplitude strata are observed. In the E10-E30 sequence are observed sandstones and shales with offlap geometries on regional seismic data (Figure 2.2). This geometry has been interpreted as resulting from tectonic uplift of the basin shoulder areas during the early Cenozoic (França et al., 2007).

2.8. **E40 to N10 sequences (Eocene to Early Miocene)**

The E40 to N10 sequences are composed of reflections deformed by closely-spaced normal faults. The age of E40-N10 ranges from the Eocene to the Early Miocene, i.e. it comprises equivalent strata to the upper part of the Urucutuca Formation (França et al., 2007). The E40-N10 sequences comprise turbidite sands intercalated with volcaniclastic deposits (França et al., 2007) (Table 2.1).

2.8.1. **N20 to N60 (Early Miocene to Holocene)**

The N20-N60 sequences comprise chaotic to continuous seismic reflections. The sequences belong to the Rio Doce, Caravelas and Urucutuca units, and are at places eroded by submarine channels. Strata in these sequences comprise sandstones (Rio Doce Formation), calcarenites (Caravelas member) and turbidite sands and marls (Urucutuca Formation). Mass-transport complexes and channel-fill deposits are abundant throughout the basin after the Early Miocene (França et al., 2007) (Table 2.1).

Table 2.1 - Summary of the seismic-stratigraphic character of interpreted units in the Espírito Santo Basin. Lithological data from França et al., (2007). Modified from Alves, 2012.

TWTT Thickness (ms)	Age (Sequence)	Seismic facies	Lithology	Description
100-850	Early Miocene (N20-N60)	Chaotic to continuous reflections.	Sandstones, calcarenites and marls	Incised by submarine channels at places. Include strata from the Rio Doce, Caravelas and Urucutuca Formations.
200 – 1000	Eocene to Early Miocene (E40 – N10)	High to moderate-amplitude internal reflections.	Coarse grained turbidites, volcaniclastic sands and fine-grained strata	Composed of prograding high-amplitude reflections deformed by closely spaced normal faults.
300 – 600	Maastrichtian to Early Danian (E10-E30)	High amplitude internal reflections	Sandstones and shales	Lower boundary coincides with an unconformity of Maastrichtian age. The top of the unit is marked by another (Danian) regional unconformity.
0 – 500	Late Santonian to Maastrichtian (K90-K130)	Moderate to high amplitude reflections. most filling erosional channels	Interbedded sandy turbidites and shales	Lower boundary comprises a sharp erosional boundary marking the base of the first submarine channels deposited in the basin.
700 – 1500	Albian to Santonian (K82-K88)	Low amplitude internal reflections. mostly continuous. Drapes Albian rafts and adjacent salt structures	Calcareous shales, intercalated with turbidite sands. Carbonate breccias. Some eroded strata derived from Albian rafts.	Lower boundary is sharp, marked by the appearance of low-amplitude reflections above Albian rafts and salt.
0 – 600	Albian (K62-K70)	High-amplitude reflections with low frequency. Localised	Sand, silts and Ooliticlimestones and marls.	The lower boundary of the Albian sequence coincides with the base of the

		growth and downlap are visible		interpreted rafts. The upper boundary of the unit comprises an angular unconformity on the proximal margin (França et al. 2007; Alves, 2012).
0 – 1800	Aptian (K50)	Chaotic to low amplitude reflections.	Halite intercalated with carbonate intervals and anhydrite.	Triangular salt anticlines structures formed between displaced rafts.

DATA AND METHODS

Chapter Three

3.1. **Introduction**

The results presented in chapter 4, 5 and 6 are based on the interpretation of three-dimensional (3D) seismic data with high-resolution, the BES-100 cube from offshore Espírito Santo Basin, SE Brazil (Figure 2.1 – chapter 2). Chapter 5 and 6 use Geographic Information Systems (GIS) by computing topographic information for morphological characterisation, spatial analysis and MTD modelling to obtain MTD favourability scores.

The aims of this chapter are: i) to present information on the seismic data set used in the thesis; ii) to give a brief overview of seismic acquisition, survey parameters and processing sequence of the BES-100 cube; iii) to outline the seismic interpretation methods followed in the thesis and the way seismic data was integrated into GIS, and iv) to outline the statistical methods used to compute the favourability scores for MTD occurrence, and corresponding scientific validation.

3.2. **Three-dimensional (3D) seismic data**

The importance of three-dimensional (3D) seismic data increased substantially in late 1980s and early 1990s (Brown, 2004, Bull et al., 2009). Its application is mainly focused on exploration for oil and gas resources and became a requisite tool in those terrestrial and marine surveys since that time (Brown, 2004). It has largely improved our understanding of sub-surface geology and associated 'geohazards' during the exploration (and production) of hydrocarbon and minerals (Cartwright and Huuse, 2005).

Three-dimensional seismic imagery derives from the acquisition of very closely-spaced data, and provides high-resolution information of the surface and subsurface strata in the horizontal and vertical directions (Bacon et al., 2003). The seismic acquisition is focused on the detection of compressive P-waves, which are reflected back to the surface at geological interfaces. The advantage of 3D seismic imagery, when compared to 2D data, is that it allows the improvement of spatial interpretations of geologic features. That improvement is particularly important in areas where the geology is markedly complex (Yilmaz, 2001).

In marine surveys, the data is acquired by generating a signal from an energy source near the surface, which is tuned to emit concentrated energy pulses downwards (Figure 3.1). Part of the energy reflected at subsurface geological boundaries is then detected by hydrophones at the surface, which record the two-way travel time (TWTT) in seconds or milliseconds that P-waves take to travel from the source until they return to the surface (Gamboa, 2011). The direction in which waves are shot is the inline direction, being coincident with the boat track and orientation of the hydrophone arrays. The perpendicular direction to this is called the crossline direction. In order to obtain high-quality data, trace spacing in 3D seismic surveys is performed at 12.5 to 25 m for inlines and at 25 to 50 m for crosslines (Yilmaz, 2001). A rule-of-thumb is that marine seismic reflection surveys mostly image P-wave reflections because fluids do not transmit S-waves (e.g. Sheriff and Geldart., 1995, Bacon et al., 2003). Essential to the seismic reflection method is the property of a layer designated acoustic impedance (Z), and can be defined as:

Equation 3.1

$$Z = pV$$

Where *p* represents the density of the rock or the sediment and *V* represent the velocity of a P-wave through the geologic body. This way, the geological boundaries between rocks or lithologies with different physical properties (density) are resolved as layers of different acoustic impedance, with strong acoustic impedance contrasts resulting in a strong reflections on seismic.

An increase in acoustic impedance is generally displayed as a "peak" on seismic data and is reflected as a positive amplitude, while a decrease in amplitude being displayed as a "trough" or negative amplitude (Bacon et al., 2003) (Figure 3.2). Seismic waves are commonly displayed in distinct colours in what is termed 'SEG' (Society of Exploration Geophysicists) normal polarity (Brown, 2004).
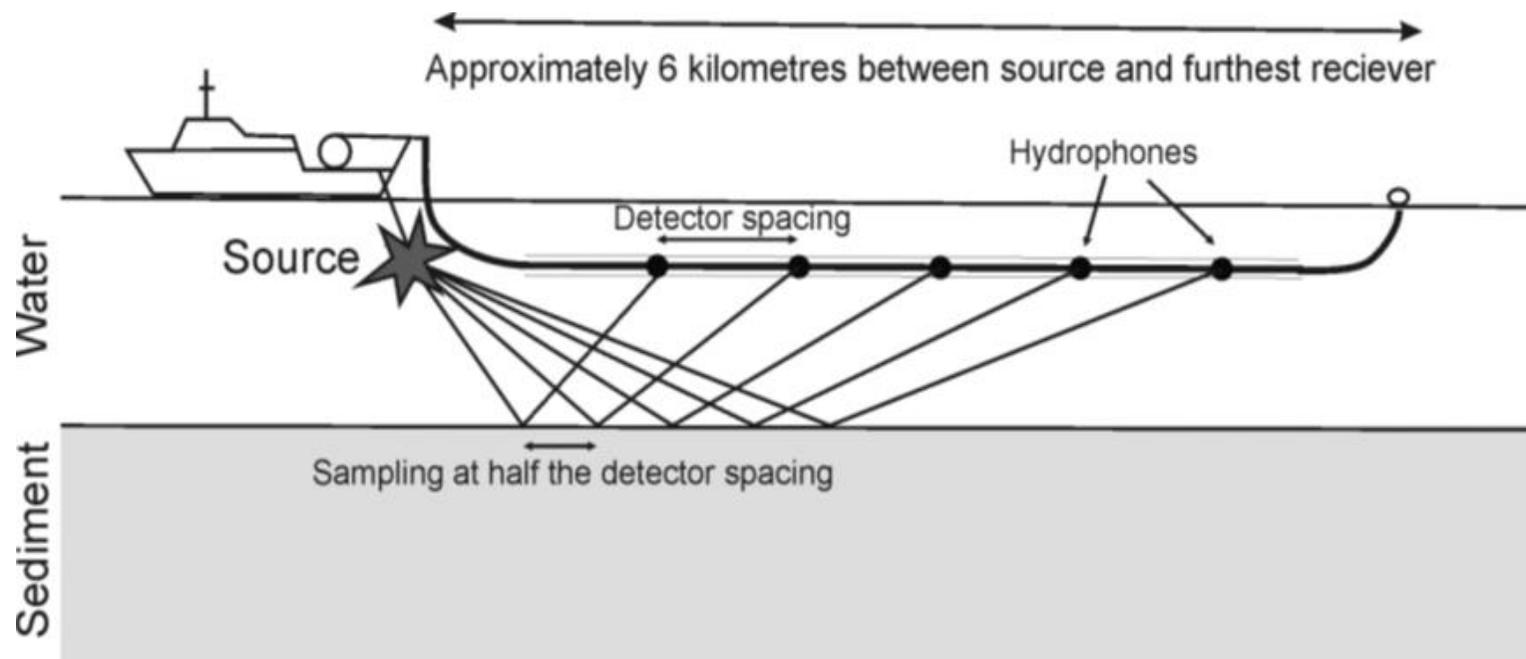
Figure 3.1 - Schematic representation of the acquisition geometry of 3D marine seismic surveys. An acoustic source on the surface emits a sound wave that travels through the water body. As soon as the wave reaches the seafloor, and the properties of the rock change, P-waves are reflected back to the surface and detected by hydrophones. Hydrophone spacing controls the horizontal resolution of the seismic (Gamboa, 2011, modified from Bacon et al. (2003).
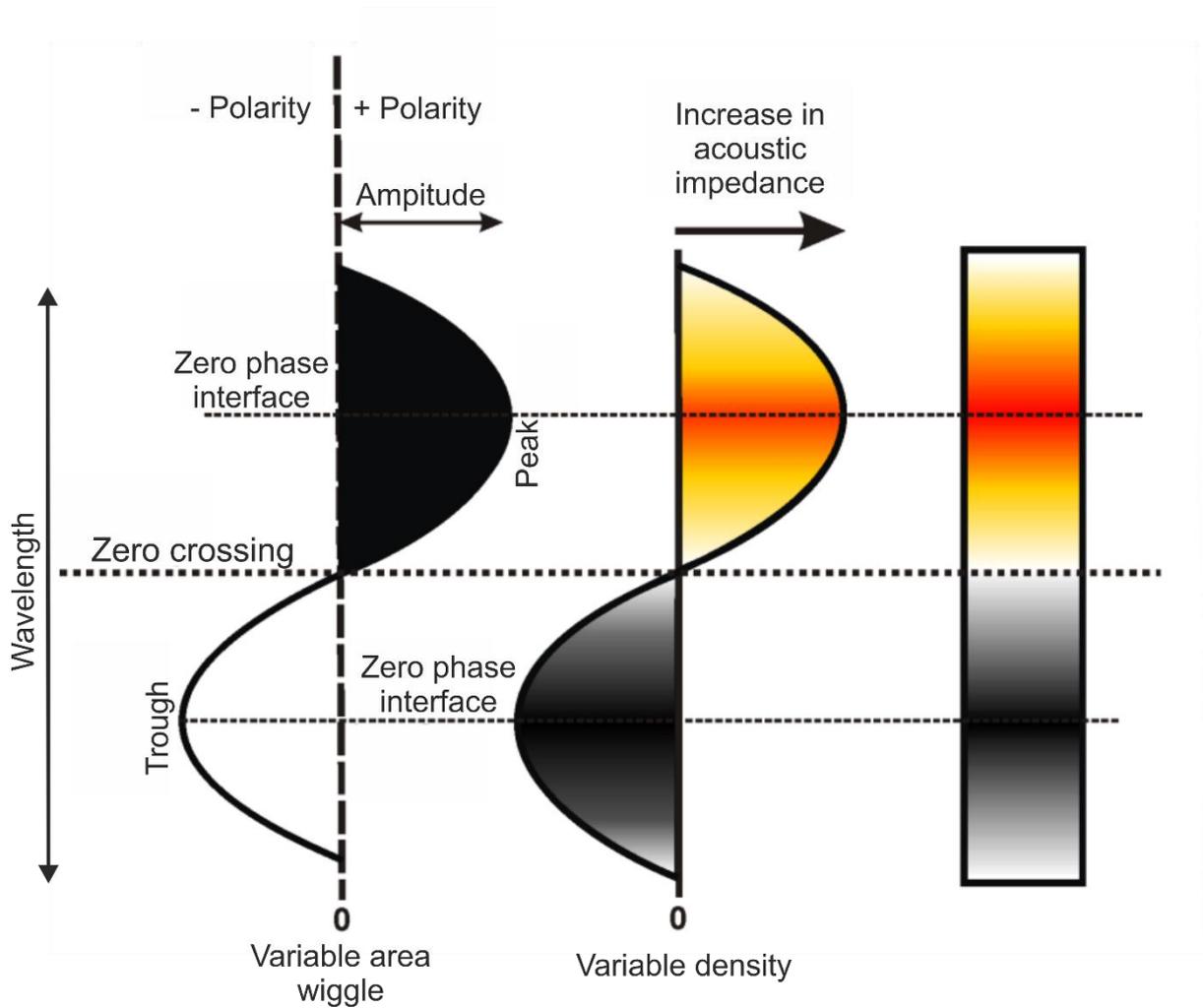
Figure 3.2 - Schematic graphic of seismic data displayed in SEG normal polarity zero phased data. The variable area wiggle display 'troughs' (negative amplitude values) are displayed in white, and 'peaks' (positive amplitude values) are displayed in black. Variations in density and p-wave velocities are displayed as colour-coded voxels, which indicate their amplitudes. Modified from Hart (1999).
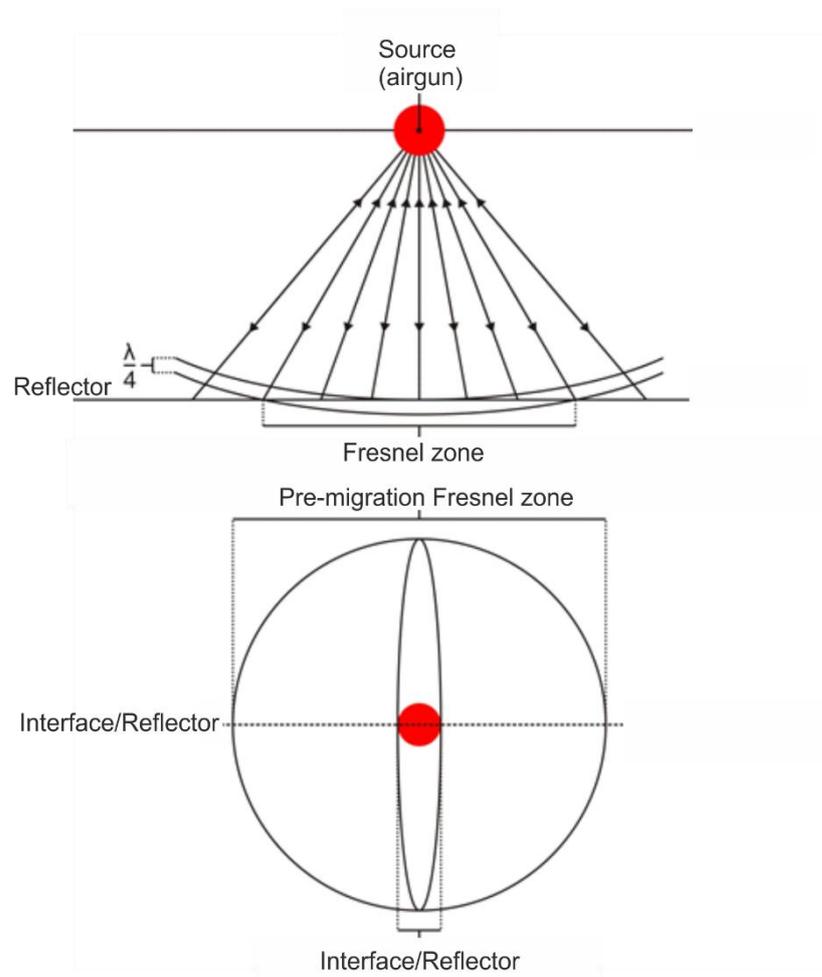
Figure 3.3 – The energy emitted from an airgun returned to the source from all the reflector points. The region of the reflector from which energy is returned within half a wavelength of the initial refection arrival is referred to as the Fresnel Zone. Fresnel Zone is the key control of the resolution and 3D seismic migration reduces Fresnel size zone. Modified from Brown (2004).
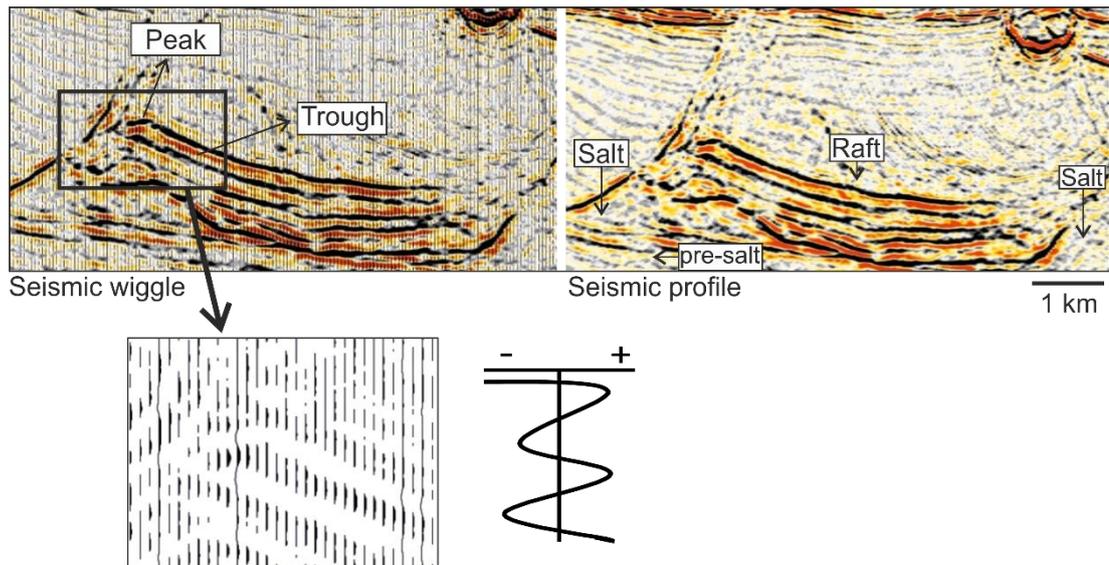
Figure 3.4 – The seismic volume used in this thesis is displayed in normal SEG convention. The figure highlights troughs and peaks on an Albian raft and their final aspect on the interpreted seismic volume.

The width of the Fresnel zone and the spacing of the detectors (hydrophones) are the two factors that control the horizontal resolution of seismic data (Figure 3.3 and Figure 3.4). The Fresnel zone is defined by the energy returned to the detector in an interval of half a wavelength of the initial arrival (Figure 3.3). Within that zone, reflected waves affect constructively to provide the reflected signal (Kearey et al., 2009). In order to prevent any inaccuracies generated by reflections that have been misplaced due to variations in dip and reflection patterns from points and edges hydrophone spacing determines the spacing, relative to the estimated depth, from which the subsurface interface can be reconstructed (Brown, 2004).

3.3. Exploration 3D data survey parameters

3.3.1. Espírito Santo Basin

A three-dimensional (3D) seismic volume from offshore Espírito Santo Basin, SE Brazil, is the dataset used in this work, acquired by CGGVeritas© (Appendix I). The interpreted seismic volume images sub-surface strata on the continental slope at water depths between 100 m and 1800 m (Figure 3.5). The seismic volume was named block BES-100 and was acquired using the coordinate reference system WGS_1984_UTM_Zone_24S.

In chapter 4 a seismic block is used covering an area of 1120 km^2. In chapters 5 and 6 are used cropped seismic volumes with 770 km^2 imaging MTD-prone areas to the south of the larger seismic cube. The datasets were acquired using a dual air gun array and six streamers, 5700 m long. Data processing included resampling, spherical divergence corrections and zero-phase conversions undertaken prior to stacking (Fiduk et al., 2004, Omosanya, 2014).

3.3.2. **Seismic processing**

The main aim of the seismic processing is to obtain the most accurate representation of geologic bodies and any relevant subsurface information. It is an ambitious and time consuming process that aims to produce high signal-to-noise ratios from the raw seismic data. Seismic processing is a complex process from which further details are provided by Sheriff and Geldart. (1995) and Yilmaz (2001).

3.3.3. **Seismic frequency and resolution**

The frequency or spacing defines the quantity of reflectors per unit of time. Vertical space changes in reflector spacing can be a useful guide to locate boundaries between depositional sequences, which make the frequency a good discriminator to identify sedimentary facies.

Equation 3.2

$$\text{Internal velocity} = \text{distance or depth (m)} / \text{TWTT (ms)}$$

Resolution varies laterally and vertically, and is defined as the minimum separation between two features. Lateral or horizontal resolution is how far two features involving a single interface must be separated to show their actually separation., Vertically, it is defined as the minimum separation between two interfaces that can be discriminated as two, rather than one (Sheriff and Geldart., 1995). Seismic velocity (v) is the product of frequency (f) and wavelength (λ):

Equation 3.3

$$v = fx\lambda$$

Vertical resolution of the seismic volume used in this thesis, which has a dominant frequency of 40 Hz is ~15.6 and 19.35 m considering velocities of 3100 m/s and 2100 m/s for the deeper and shallower horizons, respectively (Barker et al., 1993, Fiduk et al., 2004). The frequency of the highest amplitude correspond to the dominant frequency, which is obtained from the processing algorithm. For migrated data, horizontal resolution is equal to the bin size and is ~12.5 m for the interpreted volume.

3.3.4. **Seismic interpretation**

Seismic interpretation used Schlumberger Petrel$^©$ 2013 and 2014 software. It included structural and stratigraphic analyses in order to describe the internal and external character of sub-surface geological bodies, applying a combination of 3D techniques of visualisation, mapping and construction of seismic attribute maps.

3.3.4.1. Horizon mapping

Seismic horizon represent an interface such as the contact between two bodies of rock having different density, porosity, fluid content, seismic velocity and all those characteristics that can be represented by a seismic reflection. Horizon mapping was done using traditional methods of seismic facies analysis. Horizon mapping is the basic process by which 3D surfaces are created, from structural and stratigraphic perspectives. Mapping in this thesis was carried out by tracking the horizon of interest manually or auto-tracking every 20 to 20 lines, crossline and inline. In areas of low amplitude or poor signal, auto-tracking was used in a series of lines oriented perpendicular to the interpreted 'seed' lines (Figure 3.5). The auto-tracking window was narrowed in the areas where reflections have similar amplitudes, avoiding any 'jumps' in the interpreted surface.
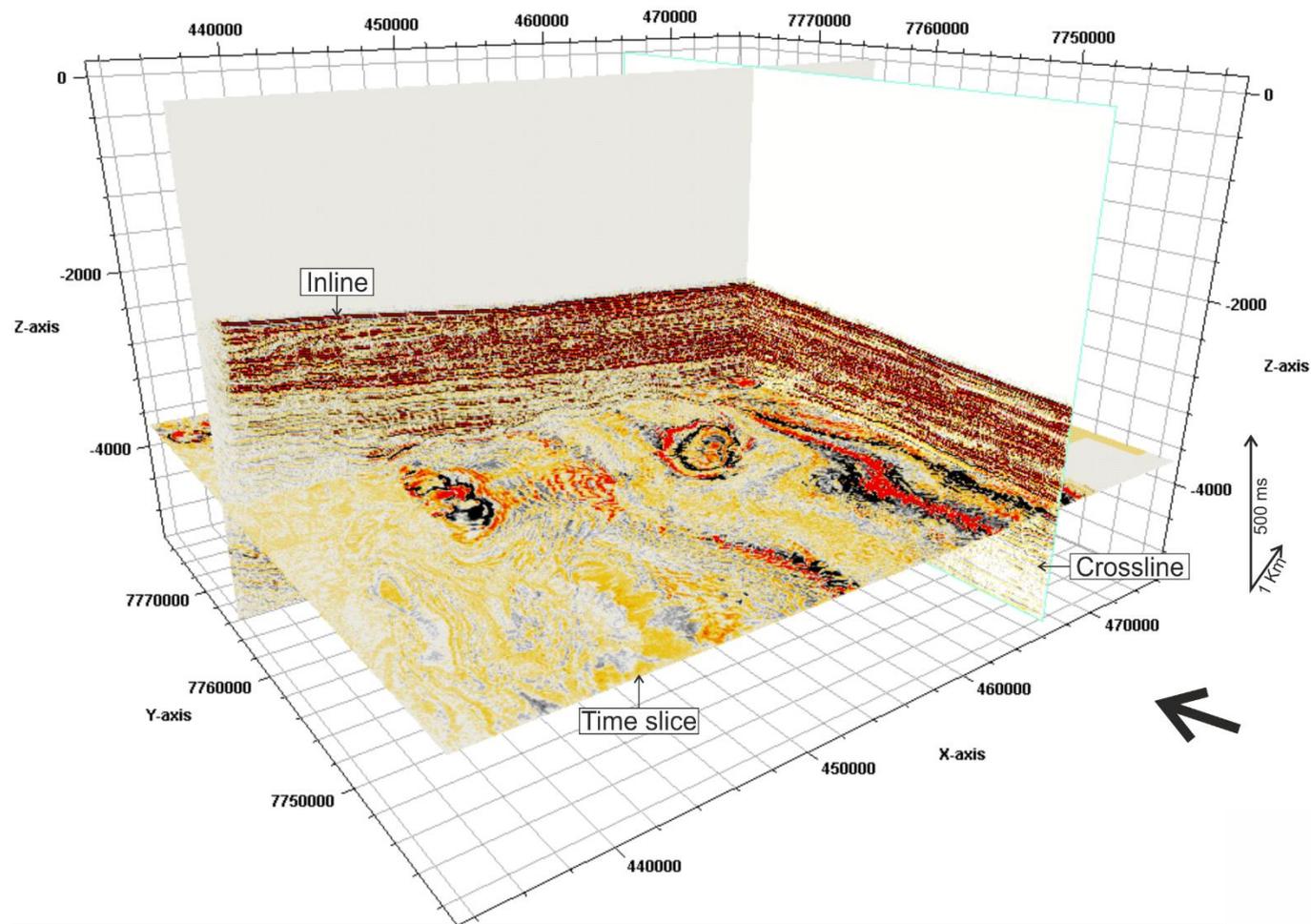
Figure 3.5 – Different perspectives of the interpreted seismic cube, Espírito Santo Basin, SE Brazil. The figure shows examples of crosslines, inlines and a time slice.

3.3.4.2. Recognition of salt and raft tectonics

The key criteria to identify raft tectonics and surrounding salt structures (see chapter 4) are summarised as follows:

a) A raft body is characterised by a predominantly continuous seismic reflection of positive and negative amplitude bounded by even stronger amplitude reflections (Figure 3.4).

b) Lateral boundaries of rafts in some parts show chaotic seismic reflections. Nevertheless, most of the rafts´ lateral boundaries show well-defined geometric shapes.

c) The basal surface is a boundary with weak and chaotic seismic reflections produced by the underlying salt. In some areas, the lower part of rafts is welded on the pre-salt units (Figure 3.4).

3.3.4.3. Recognition of faults

Faults were identified during the process of rafts and MTDs mapping to understand the linkage between them, which is mainly presented in the chapter 4, whereby are related to rafts tectonics described. Attribute maps of surfaces affected by these faults are shown to highlight how faults affect the overburden stratigraphic units.

3.3.4.4. Recognition of MTDs on seismic data

The key criteria established in the literature was followed in this thesis to recognise MTDs (e.g. Hampton et al., 1996, Frey Martinez et al., 2005, Bull et al., 2009). The main diagnostic criteria are summarised below:

a) The MTD body is characterised by chaotic seismic reflections that are bounded by distinctive upper and lower bounding reflections (upper and basal surfaces respectively) with irregular geometries (Figure 3.6).

b) The basal surface of a MTD is usually a high-amplitude reflection that is concordant with the underlying stratigraphy – named as 'depositional surface'
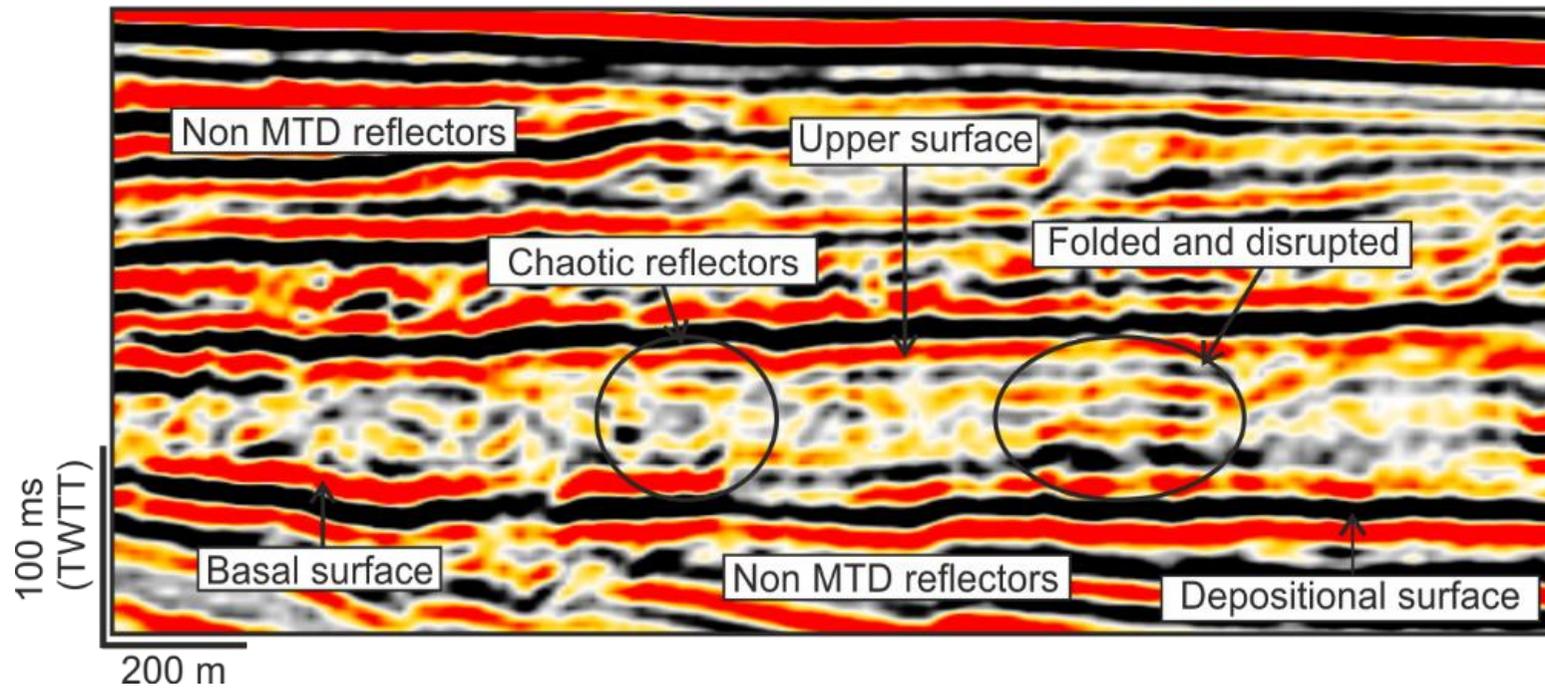
Figure 3.6 – Seismic profile showing the upper and basal surfaces top reflections in a MTD and corresponding character of the same deposit.

in chapter 5. It is also common to observe irregular features on the basal shear surface due the MTD tendency to erode the depositional surface. This is expressed by long linear grooves and striations.

c) The upper surface of a MTD body is usually marked by laterally continuous, or discontinuous and irregular reflections, depending on the degree of internal deformation of MTD strata.

3.3.5. **Seismic attributes**

Once the mapping was completed, a number of seismic attributes were obtained from the seismic volume. Seismic attributes are quantitative measures of seismic character that helps the interpreter to visualise, understand and quantify important features on the seismic data (Chopra and Marfurt, 2005). In this project, seismic attribute maps provided diverse information about unconformities, features of geologic bodies (e.g. rafts, MTDs) and internal geometries. Attributes used include:

Dip or dip magnitude: Dip attribute maps are excellent tools to characterise seafloor morphology and variations along a mapped surface, revealing changes in gradient. It is a time-derived attribute that shows changes in gradient on an interpreted horizon by comparing adjacent points in time value.

Amplitude: It measures the distance between the maximum displacement of a wave at the top of a reflection, positive or negative, to the point at which there is no displacement in acoustic impedance. There are numerous factors that can affect the variations in acoustic impedance such as porosity, lithology, fluid content, bedding, thickness and geometry (Hart, 1999, Brown, 2004).

Root mean Square (RMS) Amplitude: RMS amplitude maps display the average squared amplitude values from individual samples within a defined interval (Brown, 2004). RMS attribute maps can accentuate structural fabric due seismic wavelets are diminished across ramps/faults as a result of the destructive interference of seismic energy.

RMS amplitude maps in this thesis relate to specified horizons and were useful in identifying different geological structures such as faults, blocks and rafts.

Variance (or coherence): Variance profiles on a time-sliced cube highlight areas of discontinuities in the reflections of a succession. To obtain a variance cube there is no need to interpret a horizon (Brown, 2004). Variance uses a set of mathematical algorithms, similar to correlation, to compare adjacent waveforms (Brown, 2004). Variance is an excellent tool for identifying and mapping the margins and the remobilised MTDs in the 3D seismic volume.

3.3.6. **Volume calculations**

Volume calculations were made using Petrel© software. The mapped upper and basal horizons were computed into surfaces to compute *Volume Calculations* using the Bulk volume option.

3.3.7. **Depth conversion**

The vertical scale of the 3D seismic data is recorded in milliseconds (ms) two-way travel time (TWTT). This latter term reflects the time P-waves take to travel through the crust to a reflector and back again into the seismic hydrophones.

To convert TWTT to true depth, the one-way travel time distance (in seconds) needs to be multiplied by the P-wave velocity estimated for the stratigraphic interval considered. This conversion is represented by the following equation:

Equation 3.4

$$D = \frac{TWTT}{2} * \frac{V}{1000}$$

Where: D=Depth; TWTT= Two-way-travel-time (ms); V=velocity in m/s

In this work, time conversions in the specific intervals was calculated using the velocity information obtained at DSDP site 516 located in Santos Basin (Figure 2.1) (Barker et al., 1993). Horizontal lengths for geological features were calculated by multiplying the number of traces covered by the features by trace distance (12.5m).

3.3.8. **Quantitative measurements derived from seismic data**

Thickness measurements were calculated from seismic volume to assess the thickness of sedimentary post-raft packages (chapter 4). They were obtained across the study area, above the raft structures and along inline intervals of 20 lines (250 m). The resulting plots represent average values of thickness considering different stratigraphic intervals.

3.4. Seismic data interpretation and Geographic Information Systems data integration

Data representation and integration consists of the transformation of our own experience or data from different environments into rules and formats that can be analysed together. Following this principle, information generated from the seismic interpretation was integrated and used into GIS software.

The results chapters 5 and 6 are derived from horizons mapped using Petrel$^©$. Once the horizons were completely mapped, they were transformed into surfaces (Processes→Utilities→Make/Edit Surfaces) and depth converted (time depth to real depth) in Petrel$^©$. The multiple surfaces thus obtained were exported as Zmap+grid (ASCII) files and integrated into ArcGis$^©$ using the ArcGIS *Data Integration with E&P Software*$^©$ extension, which allows Petrel$^©$ surfaces to be directly imported as grid files into GIS software.

MTDs here mapped individually and their upper and basal surface interpreted along their full length. During the mapping, polygons were created following their shapes after mapping, to constrain the areas of the surfaces created in a second step. The adopted method was used in all MTDs mapped, which correspond do the base information on chapter 5 and included in the MTDs inventory used for modelling in chapter 6. The same process was used to compute the depositional surface right beneath MTDs representing local topography, which together with the MTDs are the key information in chapter 5 and 6, representing local topography as a proxy of Digital Model Terrain (MDT).

Based on that information, topographic profiles of MTD and depositional surface were computed into GIS and presented on chapter 5. As well as, morphometric attributes presented in chapter 5 and chapter 6.

3.5. Favourability Scores

The aim of chapter 6 is to provide a new methodology to assess which predisposing factors were present when four MTDs occurred in the study area. The methodology adopted in chapter 6 is presented in Figure 3.7.

The depositional surface mapped and used in chapter 6 (and in chapter 5 too) was imported into ArcGIS as a Digital Terrain Model (DTM) using the ArcGIS *Data Integration with E&P Software*© extension after converted to true depth (metres). Based on that, surface seven predisposing factors, or independent variables, were then computed. The chosen variables are elevation, slope gradient, profile curvature, planform curvature, flow direction, flow accumulation and slope over area ratio.

3.5.1. **Mapping units**

The evaluation of the likelihood of mass-movements in a given area requires a preliminary selection of suitable terrain units (TMUs). These TMUs refer to a surface portion of the study area containing a set of ground conditions that differ from adjacent units across definable boundaries (e.g. Hansen, 1984, van Westen et al., 1997).

The mapping of TMUs usually depends on the scale that best represents the phenomena studied. From a vast selection of terrain mapping unit categories (e.g. unique condition units, slope units, geo-hydrological units and topographic units), this thesis used grid cells. Grid cells are preferentially used by GIS models, dividing the study area into regular areas (cells) with a predefined size, which then become the mapping units of reference (Chung and Fabbri, 1999, Clerici et al., 2002, Remondo et al., 2003). To each grid cell is given a value for each predisposing factor taken into consideration (e.g. slope gradient, curvatures).
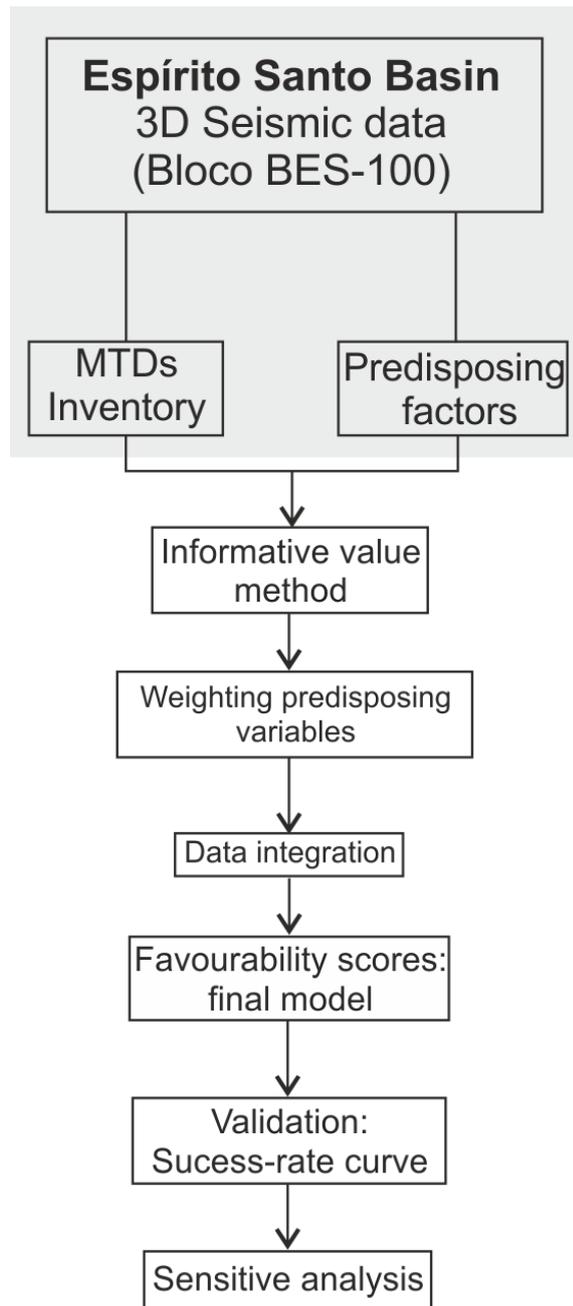
Figure 3.7 – Flowchart showing the methodology used to calculate the favourability scores for MTDs occurrence offshore Espírito Santo Basin, SE Brazil.

Each predisposing factor (independent variable) is computed into a raster file with a given cell size. The main conceptual limitation of grid cells is associated with the representation of continuous geological and morphological forms in a discrete form, and the representation of linear and area features (such as geological boundaries, landslide deposits, lithological units) using cells of predefined shape and size (Guzzetti, 2005).

In this thesis, the independent variables chosen (e.g. elevation, slope gradient, profile curvature, planform curvature, flow direction, flow accumulation and slope over area ratio) were computed into GIS in a raster format. Due to the size of the study area and mapped MTDs, terrain units (pixels) were fixed at 50 m in five of the seven variables. The exceptions were the Profile curvature and Planform curvature, which were first computed with a pixel size of 250 m and subsequently converted into 50 m pixels for modelling together with the other themes.

3.5.2. **Predisposing factors: selection and preparation**

Predisposing factors are used as independent variables within the models, as mentioned before. Their selection was based on their geomorphologic meaning and on the availability of data extracted from the depositional surface. This same surface was mapped as a topographic palaeosurface (analogous to DTM), from which the seven independent variables were extracted. All of the seven variables were classified into classes.

ArcGIS© software was used to compute all the variables following the tools represented in Table 3.1, using as a base variables which are non-classified raster files. The computation of the Slope over area ratio was made using the GIS extension *TauDEM 5.0* (developed by Utah State University). As a result, the seven independent variables were computed as raster files with 50 m cell sizes and classified into discrete classes for further use in statistical models (Table 3.1).

Table 3.1 – Seven predisposing factors used as independent variables, ArcGIS tools used in their computation and number of classes after reclassifying the variables for use in the models.

Variable	ArcGIS Tools	Considered classes
Elevation (m)	ArcTollbox→Spatial Analyst Tools→Reclass→Reclassify	[0-100],]100-200],]200-300],]300-400],]400-500],]500-600]]600-700]
Slope gradient (°)	ArcTollbox→Spatial Analyst Tools→Surface→Slope	[0-1],]1-2],]2-3],]3-4],]4-5],]5-6],]6-7],]7-8], > 8
Profile curvature	ArcTollbox→Spatial Analyst Tools→Surface→Curvature→ Output profile curve raster.	Convex, Flat, Concave
Planform curvature	ArcTollbox→Spatial Analyst Tools→Surface→Curvature→ Output plan curve raster	Concave, Flat, Convex
Flow direction	ArcTollbox→Spatial Analyst Tools→Hydrology→Flow direction	E, SE, S, SW, W, NW, N, NE
Flow accumulation (Log. Scale)	ArcTollbox→Spatial Analyst Tools→Hydrology→Flow accumulation	[0], [1],]1-10],]10-100],]100-1000], >1000
Slope over area ratio (Log. Scale)	ArcGIS TAUDEM Extension 1. Fill Pits 2. D. Inf. Flow Direction 3. D. Ind. Contributing area 4. Slope over area ratio	[0],]0-0.00001],]0.00001-0.0001],]0.0001-0.001],]0.001-0.01]

3.6. **Modelling strategy**

3.6.1. **Informative value – Bivariate statistical method**

The Informative Value (*IV*) is a bivariate statistical method used to weight each class of each variable proposed. It describes quantitatively the relationship between each class of an independent variable (*Xi*) and a set of instability events on slopes through individual scores obtained by Equation 3.5.

For each class, within each MTD variable proposed, IV was calculated using the following equation (Yin and Yan, 1988):

Equation 3.5

$$IV_i = 1n\left(\frac{S_i / N_i}{S / N} \right)$$

with:

Si – Number of pixels with instability events within variable *Xi*;

Ni – Number of pixels with variable *Xi*;

S – Total number of pixels with instability events;

N – Total number of pixels of the study area.

In Equation 3.5 *S/N* is the *a priori* probability. It is the probability for each pixel to have an MTD without considering predisposing factors. S_i/N_i is the conditional probability. It is the probability of an instability event to occur given the presence of variable *Xi*. A negative *IV$_i$* means that the presence of the variable is favourable to slope stability. A positive *IV$_i$* indicates a relevant relationship between the presence of the variable and MTDs distribution; the higher the score, the stronger the relationship (Yin and Yan, 1988). An *IV$_i$* equal to zero means no clear relationship between the presence of the considered variable and the occurrence of MTDs.

The classes of each independent variable not containing MTDs have a conditioned probability of zero. In this case, *IV$_i$* cannot be obtained considering the log

transformation in Equation 3.5, and therefore the IV_i was forced to be two decimal values lower than the lowest IV_i computed for classes of the corresponding predisposing factor.

The final model is calculated based on the following equation:

$$IVj = \sum_{i=1}^{n} X_{ji} IV_i$$

Where:

n - Number of variables,

X_{ji} - either 0 if the variable is not present in the pixel j, or 1 if the variable is present.

The IV was calculated using three different partitions of the same MTD inventory considered in the models such as:

1. Model 1: includes the total area of MTDs.

2. Model 2: includes 1/3 of the total length of the mapped MTDs.

3. Model 3: includes the upper half of the area used in Model 2.

3.6.2. **Validation. Success-rate curves**

The performance of the predictive models was assessed through the computation of success-rate curves (Fabbri et al., 2002). Success-rates curves are based on the comparison between the final model and the spatial distribution of MTDs. They are used to weight the predictive variables expressing the goodness of fit of MTDs with the final model (Chung and Fabbri, 2003). Success-rate curves were computed by crossing the distribution of the set of MTDs used to generate each model (Models 1 to 3) with the (predictive) model results.

The success-rate curves are prepared by plotting the cumulative percentage of the area most likely to fail (starting from the highest probability values towards the lowest) on

the horizontal (x) axis, and the cumulative percentage of corresponding MTDs area on the vertical (y) axis. The steeper the curve the more capable the model is to describe the distribution of MTDs in a given study area. The steepness of the curve also depends on the instability events distribution in the study area. In a situation when a large portion of the area is covered by instability, it is still possible to get steep curves (Chung and Fabbri, 1999).

The favourability values obtained for each pixel were sorted in descending order. Additionally, an "Area Under the Curve" (AUC) analysis was computed for each success-rate curve so one can quantify the performance of each model and compare results for the different success-rates. Assuming that the higher the AUC value is, better the model (Bi and Bennett, 2003, Blahut et al., 2010, Pereira et al., 2012, Guillard and Zezere, 2012), the absolute AUC value is given by:

Equation 3.7

$$AUC = \sum \left[\left(xi + 1 - xi \right) \frac{yi + 1 + yi}{2} \right]$$

where x gets the percentage of study area predicted as susceptible by descending order and y the percentage of correctly classified landslide area belonging to the validation group.

3.6.3. **Sensitivity analysis**

Sensitivity analysis of the variables were performed after the AUC analysis in order to understand which combination of factors contribute more to trigger unstable areas on the Espírito Santo continental slope.

Each predisposing factor was crossed autonomously with the MTD inventory set of the study area, generating an individual model for each one. Whereby each individual model was validated by building a success-rate and respective calculus of AUC for each variable of the model (predisposing factor). The results were ordered by growing range to purse comparing factors.

The ranking mentioned above was taken into consideration throughout the sensitivity analysis. The finally sensitivity analysis was computed by adding a systematic way through the introduction of a new variable in the model (e.g. $M_2 = f (V_1 + V_2)$; $M_3 = f (V_1 + V_2 + V_3)$; $M_4 = f (V_1 + V_2 + V_3 + V_4)$; $M_n = f (V_1 + V_2 + V_3 + V_4 + ... V_n)$. For each model obtained, AUC was calculated so to understand which variable combination obtains better predictive capacity (e.g. Guzzetti et al., 2006, Zêzere et al., 2008).

STRUCTURAL STYLES OF ALBIAN RAFTS RECORDING TECTONIC REACTIVATION AND LATE HALOKINESIS IN OFFSHORE ESPÍRITO SANTO BASIN (SE BRAZIL)

Chapter Four

4.1. **Abstract**

The SE Brazil continental margin is dominated by continental-slope embankment, incision of submarine channel systems and significant mass-gravitational processes, with salt tectonics playing a significant role in upper-crust deformation. The hydrocarbon exploration offshore SE Brazil has focused on Early Cretaceous units that were deformed due to Albian-Cenomanian gravity gliding above Aptian salt.

 A three-dimensional (3D) seismic volume from the Espírito Santo Basin (ESB), SE Brazil is here used, aiming to provide first 3D seismic images of the raft tectonics in ESB and describe tectonic reactivation on the Albian rafts and post-strata overburden. Which is based on: a) test the parameters considered to control raft tectonics on a margin tectonically reactivated in the Cenozoic; and b) investigate the impact of prolonged halokinesis on raft deformation and post-strata overburden. The combined effects of halokinesis and multiple tectonic phases are expressed by local collapse, fault reactivation and late segmentation of Albian rafts, offshore Espírito Santo Basin. As a result four main raft geometries of deformation were observed: a) rolled-over rafts, b) tabular rafts, c) collapsed rafts, and d) folded and tilted rafts on the flanks of salt rollers. This chapter conclusions shows that salt rollers formed buttresses to moving Albian rafts, with withdrawal of salt from underneath some of the rafts leading to their collapse and welding onto pre-salt strata. This phenomenon is important as it enhanced connectivity between pre-salt and post-salt units, and how it shapes the basin in general influencing the post-raft overburden, from a sedimentary and stratigraphic point of view. Importantly this process occurred, in the studied part of the Espírito Santo Basin, with minimum control of post-raft overburden thickness on raft segmentation.

4.2. **Introduction**

Raft tectonics comprises one of the most extreme deformation styles on salt-influenced continental margins (Duval et al., 1992, Demercian, et. al., 1993, Gaullier et al., 1993, Mauduit et al., 1997, Penge et al., 1999, Cobbold, et. al., 2001, Alves, 2012, Pilcher et al., 2014). Raft tectonics are characterised by downslope translation of large blocks of strata above a ductile detachment layer (Gaullier et al., 1993). A key characteristic of raft tectonics is that thin-skinned stretching in overburden strata reaches beta (β) values of 2-3, with associated gravitational gliding contributing to the fragmentation of post-salt units (Duval et al., 1992, Gaullier et al., 1993, Mauduit et al., 1997, Vendeville, 2005, Jackson, et al., 2015). The majority of published work suggests this fragmentation results from the interaction between gliding blocks (rafts), faulting and a thickening overburden. Based largely on the interpretation of regional 2D seismic data and the analysis of physical models, published results consider the thickness of the post-raft overburden and the slope gradient as the main controlling parameters on the degree and style of raft segmentation and downslope movement (Duval et al., 1992, Gaullier et al., 1993, Mauduit et al., 1997, Vendeville, 2005, Brun and Mauduit, 2009). According to these authors, differences in post-raft overburden thickness can maintain downslope gliding of rafts even if slope gradient is close to zero, as long as an efficient basal décollement is present at depth. The models essentially suggest that increasing rates of syn-kinematic sedimentation increase downslope displacement of rafts and make listric normal faulting more likely (Mauduit et al., 1997). However, the role of salt thickness and tectonic reactivation in raft evolution is still poorly understood in basins such as the Espírito Santo Basin, in which significant tectonic and igneous events are known to have controlled the structural evolution (Fiduk et al., 2004).

This chapter uses 3D seismic data from Espírito Santo Basin, offshore SE Brazil, to describe and discuss the effect of tectonic reactivation and halokinesis on the structure of six Albian rafts and overlying post-strata (Figure 4.1a and b). It focuses on a region of offshore SE Brazil where a direct relationship between post-raft overburden thickness and raft internal deformation is not observed, and concludes on the factors that may have controlled raft evolution in the Espírito Santo Basin. Importantly, the study area records multiple episodes of tectonic reactivation related to the Andean tectonic phases and Paleogene emplacement of the

Abrolhos Volcanic Plateau (Fiduk et al., 2004) (Figure 4.2). The first of these episodes, the Late Cretaceous Peruvian phase (Scheuber et al., 1994), had a profound control on fault reactivation and local erosion in the study area. The main advantage of this work, when compared with work previously done in salt tectonics areas, is that it uses a high-quality 3D seismic data volume to describe in great detail the fault families associated with salt structures and adjacent rafts. In such a context, fault families and types of raft deformation in a sedimentary basin can be identified.

This chapter describes the main raft geometries, plots overburden thickness, and documents the main fault families observed in the study area. It also relates the styles of halokinesis imaged on seismic data to the styles of deformation observed within the rafts. The discussion attempts to answer three important questions related to raft evolution:

a) Is the thickness of post-raft overburden the sole controlling factor on raft deformation offshore Espírito Santo?

b) Are growing salt structures capable of imposing renewed compartmentalisation in otherwise welded (and stable) rafts?

c) What is the importance of halokinesis to the charging of Albian rafts in the study area of the Espírito Santo Basin and its influence in the post-raft overburden?
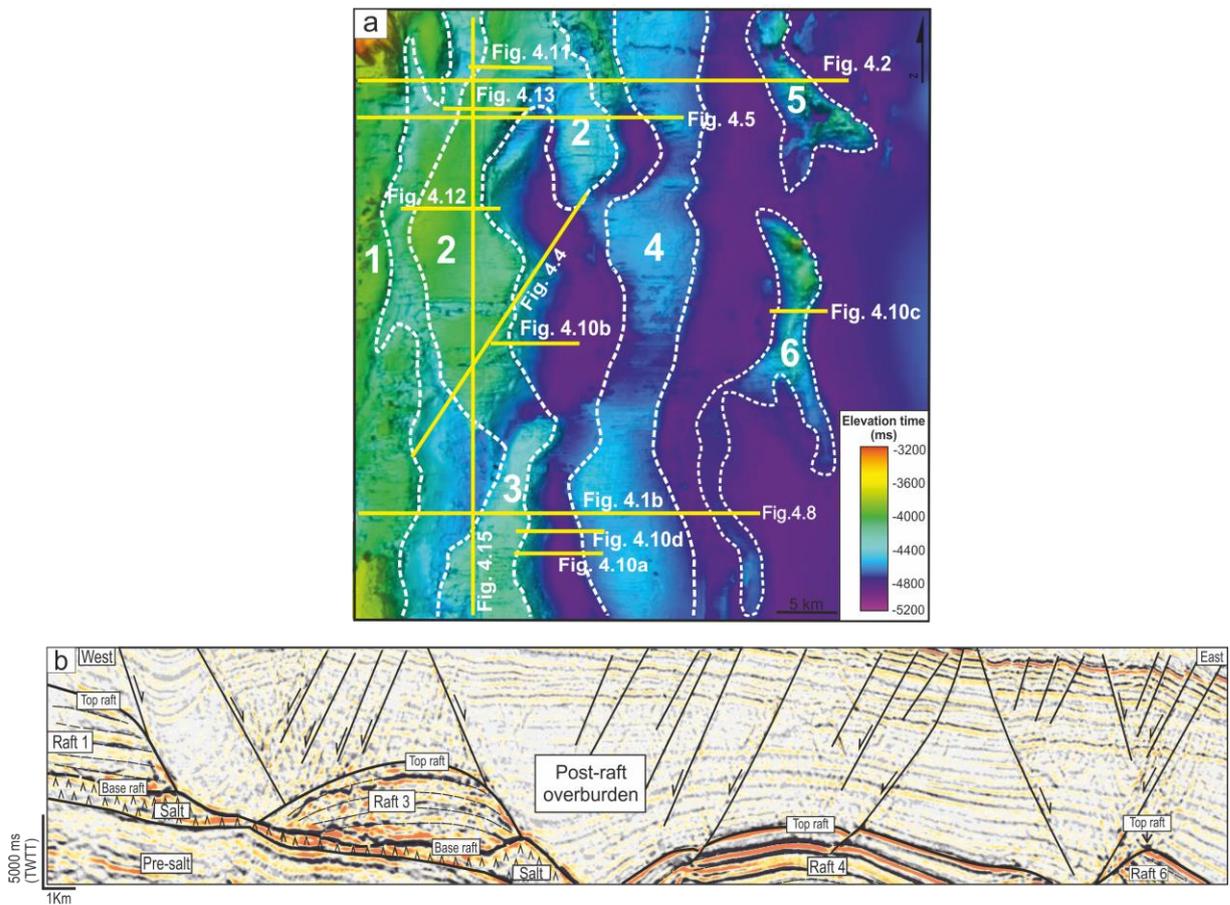
Figure 4.1 . Structural map indicating the interpreted rafts location and spatial distribution in the Espírito Santo Basin. Number 1 to 6 denote the raft structures analysed in this chapter; b) Interpreted West to East seismic profile highlighting the style of raft tectonics and geometry of surrounding units for general context. Top and base of raft 1 to 3 are observed in the seismic section, while only visible the top horizon is visible for raft 4 to 6.
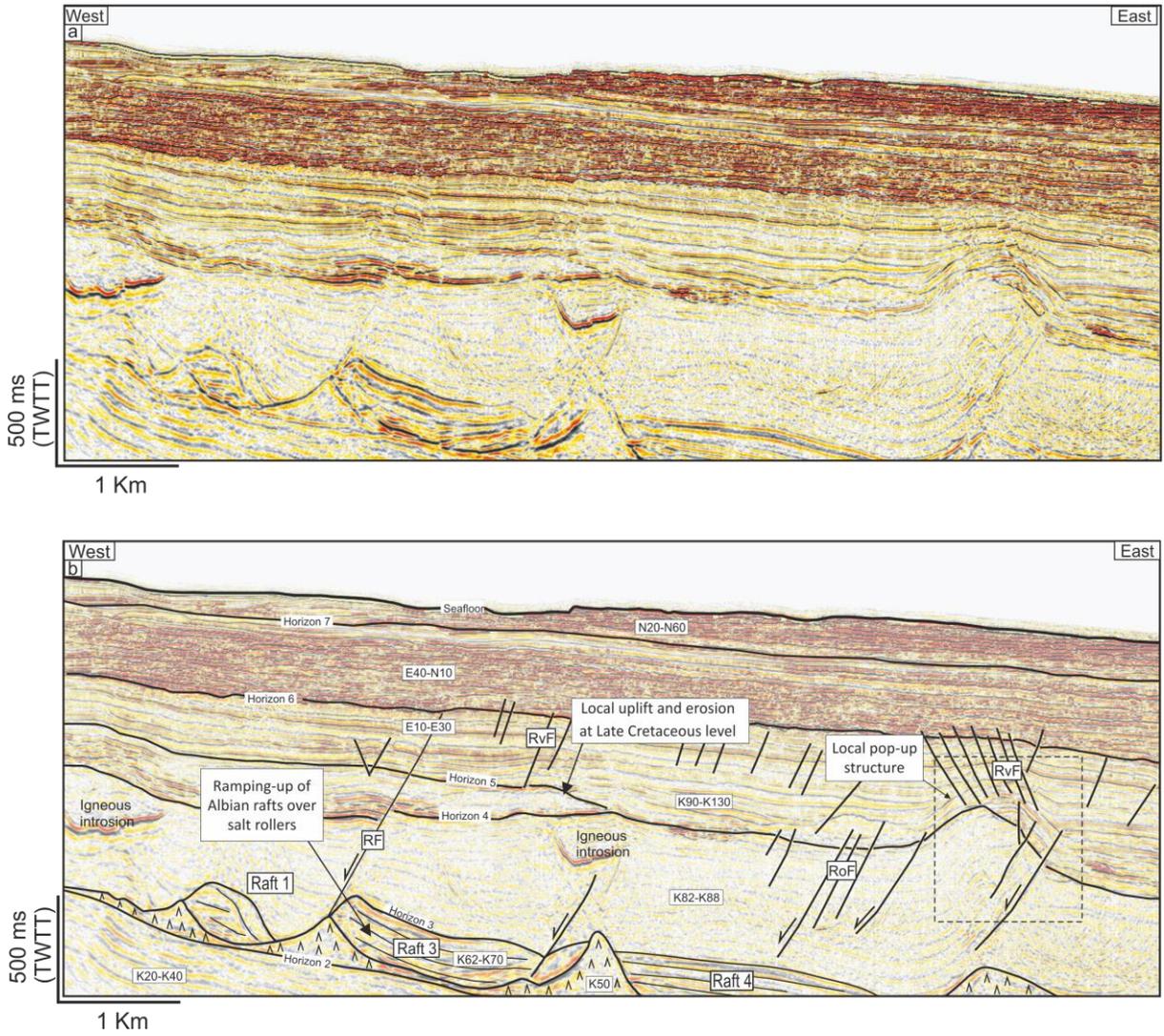
Figure 4.2 – Seismic profile highlighting the presence of reactivated structures (included local pop-up structures) in the study area. Highlighted are also roller fault (RF), rollover faults (RoF) and reactivated faults (RvF).

4.3. **Controls on raft movement and segmentation**

Raft tectonics is the most significant style of deformation accompanying thin-skinned extension on continental margins. Raft tectonics can generate regions in the upper crust where the overburden stretches by two or three times its original length (Gaullier et al., 1993, Duval et al., 1992, Mauduit et al., 1997). When fault blocks at the base of stretched overburden units are no longer in contact, they are termed rafts. If they are still partly in contact, they are termed pre-rafts (Duval et al., 1992).

Most published studies used experimental or numerical models to understand the mechanisms of raft tectonics (Duval et al., 1992, Gaullier et al., 1993, Mauduit et al., 1997, Brun and Fort, 2011). Models were based on various assumptions on the physical processes involved in downslope rafting, backed-up by regional (2D) seismic data. Assumptions basic take in consideration that the model has its own coherence that could link any input combination of the parameters to a specific structural response and the model response to variations in the input parameters. Such models were, nonetheless, crucial to understand: (i) the mechanical behaviour of raft systems (ii) how modeled systems compare to natural examples, in order to test the applicability of physical and mathematical models. Such seismic data were crucial to understand the mechanical behavior of raft systems and test the applicability of physical and numerical models (Brun and Fort, 2011).

One of the key parameters mentioned in published models as capable of controlling raft displacement is overburden thickness (Mauduit et al., 1997). In their physical models, Mauduit et al. (1997) tested how overburden sedimentation rate controlled rafting. The experiment resulted in the formation of a wide deformation zone in the lab, with tilted blocks delimited by extensional normal faults and rafts. The first structures to develop are symmetric grabens and, as sedimentation rate increases, the number of rafts or blocks increases proportionally (Figure 4.3). The models of Mauduit et al. (1997) indicate that an increase of the sedimentation rate enhances the displacement rate of rafts as a response to increasing vertical loading. Vendeville (2005) later showed that regional sediment deposition can trigger gravity spreading, in the absence of an oceanward dipping basal slope. As a key example, rafts in the Gulf of Mexico record pure spreading driven by sedimentary loading. This setting requires a thick sedimentary overburden, high sediment density and low frictional angles of

the sediments (Brun and Fort, 2011, Rowan et al., 2012). It will also imply the creation of large amounts of lateral space into which overburden units can accumulate during stretching, as recorded in the Kwanza Basin (Angola) by Duval et al. (1992).

Salt as a viscous evaporitic layer has been described as an important factor not only in raft formation, but also in raft gliding and subsequent deformation (Brun and Mauduit, 2009, Vendeville, 2005). Salt acts as a lubricant layer and forms rollers, pillows and diapirs adjacent to individual rafts (Gaullier et al., 1993, Brun and Mauduit, 2009, Alves, 2012). Brun and Mauduit (2009) performed laboratory experiments to study the development of growth faults during rafting. Where their concave shape results from the connection between a steeply dipping normal fault and a flat-lying or gently dipping décollement, a geometry prone to cause important tectonic reactivation in adjacent rafts due to the mechanical instability of rollover faults (Brun and Mauduit, 2008). In other words, changes in the dip of roller faults at depth results in the transfer of horizontal displacement towards the surface through the rolling over of strata in the rafts, and in post-raft overburden strata every time roller fault sole out into the detachment salt layer and significant lateral movement is recorded in rafts. In support of this, Alves (2012) documented significant Late Cretaceous-Early Cenozoic reactivation in raft-related faults in the Espírito Santo Basin, a phenomenon triggered by regional (Andean) tectonics and related slope oversteepening.

This chapter builds on the ideas of Alves (2012), recognizing that the thickness of post-raft overburden units does not vary significantly in the study area, a character suggesting that the salt thickness and the evolution of salt rollers are the main controlling factors in their compartmentalization and ramping up on the flanks of growing salt rollers. For that reason, thin-skinned deformation was named 'late rafting', as it occurred in the late Cretaceous after the main stage of raft movement in the Espírito Santo Basin.
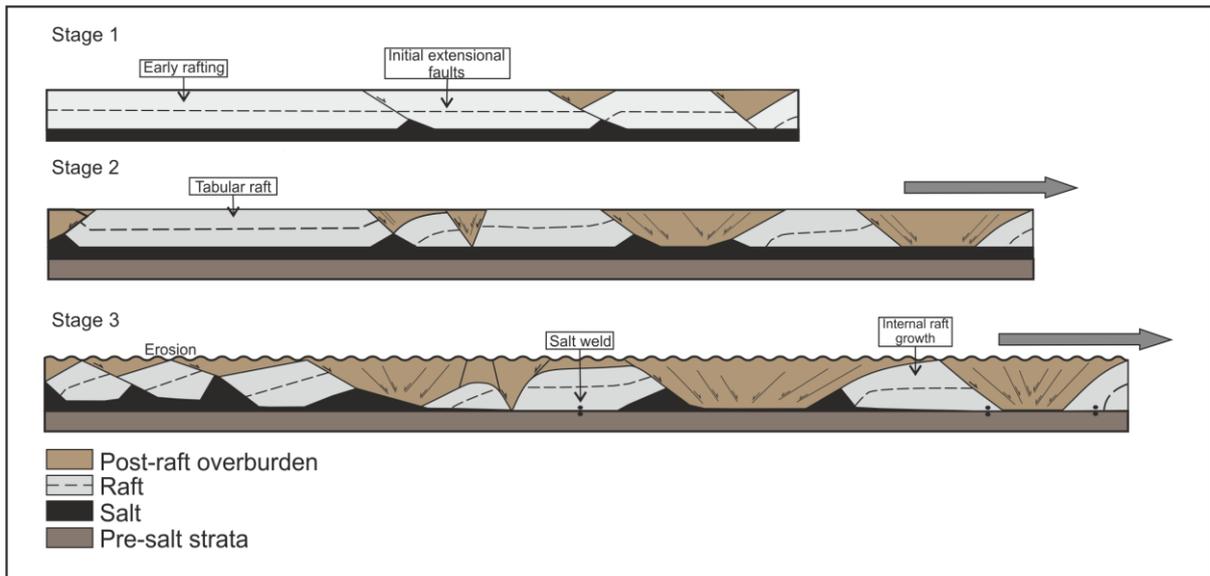
Figure 4.3 – Simplified schematic evolution of raft tectonics during Albian-Santonian period in the study area (Duval et al., 1992, Pilcher et al., 2014). In a first stage (1), early rafts are formed together with extensional faults. In second stage (2), the post-raft overburden fills the gaps between the rafts. In the last stage (3), the tabular rafts remained isolated become progressively welded on the pre-salt strata. Note the erosion at the end of this stage (Santonian). The salt accumulated into salt rollers, pillows and rafts growth internally. In the last two stages are observed extensional faults into the post-raft overburden that laterally confined the raft and/or the salt accumulations. The arrows indicate the slope direction in the Espírito Santo Basin (not to scale).
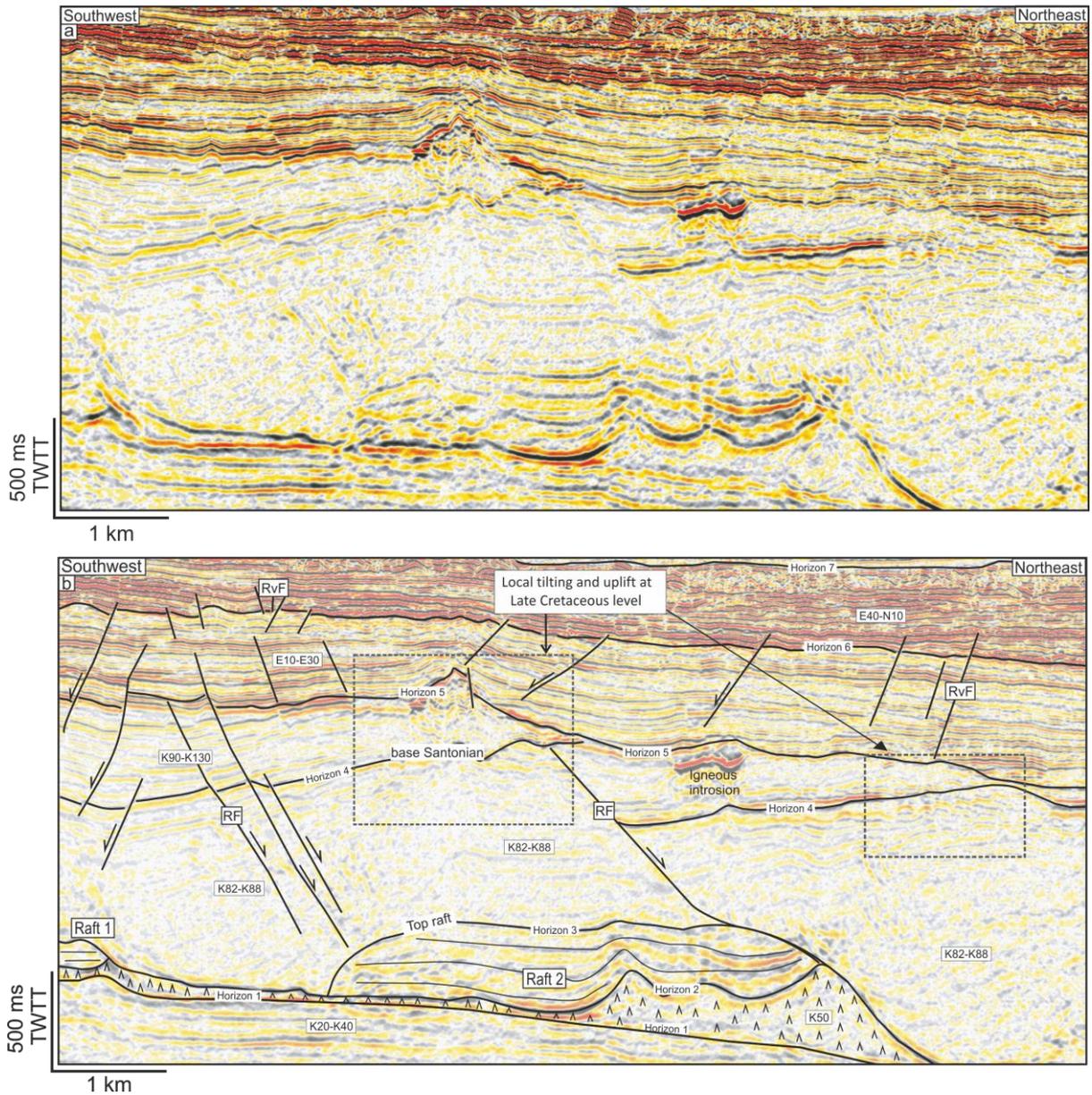
Figure 4.4 – a) Uninterpreted and b) interpreted seismic profile highlighting a phase of widespread movement and erosion of rafts at the end of the Cretaceous (Horizons 4 and 5). As with other figures, the seismic profile shows roller faults (RF), rollover faults (KF) and reactivated Faults (RvF). In this profile, raft 2 collapsed by probable withdrawal of salt from underneath.

4.4. **Observation and results**

4.4.1. **Raft tectonics in the Espírito Santo Basin, offshore Brazil**

The rafts in the Espírito Santo Basin are considered in this chapter as an element of slope instability triggering in the sense that they are large blocks gliding down slope due to the tilt of the margin and the viscous layer (salt), which are close related to raft tectonics shape and morphology. At the present, Aptian salt constitutes the viscous layer which beneath in interpreted rafts (Figure 4.4).

Raft structures are observable in the seismic profiles as a negative seismic reflection marking their upper and basal surfaces. Raft bodies are marked by positive and negative seismic reflections, forming layers whereby can be understand their internal adaptation to the movement downslope. In most of the area, the rafts structures are lateral confined by Aptian salt that forms isolated accumulation as rollers, small pods or pillows (e.g. Figure 4.2 and Figure 4.4)

At present, Aptian salt forms isolated accumulations, some of which are observed beneath the interpreted rafts in the form of rollers. Above the Aptian salt are observed symmetric and asymmetric rafts with distinct structural styles and inferred evolutions (Figure 4.4 and Figure 4.5).

A structural map of Horizon 3 (top rafts) illustrates the plan-view geometry of rafts 1 to 6 (Figure 4.1a and Figure 4.6a). In the northwest part of the study area, the rafts are intensely faulted. In east-west profiles, i.e. perpendicular to the strike of rafts, raft 1 is irregular and discontinuous, showing important segmentation (Figure 4.6a). In the map in Figure 4.6a, this raft is at least 36 km long. For raft 2, two-way travel time (TWTT) raft thickness ranges from 34 ms to 815 ms along the north-south profile. This corresponds to a thickness of 450 m-1107 m, using velocity data from Barker et al. (1983).

In contrast to raft 1, the north-south profile shows raft 2 to be continuous with a well-defined branch in its northeast portion (Figure 4.6a). The gap between the main body of the raft 2 and this latter branch is occupied by a chasm with a small salt roller Figure 4.5. The TWTT thickness of raft 2 varies between 52 ms and 991 ms, i.e. between 702 m and 1340 m. Rafts 3 and 4 are geometrically similar without any visible branches developed along their long axes (Figure 4.1a

and Figure 4.6a). Raft 4 comprises a north-trending raft with a tabular shape showing distinct degrees of bucking and faulting at Cretaceous level (Figure 4.6a).

Rafts 5 and 6 are the structures less visible on seismic data, with their base not visible in most of the study area. Their tops are irregular, with several segments visible on structural data (Figure 4.6**a**). Aptian salt viscous layer is present in the study area beneath rafts 1 to 6, in places where salt was already withdraw is present as isolated accumulations (e.g. rollers and pillows) beneath and sidewise of the raft structures. In part of the study area (e.g. beneath raft 5 and 6) due seismic restrictions is not possible to observe the basal surface of the rafts.

4.4.2. **Evidence for tectonic reactivation and late halokinesis**

The Andean tectonic phases were key events controlling the structural evolution of the Espírito Santo Basin (Lima, 2003). Tectonic reactivation was chiefly recorded at the end of the Cretaceous and in the Eocene, as revealed on seismic data. Figure 4.7 shows a series of isochron maps between the Maastrichtian and Santonian unconformities i.e., between the stratigraphic unconformities that mark Late Cretaceous and Eocene tectonic episodes in the Espírito Santo Basin (Alves, 2012). Of importance are the thickness variations recorded at Santonian-top Maastrichtian and Maastrichtian-Eocene levels. Areas recording reactivation and local erosion present the lower thickness values in Figure 4.6. Tectonic reactivation on seismic data is marked by low-amplitude folding and reactivation of extensional structures (Figure 4.2 and Figure 4.4). Erosion of Horizons 5 and 6 accompanied Late Cretaceous and continued during Eocene tectonism, and resulted in the deposition of less than 400 ms TWTT between the two mapped unconformities (Figure 4.4).

Reactivated faults occur in the imaged seismic line between rafts 1 and 2, towards the upper part of the continental slope. In other regions, pop-up structures intersect Late Cretaceous and early Cenozoic strata (Figure 4.2 and Figure 4.4).

In summary, Late Cretaceous tectonic reactivation on the Espírito Santo continental slope area is marked by: a) localised back-thrusting of raft-bounding normal faults, forming local pup-up structures b) shortening of Meso-Cenozoic strata to form local pop-up structures (Figure 4.2).
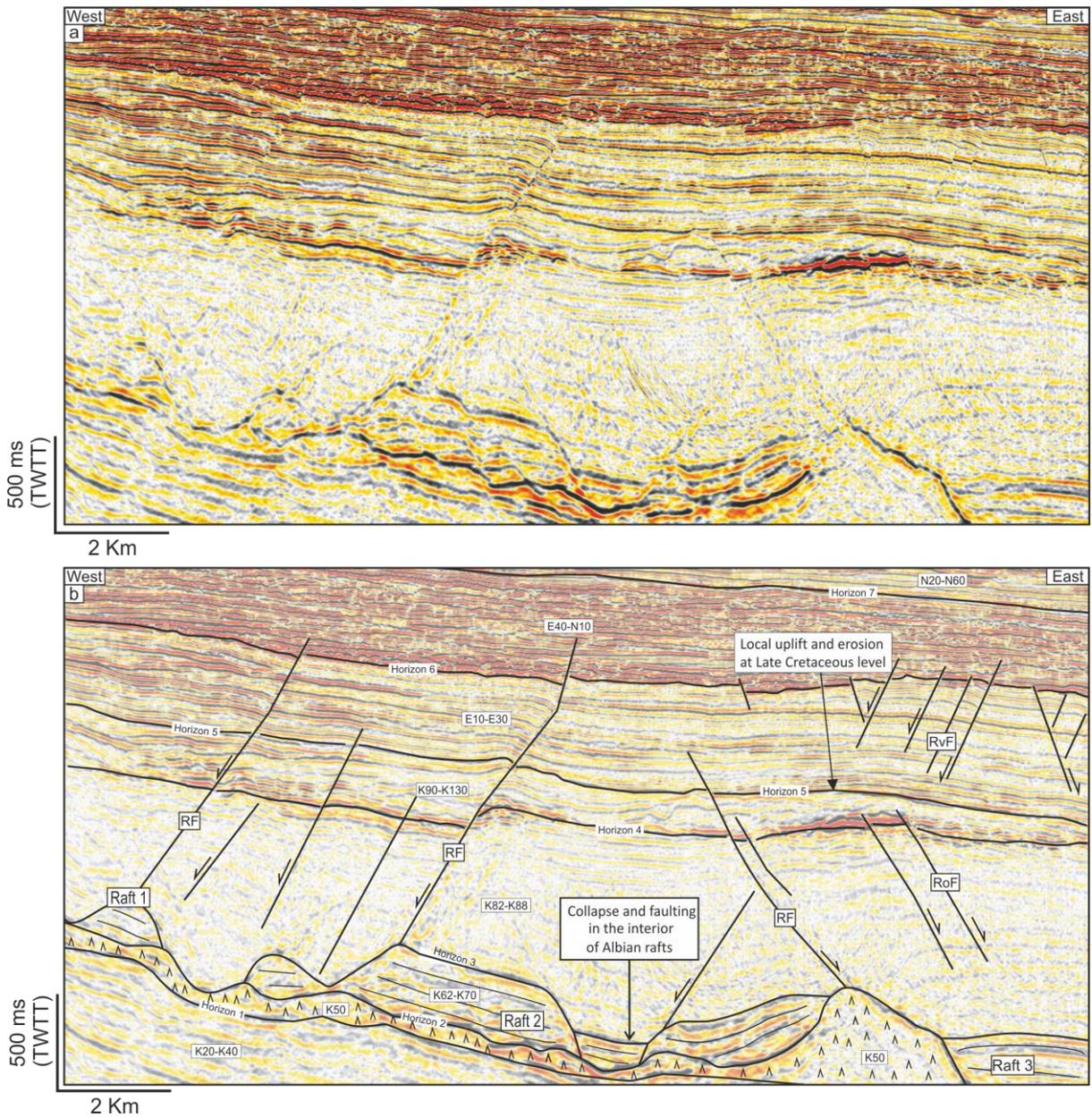
Figure 4.5 – a) Uninterpreted and b) interpreted seismic profile showing the geometry of collapsed raft (see Horizon 3 and 4 for reference). As with other figures, the seismic profile shows roller faults (RF), rollover faults (RoF), keystone faults (KF) and reactivated faults (RvF). In this profile, raft 2 collapsed by probable withdrawal of salt from underneath.
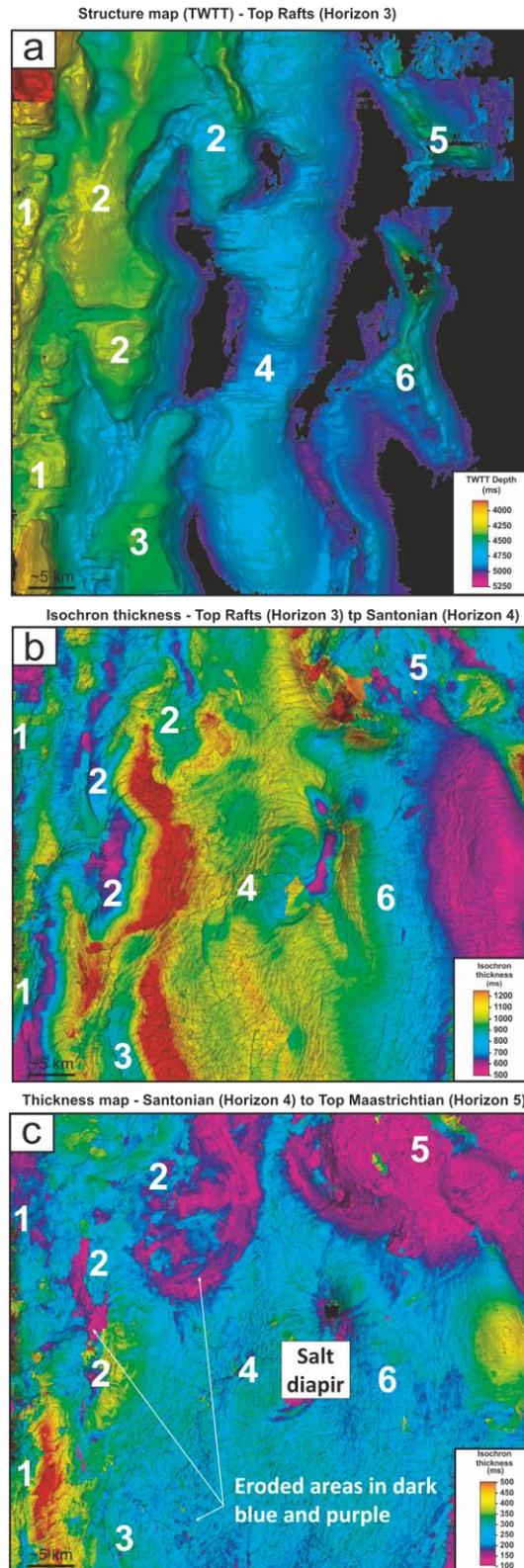
Figure 4.6 – TWTT structure and isochron maps of key horizons in the study area. a) TWTT of the top rafts horizon 3, showing the relative location of rafts 1 to 6; b) Isochron map for strata between top rafts (horizon 3) and base Santonian (horizon 4) and c) Isochron map for strata between horizons 4 and 5 (Santonian to Maastrichtian). Note the marked variations in thickness in these last two maps.

4.4.3. **Thickness variations in the post-raft overburden**

Thickness plots were calculated from seismic data (Figure 4.7). The plots are separated into two main packages comprising post-raft sediments: (i) top rafts (Albian to Early Cretaceous) to base Santonian (Late Cretaceous) and (ii) top rafts (Albian to Early Cretaceous) to seabed (Figure 4.8). Over the northern part of raft 1, overburden thickness is ~700 ms (875 m) from top raft to the base Santonian (K82 to K88 sequences); and ~1600 m for the Santonian to the seafloor (K90 to N60 sequences) (Figure 4.7a). Trend curves for overburden thickness are similar for the two intervals considered: top raft to base Santonian and base Santonian to seafloor, and when plotting the curves for the total post-raft overburden (Figure 4.7 and Figure 4.8).

Overburden strata draping rafts 2 and 3 show a similar thickness trend to equivalent strata above raft 1, recording ~1250 ms (1562 m) and 2600 ms (2860 m) for the top raft to base Santonian, and base Santonian to seafloor intervals (Figure 4.7c). Strikingly, rafts 4 and 5-6 show marked thickness variations in north-south profiles, but with the thicker overburden strata occurring to the north and central parts of the rafts. Raft 6 shows larger thickness in its central part (Figure 4.7d). In essence, the thickness of post-raft overburden increases towards the south when considering the sequences between Horizon 4 and 5, and decreases for the Santonian-Seafloor sequence (Figure 4.7).
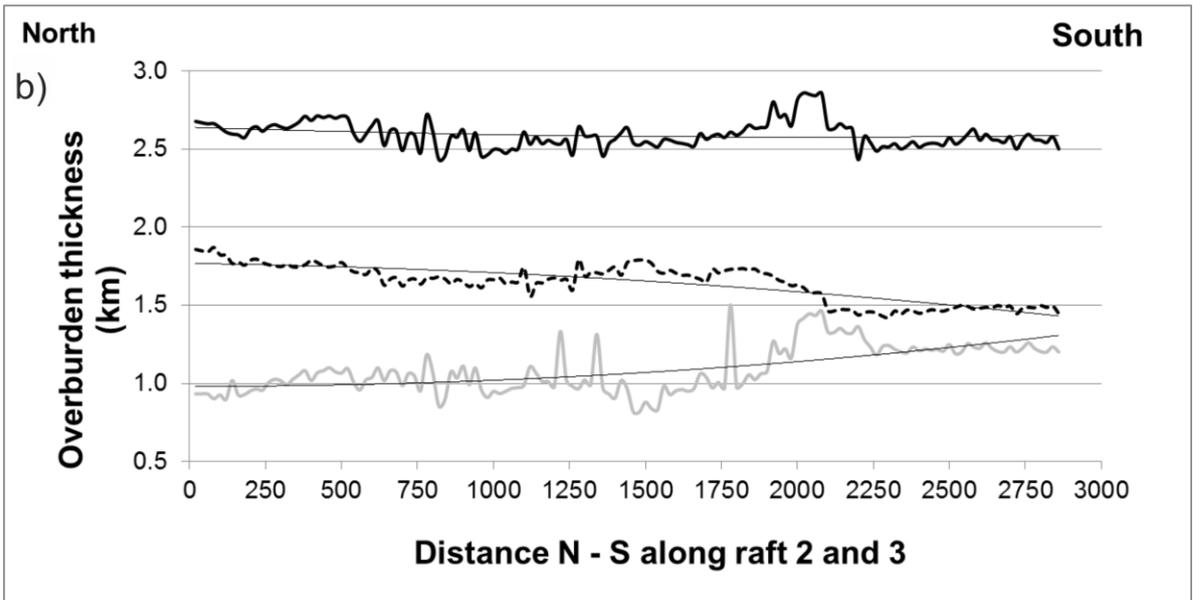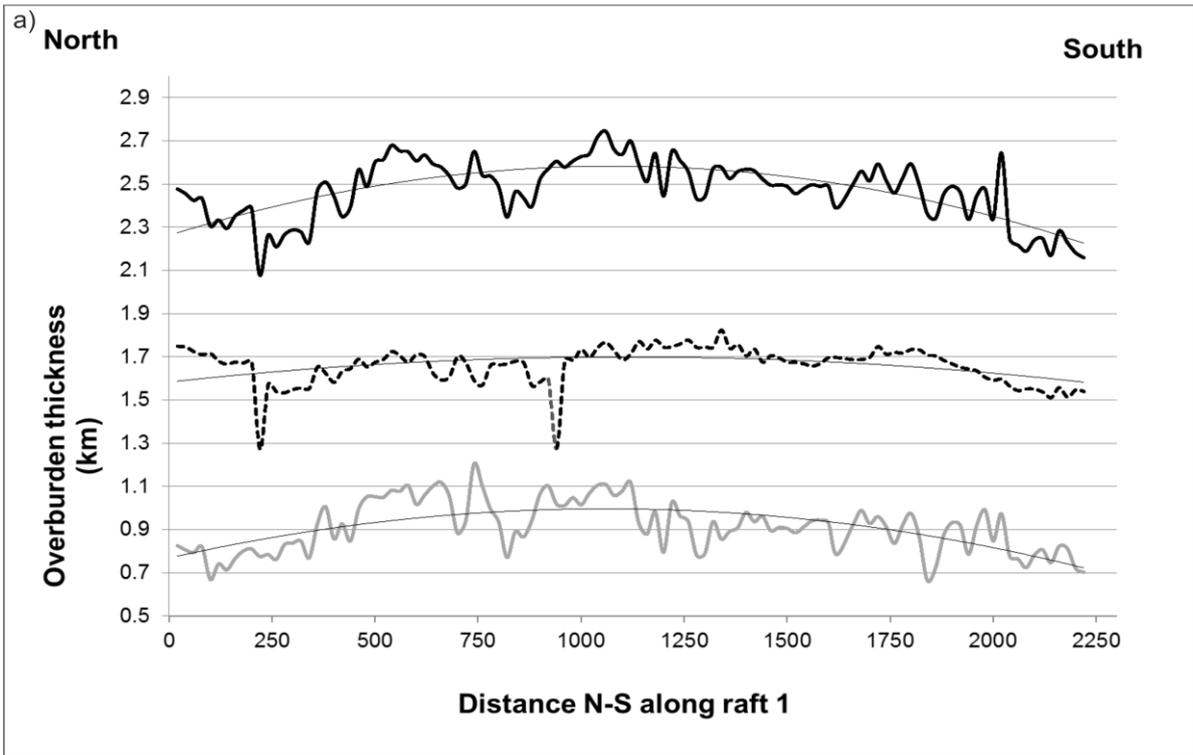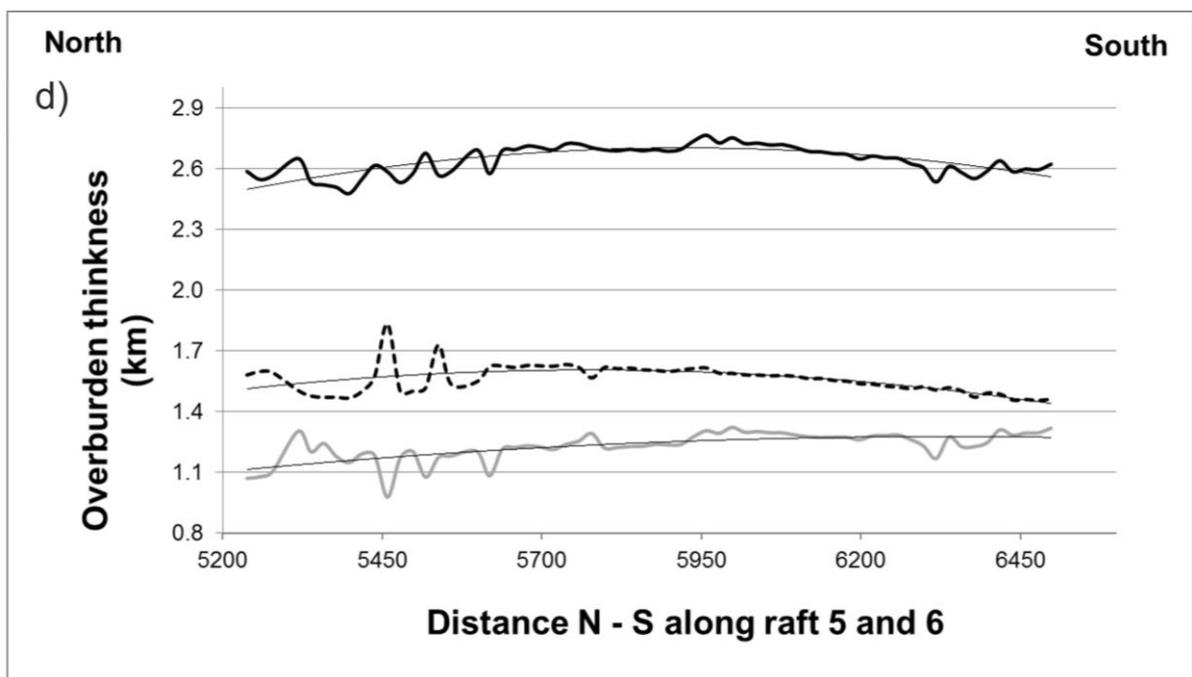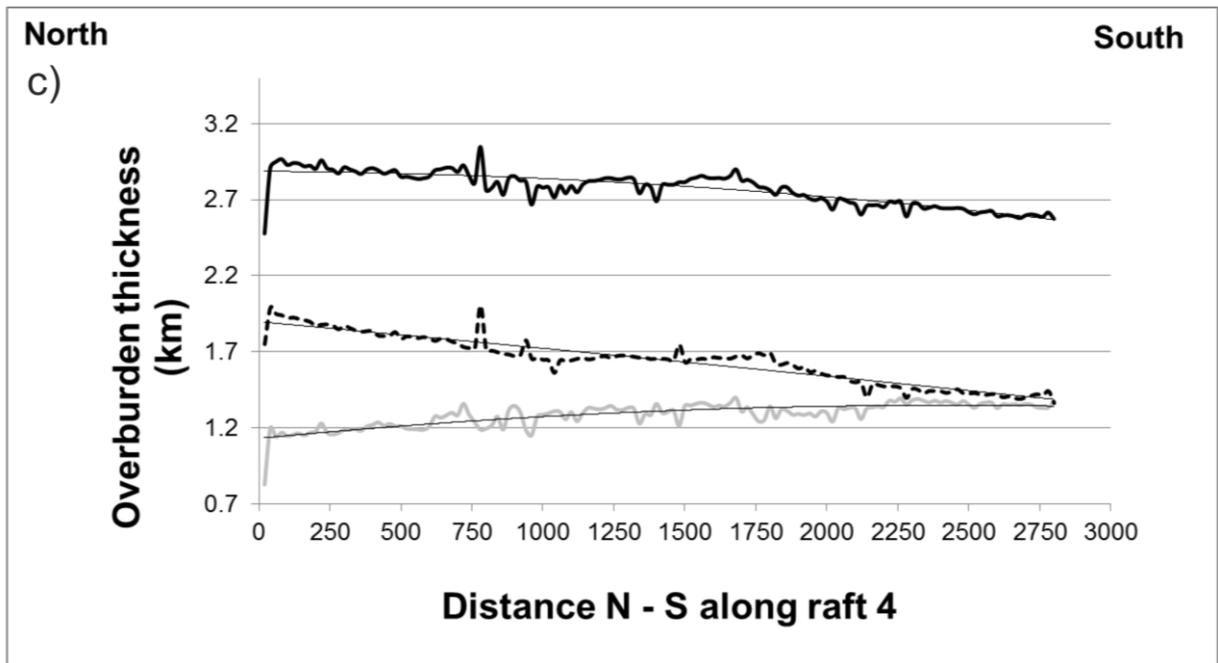
Figure 4.7 - Thickness of post overburden strata of raft 1 in offshore Espírito Santo Basin (SE Brazil). Data acquired N-S direction on the seismic volume. The data and trend lines refers to different intervals: (i) top raft to base Santonian (grey line); (ii) base Santonian to seafloor (dashed line in back) and (iii) total overburden which includes thickness of post Albian rafts until the seafloor (back).

4.4.4. **Fault families**

The isochron map in Figure 4.6c between Horizons 4 and 5 (Santonian to top Maastrichtian). In addition, the seismic profiles in Figure 4.4, Figure 4.5 and Figure 4.8 highlight the main fault families developed above the Aptian salt and in Albian rafts. Figure 4.6c is complemented by the TWTT structural maps in Figure 4.9. The maps show the complex sets of faults affecting post-salt overburden units near the base of the Santonian and above. The seismic profiles in Figure 4.8 show that overburden faults propagated vertically until they reached horizon 4 (base Santonian) and overlying strata. Fault families in rafts 1 to 6 include: a) roller faults, b) rollover faults, c) keystone faults; d) reactivated faults and f) concentric faults. A schematic map of these types of faults is shown in Figure 4.10.

4.4.4.1. *Roller Faults*

Roller faults accommodated bulk downslope displacement in rafts. Roller faults dip both oceanwards (east) and landwards (west), offsetting strata in rafts 1 to 6 and overlying strata above them (Figure 4.5, Figure 4.8, Figure 4.10 and Figure 4.14a). Roller faults sole out into the Aptian salt. Triangular salt rollers are observed in the footwalls of roller faults (Figure 4.11). Some of the roller faults propagated upward into lower Cenozoic strata, topping out at the base of a mass-transport deposit that contains large remnant blocks (Alves, 2012).

4.4.4.2. *Rollover Faults*

Rollover faults comprise closely-spaced antithetic and synthetic faults generated on top of monoclinal rollovers and turtle anticlines, themselves formed due to movement on adjacent roller faults. Together with keystone faults, rollover faults accommodate some of the bending strain related to the downslope displacement of collapse of underlying rafts. They are formed due to progressive bending of rollover structures above the Albian rafts (Figure 4.5, Figure 4.8 and Figure 4.14a).

4.4.4.3. Keystone faults

Keystone faults are pairs of conjugate normal faults that dip in the opposite direction to, and accommodate displacement occurring on rollers faults (Figure 4.8 and Figure 4.4b). Keystone faults can also manifest as planar growth faults rooted into the crests of triangular salt rollers. Throws on keystone faults are small in the regions where they intersect collapsed salt rollers (Alves, 2012).

4.4.4.4. Reactivated faults

Reactivated faults comprise fault sets initially formed by the arching of overburden units above the Albian rafts. They were later reactivated in late Cretaceous anticlines, as shown in Figure 4.8. The geometry of inverted roller faults resemble that of keystone faults, but they form anticlinal structures towards their top (Figure 4.14d). They are interpreted as rollover, keystone faults that were reverse-reactivated.

4.4.4.5. Concentric faults

Concentric faults are observed above the depocentres formed by raft tectonics (Alves, 2012) (Figure 4.10b). They are developed on the margins of extensional sub-basins, dying out downwards the main Cretaceous depocentres, accommodating local strain at the tips of the oval-shaped sub-basins formed on the hanging-wall blocks of roller faults.
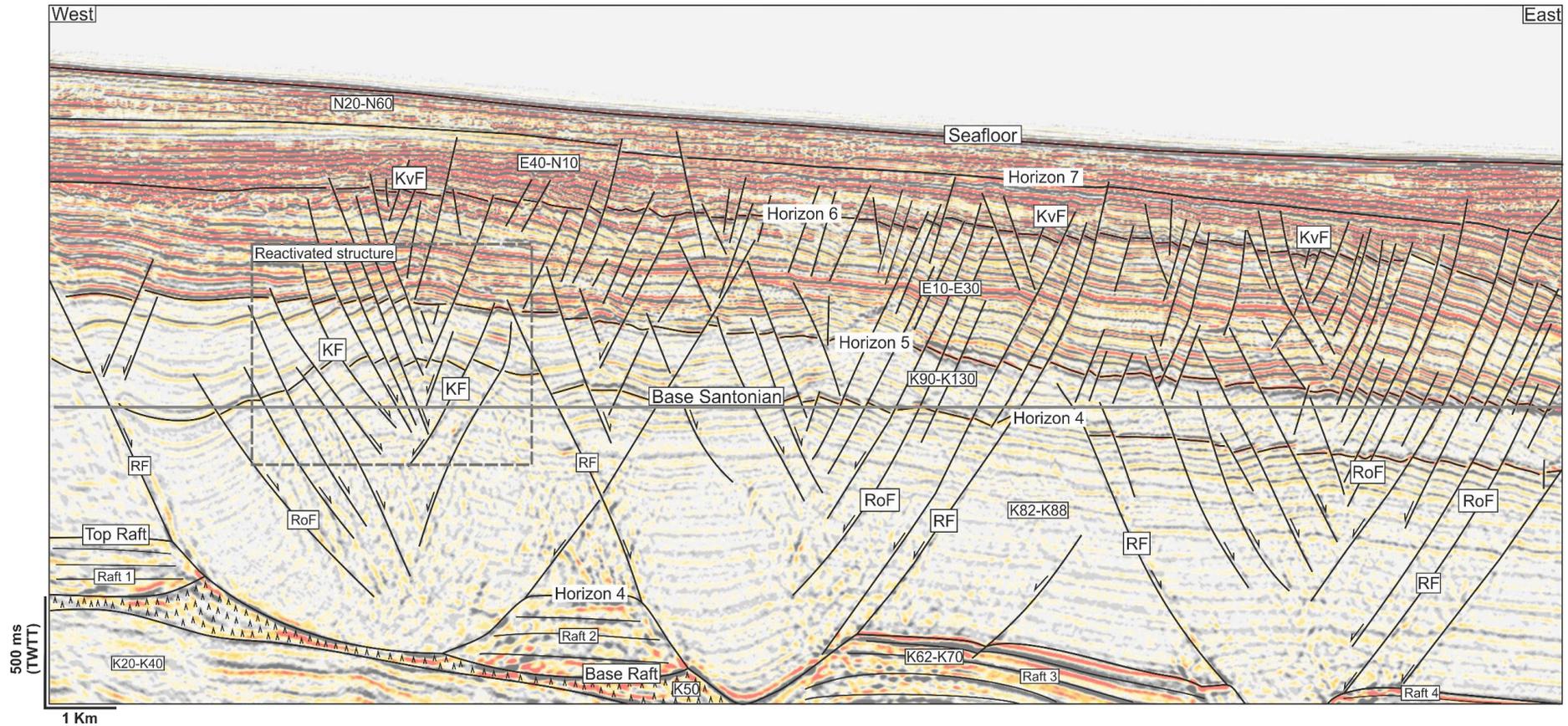
Figure 4.8 – Seismic profile highlighting the principal fault families related to raft movements. The figure shows roller faults (RF), rollover faults (RoF), keystone faults (KF) and reactivated faults (RvF). The raft reactivation is observed on the base Santonian unconformity, showing local pop-up and tight anticlinal structures (square dashed line). The main horizons considered for thickness plots in the Figure 4.7 are also pointed out: base and top rafts, base Santonian and seafloor. The figure include a line (in grey) for horizon reference.
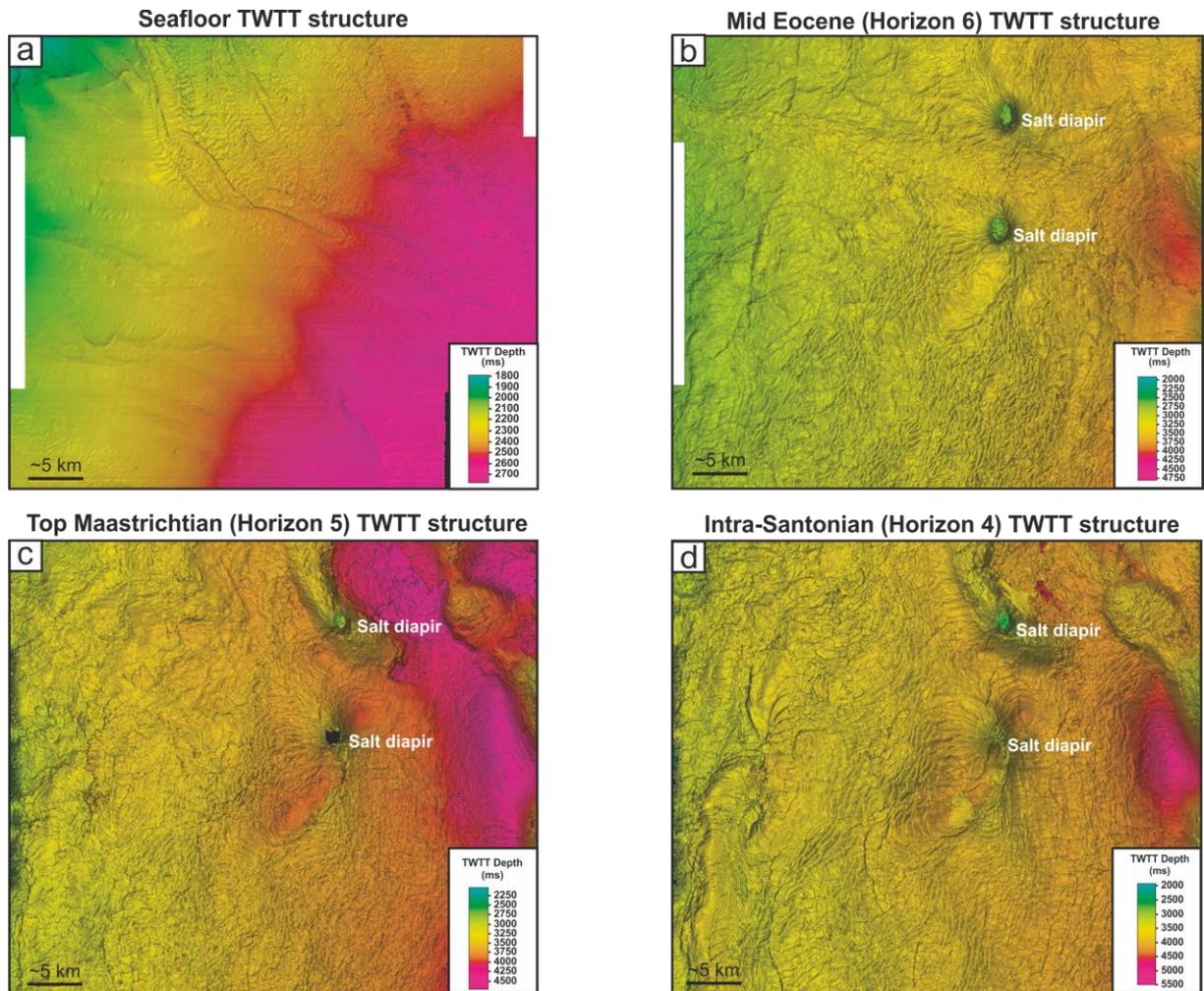
Figure 4.9 – Structural maps for key horizons mapped in the study area a) seafloor; b) Eocene unconformity (horizon 6); c) top Maastrichtian uniformity (horizon 5); d) intra-Santonian unconformity (horizon 4). Note the masked faulting of the mapped horizons.
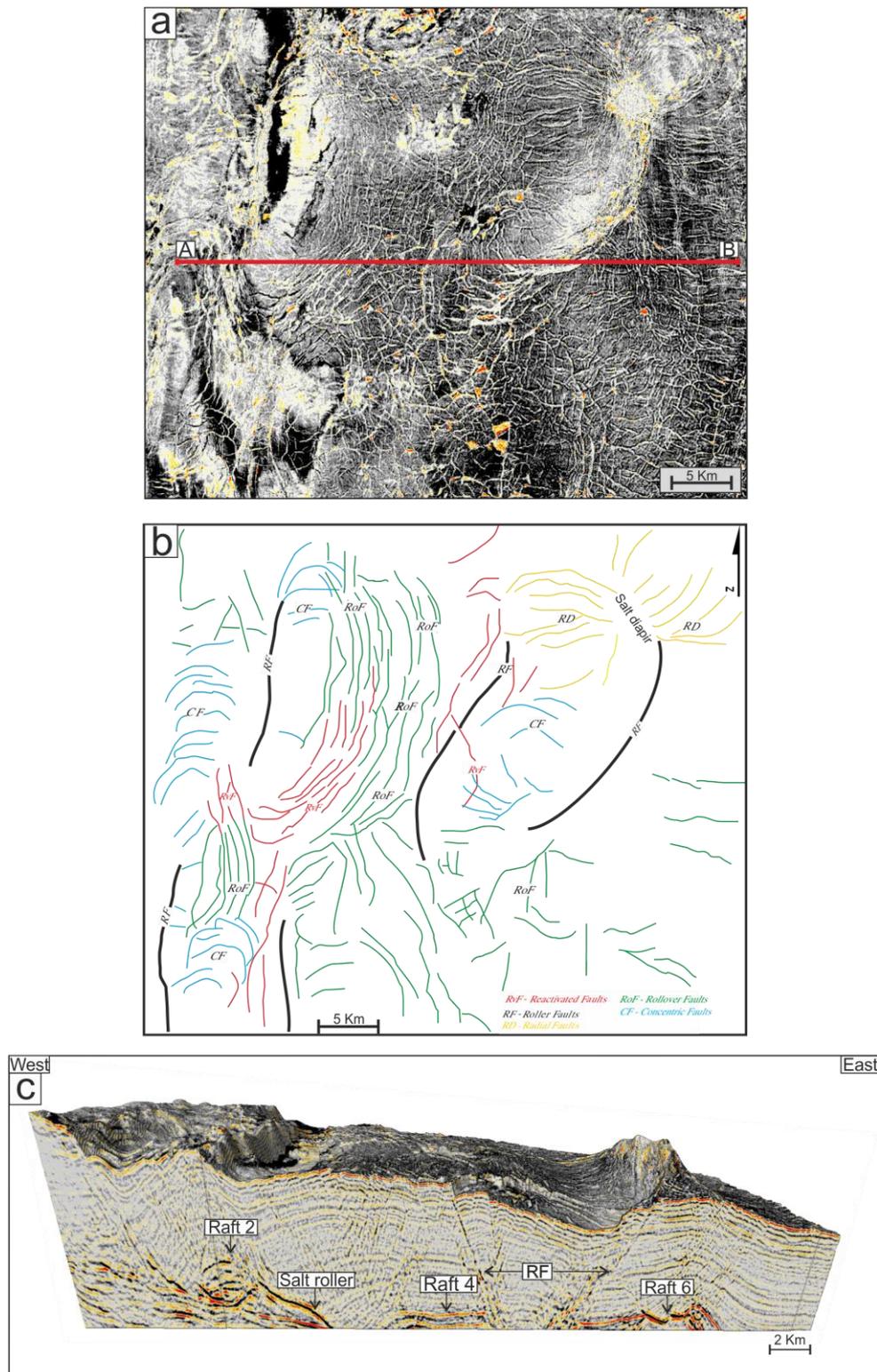
Figure 4.10 – Amplitude map of base Santonian showing the main fault families that intersect Horizon 4 (base Santonian); b) interpreted based on the amplitude map highlighting the faults families; c) block diagram though segment A-B (Figure 4.10a) highlight the faults families; c) block diagram through segment A-B' (Figure 4.10a), with ~5x vertical exaggeration. It shows raft 2, 4 and 5, and the main roller fault adjacent to the raft. (Radial fault from Alves (2012).
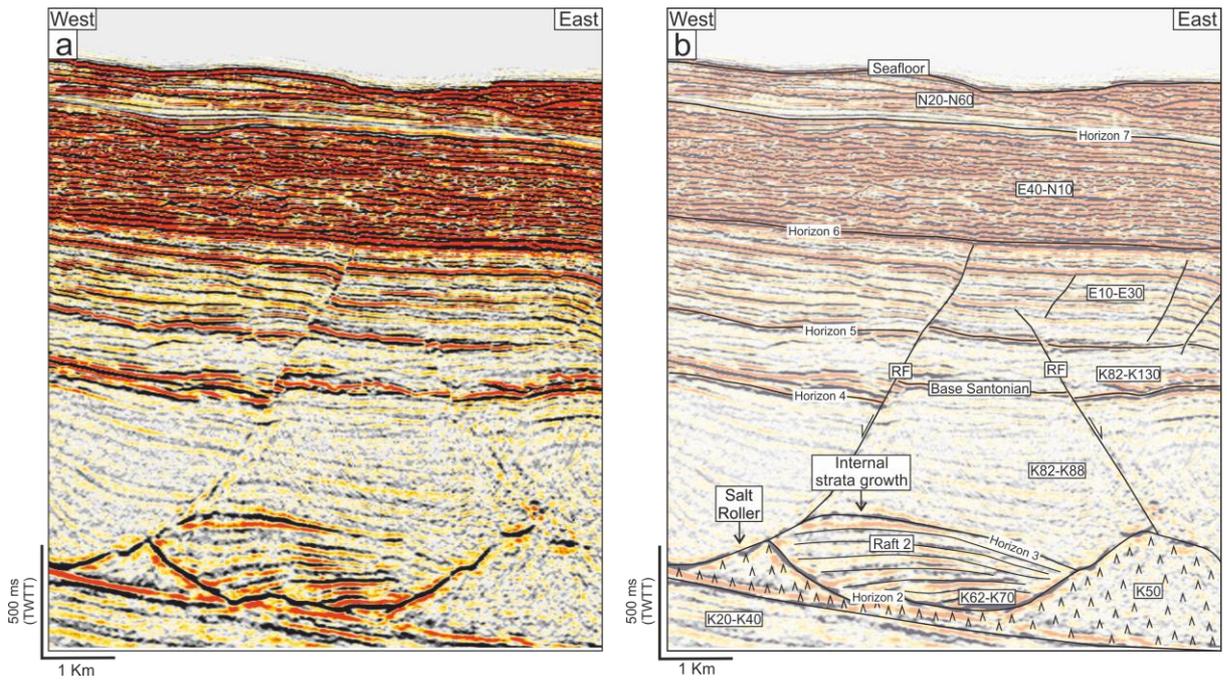
Figure 4.11 – a) Uninterpreted and b) interpreted West to East seismic profile showing gentle internal strata growth in raft 2. Note the presence of growth raft strata above the salt roller to the east, and the initiation of a triangular-shaped structure above raft 2. The raft is lateral confined by salt structure, salt roller to the east and salt pillow to west.
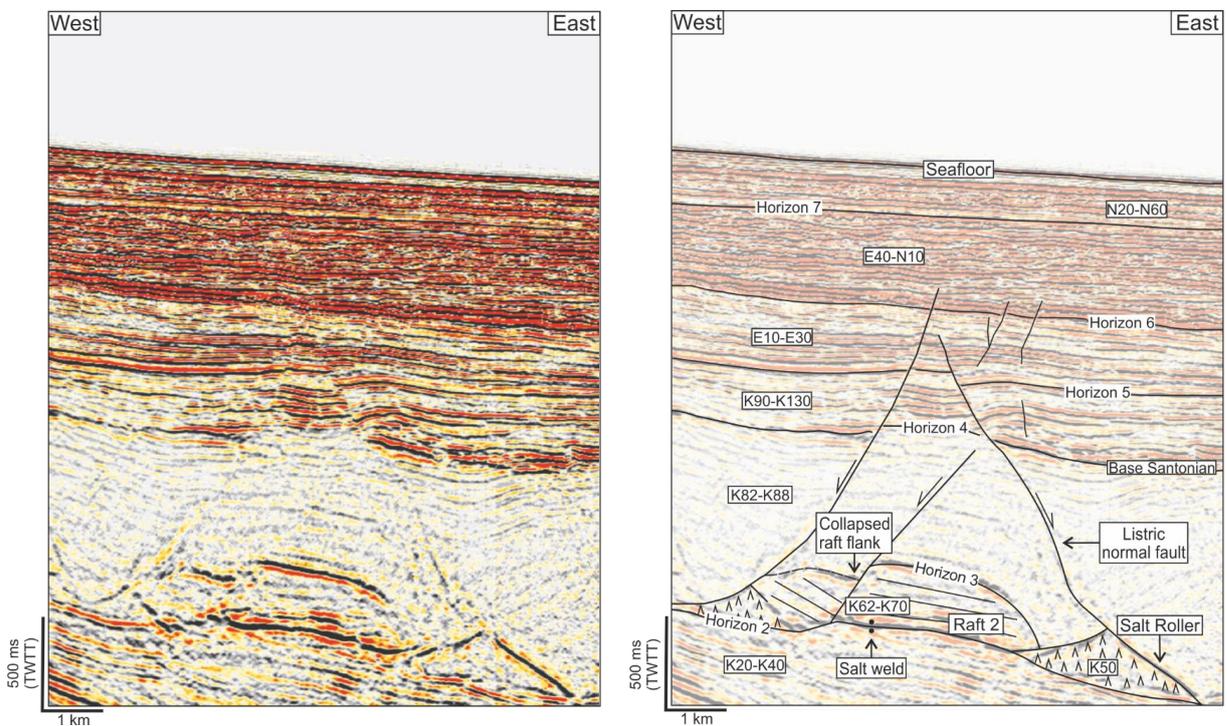
Figure 4.12 – a) Uninterpreted and b) interpreted West to East seismic profile showing collapsed lateral part of raft 2, roller faults and salt welded on the pre-salt units.
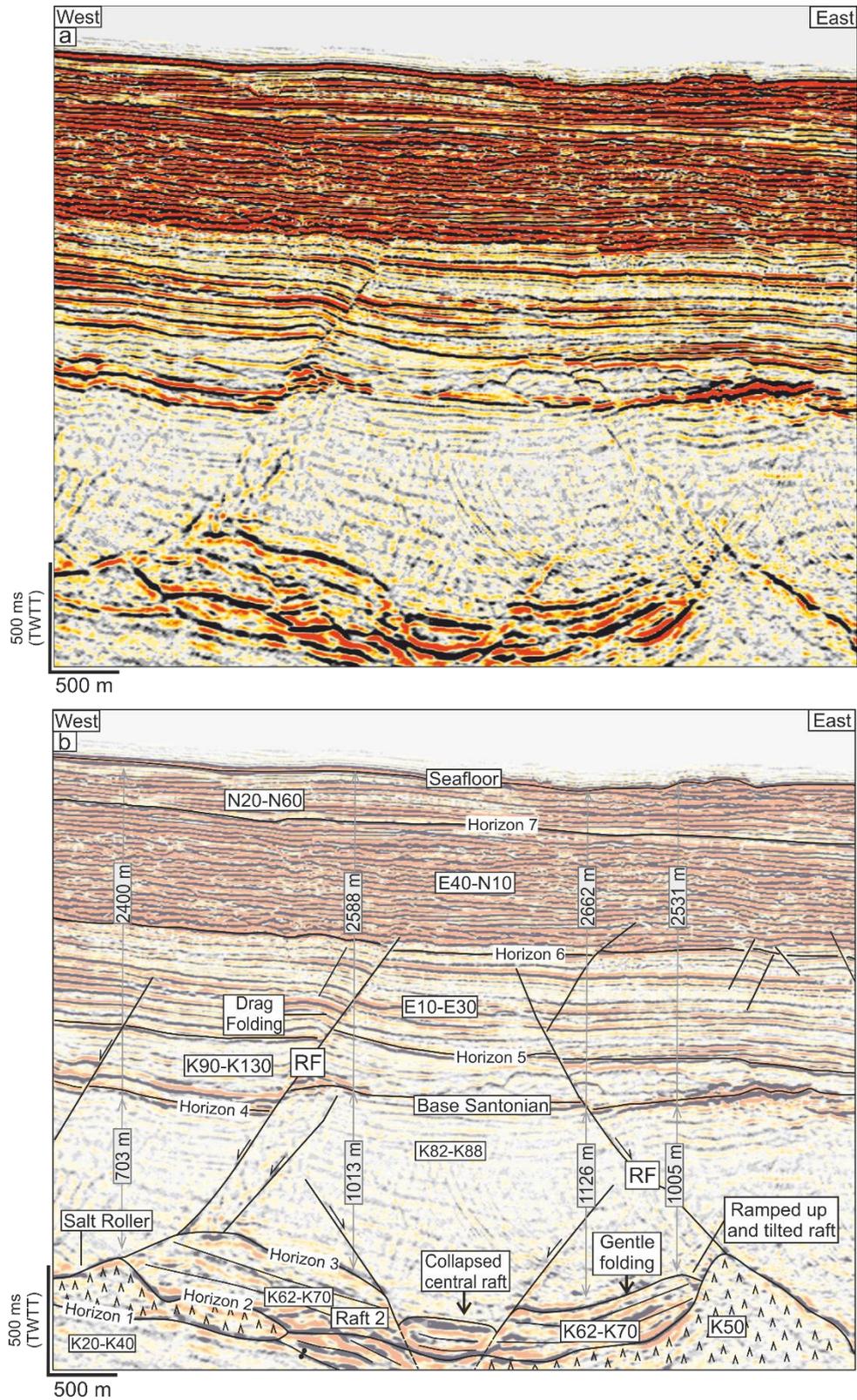
Figure 4.13 – a) Uninterpreted and b) interpreted West to East seismic profile showing the structural deformation in raft 2. Deformation styles include the tilting of flaking strata, ramping up on the salt structures and collapse of central part of the raft 2, lateral constrained by extensional faults and welded on the pre-salt units. Is highlight the thickness (m) between the i) top raft to base Santonian and ii) base Santonian to seafloor, for reference.
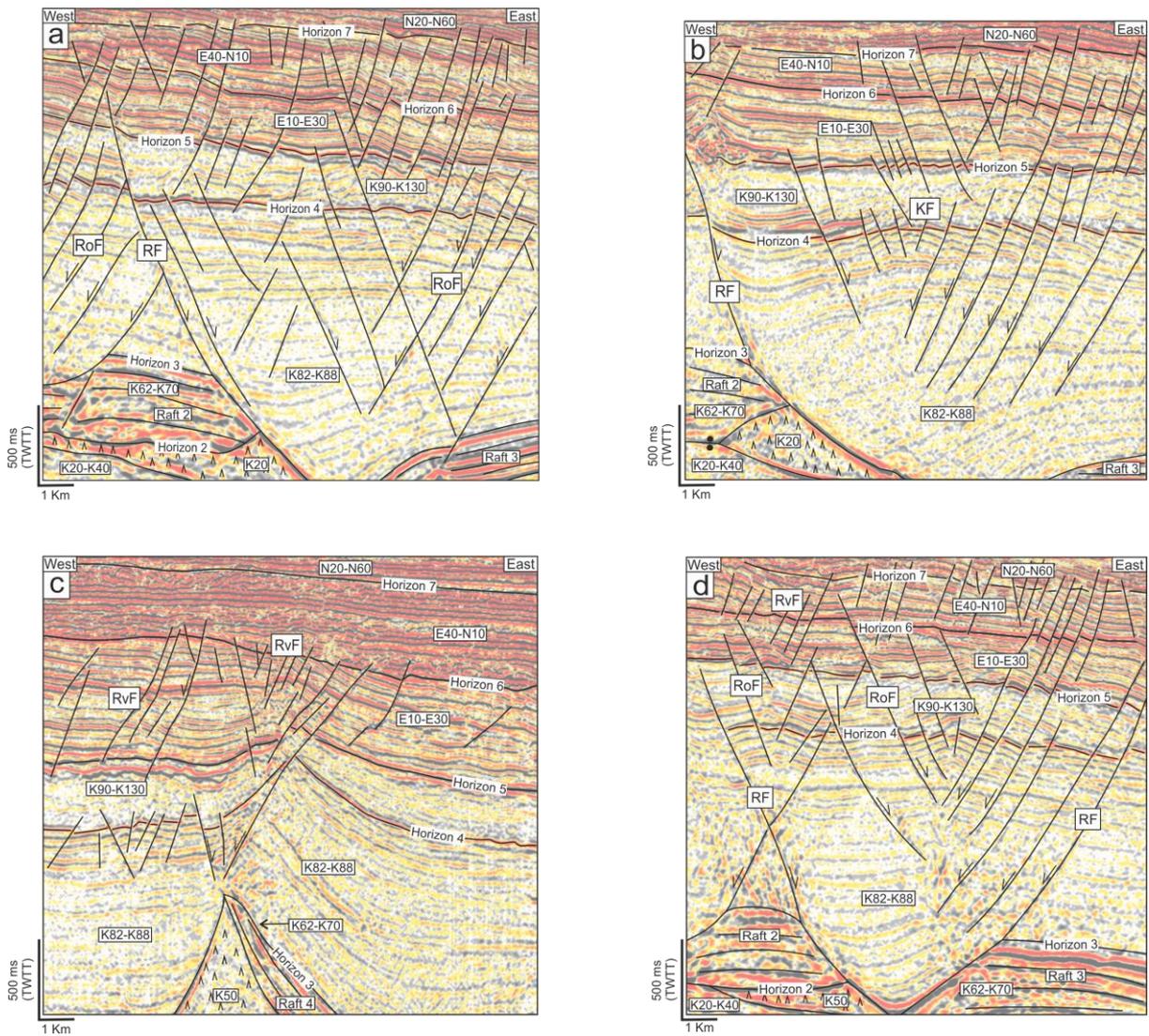
Figure 4.14 – Seismic profile highlighting the major fault types triggered by the movement of rafts and post-raft overburden: a) Roller and rollover faults; b) Keystone faults; c) Reactivated faults; d) Rollers, reactivated and rollover faults. See Figure 4.1a for location of the seismic profiles.

4.4.5. **Structural styles documenting raft deformation over Aptian salt structures**

4.4.6. **Rolling-over and internal strata growth**

Rolled-over rafts are those showing important growth of strata adjacent to salt rollers and roller faults (Figure 4.12). These rafts are not cross-cut by major faults, and are mostly bounded landwards and oceanwards by large roller faults. Rolled-over rafts formed during Cretaceous gravitational collapse of the margin, but with most of the extension concentrated on the larger roller faults. Turtle-back structures are not developed above these rafts (Figure 4.4 and Figure 4.8).

The raft imaged in Figure 4.11 shows important growth of strata in the areas where salt was withdrawn from the base of the raft towards adjacent salt pillows. It is also noted the increasing angle of basal strata in the raft as the rolling-over of the raft continues in time (Figure 4.8).

4.4.7. **'Passive' fragmentation in the form of tabular rafts**

Tabular rafts are structures displaced over salt without significant control of roller faults on local subsidence (Figure 4.8 and Figure 4.12). Instead, these rafts are interpreted to have evolved with large salt rollers separating them from adjacent rafts, and hindering any rolling over of strata on their flanks (Figure 4.8 and Figure 4.12). Faults are scarce in their interior and, when present, show predominant normal offsets resulting from salt withdrawal at flanks of the rafts. Turtle anticlines can form in younger overburden units in response to folding of latest Cretaceous-early Tertiary strata (Figure 4.15).

Raft 2 is also an example of a tabular raft in the study area of Espírito Santo presented in Figure 4.15. Tabular rafts show no significant growth of strata in their interior, suggesting they were 'passively' translated and fragmented on the continental slope. In the study area, most of the tabular rafts seem to be partly welded on pre-salt successions and are bounded by small to moderate size salt rollers that did not deformed their flanks (Figure 4.15).

4.4.8. **Collapse and folding of rafts' flanks due to salt withdrawal**

Collapsed blocks are observed in flanking strata to sub-tabular rafts, always in association with withdrawal of salt from evolving salt rollers Figure 4.13. Resulting fault styles include normal faults showing no growth at the level of the Albian rafts, but showing growth and erosional truncation at Late Cretaceous level (Figure 4.13). This character suggests the faults post-date the deposition of Albian-Cenomanian strata draping the interpreted rafts. As a result of the withdrawal of salt from salt rollers, most of these collapsed blocks are, at present, welded onto pre-salt successions (Figure 4.13).

Rafts are usually folded in the immediate footwall of the larger roller faults (Figure 4.13). They reflect later growth of roller faults and associated growth of salt rollers on the flanks of relatively stable rafts. Roller faults show predominant normal offsets and, in some parts of the study area, were reactivated to form pop-up structures expressed in Upper Cretaceous strata.

The withdrawal of salt from underneath of the raft 2, and subsequent growth of the salt pillow to the west, resulted in the collapse of the flank of the imaged rafts (Figure 4.13). This structural style is more obvious to the north of the study area, where rafts 1 to 6 are close together and segmented in smaller rafts. Local collapse structures accompany the tilting and fragmentation of rafts on the flanks of salt rollers that grew, or where shortened, during the Late Cretaceous and Cenozoic.
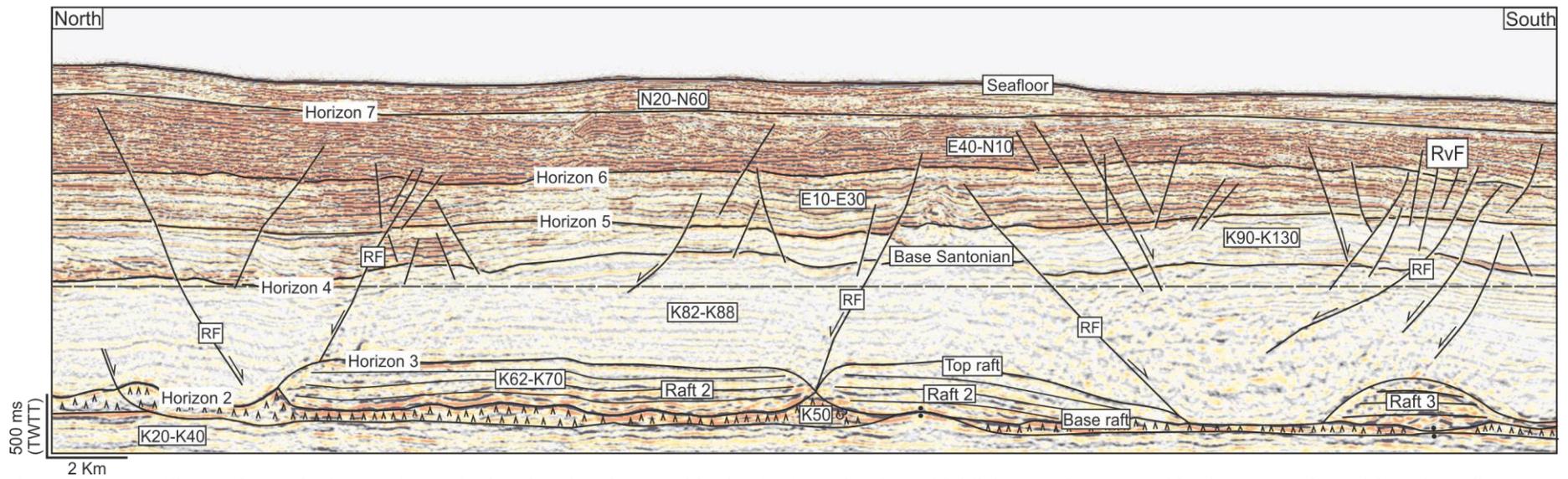
Figure 4.15 – Profile North-South above raft 2. It is showing the elongated body of raft 2. The figure highlights any interpreted horizons together with main sedimentary and structural bodies in the study area. Dashed line (in grey) included for reference.

4.4.9. **Tilting and fragmentation of rafts on the flanks of growing salt rollers**

The most striking example of late reactivation in rafts comes from the array of faults and rafts formed and tilted on the flanks of growing salt rollers. An example of one of such structures is shown in Figure 4.13, in which the oceanwards half of raft 2 is fragmented collapsed and tilted on the flank of the salt roller separating raft 2 into two parts. Normal faults related to the collapse of rafts over withdrawn Aptian salt are observed in Figure 4.5 and Figure 4.13. Faults show predominant normal offsets resulting from extension and salt withdrawal, but do not extend up into Upper Cretaceous strata i.e., they were chiefly generated by short-lived collapse of rafts during the Late Cretaceous. As a result of collapse, complex sets of conjugate normal faults are often observed in Upper Cretaceous rollovers, as structures formed to accommodate the collapse of underlying rafts (Figure 4.13).

The imaged raft was tilted and fragmented on the flank of a growing salt roller, which shows evidence for Late Cretaceous reactivation. Part of this fragmentation results from withdrawal of salt from the base of the rafts to inflate the adjacent salt pillow, thus resulting in complex structural compartmentalisation of intra-raft strata.

4.5. **Discussion**

Fiduk et al. (2004) assumed tectonic contraction in post-salt units began early in the Albian and continued until the present day. Rafting ceased at different times depending on the initial thickness of the salt available and overburden thickness. Based on these two principles, we discuss in this section: (i) the different styles of deformation observed on the rafts and (ii) reactivation of faults as a function of salt roller growth.

4.5.1. **Why is there a poor correlation between basal slope angle, overburden thickness and the degree of raft deformation?**

The key question posed by this work is why there is a poor correlation between slope angle, overburden thickness and the degree of raft deformation in the Espírito Santo Basin? Based on the evidence of moderate, but widespread tectonic reactivation of the continental slope during the Late Cretaceous and Eocene, a plausible explanation should consider important raft movement in Espírito Santo after the Santonian. An example of late-stage raft tectonics, in which the reactivation of salt rollers is a key control on rafts' structural deformation, is provided by raft 2 (Figure 4.8 and Figure 4.9). Ramped-up strata on the flanks of a salt roller, with associated uplift and erosion of the Late Cretaceous Horizon 4 demonstrates a later stage of deformation in the study area (Figure 4.4 and Figure 4.5). This geometry was interpreted as reflecting late evacuation of evaporites from upper-slope regions of the Espírito Santo Basin to the base of the continental slope. Downslope salt flow resulted in the collapse of minor salt pillows below individual rafts, in the growth of the larger salt rollers, and in the progressive welding of rafts 1 to 6 onto pre-salt units. Most of this collapse occurred in the Late Cretaceous, as shown by the collapse faults developed above Horizon 4.

The history of gravity-gliding extension of the Albian rafts and the relationship with Aptian salt layer are summarized in Figure 4.16. At the scale of the interpreted 3D seismic volume, we observe that syn-kinematic sediment thickness is relatively constant, a character suggesting that vertical loading imposed by overburden strata was not the key factor controlling raft movement and deformation in the study area. Instead, lateral spreading and downslope gliding of the rafts was likely controlled by the presence of intra-raft salt structures – which

closely controlled the degree of downslope movement and faulting experienced by rafts 1 to 6 (Figure 4.11 and Figure 4.16).

Based on the interpreted data, is suggest that 'late' compartmentalisation of rafts offshore Espírito Santo is an important phenomenon, with overburden thickness playing only a minor role. In this work is demonstrate that salt rollers and the relative thickness of salt underneath individual rafts are the main factors controlling raft movement. In regions where raft movement was overprinted by the growth of salt rollers, rafts are highly segmented by reactivated faults (Figure 4.4, Figure 4.5 and Figure 4.16). In regions where smaller volumes of salt were available below the rafts and ramping-up over growing salt rollers was hindered, rafts were static throughout most of their late evolution and structural compartmentalisation was accordingly moderate.

A second question that arises when interpreting the seismic data in this paper is why are structural collapse, tilting and local deformation so prominent in raft 2? One possible answer to this question assumes that extension-related faulting was predominant in the study area, and that no major reactivation occurred in response to the Andean tectonic stages. A second potential explanation is that tectonic reactivation was significant, and that a later stage of roller growth and salt withdrawal may have occurred, even if in a predominantly extensional regime.

Locally reactivated faults and associated pop-up structures indicate that a late stage of horizontal shortening affected the study area, particularly during the latest Cretaceous and Palaeogene (e.g. Alves, 2012) (Figure 4.8 and Figure 4.16). These structures were previously interpreted as partly accommodating strain across the hinge of extensional rollovers. It was interpreted as reflecting a later stage of gravitational gliding in the study area, in which Late Cretaceous strata (K82-K88) were compressed against Aptian rafts (and overburden strata) due to the change from vertical subsidence, recorded on the upper part of roller faults, to sub-horizontal strain in the regions where roller faults sole into the Aptian salt (Alves, 2012).

Deformation in raft 2 is interpreted as a result from the combination of factors described above, but the surprising result in our analysis is that the thickness of the sediments overburden is not a key factor in the onset of late raft deformation. Instead, it is suggested that deformation in raft 2 resulted from a combination of factors, including slope

oversteepening and resulting stresses imposed by a gravitationally unstable, downslope-moving overburden sequence against rafts 1 to 6. In this model, the evacuation of salt from beneath the rafts, and their eventual grounding, was an important process controlling the degree of deformation in Albian-Cenomanian rafts. Rafts overlying thin salt successions were quickly grounded, and faults mostly occur within Late Cretaceous-Early Cenozoic overburden strata (Figure 4.4 and Figure 4.5). Rafts with significant thickness of salt underneath record important collapse, with salt withdrawal contributing to the growth of adjacent salt rollers. The combined effect of salt roller growth and horizontal shortening of these same salt structures (contributing to an increase in the angle of rollers' flanks) acted together to further tilt and deform Albian-Cenomanian strata (Figure 4.16). As a conclusion, is observed in the study area styles of raft compartmentalisation distinct to those published in the literature, with the thickness of overburden units and slope oversteepening being locally replaced, as primary factors in raft compartmentalisation, by the thickness of available salt below and adjacent to fully developed rafts. The Figure 4.16 shows the advances in raft tectonics knowledge after Alves (2012), where is proposed as first stage (Albian to Post-Albian) highlighting a stage of pre-raft structures. The salt withdraw and consequent salt weld, raft deformation and compartmentalisation of Albian raft are also proposed as a tectonics and structural evolution of the salt tectonics areas in the Espírito Santo Basin.

4.5.2. **Importance of collapse features to the generation of salt welds**

Salt welds are formed at the base of post-salt strata by the complete evacuation of salt from below these strata (Jackson and Cramez, 1989; Rowan et al., 1999). A consequence of welding of post-salt strata onto pre-salt units is the establishment of fluid conduits between stratigraphic intervals that, otherwise, would be hydrodynamically separated (Rowan, 2014). A key observation from the interpreted seismic data is the generation of salt welds in regions recording collapse and tilting of strata on the flanks of salt rollers (Figure 4.16). In these cases, the timing in which the salt was withdrawn from the base of the rafts, and a full weld was formed, is an important piece of information when assessing the degree and timing of connectivity between pre-salt and post-salt units. An example of these salt welds in shown in (Figure 4.12 and Figure 4.15), in which only a small part of the raft is in contact with pre-salt

strata (salt weld). It is assuming that most of this welding occurred relatively late in the Espírito Santo Basin, allowing the migration of fluids from pre-salt source intervals into rafts and Cretaceous reservoirs only after welds were present below individual rafts. This is an important observation, and one that confirms that palaeoreconstructions of raft movement, and fluid migration, are key to explaining discrepancies in the charging of post-salt reservoirs on continental margins dominated by gravitational collapse. Still to explain is the importance of deeper (raft-related) structures in controlling slope depositional systems in the post-overburden strata and the deformation of near-seafloor strata.
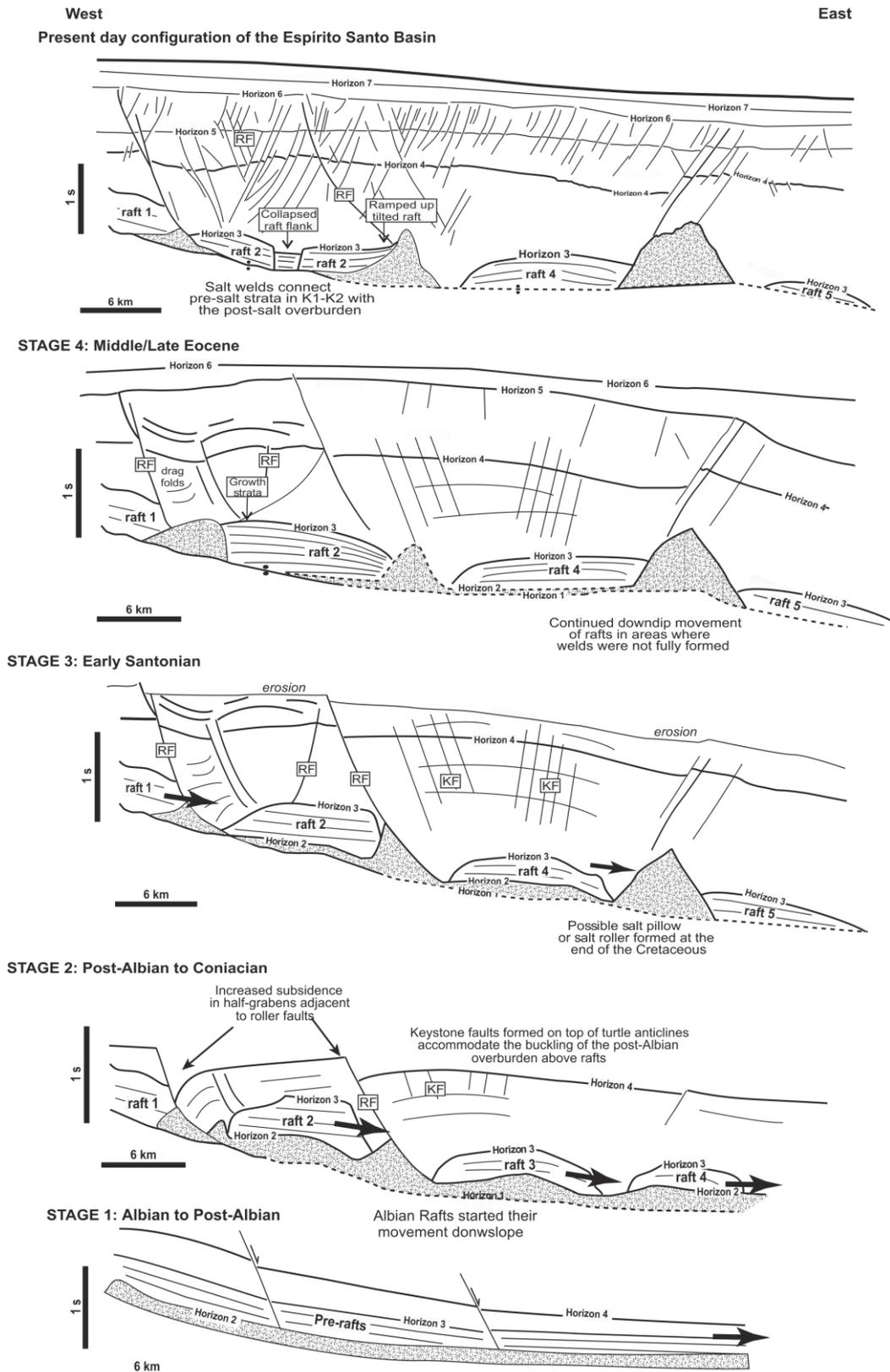
Figure 4.16 – Conceptual schematic evolution of rafts in the study area, highlighting the effect of salt pillow growth on structural compartmentalisation of Albian (and younger) strata in the Espírito Santo Basin. Fault systems in the figure are associated with different styles of raft deformation, as described in this chapter. After Alves (2012).

4.6. **Conclusions**

This chapter shows that the most developed styles of faulting and raft deformation occur where salt was withdrawn from the base of rafts in the Late Cretaceous/Early Cenozoic. This withdrawal likely resulted from tectonic imbalance between overburden loading and slope gradient imposed by the Andean tectonic phases affecting SE Brazil.

The most important conclusion from the observations are summarised as follows:

- Identification of different styles of raft deformation:

   i) Rolling-over and internal strata growth in rafts that were displaced in the Albian-Cenomanian;

   ii) Fragmentation in the form of sub-tabular rafts whenever they were 'passively' translated on the continental slope;

   iii) Collapse of rafts' flanks due to salt withdrawal from beneath them; - Tilting and fragmentation of raft on the flanks of growing salt rollers;

   iv) Tilting and fragmentation of raft on the flanks of growing salt rollers.

- By the above documented raft deformation is assumed their contribution to a large degree of faulting which is documented in this chapter which affects the post-raft overburden.

- The faults resulting from the adaptation of raft tectonics deformation and salt withdraw is influencing the post-raft stratigraphic units and consequently affect the slope instability in the area. Not only around diapirs (Omosanya and Alves, 2013), but also in areas where is not direct affected by salt structures but by stratigraphic accommodation.

PALAEOGEOMORPHOLOGICAL CONTROLS ON MASS-TRANSPORT DEPOSITS OFFSHORE ESPÍRITO SANTO BASIN (SE BRAZIL)

Chapter Five

5.1. **Abstract**

Mass-transport deposits form a significant part of the stratigraphic record of ancient and modern deep-water basins worldwide. Three-dimensional (3D) seismic data is used in this chapter to analyse two different types of buried mass-transport deposits offshore Espírito Santo Basin (SE Brazil). Both types are developed within Early Miocene to Holocene stratigraphic units composed of sandstones, calcarenites, turbidite sands and marls. The high resolution images provided by the interpreted 3D seismic data allowed a detailed analysis of the seismic stratigraphy and internal structure of mass-transport deposits. In addition, improvements in visualisation techniques were used to compute simple morphometric attributes of buried mass-transport deposits in continental slopes.

This study classifies the interpreted mass-transport deposits in two different types according to the relationship between the morphology of mass-transport deposits and the surrounding topography. Locally *confined* mass-transport deposits are laterally constrained by non-deformed strata that surround the mass-transport deposit and by the local topography of the depositional surface. Their dimensions are relatively small (area of ~5.251 km^2). *Unconfined* mass-transport deposits show a much larger volume compared to the previously type (~87.180 km^3), and local topography does not have control on their geometry. The analysis in this chapter proves that local topography and geometry of the depositional surface are key controlling factors on the spatial distribution and dimensions of the two types of mass-transport deposits. However, the two types differ in size, geomorphological expression, local structural controls and run-out distance.

This work is important because it relates variations in the character of the depositional surface with the morphology of mass-transport deposits and run-out distance. As a result of the methodology used, two different styles of mass-transport run-out are identified and local factors controlling their morphology are addressed, such as roughness and local morphology of the depositional surface. Separating these two styles, or types, of mass-transport deposits it is of critical importance to understand their mechanisms of gliding, downslope spreading and emplacement. Furthermore, the

results from this chapter are an important scientific contribution, because the effect of local topography beneath mass-transport deposits are not been fully addressed in the literature.

5.2. **Introduction**

Mass-wasting is one of the most important processes shaping and filling offshore sedimentary basins (McAdoo et al., 2000, Locat and Lee, 2002, Gee et al., 2005, Gee and Gawthorpe, 2006, Masson et al., 2006, Moscardelli and Wood, 2008). Mass-transport deposits (MTDs) comprise 10% - 30% of continental slope strata in all latitudes (Talling et al., 2007), and occur on both tectonically 'passive' and 'active' margins (Urgeles et al., 1999, Garziglia et al., 2008, Bull et al., 2009, Scholz et al., 2012). While their kinematic indicators and seismic expression have been comprehensively documented worldwide(Frey-Martínez et al., 2006, Moscardelli and Wood, 2008, Bull et al., 2009, Alves, 2010, Dalla Valle et al., 2013, Omosanya and Alves, 2013b, Gong et al., 2014, Harishidayat et al.), new techniques and tools have improved the way their internal character and distribution on continental margins is documented in the literature (e.g. Mienert et al., 2003, Micallef et al., 2007, Camerlenghi et al., 2010, Micallef, 2011, Moscardelli and Wood, 2015, Harishidayat et al., 2015). For instance, the continental slope of Espírito Santo (SE Brazil) has recently been the focus of several studies which contributed largely to the understanding of the mentioned sedimentary deposits (Gamboa et al., 2010, Alves, 2010, Omosanya and Alves, 2013a, Omosanya and Alves, 2013b, Omosanya, 2014). Frey-Martínez et al. (2006) identified two different types of submarine landslides, which were classified according to their frontal geometry: a) frontally confined and b) frontally emergent. A few years later, Bull et al. (2009) "defined kinematic indicators as geological structures or features recording the type and direction of motion at the time of landslide emplacement", contributing greatly to the understanding of the initiation, dynamic evolution and cessation of continental slope failure. The work of Bull et al. (2009) confirms the processes and mechanisms pointed out in Frey-Martinez (2006). Nevertheless, the relationship between mass-movement(s) morphology and the characteristics of the surface over which the mass movements

occur is still unclear. The published literature commonly focuses on describing the geomorphology of the movements *per se* (e.g. Moscardelli et al., 2006, Posamentier et al., 2011, Gong et al., 2014, Alfaro and Holz, 2014, Rovere et al., 2014), but the local topography under the movements is seldom investigated as a key factor controlling the morphology and internal character of mass-transport deposits.

This chapter aims to document how the local topography of the depositional surface and the surrounding (unaffected) stratigraphy controlled the shape and the run-out of a set of mass-transport deposits (MTDs) interpreted in SE Brazil (Espírito Santo Basin). This is achieved by considering the run-out area to comprise the distance from the source area of the slope movement to the distal toe of its depositional area (McAdoo et al., 2000, Dai et al., 2002). In order to better understand the behaviour of MTDs, one should predict their run-out behaviour, namely how far they can travel once mobilised, and the factors controlling their resulting morphology. In general, run-out behaviour depends on a set of quantitative and qualitative parameters (e.g. slope characteristics, downhill path, residual strength behaviour of sheared zones, mechanisms of failure and types of movement) that control the MTDs spatial distribution and ultimately define the type of mass movement(s) on a continental slope (Dai et al., 2002). The understanding of the factors controlling run-out behaviour depends on the adequate interpretation of topographic factors affecting MTDs` transport and deposition. Dai et al. (2002) pointed out the relevant parameters that need to be taken into consideration when studying run-out behaviour. They include slope characteristics, the mechanisms of failure and modes of mass movement, the downhill path and residual strength behaviour of basal sheared zones (Dai et al., 2002). Part of the parameters are depending of slope roughness, which in geomorphometric point of view is described as an expression of the variability of a topographic surface elevation at a given scale. Where the scale of analysis is determined by the size of the forms or geomorphic features of interest, either local or regional scale (Grohmann et al., 2009).

This work intends to study two main types of MTDs observed in offshore Espírito Santo Basin (SE, Brazil). The two MTD types match the classification in Frey-Martínez et al. (2006) and Bull et al. (2009). The main contribution of this chapter is to provide an

understanding of the relationship between the MTDs described and the topography on which these MTDs were triggered and later deposited. The interaction between MTDs and surrounding (non-deformed) slope strata is also discussed in this chapter. This analysis has been undertaken thought the use of high-quality 3D seismic data integrated into Geographic Information Systems (GIS). Hence, this chapter aims:

(i) To describe two types of MTDs based on their stratigraphic architecture and geomorphological characteristics;

(ii) To characterize the depositional surface of the MTDs based on their local topography features;

(iii) To understand how changes in the geometry of the depositional surface control MTDs internal character and dimensions.

iv) To relate MTDs' transport distance and local depositional surface topography.

This chapter starts with a description of the internal character, seismic geometry of lateral contacts, thickness and geometries of basal and upper surfaces of the interpreted MTDs. It is followed by the morphological description of the depositional surface where the MTDs occurred. Detailed topographic profiles and maps highlight possible topographic barriers at the base of MTDs. The discussion establishes the main differences between the two types of MTDs and addresses depositional surface morphology as a plausible controlling factor for their differences in geometry and internal character.

5.3. **Depositional surface – definition and characteristics**

In this chapter is introduced the concept adopted in this thesis as depositional surface, which is important in this chapter and further analyses in the next chapter.

As depositional surface is defined the high-amplitude seismic reflection (negative, in this case) which reflect the boundary (superior or inferior) of a stratigraphic unit, or bed for an accumulated sediment package. It can represent the lower boundary of a stratigraphic package, but at the same time, making the upper limit of another and older stratigraphic unit (Figure 5.1a).

In this thesis, the high amplitude seismic reflection mapped as a depositional surface marks the boundary between the Early and upper Miocene strata (17 – 18 Ma; Horizon 7), which covers an area of approximately 756 km^2. As it is mentioned in methodological chapter, depositional surface was acquired by mapping a horizon across the entire study area (Figure 5.1), taking extremely care to follow along the entire area the same seismic reflection using Inline and crossline mapping during the interpretation process (chapter 3). The process of mapping a horizon reflection was hampered by physical process, as erosion or cementation, that may been affected the reflections along the entire area.

Depositional surface used in this analysis represents the base of emplacement for the identified MTDs which materialise the palaeo-topography behind MTDs occurrence. In this sense, the depositional surface is used in this work as a Digital Terrain Model (DTM) representing the topography of a palaeo-slope behind where the considered unstable events occurred. Despite the movements occurred just above the depositional surface, the surface itself was not affected by the downslope movement, during the event of instability. The mapping followed a horizon that did not show any disturbance by the downslope slope movements (Figure 3.6).

In turn, the basal shear surface is defined as the lower boundary of the deformed and chaotic of the MTD body, formed in its translation zone above relatively undeform slope strata. In general, basal shear surfaces are concordant with the slope where MTDs are emplacement (Figure 5.2), which partly of it is also concordant with the depositional

surface, except in the headwall domain (or in some examples, scarps) and in the toe domain (Figure 5.2), where basal shear surface cut up-section and in areas where MTDs encountered basal ramps (Frey Martinez, et al 2005).

The depositional surface works in this thesis as a topographic layer (DTM) and is used to compute the predisposing factors for slope instability modelling presented in the chapter 6. The slope morphology observed on the depositional surface is characterised by low slope gradients, which range from 0 to 8° in the steeper areas, making it a very gentle slope of the continental margin. The morphology is marked by a salt diapir in the north, sediment ridges and gentle depressions (Figure 5.3).

5.4. **Chapter specific methodology**

The interpretation of MTDs follows previously established criteria to describe packages of remobilised material and corresponding kinematic indicators (e.g. Hampton et al., 1996, Frey-Martínez et al., 2006, Moscardelli and Wood, 2008, Bull et al., 2009, Gamboa et al., 2010, Omosanya and Alves, 2013a). The upper surface of an MTD is usually a ridged and rugged surface located right above chaotic to moderate seismic reflections of different amplitude. Internal reflections within MTDs are characterised by chaotic to imbricated blocks of distinct amplitude (e.g. Frey-Martínez et al., 2006). The basal surface is identified as coinciding with the first lateral continuous reflection below MTD strata. The top of the MTDs is marked by a continuous positive reflection covering the chaotic strata (Frey-Martínez et al., 2006).

In this study, the MTDs mapped and considered along this thesis are a specific population which are emplaced exactly on the depositional surface and the entire MTD body was observed. During the mapping process were observed others unstable events, nevertheless the mass movements in this analysis needed to fill some criteria as, i) the entire MTD body was within the seismic data and possible to map is entire body, plus ii) the MTDs needed to be emplaced exactly in the depositional surface. The two typologies presented in this chapter are representative of most the mass movements is the study are and documented in the literature (e.g. Omosanya and Alves, 2013a, Omosanya and

Alves, 2014) The interpretative methods used in this chapter are described in chapter 3 and consist mainly of seismic mapping and computation of seismic attributes. The depositional surface was integrated into a GIS environment and used to compute the bulk of the morphometric analyses presented in this chapter.
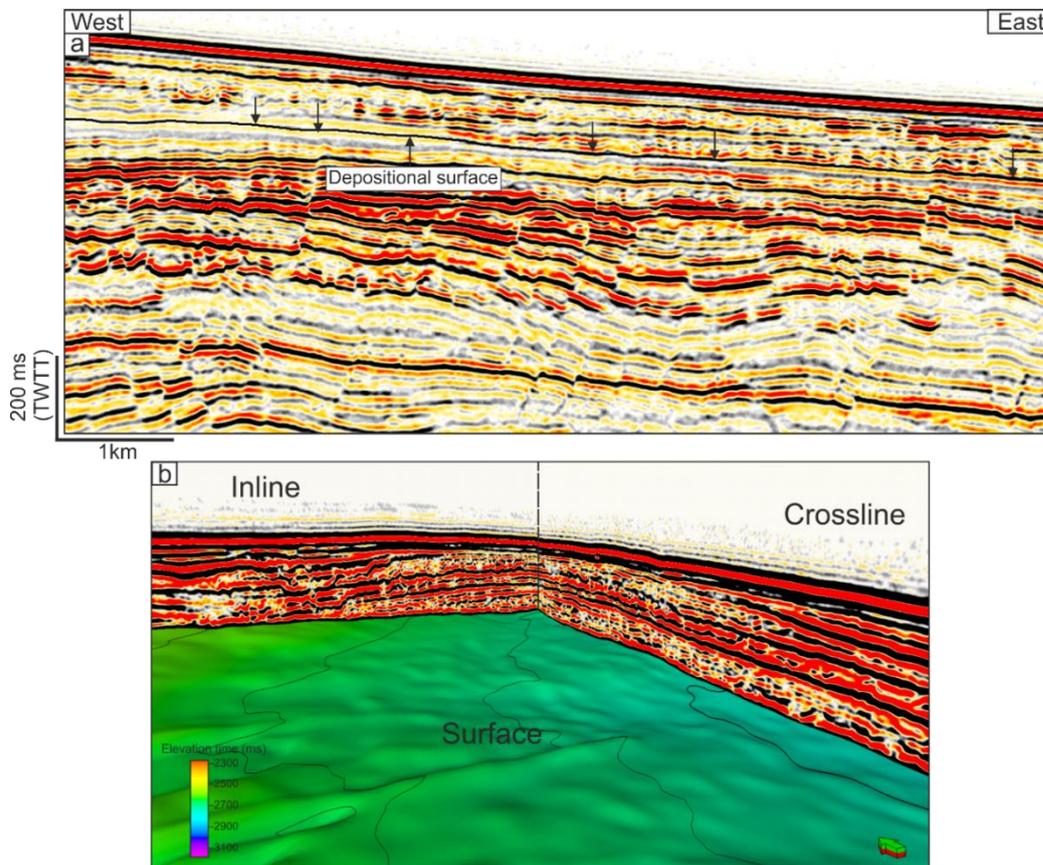
Figure 5.1 - a) Seismic profile highlighting the high amplitude reflector mapped as representing the Depositional Surface and b) 3D view of the Depositional surface with a selected inline and crossline, for context.
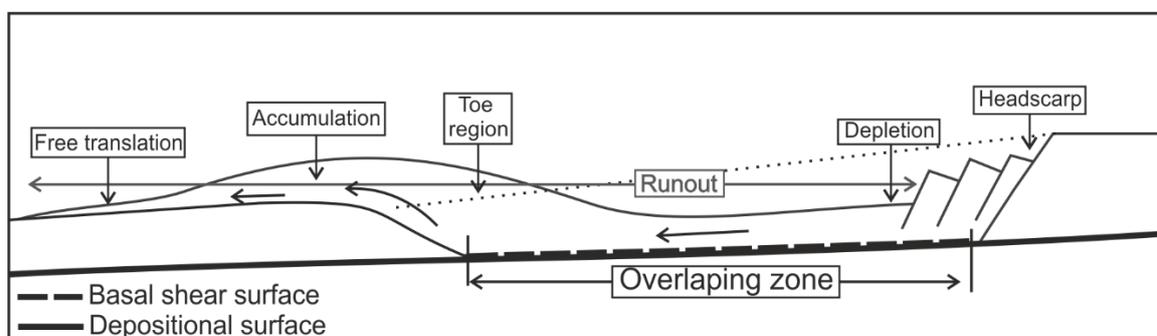
Figure 5.2 - Schematic illustration highlighting what is considered in this chapter to be the Basal shear and Depositional surfaces. The figure represents a submarine landslide and its main geomorphological members. Modified from Frey-Martínez et al. (2006).

5.5. **Seismic stratigraphic framework**

The two studied examples of MTDs are located within stratigraphic sequences N20 to N60 (Early Miocene to Holocene – see chapter 2). These sequences comprise sandstones in the Rio Doce Formation, calcarenites in the Caravelas member, and turbidite sands and marls in the Urucutura Formation (França et al., 2007) (chapter 2). The internal character and geometry of MTDs are characterized by chaotic to continuous reflections within seismic intervals that are continuous and of high amplitude, which likely represent interbedded turbidites (Gamboa, 2011). The unconformity used as a depositional surface which makes the bedding for the two MTDs correspond to Horizon 7 (Figure 2.2). This high-amplitude continuous reflection corresponds to the base of Holocene strata in the study area, and is located at a depth of 1700 to 2400 m below the seafloor (Figure 2.1).
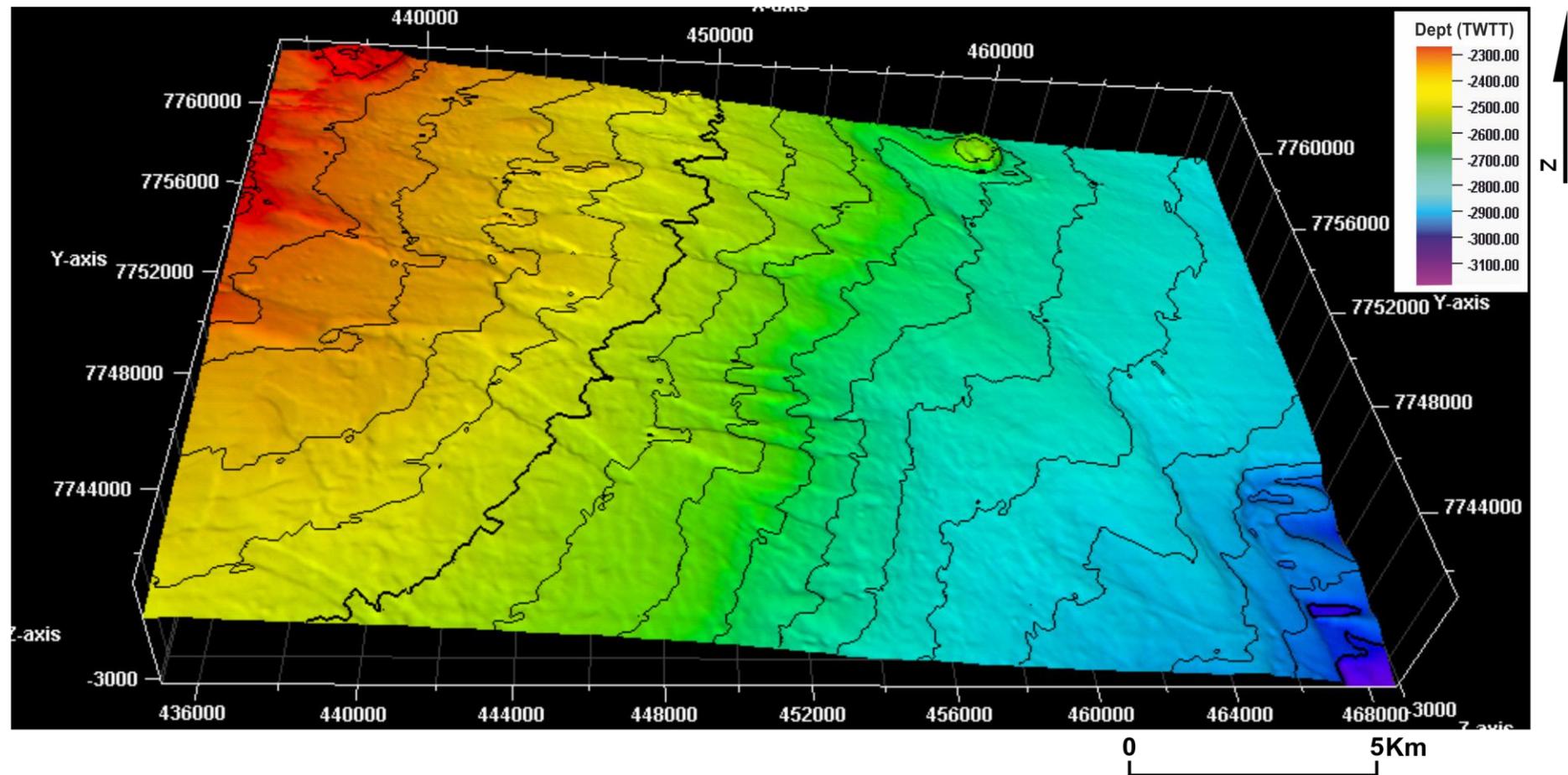
Figure 5.3 – Three-dimensional perspective of the depositional surface.

5.6. **Results**

This section focuses on the analysis of two different MTDs (MTD A and MTD B) within the same stratigraphic unit in the Espírito Santo Basin (SE Brazil). First, the section presents a description of the two MTD types such as size, kinematic features and seismic internal characters. Later in the section, the local topography beneath the MTDs is characterised in detail.

5.6.1. **Locally confined – MTD A**

MTD A covers an area of approximately 5.251 km^2, presenting a maximum width of 1.386 km and a maximum length of 5.915 km. Its total volume approaches 0.128 km^3 (Figure 5.4). MTD A shows a rupture zone marked by a headwall scarp that is marked by a change in seismic character, from continuous strata on the headwall to folded, high-amplitude seismic reflections in the MTD (Figure 5.5). Internal reflections within MTD A are mainly sub-parallel, showing imbricated reflections at places. Generally, imbricated reflections verge to the SE and are tilted at ~ 45° (Figure 5.6). The toe domain records an abrupt change from disturbed seismic reflections within MTD A to continuous strata (Figure 5.5). Lateral margins in Figure 5.6 are also marked by an abrupt change in seismic facies, from continuous to chaotic, with these latter corresponding to the remobilised mass. The geometry of MTD A denotes a laterally confined mass-transport body. The west margin exhibits a positive topography within remobilised strata. The high variance coefficients in Figure 5.7 mark the lateral margins, headwall scarp and toe domains of MTD A. In both figures (Figure 5.7a and b) the high variance from the remobilised MTD body contrasts with the low-variance character of undeformed strata surrounding it. The headwall scarp and lateral margins in MTD A show significant changes in variance coefficient when compared to the main body of the MTD (Figure 5.7). The basal shear surface can be traced with confidence throughout the study area (Figure 5.5 and Figure 5.6). It is characterised by a seismic positive reflection that is affected by the displaced MTD. In some areas of the MTD the basal shear surface is continuous and uniform, whereas in others is clearly eroded and shows prominent grooves. The basal shear

surface is often continuous and concordant to the depositional surface (bedding) (Figure 5.5. and Figure 5.6).
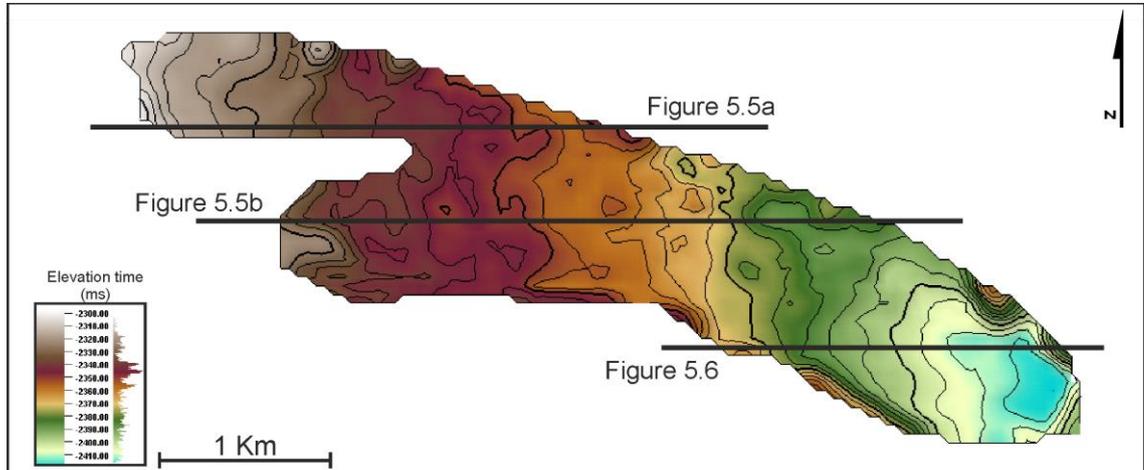
Figure 5.4 – Basal surface of the Confined MTD A. The figure highlights the shape and elevation in time. The location of seismic profiles referred to in the chapter is also highlighted in the figure.
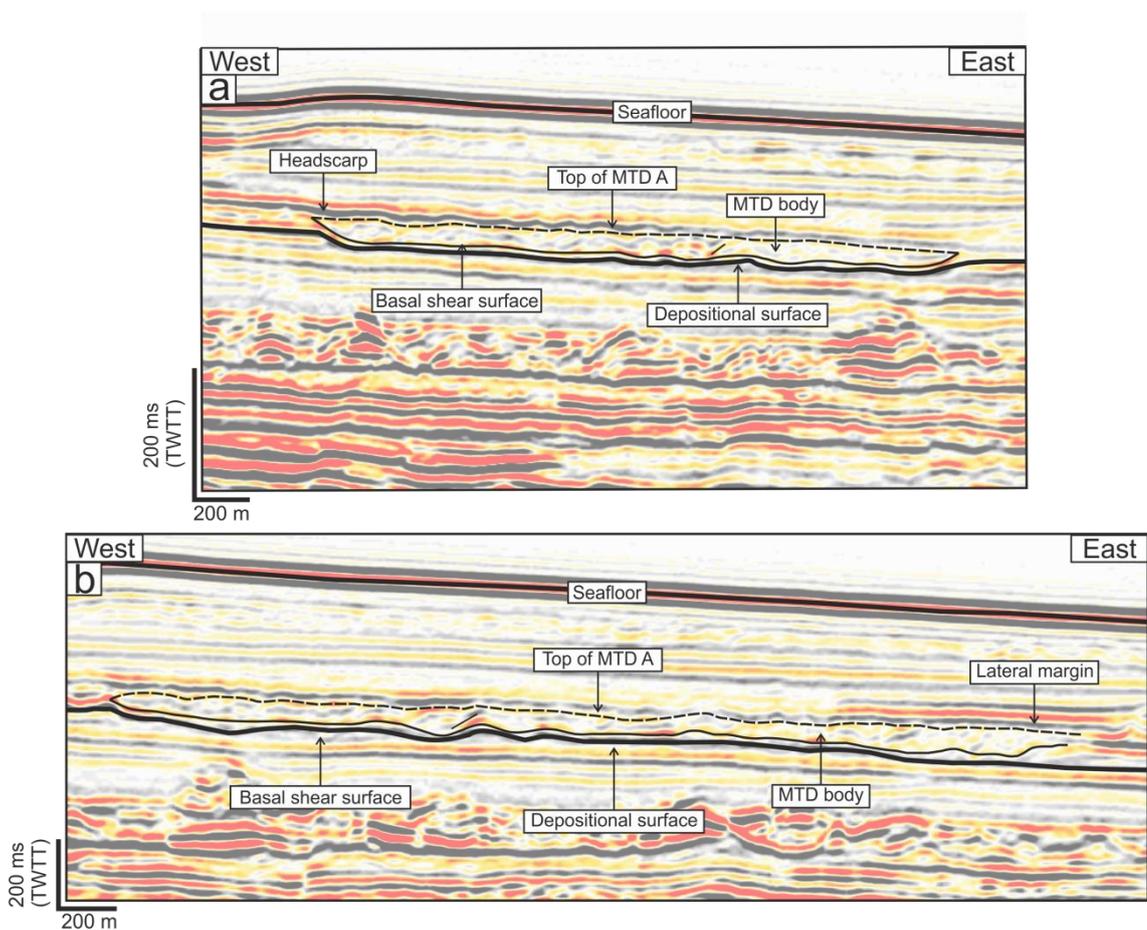
Figure 5.5 - Longitudinal seismic profile through MTD A. a) upper part crossing the headwall scarp (see Figure 5.4 for location). The headwall scarp forms a steeply dipping boundary between undisturbed and

disturbed seismic reflections. b) Seismic profile providing another perspective of MTD A (see Figure 5.4 for location). This figure highlights the eastern margin of MTD A, and shows an abrupt change from disturbed to undisturbed material. The basal shear surface corresponds to the depositional surface. Vertical Exaggeration = 2.5x.
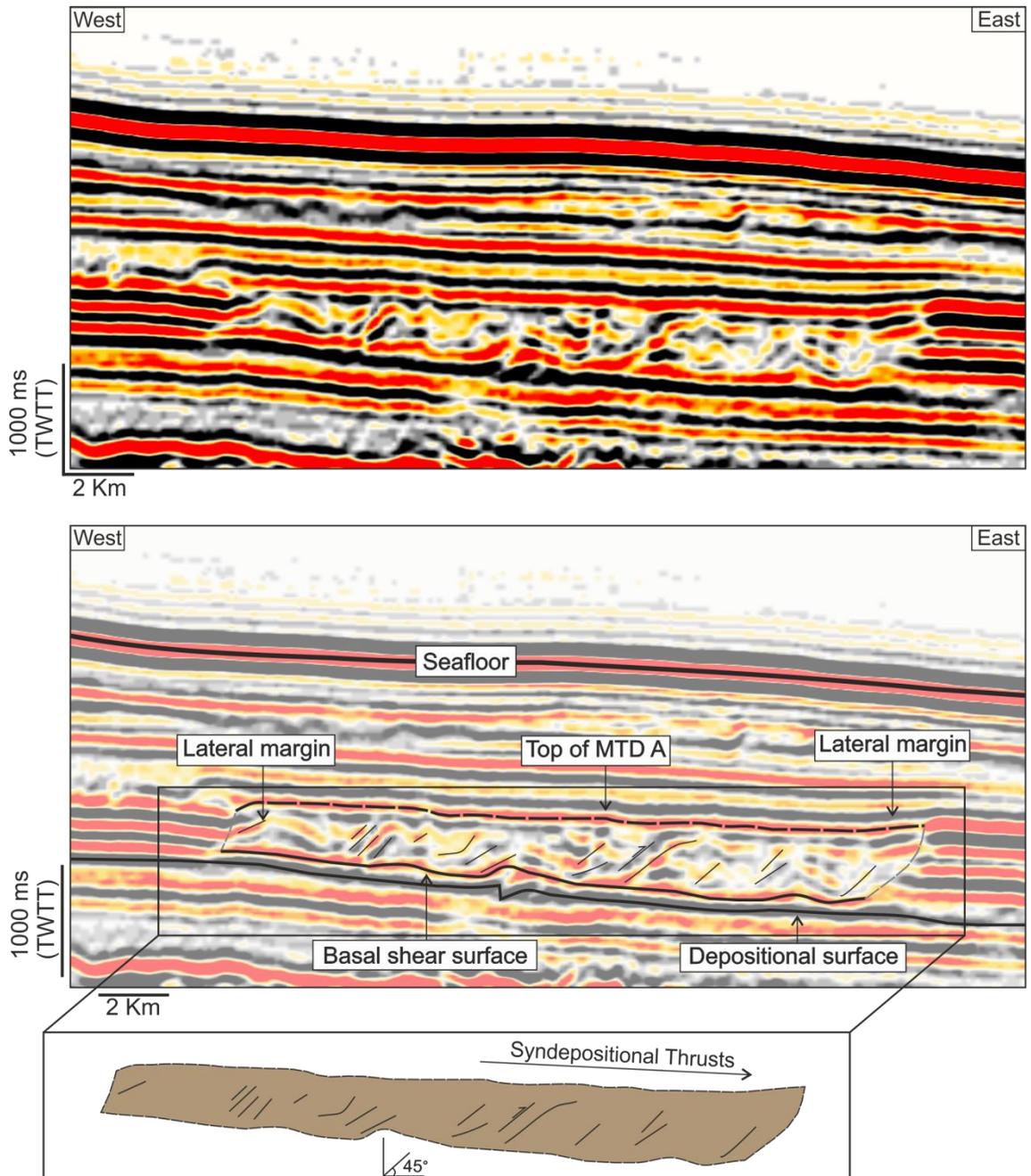
Figure 5.6 – a) Uninterpreted and b) interpreted west-east seismic profile of the Confined MTD A (see Figure 5.4 for location). The western margin of MTD A is shown as the boundary between chaotic seismic facies in the MTD and continuous reflections in undeformed slope strata. The eastern margin is also shown as an abrupt boundary between chaotic seismic facies in MTD A and continuous slope strata. Vertical Exaggeration = 2.5x.
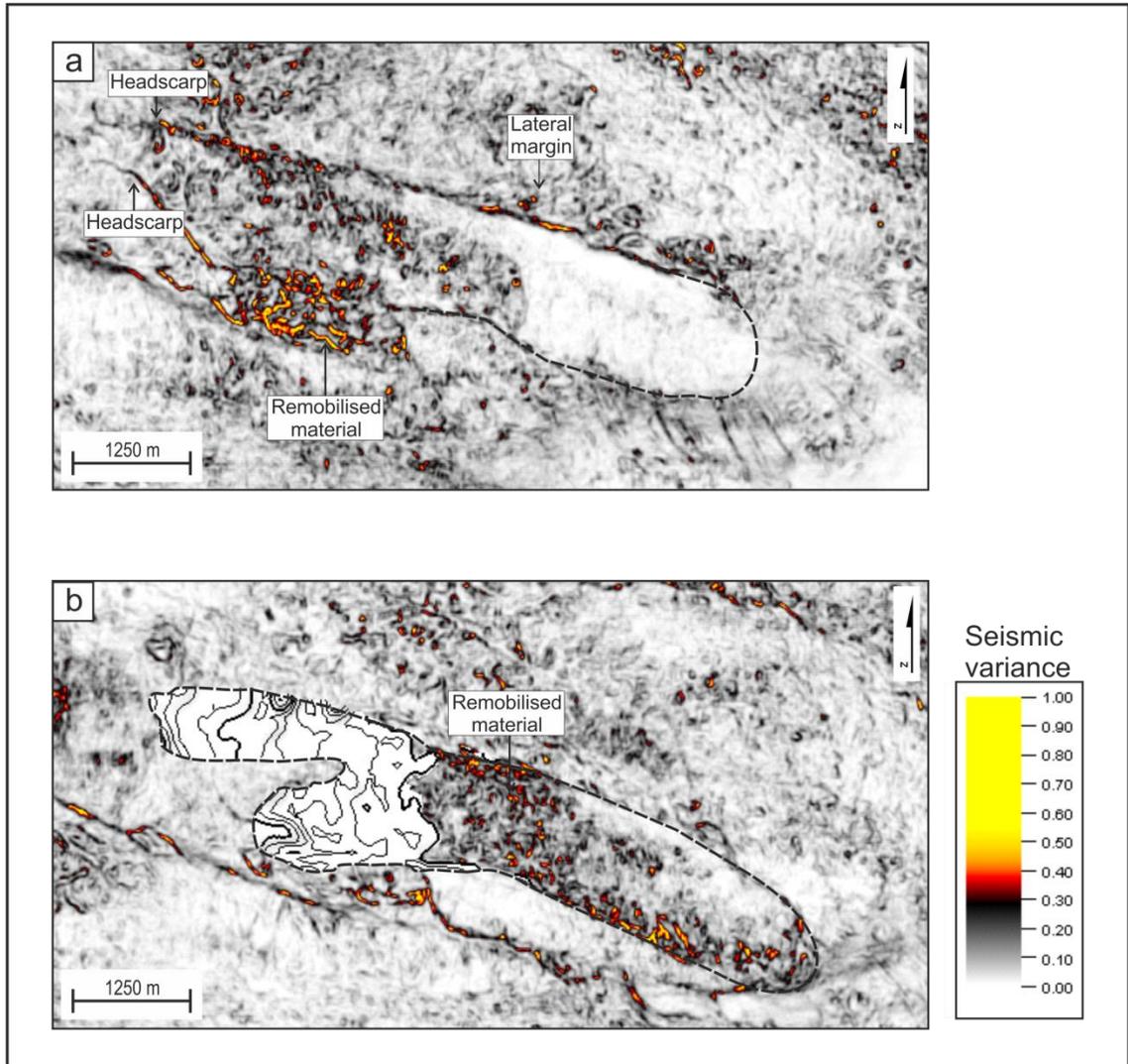
Figure 5.7 - a) Variance time-slice above the basal surface of MTD A (Z=-2328). The figure illustrates the variance character of the headwall scarp and rupture zone in contrast to the highly deformed MTD. b) Variance time-slice above the basal surface of MTD A (Z=-2360) illustrating the variance character of the main MTD body and its toe domain. Note the high variance coefficients associated with remobilised strata in MTD A.

5.6.1.1. Thickness and morphological variations in MTD A

The thickness of MTD A varies between 0 to 60 m, its thinner part is located on its lateral margins, whereas the thicker regions are located at the toe domain (Figure 5.8). The remainder of MTD A shows a thickness ranging between 15 and 25 m (Figure 5.8), with a maximum thickness (60 m) recorded at the toe. Topographic profiles in Figure 5.9 represent the basal and upper surfaces of MTD A across the area marked in Figure 5.8 (black line). The profile of the basal surface of MTD A is mostly continuous and concordant to the Depositional surface (Figure 5.10), showing a topographic concavity in the toe domain - which represents the accumulation zone of the MTD. The upper surface essentially follows topographic variations in the basal surface but, in contrast to this latter, shows a positive topographic convexity at the toe domain (Figure 5.9). The mass accumulated at the toe domain is buttressed against undisturbed strata that are the stratigraphic equivalent to the MTD mass, forming a frontal ramp (Figure 5.10).

5.6.2. **Unconfined MTD B**

The unconfined MTD B is much larger than MTD A and covers an area of ~87.180 km^2 (Figure 5.11). Its maximum width reaches 8.5 km with a maximum length of 18 km (Figure 5.11). The estimated volume of remobilised material approaches 3.163 km^3. MTD B forms an elongated body that is marked by a smooth headwall scarp and smooth lateral margins changing gradually to disturbed strata (Figure 5.12,Figure 5.13, Figure 5.14 and Figure 5.15). Despite being marked by this gentle transition, the rupture zone is clearly marked by the headwall scarp on variance data. The headwall scarp is clearly marked as a feature of high variance coefficients showing a characteristic 'crown' shape (Figure 5.16). Internal seismic reflections within MTD B vary from chaotic to patches of imbricated, sub-parallel and continuous reflections. Relatively continuous seismic reflections within MTD B are often associated with local
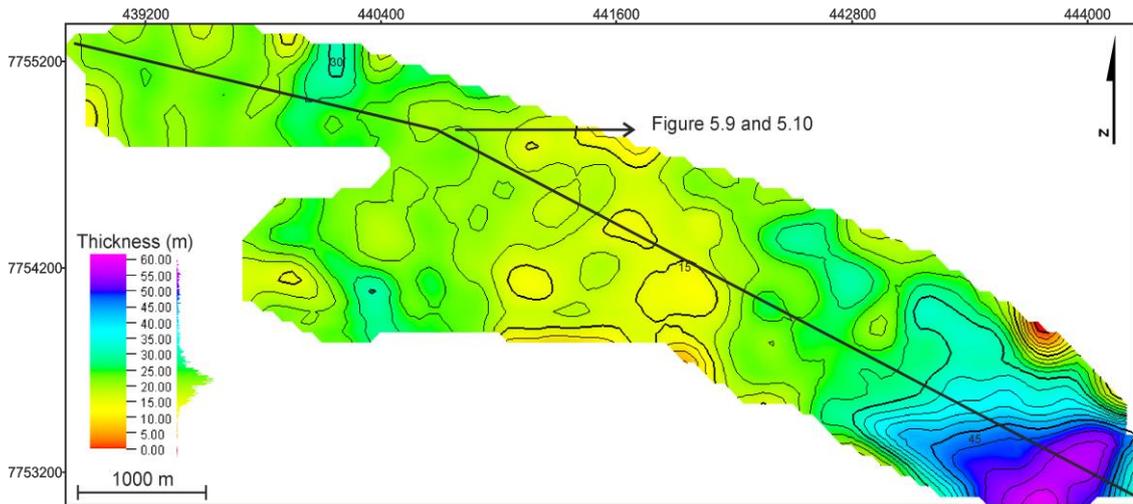
Figure 5.8 – Thickness map of the Confined MTD A, in meters. The thickness of MTD A increases significantly towards the toe domain where the mass is accumulated against continuous seismic reflections. Black line shows the location of the upper and basal profiles in Figure 5.9.
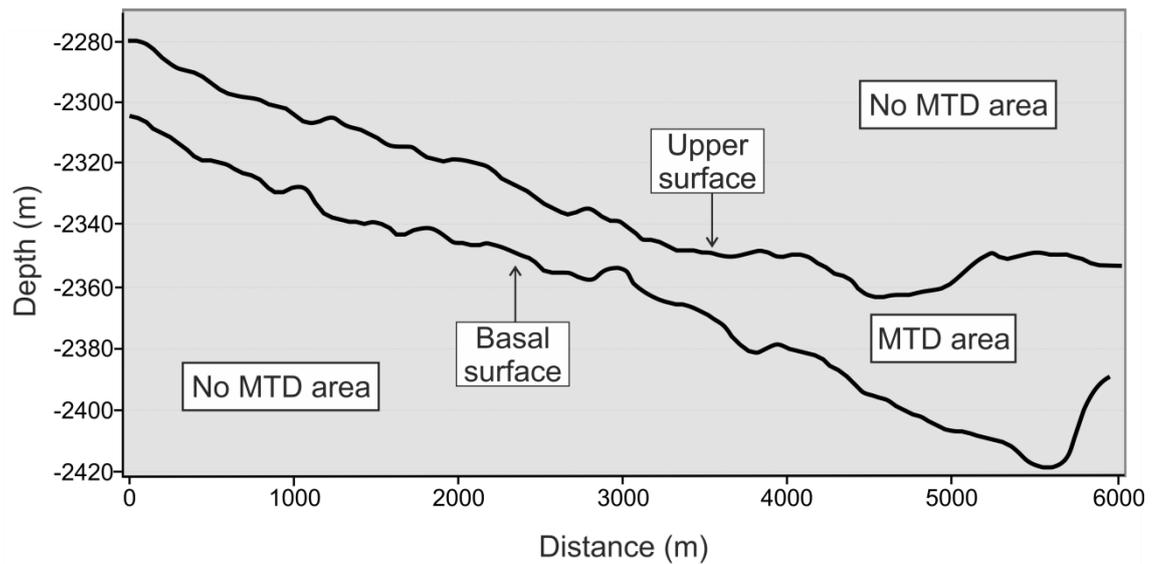
Figure 5.9 – Topographic profile illustrating the upper and basal shear surfaces of MTD A. The space between the two surfaces represents the thickness of remobilized sediment along the MTD body. Note that the thickest area in MTD A occurs in its toe domain. No vertical exaggeration.
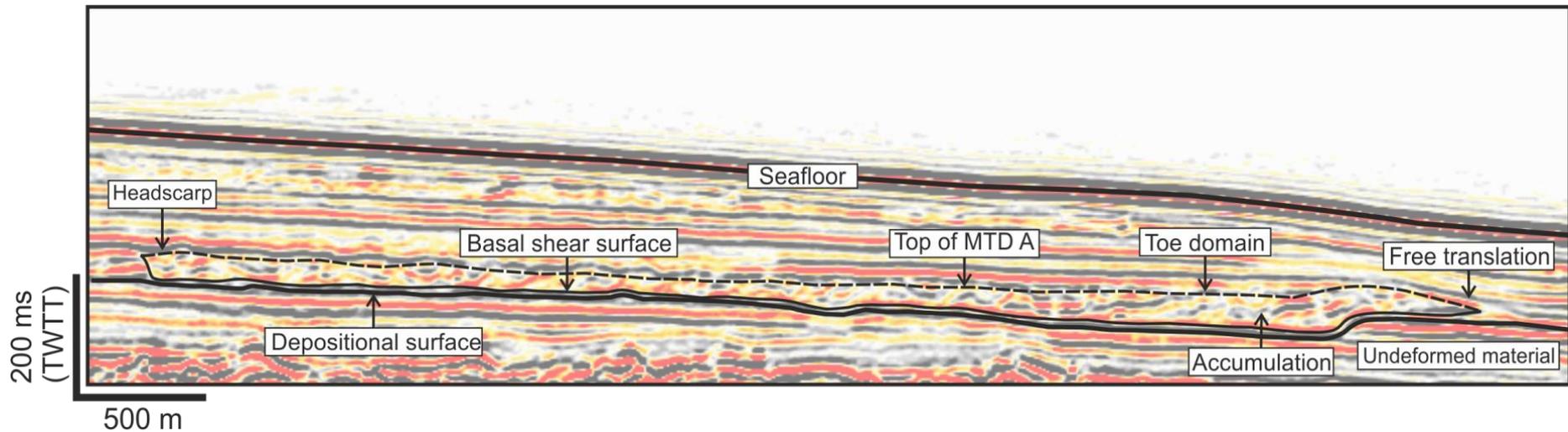
Figure 5.10 – Seismic profile through the topographic profile of MTD A shown in Figure 1.8. The headwall scarp forms an abrupt transition between undisturbed and disturbed seismic reflections. The toe domain shows accumulations and a clear basal ramp. MTD A was translated through a relatively short distance. Seismic reflections at the toe domain are folded and disrupted, suggesting ramping-up of the glided mass.
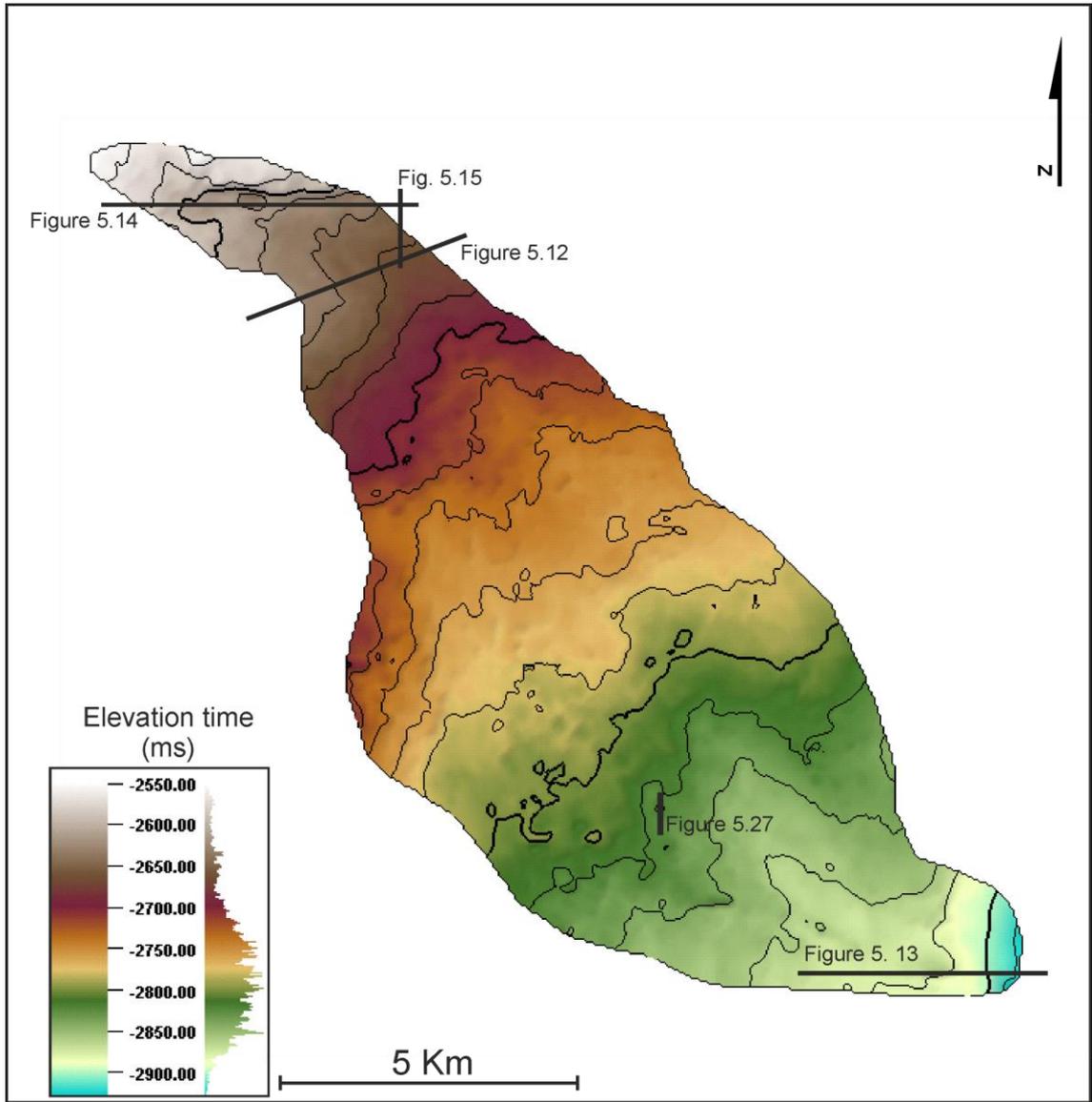
Figure 5.11 – Basal surface of unconfined MTD B, shown in two-way time. Note the location of seismic profiles referred to in the text.
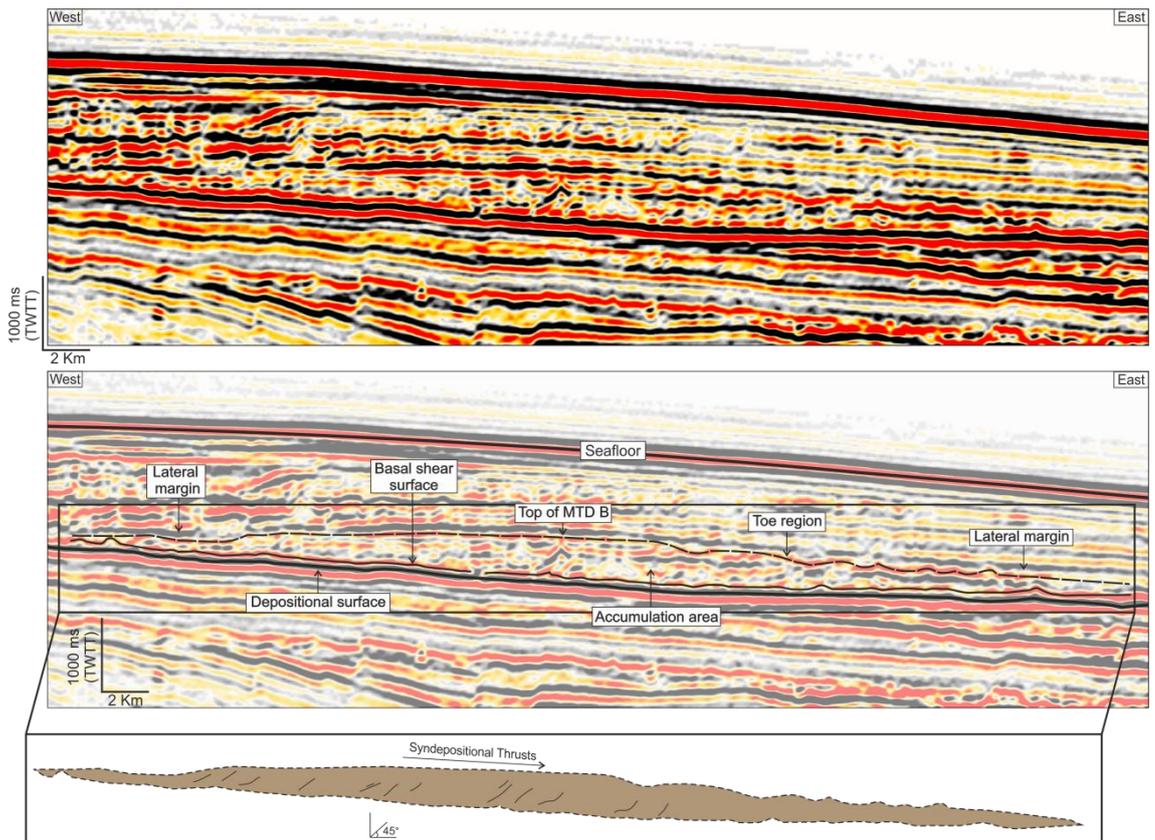
Figure 5.12 – Uninterpreted and b) interpreted W-E seismic profile of unconfined MTD B. The lateral margins of the MTD are shown as smooth transitions from the main MTD body and undeformed strata See Figure 5.11 for location. Vertical Exaggeration = 2.5.
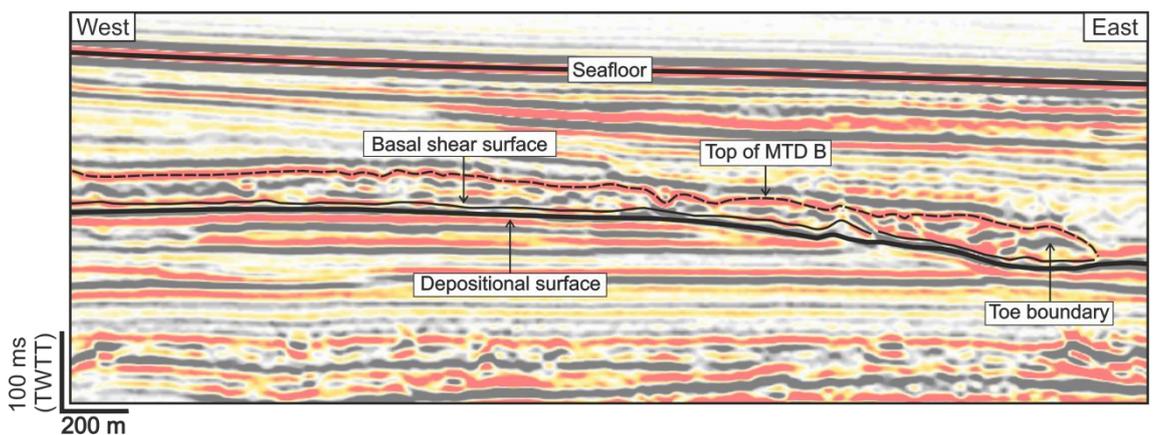
Figure 5.13 - Seismic profile of unconfined MTD B at its toe domain. Seismic reflections are folded and disrupted in the figure. See Figure 5.11 for location. Vertical Exaggeration = 2.5.
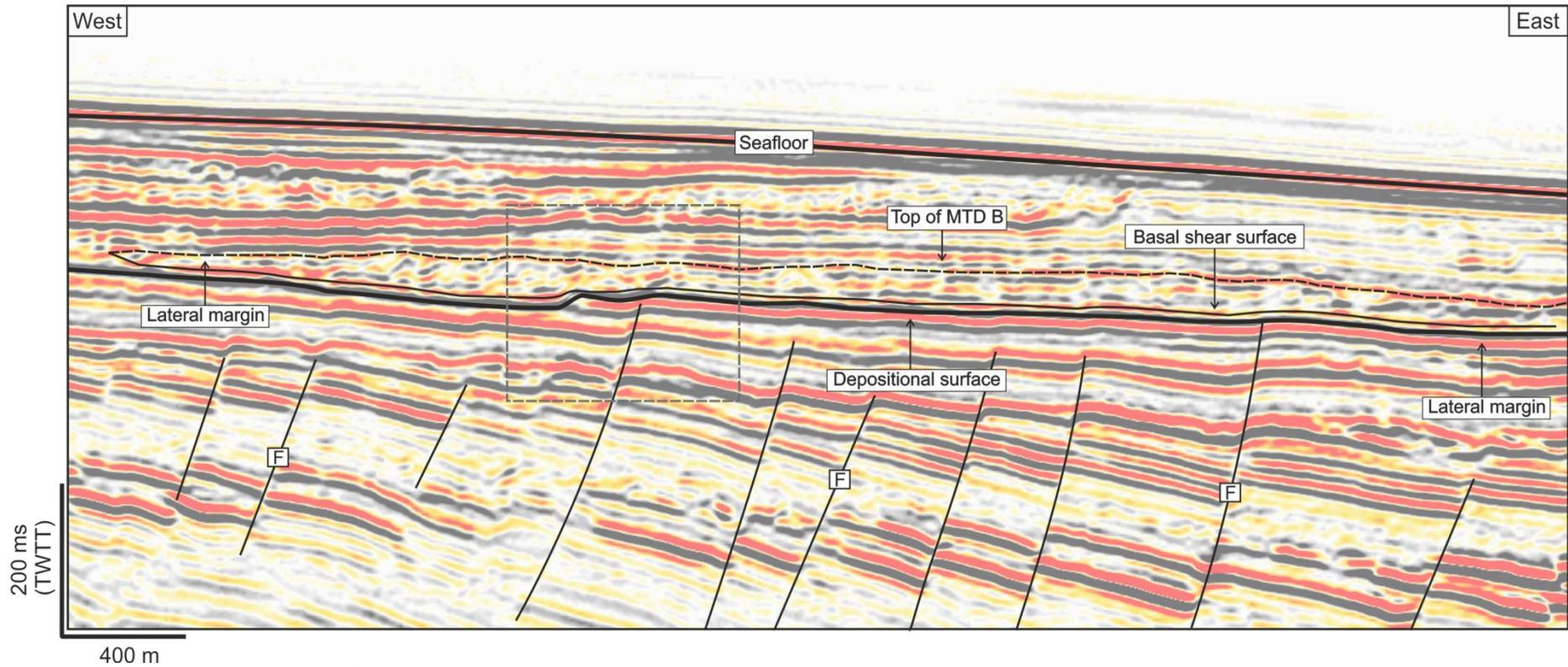
Figure 5.14 – Interpreted seismic profile showing part of unconfined MTD B. The figure highlights the presence of fault sets at depth and their inferred influence on the Depositional surface and basal shear surface of MTD B. The dashed rectangle highlights the presence of a basal ramp in MTD B that generated considerable topography. See Figure 5.11 for location. Vertical Exaggeration = 2.5.
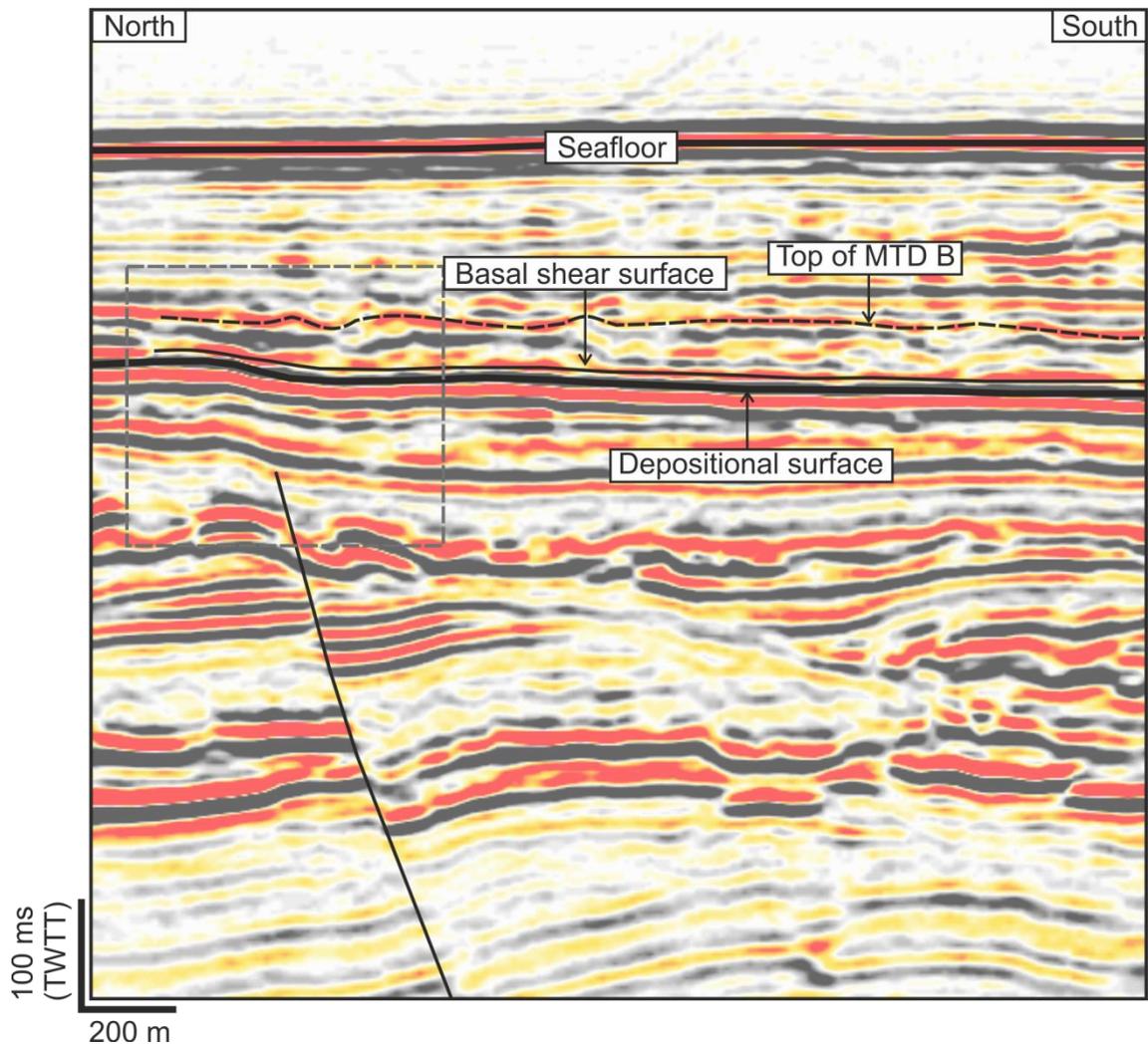
Figure 5.15 – Interpreted N-S seismic profile highlighting a portion of the lateral margin of MTD B. In this particular example, the position of the lateral margin is coincident with underlying fault. See Figure 5.11 for location. Vertical Exaggeration = 2.5.
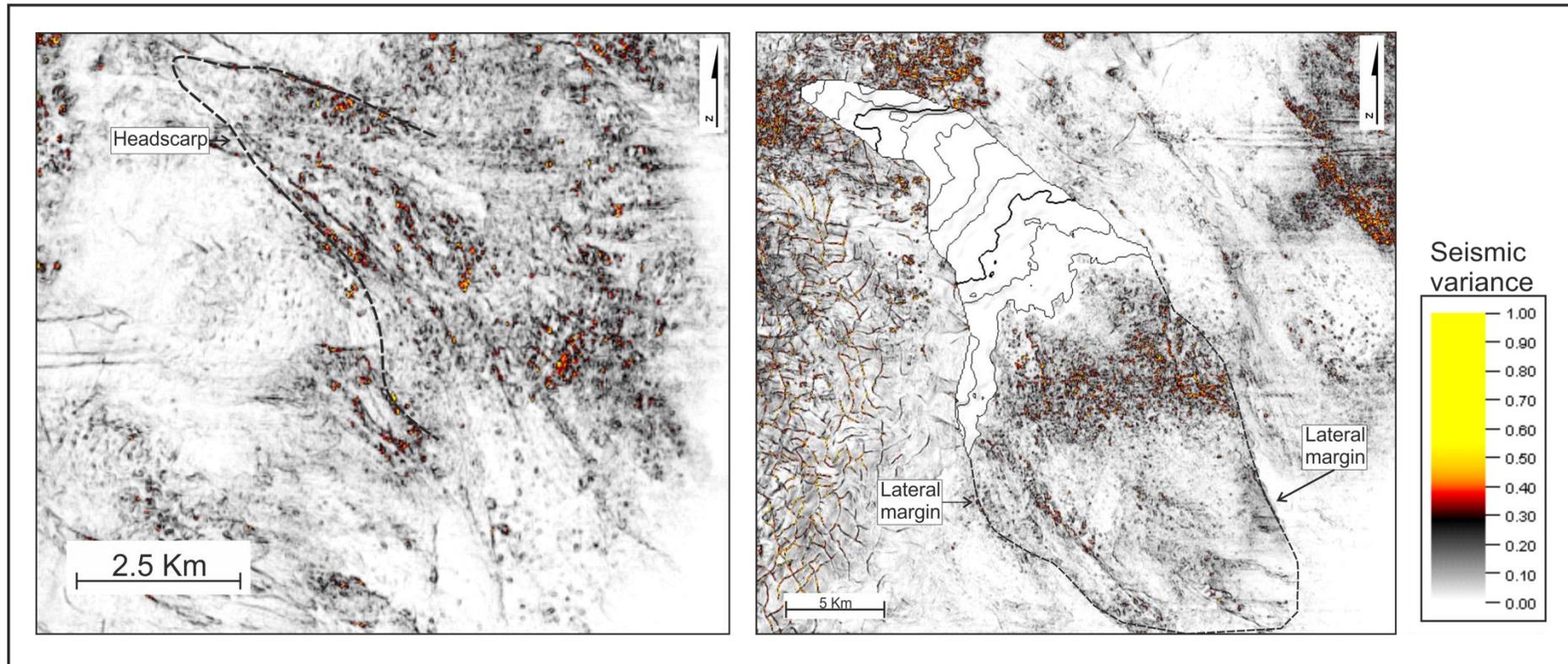
Figure 5.16 - a) Variance time-slice above the basal surface (Z=-2556) of MTD B. The figure illustrates the variance character of the headwall scarp of MTD B. b) Variance time-slice of the basal surface of MTD B (Z=-2684) illustrating the seismic character of the main MTD body and toe domain. Once again, note the larger variance values that are associated with the deformed body.

thrusts (Figure 5.12). The toe domain shows a marked tongue shape, which changes downslope into a very smooth transition between MTD B and confining strata. Seismic reflections in this area are chiefly undulated and continuous, rather than chaotic (Figure 5.13).

The upper surface of MTD B is a positive high reflection overlying chaotic reflections in the main body. Some areas are interrupted by low amplitude folds and erosional surfaces (Figure 5.12, Figure 5.14 and Figure 5.15). The basal shear surface is traceable with a high degree of confidence but exhibits lateral variations in seismic amplitude and geometry separating the chaotic MTD body from the depositional surface (Figure 5.12, Figure 5.14 and Figure 5.15). Local ramps at the basal shear surface generated internal deformation in MTD B. Figure 5.16 shows changes in variance within MTDs that mark the range of remobilised material vs. non-remobilised strata.

5.6.2.1. Thickness and morphological variations in MTD B

The thickness of unconfined MTD B ranges from 0 to 70 m (Figure 5.17). The minimum thickness is observed on the lateral margins of the MTD. Its thickest area is observed in the middle of the MTD, increasing from its lateral margins to its central part (Figure 5.7). This trend is also noted in the topographic profile of the basal and upper surfaces, which shows that maximum thickness is reached 8 km to 14 km downslope from the headwall (Figure 1.17). In these profiles, the headwall and toe domain show the lowest thickness values (Figure 5.17). Topographically, the upper and basal profiles follow a similar trend and showing a reduction at the headwall of MTD B. Topographic variations follow the headwall in the form of small-scale roughness at the basal surface. The upper surface profile at 8 km presents a convexity that corresponds to the largest thickness of gliding mass. The toe domain is marked by a gently confluence of the two profiles and a small concavity on the basal surface profile (Figure 5.18).
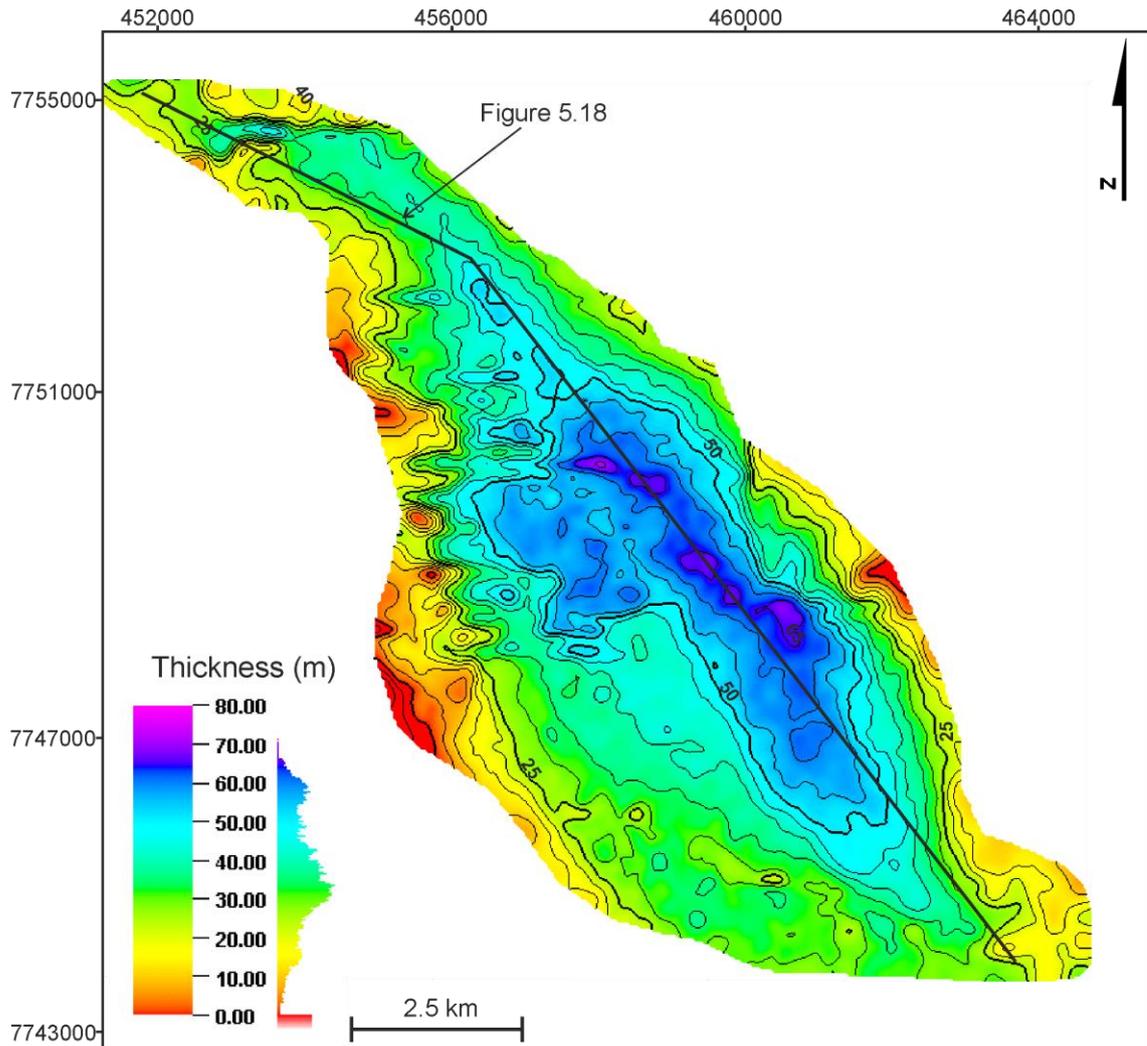
Figure 5.17 - Thickness map of MTD B. The MTD is thick at the central core. Lateral margins shows the lower thickness. Contours gives information about accumulation patterns. It is also indicated the location of Figure 5.18.
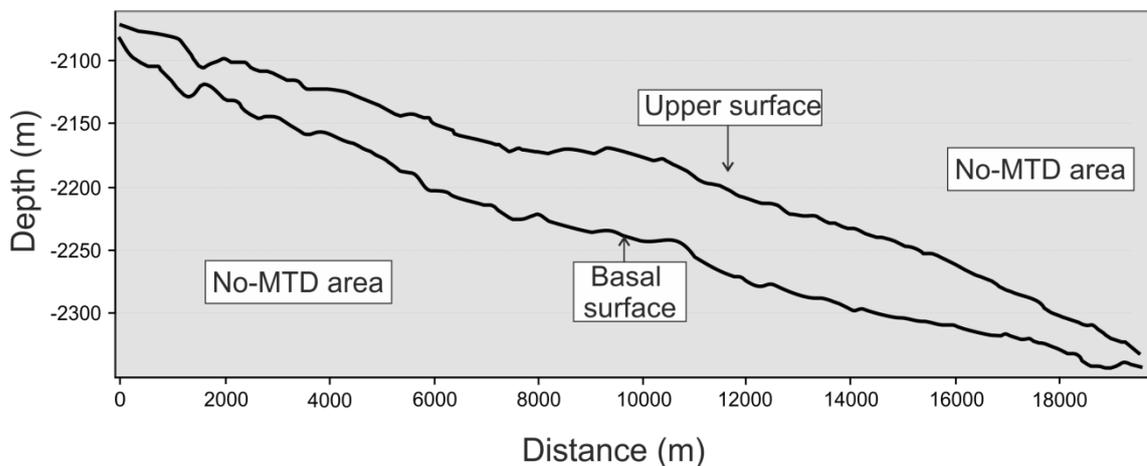
Figure 5.18 - Profile illustrating the upper and basal surfaces of MTD B. The space between the two profiles represents the thickness of remobilised strata in MTD B.

5.6.3. **Palaeogeomorphology of the Depositional surfaces**

This section investigates the main characteristics of depositional surfaces in MTD A and B that influenced their internal deformation and run-out distances. On seismic data, the Depositional surface is a negative high-amplitude reflection marking the boundary between Miocene and Holocene strata. It corresponds to Horizon 7 on the interpreted seismic volume.

5.6.3.1. Depositional surface beneath the confined MTD A

The hillshade map in Figure 5.19 represents the topography of the surface under (and surrounding) MTD A and highlights relevant geomorphological features. The map in Figure 5.19 shows the limits of the MTD A as dotted lines. In this figure the topographic features delimiting MTD A and forming topographic constraints to it are observed. Lateral margins and a barrier in the toe area are also observed. The depositional surface where MTD A is located shows roughness at the basal shear surface, highlighting local topography as an important conditioning factor.

Topographic profile showed in Figure 5.20 is oriented NW-SE (A – A' on Figure 5.19). In the same figure, the location of the confined MTD A is also highlighted, together with its headwall scarp, which is delimited by a slope change consistent with the rupture zone. Roughness along the depositional surface (Figure 5.20) highlights the presence of a promontory between 4500 m and 6500 m. At the toe domain, an accumulation area is observed corresponding to a lateral wall imaged on the hillshade map (Figure 5.19).

The slope profile in Figure 5.21 shows segment B – B', oriented N–S. In addition, Figure 5.19 shows MTD A to be located between two lateral features (or ramps), which act as topographic barriers to the MTD and correspond, as such, to its lateral margins. This is confirmed by the seismic profile in Figure 5.6.

The slope gradient in the area surrounding MTD A is very gentle and ranges between 0 and 3 degrees. However, in Figure 5.22 local changes on slope gradient are observed, and the uppermost limit of the MTD is actually followed by a high slope gradient where the headwall scarp is located (i.e., on the N – NE), and also in the toe domain. Within MTD A, the depositional surface shows a high slope gradient (approximately 6 to 8 degrees), which corresponds to the promontory mentioned above.
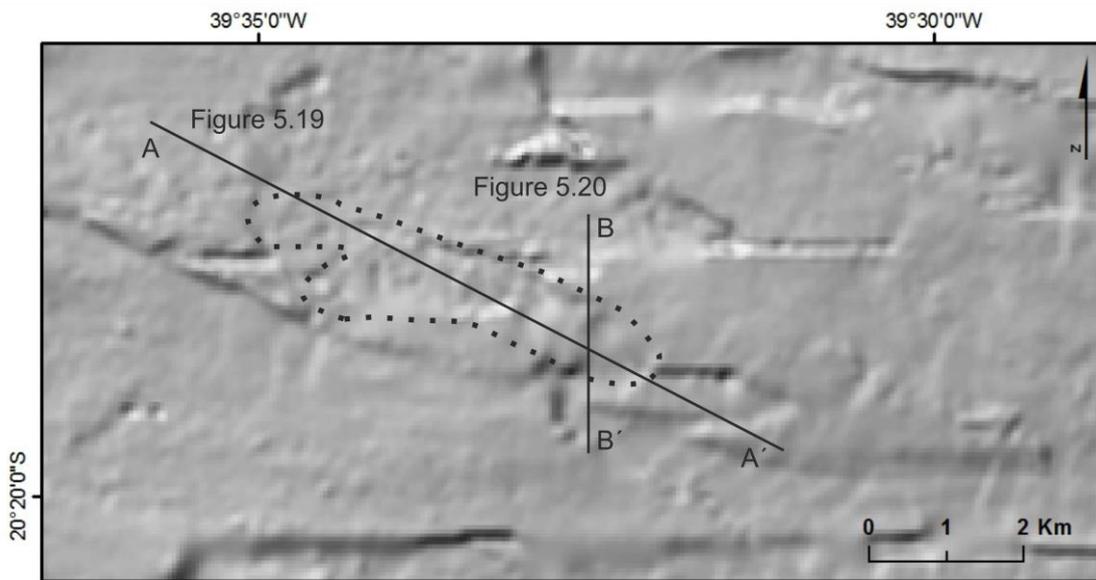
Figure 5.19 - Hillshade map of the depositional surface under the confined MTD A, as highlighted by the dotted line. The cross-section A – A' is oriented NW – SE and B-B' is N – S. Vertical exaggeration = 5x.
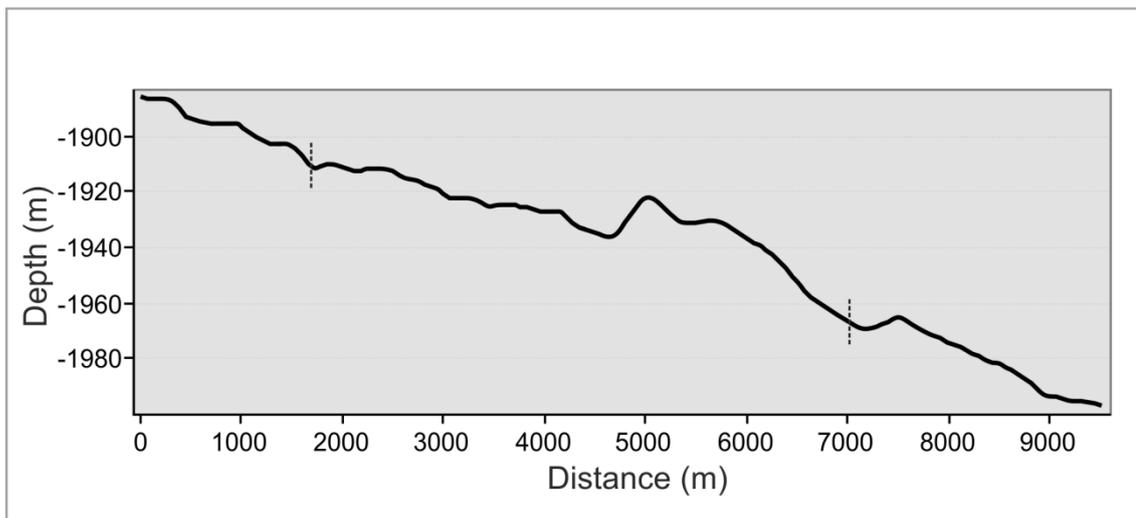
Figure 5.20 – Cross-section through the depositional surface highlighting the morphology underneath the confined MTD A (A-A'). Dashed vertical lines mark the location of MTD A. Vertical exaggeration = 5x.
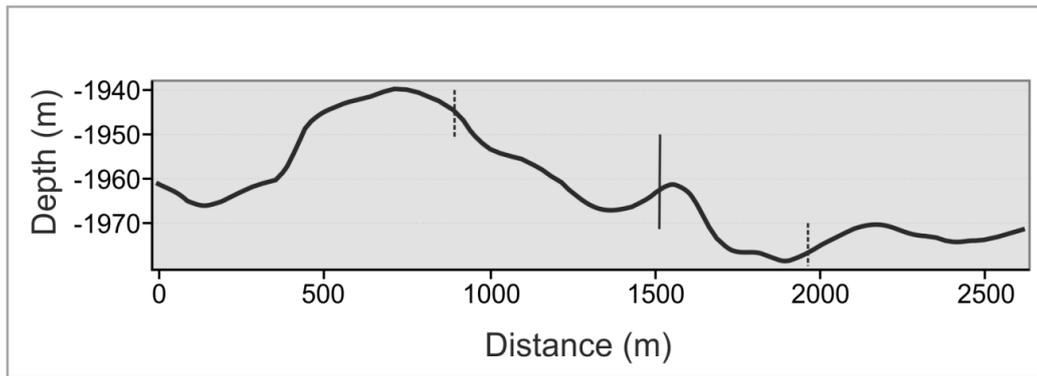
Figure 5.21 Cross-section through the depositional surface under MTD A (B-B'). Dashed vertical lines highlight the location of confined MTD A and its limits. The black line in the figure denotes the position in which cross-section A-A' crosses B-B'. Vertical exaggeration = 5x.
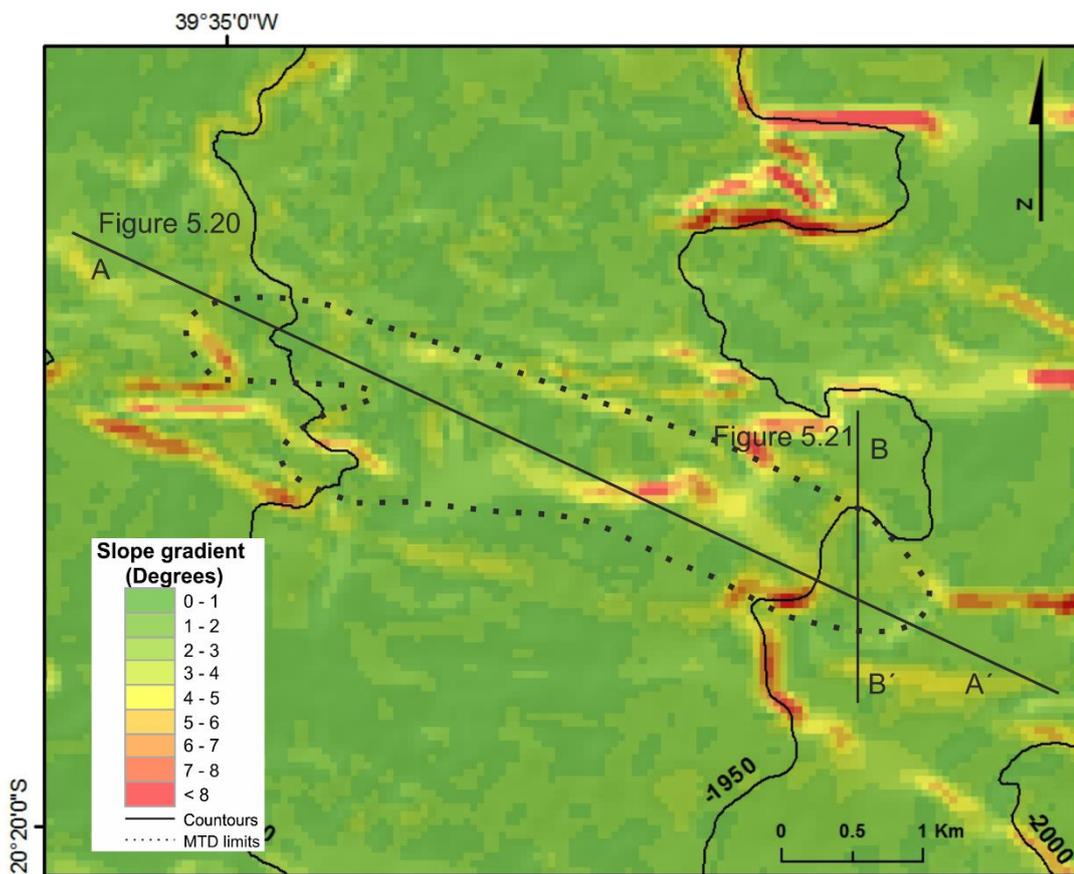
Figure 5.22 – Slope gradient map of the depositional surface beneath MTD A, as highlighted by the dotted line. The cross-sections A – A' are oriented NW – SE and B-B' are N – S. No vertical exaggeration.

5.6.3.2. Depositional surface beneath the unconfined MTD B

The depositional surface beneath MTD B shows distinct characteristics from MTD A. As previously mentioned, MTD B is larger than MTD A and does not show considerable topographic (or structural) barriers constraining its downslope gliding (Figure 5.24). The headwall scarp of MTD B is defined on the hillshade map as a topographic elevation when compared to the surrounding areas (Figure 5.23).

Figure 5.24 presents a topographic profile along cross-section A – A', which is oriented NW – SE (see Figure 5.23 for location). It shows the local topography of the Depositional surface, with the dashed line marking the approximately boundaries of unconfined MTD B. The headwall scarp is visible where the topographic profile denotes a marked rupture. It is followed by a smooth promontory and multiple topographic features along the downslope. In general does not show marked roughness. Figure 5.25 shows the topographic profile for cross-section B – B' (see Figure 5.23 for location), in which the dashed lines mark the lateral margins of MTD B location. The lateral margin to the SW shows small ramps acting as lateral topographic barriers to MTD B.

The local geomorphology shows features that are associated with the vertical propagation of faults from below the depositional surface, thus creating roughness in the latter. In Figure 5.15 a fault is observed whose vertical propagation does not directly affect the Depositional surface. However, its location corresponds to a topographic depression where the lateral margin of the MTD is located. A similar control of pre-existing faults is observed in Figure 5.27, where a normal fault does not propagate through the depositional surface but is affecting its shape, creating a local promontory or elevation.
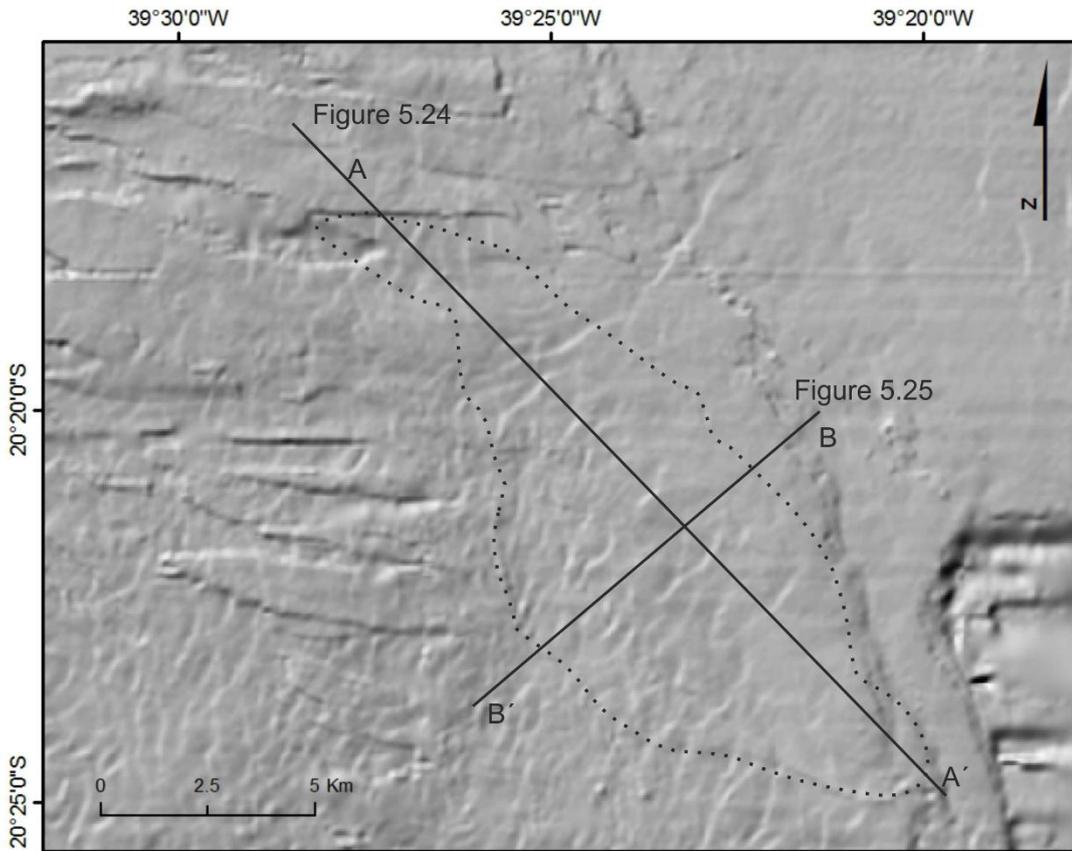
Figure 5.23 – Hillshade map of the Depositional surface of MTD B, whose limits are shown by the dotted line. Cross-section A – A' is oriented NW – SE and B-B' is oriented SW – NE. Vertical exaggeration = 5x.
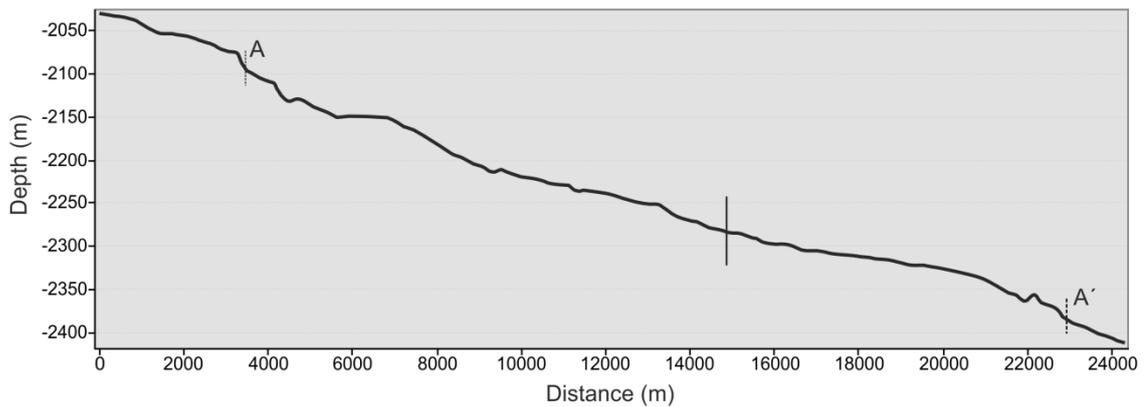
Figure 5.24 - Cross-section through the Depositional surface of MTD B highlighting its basal morphology (A-A'). Dashed vertical lines mark the location of MTD B on the continental slope. Vertical exaggeration = 5x.
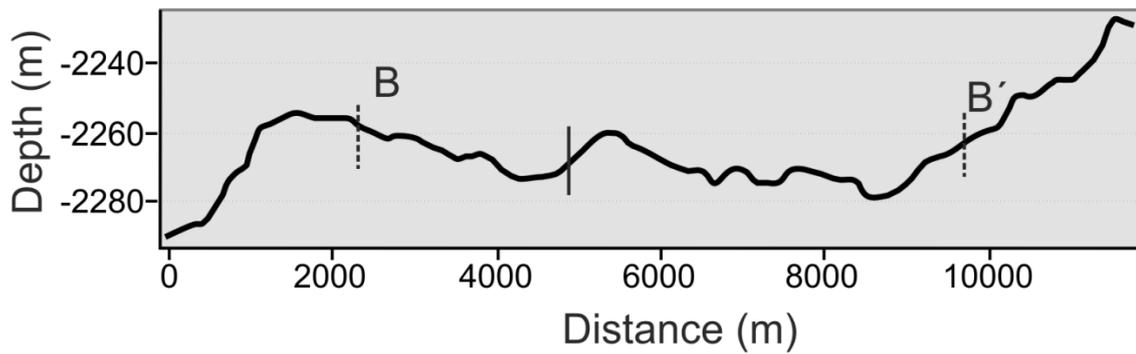
Figure 5.25 - Cross-section through the depositional surface of MTD B (B-B´). Dashed vertical lines mark the location of MTD B and its limits. The black line highlights the position in which cross-section A-A' intersects B-B'. Vertical exaggeration = 5x.
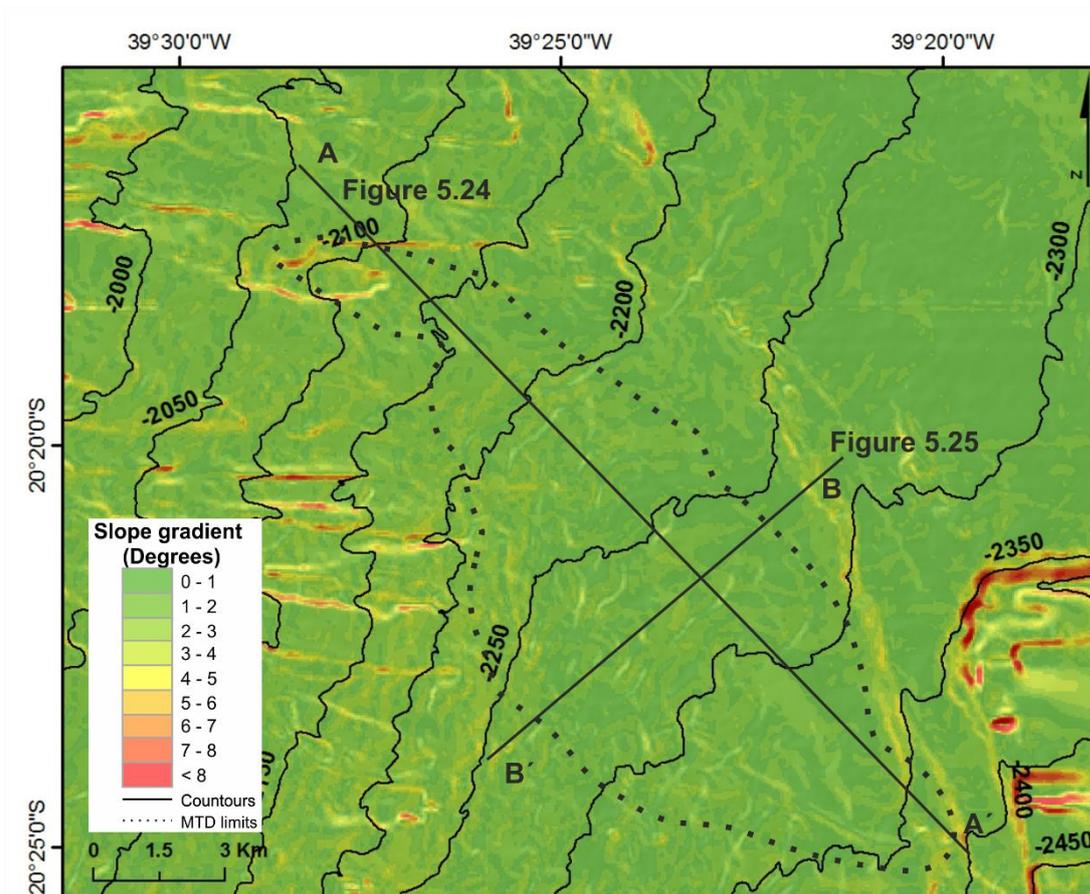
Figure 5.26 – Slope gradient map of the Depositional surface of MTD B, whose limits are shown by the dotted line. Cross-section A – A' is oriented NW – SE and B-B' is oriented SW – NE. No vertical exaggeration.
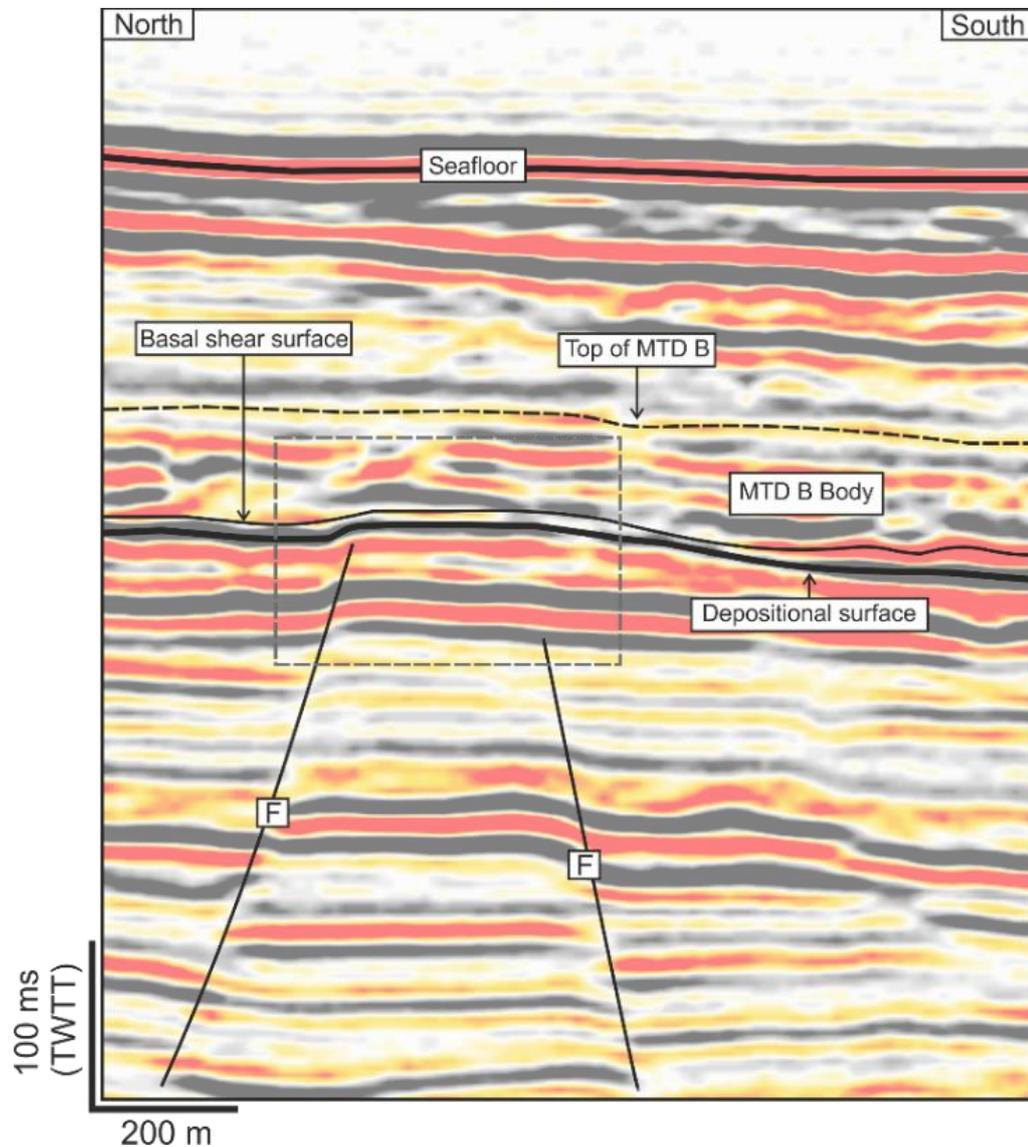
Figure 5.27 - Interpreted N-S seismic profile highlighting two faults beneath unconfined MTB B and their influence on the shape of the Depositional surface. A local ramp is formed just above the faults. Seismic reflections within the MTD body show low- to moderate-amplitude seismic reflections that are essentially continuous. See Figure 5.11 for location of the seismic profile. Vertical exaggeration = 2.5

5.7. **Discussion**

The most important observations regarding the two types of MTDs described relate to: a) their distinct sizes and any observed interactions with surrounding structures, b) the Depositional surface morphology, and c) the location of undisturbed material within the same stratigraphic unit. The modes in which the two types of MTDs accumulate at their toe domain are also strikingly different. Furthermore, their headwall scarps, toe domains and lateral margins are very different when comparing the two MTD types.

A summary of the MTDs' characteristics is shown in Table 5.1. The table summarises the most important observations from seismic interpretation and GIS spatial analyses, and constitutes the base for this discussion.

Table 5.1 – Summary of characteristics of confined MTD A and unconfined MTD B

	Confined MTD A	Unconfined MTD B
Morphology	Comprises a small-scale movement that was abruptly confined between undeformed stratigraphy. Its L/W ratio approaches 4.27.	Unconfined MTD B is much larger than MTD A, showing margins that gradually change into undeformed stratigraphy. Its L/W ratio approaches 2.18.
Headwall domain	Headwall domain is marked by a scarp, as shown in Figure 5.10. Figure 5.7 shows remobilized material of high variance coefficients. Headwall scarp domain is ~25 m in height and ~900 m in length.	Headwall scarp is marked by a smooth transition on seismic profiles from undeformed to deformed seismic reflections (Figure 5.12 and Figure 5.14). Headwall scarp domain in ~80 m in height and ~3000 m in length.
Translation domain	Abrupt lateral margins (Figure 5.6 and Figure 5.7).	Lateral margins are marked by a smooth transition from undeformed to deformed seismic reflections (Figure 5.12 and Figure 5.14).
	The basal shear surface is marked by irregular topography, such as promontories, ramps and other features that may hinder downslope movement (Figure 5.20).	Basal shear surface shows an irregular topography and coincides with the depositional surface (Figure 5.18Figure 5.8).
Toe Domain	Positive topographic convexity formed by a frontal ramp (Figure 5.10).	Gentle confluence of the basal and upper profiles showing small concavity (Figure 5.13)
Thickness	Range between 0 to 60m. The thickest is located at its toe	Range between 0 to 70m. The thickest area is observed at the

	domain (Figure 5.8 and Figure 5.9).	centre of the MTD body (Figure 5.17 and Figure 5.18).
Run-out	Run-out domain is ~105 m height and ~5000 m in length.	Run-out domain is ~340 m in height and ~15400 m in length.

The two MTDs are very similar to the typology described by Frey-Martínez et al. (2006): frontally confined and frontally emergent landslides. However, Frey-Martínez et al. (2006) focused on the movement of landslide masses *per se*, rarely focusing on surrounding undisturbed strata or on any relationships with the surrounding topography (Frey-Martínez et al., 2006). In this work the two types of mass movements in Frey-Martínez et al. (2006) were reassessed by focusing in topographic features that can be influencing MTDs' downslope movement and accumulations patterns.

From the summarized observations, differences are clear between the two MTD types. Considering Moscardelli and Wood (2008) classification, MTD A has a L/W ratio of 4.27 and is classified as attached (>4), while MTD B has a L/W ratio of 2.18 and is classified as detached (<4).

5.7.1. Are MTDs depositional styles controlled by underlying topography?

5.7.1.1. Locally Confined – MTD A

Confined MTDs are described by Frey-Martínez et al. (2006) as presenting a frontal region buttressed against local topographic features, as also observed in MTD A (Figure 5.10). Trincardi and Argnani (1990) attributed frontal confinement to the presence of morpho-structural obstacles, arguing that confinement happens where topographic features provide necessary resistance forces to prevent further translation. The authors mentioned that in this case the gliding material stops against topographic barriers and propagates from the area of the impact (Trincardi and Argnani, 1990). Such a description adjusts perfectly with MTD A's (confined) geometry. The TWTT time-structure map of the basal and upper surface of MTD A in Figure 5.28b and 1.28a show an abrupt end at a toe wall (Figure 5.28b). In addition, MTD A's upper surface shows a correlative topographic elevation, suggesting that the sliding

material has encountered a topographic barrier and jumped over it, propagating shortly on the palaeo-seafloor. This mechanism is well illustrated in the seismic profile in Figure 5.10, which shows glided material accumulated on the toe domain, confined by a topographic ramp that makes the material propagate in free translation over the palaeo-seafloor. This material did not travel far, accumulating after a short free translation.

Lateral margins dip parallel to MTD A and were identified and imaged on variance maps (Figure 5.7). Identifying the lateral margin of the entire body can be crucial to understand the gliding direction of both confined and unconfined MTD. By computing the Depositional surface of MTDs into GIS one can obtain hillshade and slope gradient data that are useful to distinguish their lateral margins. The lateral margins of MTD A correspond to the regions with the highest slope gradients (Figure 5.22), inducing that they can work as natural barriers to the mass propagation.

Confined submarine slope movements show small to moderate downslope translation (Frey-Martínez et al., 2006, Moscardelli and Wood, 2008) as also observed for MTD A. The basal surface presented in Figure 5.28b shows structural contours that are an indication of how failed strata flowed within the MTD body. The contours at the toe domain mark a convex area on the basal surface, suggesting accumulation against undeformed material on the toe area that is stratigraphically equivalent to the failed material. In turn, the upper surface contours express chaotic accumulation by observing the contours patterns presented in the Figure 5.28a. This latter topographic character signs that the material has been stopped by a barrier and ramp and quickly accumulated. This fact is also discernible on seismic profile in Figure 5.10 that shows accumulation of sediment on the toe domain, ramping-up of sediment above undeformed strata and a short translation.
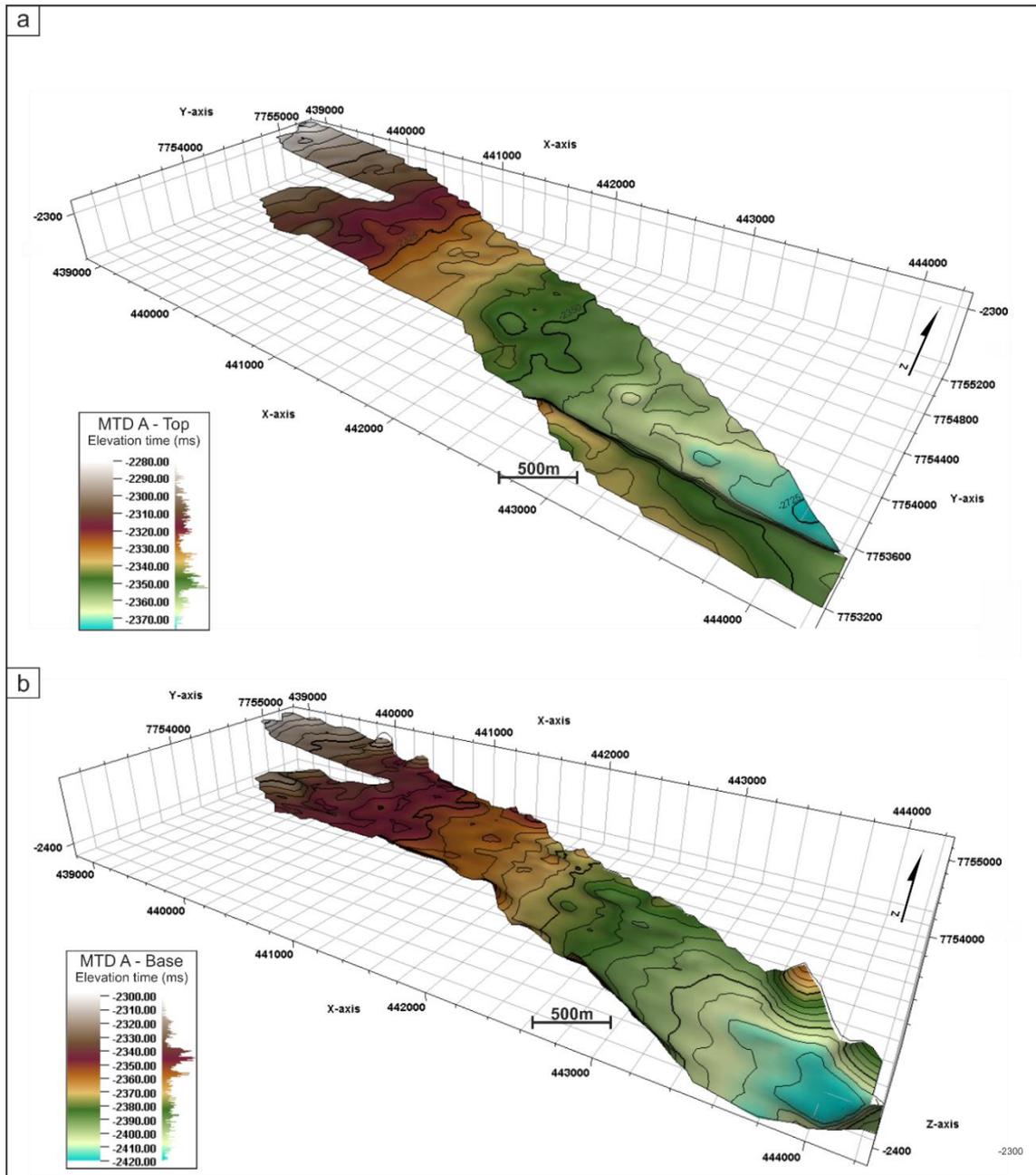
Figure 5.28 - Time structure map of the (a) top and (b) basal surfaces of confined MTD A, in time (ms). The contours image slide movement and accumulations patterns within the MTD body, highlighting its morphology. Vertical exaggeration = 5x.

5.7.1.2. Unconfined – MTD B

The typology of unconfined MTDs is well known from the literature. Depositional mechanisms have been described by Frey-Martínez et al. (2006) and named frontally emergent landslides. A vast portion of slope movements described in the last decades focused on unconfined MTDs.

The unconfined MTD B overlies the depositional surface in all its extension (Figure 5.12, Figure 5.13, Figure 5.14 and Figure 5.15). The depositional surface beneath MTD B has been partly affected by the growth and vertical propagation of faults formed in association with salt tectonics in the Espírito Santo Basin (Alves, 2012, and Omosanya and Alves, 2014). Salt tectonics can be associated with submarine mass movements and resulting faults can propagate enough to interact with near-seafloor MTDs (McAdoo et al., 2000, Omosanya and Alves, 2014). In this work, the depositional surface underneath MTD B is affected by faults designated by Omosanya and Alves (2014) as decoupled faults - their tips are confined to the basal shear surface of the interpreted MTD. Omosanya and Alves (2014) discussed the way of vertical fault propagation can be hindered by MTDs. However, this chapter does not discuss fault propagation from a structural point of view, for the reason that neither the Depositional surface mapped nor the MTDs have been affected directly by the faults themselves. It is therefore induced that MTDs did not hinder fault propagation in the stratigraphic unit analysed.

Observing the seismic profiles in Figure 5.14 and Figure 5.15 it is induced that fault propagation have had indirect effect on the local morphology of the depositional surface of MTD B. Consequently, extensional forced-folding is observed in the area just above the fault. The faults also created a relatively brittle area on the seafloor which is actually coincident with lateral margins of MTD B (dashed line in Figure 5.5). The basal shear surface of MTD B is often continuous and concordant to the depositional surface (bedding) (Bull et al., 2009), nevertheless, it can be affected by sediment variations or faults. This fact is observed in Figure 5.27, where the dashed line highlights the area of extensional forced-folding, which coincides with local ramp on the Depositional surface - and associated basal shear surface of MTD B.
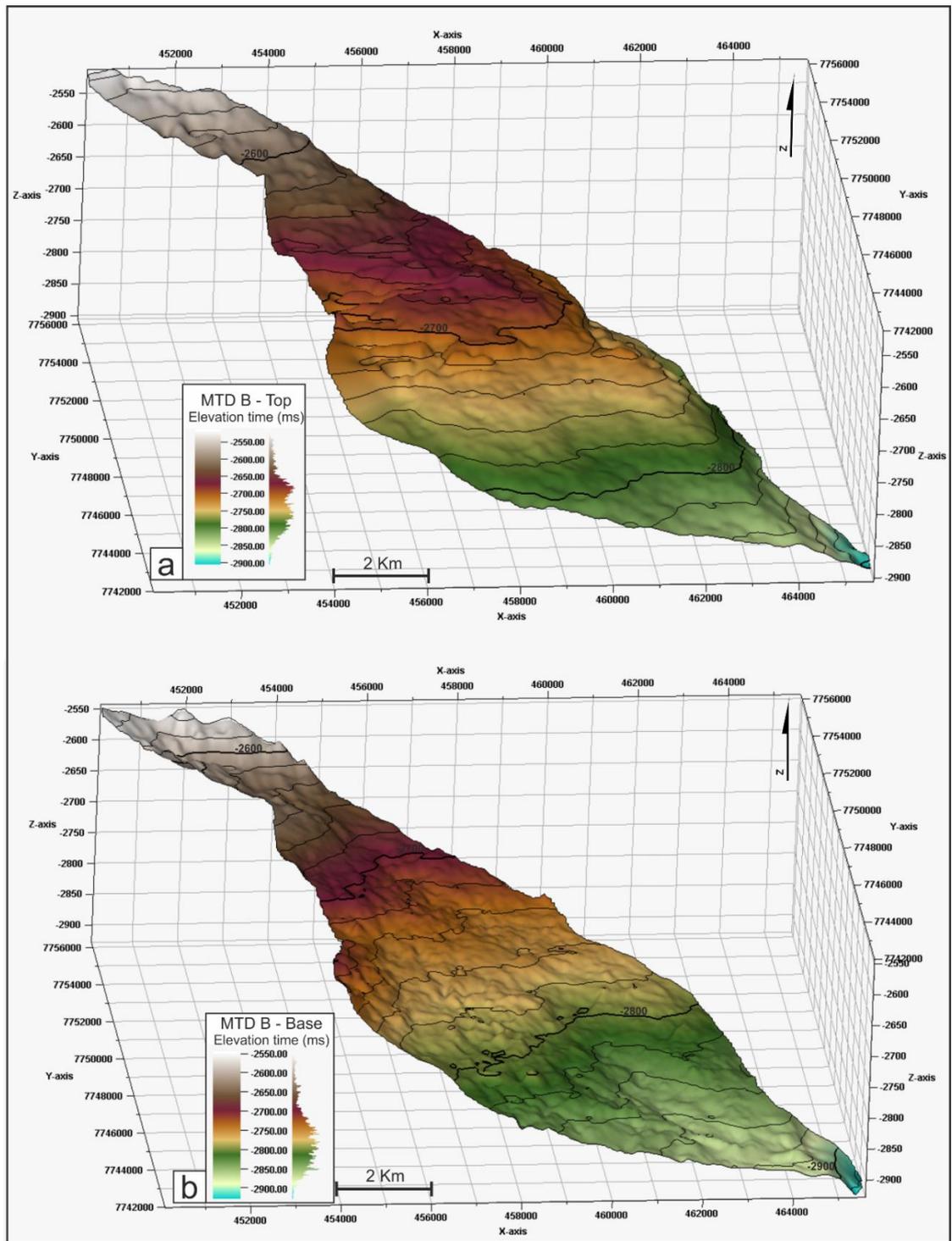
Figure 5.29 - Time structure map of the (a) top and (b) basal surfaces of the unconfined MTD B, in time (ms). The contours shown help identifying the directions of slide movement and accumulations patterns within the MTD body. Vertical exaggeration = 2.5x.

The basal surface of MTD B shows convexity across its body, a fact highlighting that the headwall scarp domain is rather prominent in this type. This same convex areas highlight portions of MTD B where erosion prevailed (Rovere et al., 2014) (Figure 5.29b). The opposite effect is observed throughout the upper surface of MTD B, where the headwall scarp domain that shows little convexity. (Figure 5.29a). The main body of the MTD B shows an upwardly concave surface, indicating deposition, and highlights the main body of the unconfined MTD B. The thicker part of the MTD corresponds clearly to the more expressive concavity showed by the upper surface.

5.7.2. Role of topographic barriers in controlling MTD run-out distance and deposition

Run-out distance is the limit of the disturbed area on a continental slope away from the headwall scarp (McAdoo et al., 2000). Usually, it is represented by the horizontal distance between the headwall scarp and the toe region of the MTD (Moernaut and De Batist, 2011). As pointed out by Moernaut and De Batist (2011) for sub-lacustrine landslides, median length, width and run-out distance are larger for emergent types when compared to confined MTDs. Moernaut and De Batist (2011) also pointed out that median depth of the basal shear zone is shallower for emergent landslides, a character that is not observed in the two studied MTD A and MTD B. Nevertheless, considered that MTD A headwall scarp drops 25 m through a distance of 900 m, while MTD B drops 80 m through a distance of ~3000 m (Table 5.1), the headscarp domain of MTD B is relatively smoother and meets the observations in {Moernaut, 2011 #353@@author-year}. The run-out area of MTD A is smaller than for MTD B, showing a drop of 100 m height for a distance of 4750 m (Table 5.1; Figure 5.30). In comparison, MTD B drops 200 m in height at its headwall domain, which extends as far as 16200 m in distance (Table 5.1; Figure 5.31).

The proposed headwall scarp and run-out area were considered the major morphological changes on the basal topographic profile. However, their morphometric attributes are considerably different when considering the two MTD types proposed. The depositional surface on which MTD A is resting (Figure 5.19) shows topographic barriers at the limits of the MTD body, as highlighted on the slope gradient map (Figure 5.22). The headwall scarp, northern lateral margin and toe domains are marked by high slope gradients, which changing

148

to a relatively flat area away from MTD A (between 0 to 2° and 4 to 8°, approximately). This character suggests that MTD A was triggered in a relatively steep zone and its movement was somehow stopped by adjacent topographic barriers. The depositional surface beneath MTD A also shows a marked promontory presenting the largest slope gradients (4 to 8°, approximately) (Figure 5.19 and Figure 5.20). This latter observation suggests that MTD A was first triggered as a small slope movement, in a region of relatively low slope gradient, having lost downslope inertia against the promontory. MTD A, however, continued to glide downslope until it was buttressed once more against a seafloor barrier and accumulated at the toe domain, emerging from its glide plane only shortly (Figure 5.10 and Figure 5.30).

Considering the morphology where MTD B is resting (Figure 5.23), a steeper change on its headwall scarp is observed when compared to MTD A. The slope gradient is also comparatively steeper (Figure 5.26), and suggestively predisposing MTD B at its maximum. The slope does not show strong topographic changes, revealing a rather smooth Depositional surface for MTD B. Nevertheless, it shows some minor ridges downslope, reflecting the local expression of vertically propagating faults. Normal faults in the study area created weakness zones at the seafloor, which bounded MTD B in multiple directions (Figure 5.14, Figure 5.15 and Figure 5.27).
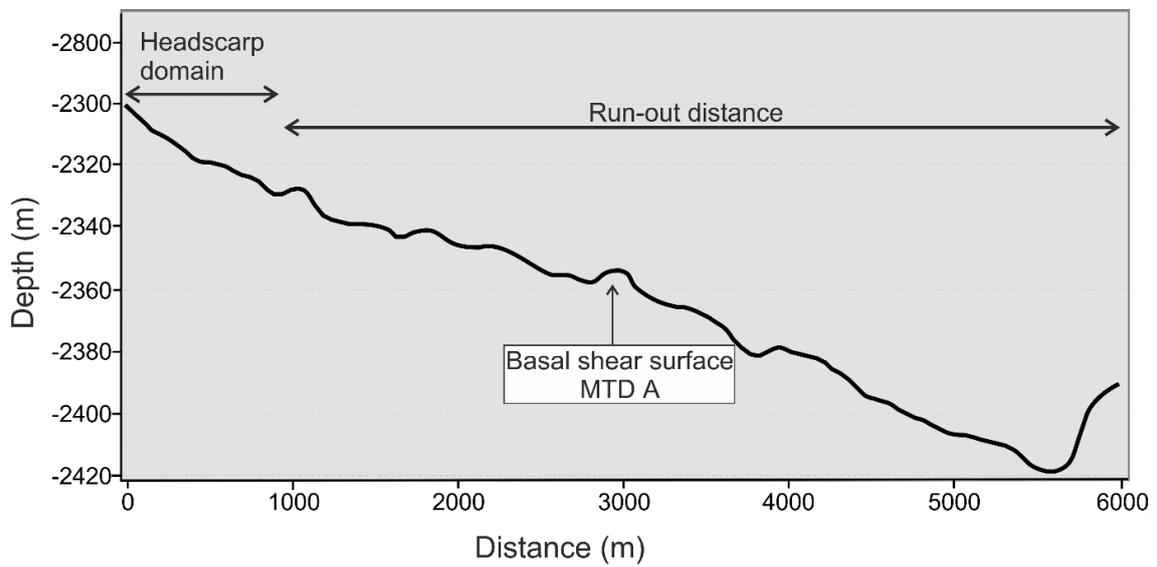
Figure 5.30 - Topographic profile of the basal surface of the confined MTD A with interpreted limits of headwall scarp domain and run-out distance, based on profile morphology.
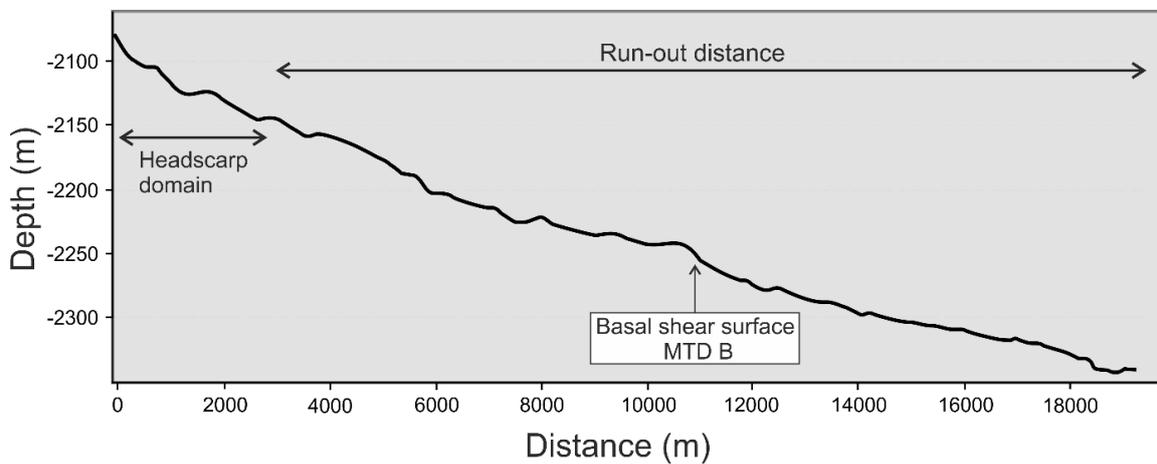
Figure 5.31 – Topographic profile of the basal surface of unconfined MTD B with interpreted limits of headwall scarp domain and run-out distance, based on profile morphology.

5.8. **Conclusions**

The most important conclusions from the observation of the two types of MTDs are summarised as follow:

- Three-dimensional (3D) seismic reflection data, used together with Geographic Information Systems (GIS), proved to be valid tools to study the morphometric attributes of submarine slope movements and surrounding areas.

- 3D seismic interpretation offshore Espírito Santo Brazil reveals the existence of two types of MTDs, Confined (MTD A) and Unconfined (MTD B), within the same stratigraphic package (Sequences N20 to N60 - Early Miocene to Holocene).

- The *Confined MTD A* is relatively small and was controlled by buttresses on the continental slope (chiefly hard, undisturbed strata) within Sequences N20 to N60. The thickest part of MTD A is located at its toe domain.

- The *Unconfined MTD B* is must larger when compared to MTD A. This unconfined MTD appears to have moved in a free translation mode until 'frozen' in place and buried.

- The local morphology of the depositional surface where MTDs are resting needs to be taken into consideration as a controlling factor to the total run-out distance of MTDs.

- Both MTDs are located where the Depositional surface shows the smaller slope gradients. However, kinematic indicators such as the headwall scarp (in both MTD A and MTD B), the lateral margins (MTD A) and toe domain (MTD A) are located where the slope gradient increases substantially in comparison to the surrounding slope.

- Depositional surface topography, based on the data analysed in this chapter, is an important factor controlling MTDs' morphology and sizes.

- Both MTD types can be characterised, and distinguished, by simple morphometric attributes such as MTD area, volume and thickness, slope gradient, headwall scarp

height, run-out area and slope gradient adjacent to failed strata. However, sedimentation and erosion patterns, together with local geology, are very important factors controlling slope movement (and sizes) that were discarded from this chapter. Detailed geological information is not available for this study as well as seismological data from nearby stations.

FAVOURABILITY SCORES FOR THE OCCURRENCE OF MASS-TRANSPORT DEPOSITS (MTD), OFFSHORE ESPÍRITO SANTO BASIN, SE BRAZIL

Chapter Six

Abstract

Slope instability is one of the most effective processes shaping the seafloor on both passive and tectonically active continental margins. Their end-product, mass-transport deposits (MTDs) have been documented on several continental margins using diverse approaches and methodologies.

This chapter tests a new methodology for the evaluation of MTD occurrence, and applies it to an area offshore Espírito Santo, SE Brazil. An MTD inventory was made for an area cropped from a 3D seismic volume (BES-100). The MTD inventory consists of four MTDs integrated into a Geographic Information Systems (GIS) database. MTD favourability scores were computed using algorithms based on statistical/probabilistic analyses (Information Value Method) over unique condition terrains in a raster basis. Terrain attributes derived from the Digital Terrain Model (DTM), were used as proxies to several driving factors of MTDs and as predictors in the models. Three models are discussed independently according to the different parts of the interpreted MTD (Model 1, Model 2 and Model 3). The final results were prepared by sorting all pixels according to the pixel favourability value in descending order. The robustness and accuracy of the MTD favourability models were then evaluated through the use of success-rate curves. The curves aided in the quantitative interpretation of the models expressing their goodness of fit to the interpreted MTDs.

The results in this section confirm that the method is valid for submarine slopes. From the three models, Model 3 obtained the highest goodness of fit (0.862). Based on these results, a sensitivity analysis was undertaken and key predisposing factors were identified.

This methodology was never applied before to submarine environments and has the potential to become a very important and valid approach for the recognition of submarine slopes prone to failure.

6.1. **Introduction**

Submarine slope instability is one of the key natural hazards affecting continental margins and can result in direct and indirect damages to seafloor substructures (Dai et al., 2002). The last few decades witnessed great improvements in submarine landslide characterisation and in the understanding of the local conditions leading to slope instability at small and large scales (Nadim, 2006, Hough et al., 2011, Gilbert et al., 2013, Rodríguez-Ochoa et al., 2015). The development of new techniques such as three-dimensional (3D) seismic data has contributed greatly towards the understanding of submarine slope instability, and allowed its integration in GIS. The use of GIS techniques thus far applied in onshore risk assessments has improved our knowledge on the factors that lead to the triggering of offshore instability events (McAdoo, 2000). By combining 3D seismic datasets with GIS databases we can explore the different tools used in GIS spatial analyses (Haneberg et al., 2015), taking advantage of methodologies tested onshore.

Onshore, slope stability analyses have recently benefited from improvements in data acquisition, data processing and analytical techniques. Some of these improvements include the completion of susceptibility assessments using several maps representing the spatial distribution of physical parameters that may influence the occurrence of mass movements (Urgeles et al., 2006, Micallef et al., 2007, Micallef, 2011, Li et al., 2014, Haneberg et al., 2015). Susceptibility analyses are undertaken with the final aim of understanding the conditions and parameters that favour the occurrence of mass movements in specific locations (Soeters and Van Westen, 1996, van Westen et al., 2006, van Westen et al., 2008, Thiery et al., 2007). In its final stage, the analyses are able to identify the areas where, under a set of favourable conditions, mass movements will probably occur. A great part of slope instability predictive studies uses statistical methods which cross predisposing factors with inventories of (past) events, within a GIS environment (van Westen et al., 1997, Carrara et al., 1999, Piedade et al., 2010, Pereira et al., 2012).

Submarine slope instability occurs when there is a significant reduction in the shear strength of continental slope sediment, usually at the location of a future basal glide

plane, or shear zone (Varnes, 1978, Hampton et al., 1996). Slope stability analyses have been based on a deterministic approach, where the level of safety of a slope is quantified by a 'safety factor' (Nadim, 2006). The factors that cause slope failure include: preconditioning factors, preparatory factors and triggering factors (Glade and Crozier, 2005). Even so, it is common to distinguish between trigger and predisposing factors in slope stability analysis (Zêzere et al., 1999, van Westen et al., 2008, Pereira et al., 2012).

This chapter focuses on predisposing factors (e.g. Glade and Crozier, 2005, Pereira et al., 2012), that were present during slope failure in parts of the Espírito Santo Basin, SE Brazil. This was undertaken via integration of data from the interpreted 3D seismic volume into GIS integrated using a statistical method, the Informative Value (IV). As a result, the aims of this chapter are as follows:

(a) To determine a set of predisposing factors that can reflect the natural conditions for the occurrence of MTDs on the continental slope,

(b) To perform a bivariate statistical model that integrates the mapped MTDs and the predisposing factors into GIS and performed a predictive map to MTDs occurrence for the area,

(c) To determine the favourability scores of predisposing factors that are capable of triggering MTDs,

(d) To validate the statistical model applied using Success-Rate and Area Under the Curve (AUC) validation techniques,

(e) To run a sensitivity analysis of the variables used for modeling in order to understand which variables influence the model in greater degree (s).

The key objective of this work is to understand how the bivariate statistical model of Informative Value (IV) responds to marine mass movements by using data derived from 3D seismic volumes. It was based on the following research questions (i) is it possible to use statistical methods integrated in GIS environments to identify the predisposing factors that constrained the location of MTDs offshore Espírito Santo? (ii) Are 3D seismic volumes a valid data source for these kind of studies? (iii) Are the obtained models scientifically valid to justify their application to others 3D seismic datasets?

In this chapter, a horizon at the base of multiple MTDs was mapped (depositional surface) and computed into seven predisposing factors, which were later integrated into a GIS environment. The aim was to identify the natural conditions present at the time of the slope failure, presumed to have occurred at the end of the Miocene. Three different models were run using the i) total area of MTDs (model 1), ii) 1/3 of the MTDs total length (model 2) and iii) half of the lenght used in model 2 (model 3). An attempt at constraining the probable rupture zone of these MTDs is undertaken by model 2 and model 3. Favourability scores were calculated for each class of each variable and for the three models. The models were validated through success-rate curves and corresponding AUC´s. The results are very positive and the rationale of applying the bivariate statistical methods to a submarine environment is validated. These results are robust and are found to be valid for other continental slopes on where 3D seismic data is available.

An important statement is needed to present at this time, as a data limitation for the methodology proposed. The population of MTDs are constituted by only four movements, included the two examples described in chapter 5. The population is considered valid to proceed with the methodology application. Nevertheless, is not big enough for data partition, whereby the same inventory is used to run the model and to validate (success-rates). As the population is relative small, the different MTD typologies are not considered into the models and the four MTDs entered in the same model. This limitation from the database point of view will be under discussion further in this thesis.

This chapter starts by describing the depositional surface that was the base to compute the predisposing factors and works as a Digital Terrain Model (DTM), representing the relief. The results chapter presents the favourability scores that are determined through a statistical integration for MTDs instability. The three models (models 1 to 3) obtained using different areas of the same MTDs inventory are presented and validated. A sensitivity analysis is undertaken for the models which obtained the best predictive capacity. A key aim of this chapter is to discuss the importance of this new approach, in order to define the predisposing factors that are favourable in the occurrence of MTDs in the Espírito Santo continental slope. The limitation of the method and input dataset (MTDs inventory and DTM) obtained from 3D seismic data will also be discussed. At the

end of the chapter, information on improvements to the models are suggested bearing in mind its application to marine datasets.

6.2. **Mass-Transport Deposits**

The interpretation of four MTDs follows previously-established criteria to describe the internal character of remobilized material (e.g. Hampton et al., 1996, Frey-Martínez et al., 2006, Moscardelli and Wood, 2008, Bull et al., 2009, Gamboa et al., 2010, Omosanya and Alves, 2013). Internal reflections in the interpreted MTDs show chaotic stratigraphy and imbricated blocks (e.g. Frey-Martínez et al., 2006). The basal surface is shown as a high-amplitude seismic reflection below chaotic reflections within the MTDs (Frey-Martínez et al., 2006). The top of the MTDs is marked by a continuous high amplitude reflection that overlies chaotic internal reflections. The four MTDs mapped in this chapter exhibit varying areas, volumes and slope locations, but the thickness of the remobilized material is very uniform among all MTDs (Table 6.1).

Table 6.1 - Morphological characteristics of MTDs interpreted in the Espírito Santo Basin.

	Area (km^2)	Volume (km^3)	Max. Thickness (m)	Location
MTD 1	5. 251	0.128	~60	Sub-parallel to slope
MTD 2	20.88	0.659	~65	Upslope to mid-slope
MTD 3	87.180	3.163	~70	Mid-slope to lower slope
MTD 4	19.790	0.470	~80	Sub-parallel to slope

Figure 6.1 displays the general location of the MTDs in the continental slope offshore Espírito Santo, SE Brazil and the area of each MTD that was later considered in Models 1 to 3. For Model 1, the total unstable area considered is 133.8 km^2, 17.7% of the total study area. In Model 2, the unstable area considered is 30.2 km^2, 4% of the total area. Model 3 considered an unstable area of 11.1 km^2, which corresponds to 1.47% of the total area (Table 6.2).
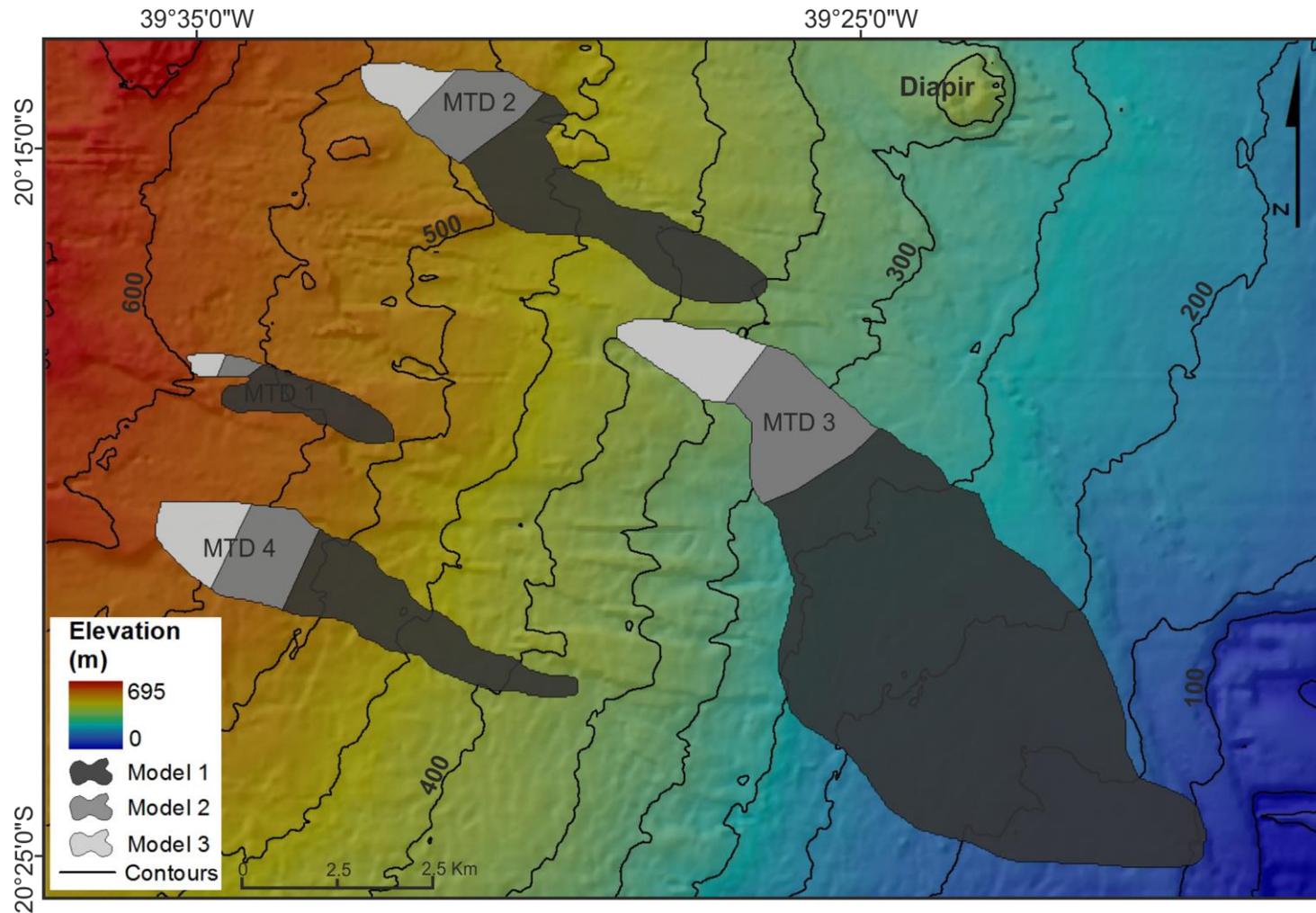
Figure 6.1 - Study area offshore Espírito Santo Basin (SE Brazil). The figure shows the location of four MTDs considered in the models. Different shades of grey show the areas of the MTD used for each model. The map shows also the elevation across the study area after depth-converting from time-depth to true-depth.

Table 6.2 - Unstable area in square kilometres and relative percentage for the three different models used and total area of the depositional surface for comparison.

	Unstable area (km^2)	Unstable area (%)
Model 1	133.8	17.7
Model 2	30.2	4
Model 3	11.1	1.47
Study area	756 km^2	100%

6.3. **Characterization of predisposing factors**

Predisposing factors considered in this section are elevation, slope gradient, profile curvature, planform curvature, flow direction, flow accumulation and slope over area ratio. These predisposing factors are considered in the models as independent variables.

The characteristics of the seven predisposing factors for slope instability that are considered in this study are synthesized in Table 6.3. It also shows a class code, the number of cells (pixels) that each class contains and the percentage of area which each class covers.

Table 6.3 - Absolute and relative frequencies for each class of each variable for the seven predisposing factors (variables).

Variable	Class Code	Class	N. of pixels	Area of the class (%)
Elevation	E1	0-100	9721	3.2
(m)	E2	100-200	48435	16.0
	E3	200-300	66999	22.0
	E4	300-400	52189	17.2
	E5	400-500	57874	19.2
	E6	500-600	53176	17.4
	E7	600-700	15130	5.0
Slope	S1	[0-1]	108560	35.8
gradient	S2	]1-2]	131386	43.3
(º)	S3	]2-3]	39530	13.0
	S4	]3-4]	12232	4.0
	S5	]4-5]	5377	1.8
	S6	]5-6]	2751	0.9
	S7	]6-7]	1651	0.5
	S8	]7-8]	898	0.3
	S9	>8	1139	0.4
Profile	PrC1	Convex	4151	34.2

curvature	PrC2	Flat	3827	31.5
	PrC3	Concave	4172	34.3
Platform curvature	PlC1	Concave	5556	45.7
	PlC2	Flat	959	7.9
	PlC3	Convex	5635	46.4
Flow direction	FD1	E	86791	28.6
	FD2	SE	86456	28.5
	FD3	S	53672	17.7
	FD4	SW	13530	4.5
	FD5	W	7613	2.5
	FD6	NW	3839	1.3
	FD7	N	14827	4.9
	FD8	NE	36796	12.1
Flow accumulation (Log scale)	FA1	0	67875	22.4
	FA2	1	49210	16.2
	FA3	1-10	126086	41.5
	FA4	10-100	46277	15.2
	FA5	100-1000	12739	4.2
	FA6	>1000	1337	0.4
Slope over area ratio (log scale)	SAR1	0	9648	3.2
	SAR2	0-0.00001	47399	15.7
	SAR3	0.0000-	101146	33.6
	SAR4	0.0001	138112	45.8
	SAR5	0.0001-	4973	1.7
		0.001		
		0.001-0.01		

6.3.1. **Elevation**

Elevation is useful to classify any changes in local relief and locate the maximum and minimum height within the study area. In this particular case, the relief changes continually from the highest to the lower elevation along the Espírito Santo slope (Figure 6.2).

Elevation is classified into seven classes which are described in Table 6.3. Class E1 (0 – 100 m) and class E7 (600-700 m) are the classes covering the smaller percentage of area ~8.2%. The rest of the study area is distributed homogeneously among the other classes. Class E3 (200-300 m) covers the high percentage of area in the study area (22%) (Figure 6.2).
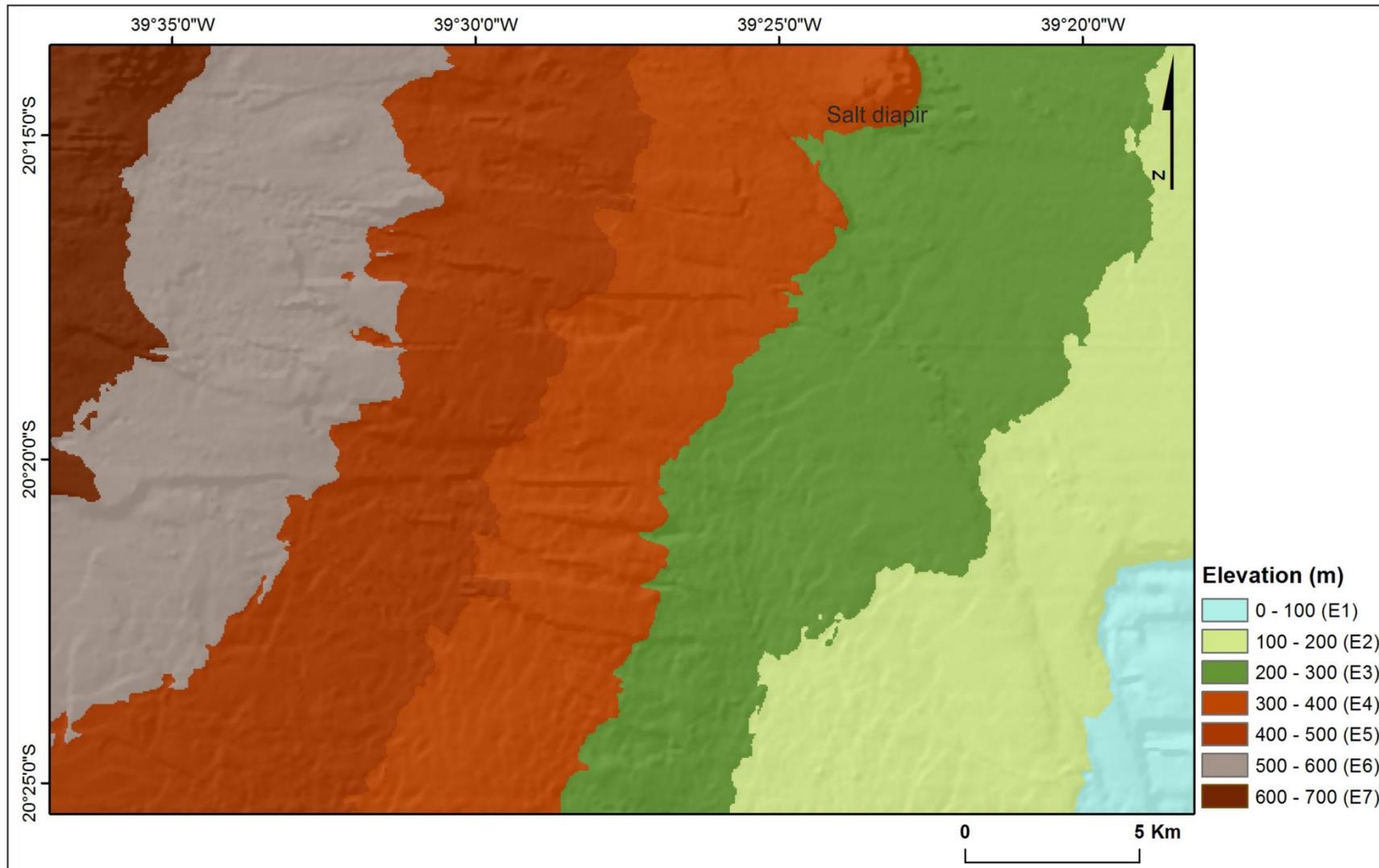
Figure 6.2 – Thematic layer showing the spatial distribution of each Elevation class (E) in meters.

6.3.2. **Slope gradient**

The slope gradient (in degrees) of the depositional surface is presented in the map in Figure 6.3. The class limits were defined considering particular conditions of the continental slope, which is very smooth along the Espírito Santo margin, due this fact, slope gradient is classified in eight distinct classes, in order to discriminate in detail the physical characteristics of the slope, as shown in Table 6.3 Class S2 represents most of the total area (43.5%) and exhibits slope gradients between 1 and 2° (Figure 6.3). Class S1 represents 35.8% of the total area and exhibits a gradient 0 – 1°. Approximated 13% of the study area comprises slope gradients of 2-3° (class S3). These three classes combined cover 92.1 % of the total area studied in this chapter (Figure 6.3).

6.3.1. **Profile curvature**

The spatial distribution of profile curvature in the study area is presented in Figure 6.4. Profile curvature directly affects the acceleration or deceleration of mass-flows along the depositional surface. Profile curvature relates to the convergence and divergence of mass-flows across a surface (Menno-Jan, 2013). In summary, profile curvature reflects the change in slope angle, and mainly controls the change of velocity of mass flowing down along the slope (Clerici et al., 2010). It is parallel of the maximum slope (Menno-Jan, 2013) and negative values indicate that the surface is upwardly convex at the cell. A positive profile indicates that the surface is upwardly concave at that cell, whereas zero value indicates that the surface is linear (Figure 6.5). The contours in the image help to identify the areas where the slope presents a concentration of convex, rectilinear/flat and concave forms.

The classes and the distribution of Profile curvature in the study area, for the three classes mentioned above is displayed in Figure 6.4. The classes are seen as roughly equally distributed in Table 3. The class PrC2 occupies a small part (31.5%) of the study area. The two other classes each occupy ~34% of the study area (Table 6.3).
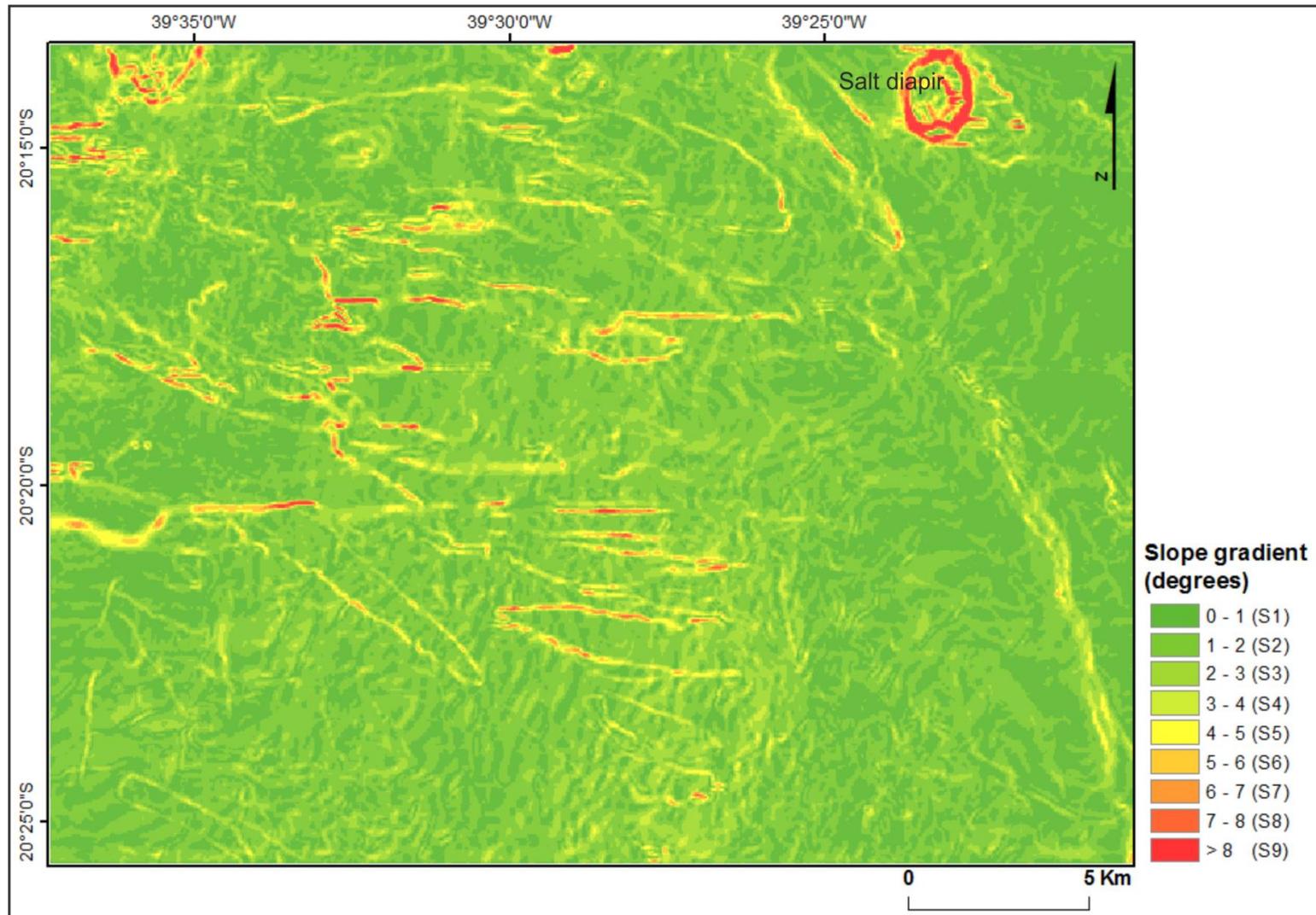
Figure 6.3 - Thematic layer showing the spatial distribution of each Slope gradient theme (S), in degrees. In Espírito Santo (SE Brazil).
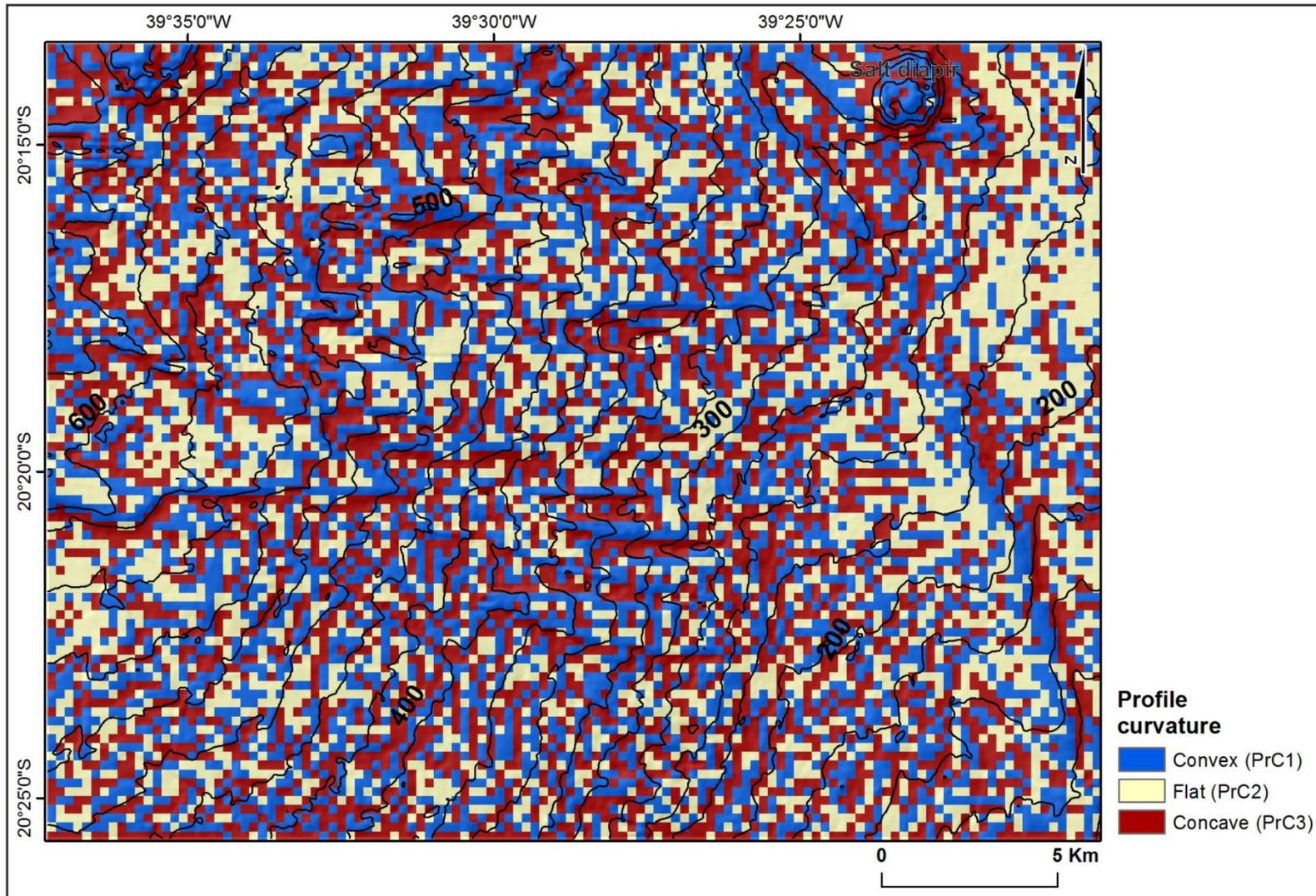
Figure 6.4 - Thematic layer with spatial distribution of each class for Profile curvature (PrC1), offshore Espírito Santo (SE Brazil). The contours are equidistant 25 meters.
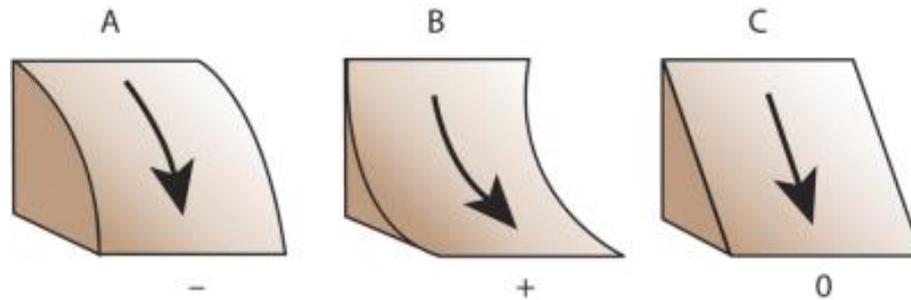
Figure 6.5 - Profile curvature as represented on theoretical surfaces. The arrow indicates the direction of the slope. A) convex slope, B) concave slope and C) linear slope (Menno-Jan, 2013).

6.3.2. **Planform curvature**

Planform (or plan) curvature is perpendicular to the direction of maximum slope. Positive values of planform curvature indicate the surface is sideward convex at this cell. Negative values indicate the surface is sideward concave, whereas zero value indicates the surface is flat (Figure 6.6). Planform curvature reflects the changes in aspect angle and control the mass flow divergence/convergence (Clerici et al., 2010). It is related to the superficial and sub-superficial runoff flow on the slope. The spatial distribution of classes within the study area are displayed in Figure 6.7, where it is observed that 46.4% diverge and 45.7% converge the slope and 7.9 % exhibit a flat slope (Table 6.3). The contours lines in Figure 6.7 help to identify the forms of the 3 classes proposed.
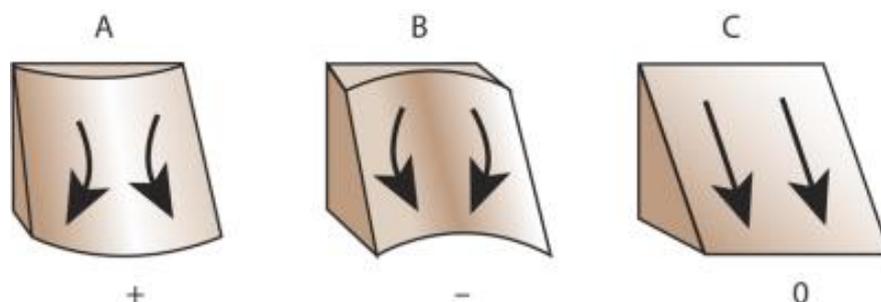
Figure 6.6 - Planform curvature as represented on a theoretical surface. The arrow indicates the direction of the slope. A) convex slope, B) concave slope and C) linear slope.
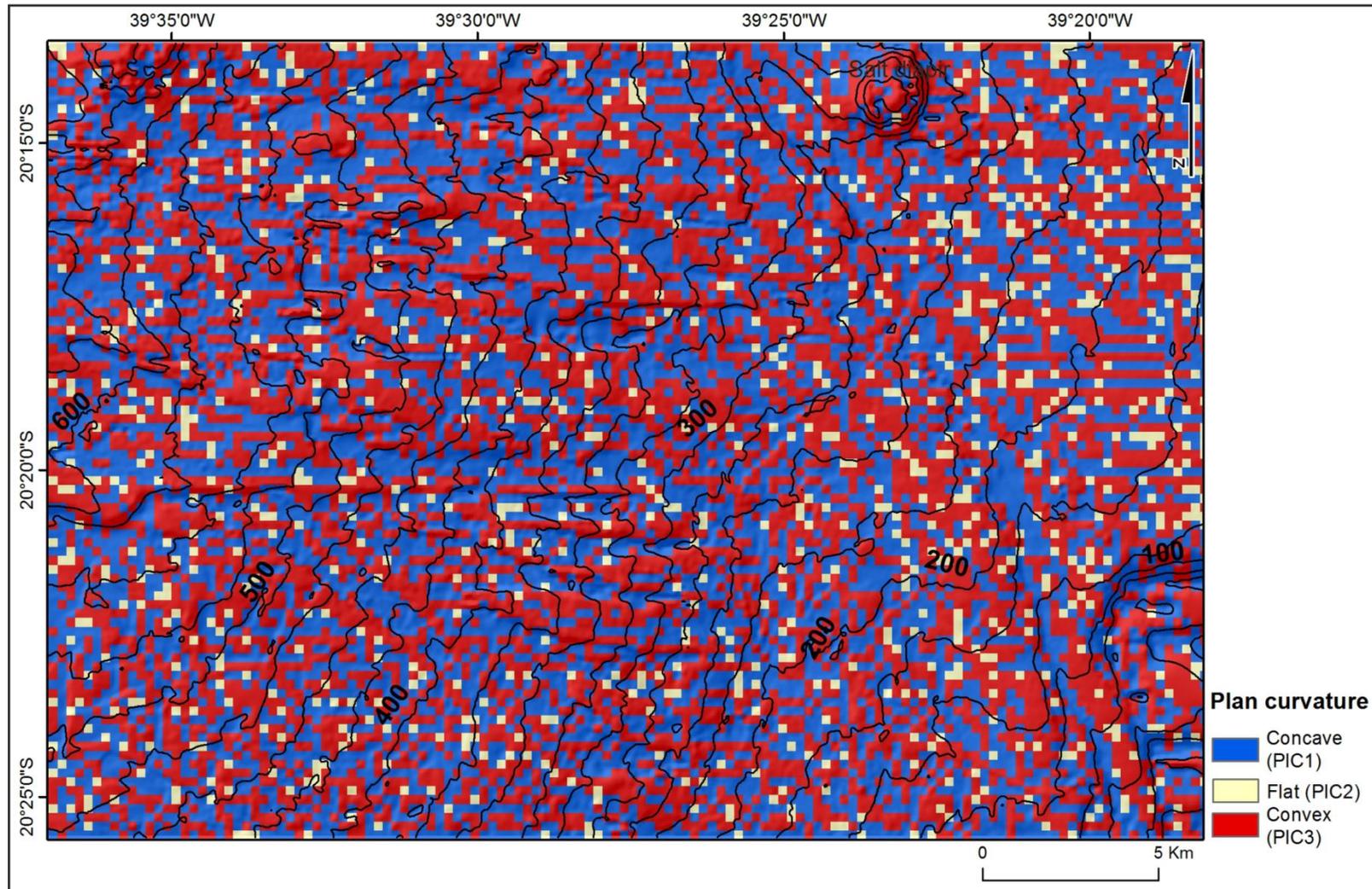
Figure 6.7 - Thematic layer showing the spatial distribution of each class for plan curvature (PIC), offshore Espírito Santo (SE Brazil). The figure shows contours lines with an equidistance of 25 m.

6.3.3. **Flow direction**

The greater percentage of area is occupied by the first two classes, FD1 and FD2, which cover an area of 28.6 and 28.5%, respectively. These values indicate that these mass-flows have an east to southeast direction in 57% of the study area. In 17.7% of the study area, the flow direction is south as represented by class FD3. This is followed by the northeast-trending class FD8, which occupies 12.1% of the study area. The remaining 8.7% of the area is occupied by mass-flows directed to the north, east and northeast, with 4.9, 2.5 and 1.3% of the total study area, respectively (Table 6.3 and Figure 6.8).

6.3.4. **Flow accumulation**

Flow accumulation is classified into six classes (Table 6.3) and is represented spatially in Figure 6.9. The class FA3 covers the greatest percentage of the study area with 41.5% coverage. This is followed by class FA1 with 22.4% of the study area. Classes FA2 and FA4 cover 16.2% and 15.2%, respectively. The last two classes, FA5 and FA6 cover together less than 5% of the total area. Areas classified by high accumulations are areas of concentrated mass-flows and can be used to identify stream channels (Figure 6.9). Areas classified as 0 comprise topographic highs where there is no mass-flow accumulation.

6.3.5. **Slope over area ratio**

Slope over area ratio calculates the ratio of the slope to the specific catchment area or contributing area for each pixel. The final map is classified in a logarithmic scale into fixed classes (Table 6.3) as represented in Figure 6.10. Class SAR4 observed in 45.8% of the study area, followed by the class SAR3 with 33.6% and SAR2 with 15.7%. Class SAR1 and SAR4 occupied respectively, 3.2% and 1.7% of the study area (Table 6.3, Figure 6.10).
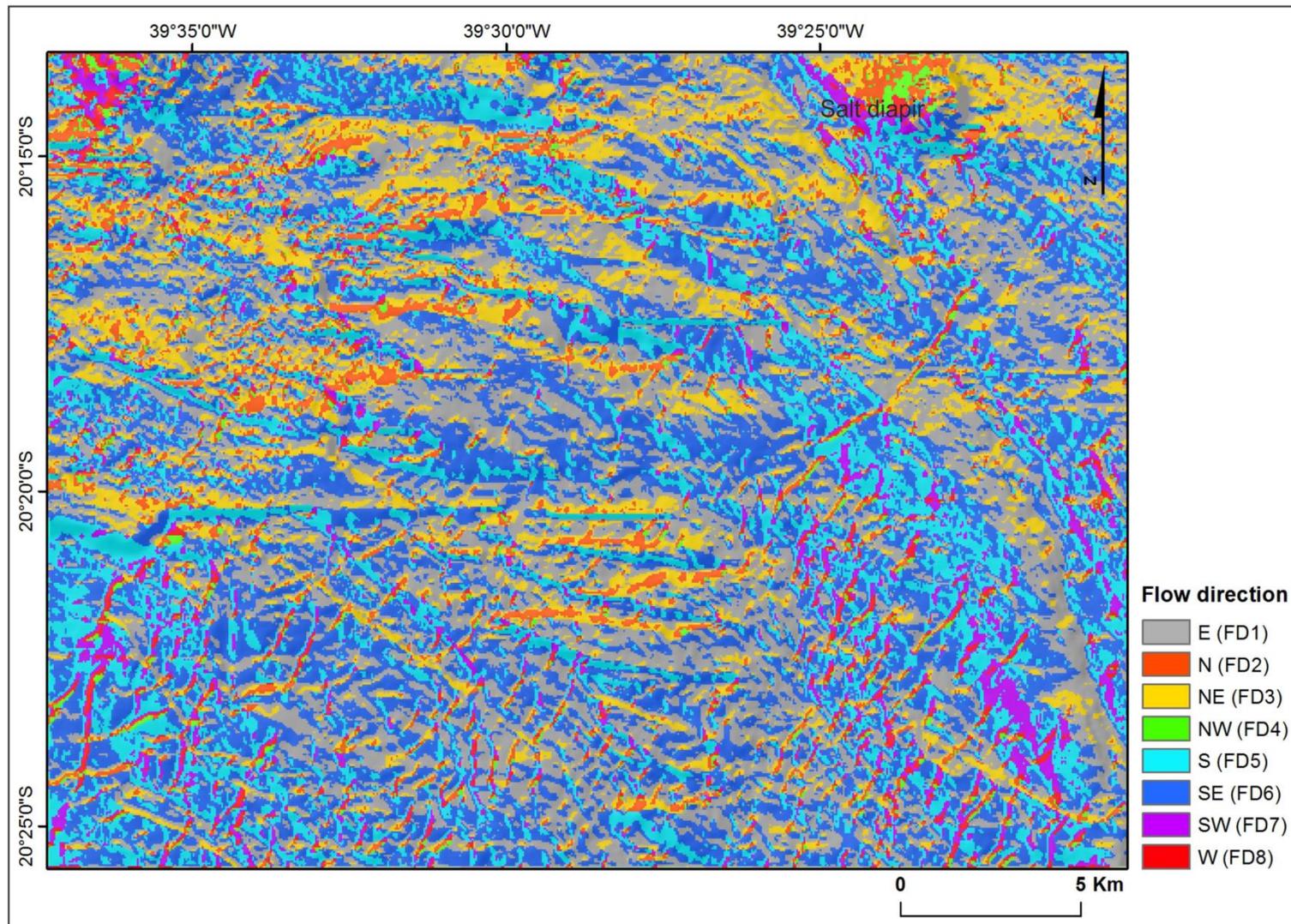
Figure 6.8 - Thematic layer showing the spatial distribution of each class for flow direction (FD), offshore Espírito Santo, (SE Brazil).
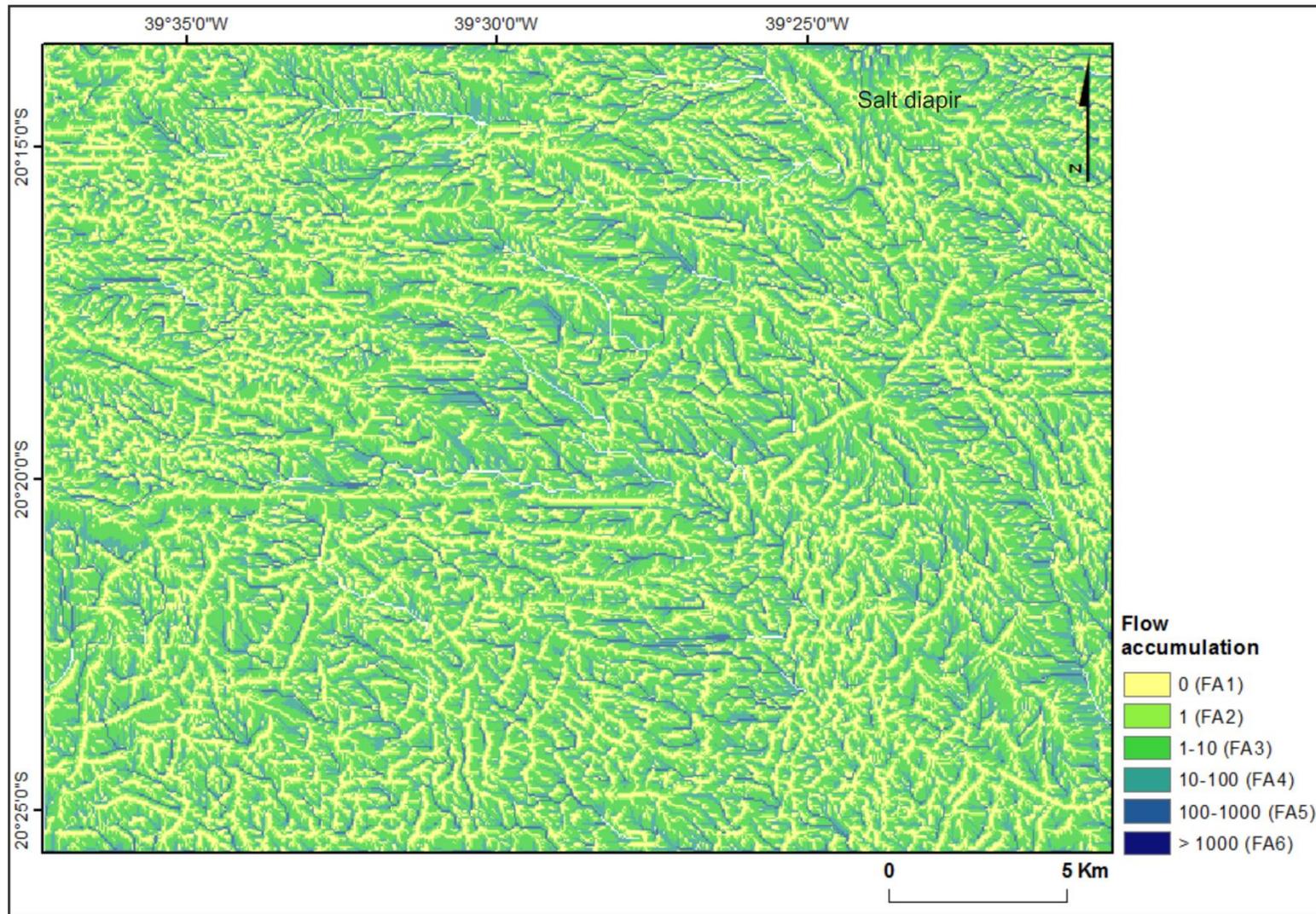
Figure 6.9 – Thematic layer with spatial distribution of each class for flow accumulation (FA), offshore Espírito Santo (SE Brazil).
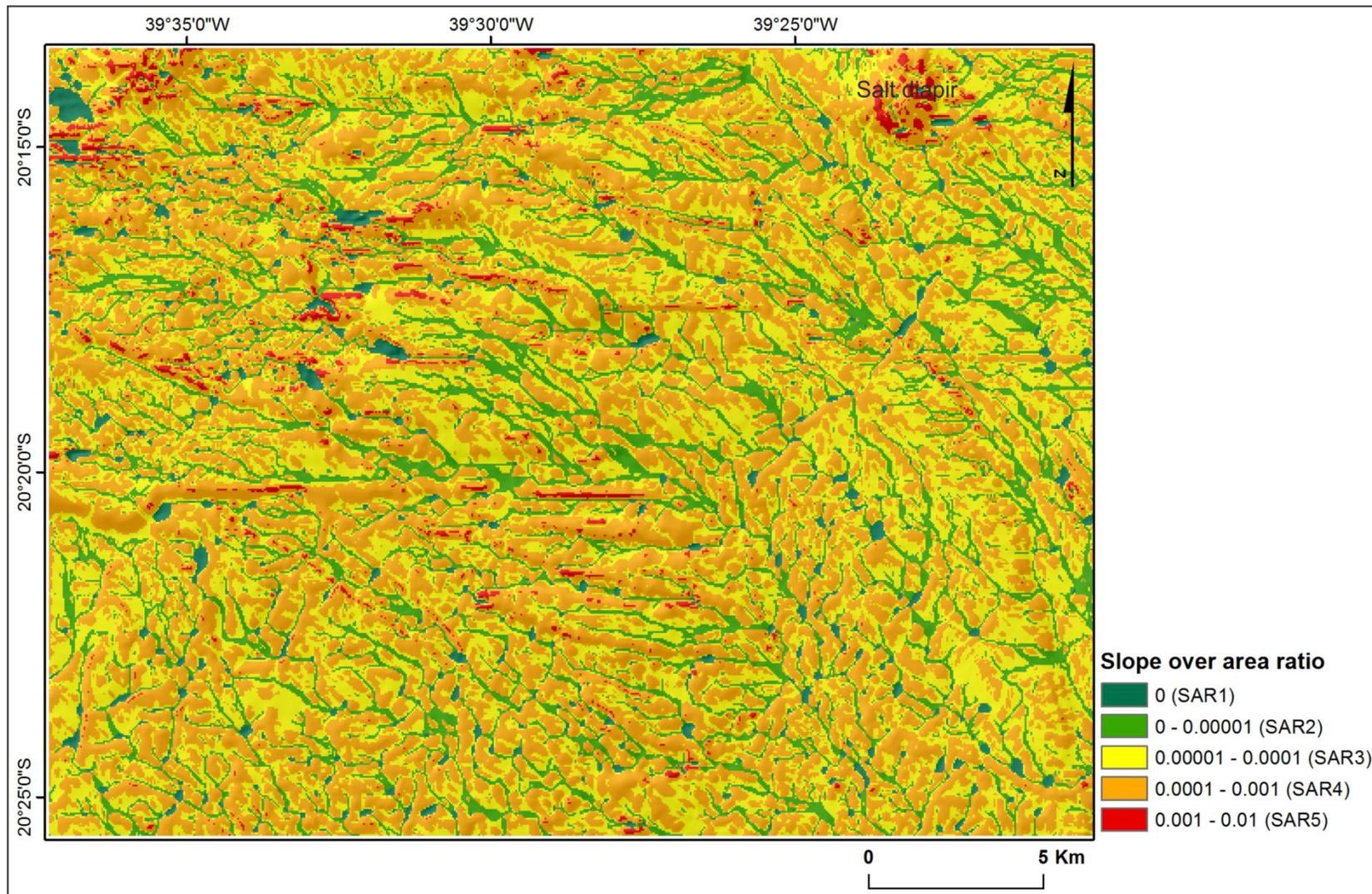
Figure 6.10 - Thematic layer showing the spatial distribution of each class for slope over area ratio (SAR), offshore Espírito Santo (SE Brazil).

6.4. **Results**

6.4.1. **Weighting of variables**

The weighting of variables for the evaluation of MTDs favourability scores is calculated applying the Informative Value (IV) bivariate statistical method, the methodology of which is described in chapter 3.

The weighting is prepared using three different partitions for the same MTDs inventory: 1) Model 1, using the total area of MTDs inventory; 2) Model 2 – using 1/3 of MTDs total length and; 3) Model 3 – using half of the length in used in Model 2.

In the plots shown in Figure 6.11, Figure 6.12 and

Figure 6.13 show the relationship between the class occupancy and favourable scores for MTDs occurrence. In practice, the figures plot the number of pixels containing MTDs (Si) and the number of pixels with variable xi (Ni). The classes that do not contain pixels of MTDs have no representation on the plots (i.e. Si equal to 0).

6.4.1.1. Model 1

The classes covering large areas do not necessarily present high favourability to the occurrence of MTDs. As it is observable from the plot of variable Elevation in Figure 6.11a, class E2 reveals the highest favourability to the occurrence of MTDs (0.321), but this is not the class occupying the larger area (16%). Class E3, corresponding to an elevation between 200 to 300 m, covers a larger percentage of total area (22.1%) that E2, and presents the second high favourability to the occurrence of MTDs (0.234) (Figure 6.11a).

The Slope gradient class S2, corresponding to slopes with 1-2° in gradient, occupies the larger area (43.3%) and it is the class with the highest favourability score; 0.20. Class S2 is followed by classes S3 (2-3°) and S1 (0-1°), which occupy 13% and 34.8% of the total area of the study. They present, respectively, favourability scores of 0.176 and 0.161. Classes S4, S5 and S6 are represented in very small areas and have favourability scores above 0.10 (0.134, 0.125 and 0.118) respectively (Figure 6.11b).

Profile curvature correlates with area and favourability scores. Three Profile curvature classes PrC1, PrC2 and PrC3 covering 34.2%, 31.5% and 34.3% of the total area, corresponding to favourability scores of 0.181, 0.156 and 0.186 respectively are displayed in Figure 6.11c.

The plan curvature variable presents a higher discrepancy between classes and favourability scores for MTDs that follow the observed tendency. The pixels constituting the study area in Figure 6.11d are distributed in the form of two main classes, PlC1 (45.7%) and PlC3 (46.4%), contributing for favourability scores of 0.183 and 0.175. This leaves only 7.9% of total area to PlC2, which presents a favourability score of 0.136 and corresponds to a relative flat area on the continental slope (Figure 6.11a).

The flow direction variable is plotted in Figure 6.11e. The higher favourability score for this variable correlates with the class covering the smaller area. It corresponds to class FD4 (SW), which presents a favourability score of 0.29 and covers an area of 4.5%. Classes FD1 and FD2 each cover ~28% of the total area and their favourability scores are 0.145 and 0.174, respectively. Considering variable flow accumulation, the favourability scores are for five of the classes around 0.170. The highest favourability scores are related to the class FA6 presenting 0.24, which is the class that covers the least area, 0.4% of the total area.

Slope over area ratio follows a trend similar to the previous variable Figure 6.11g. Class SAR1 covers only 3.2% of the total area, and is the class that presents higher favourability scores (0.216) for the occurrence of MTDs. The class that occupied 45% of the area shows a favourability score of 0.181.

a) Elevation

b) Slope gradient

c) Profile curvature

d) Plan curvature

e) Flow direction

f) Flow accumulation
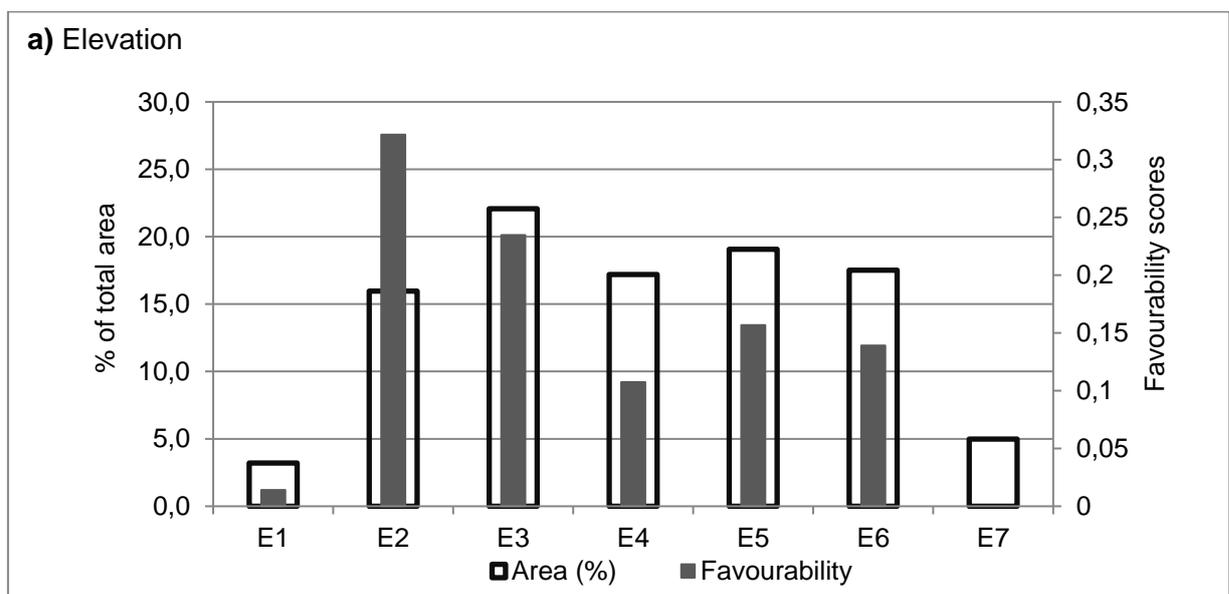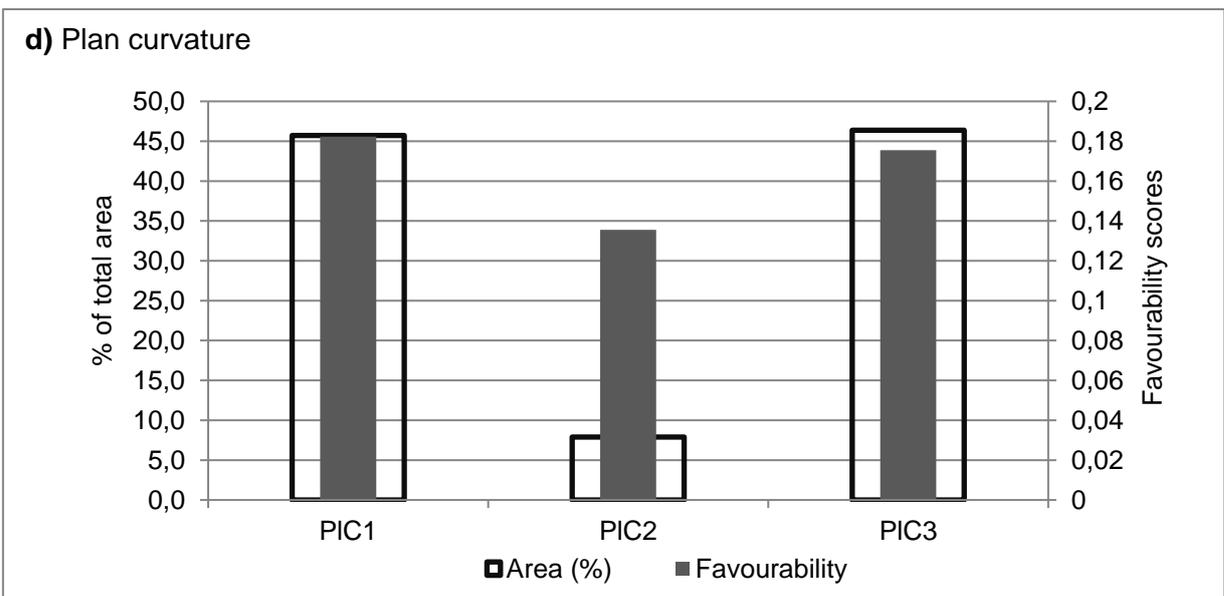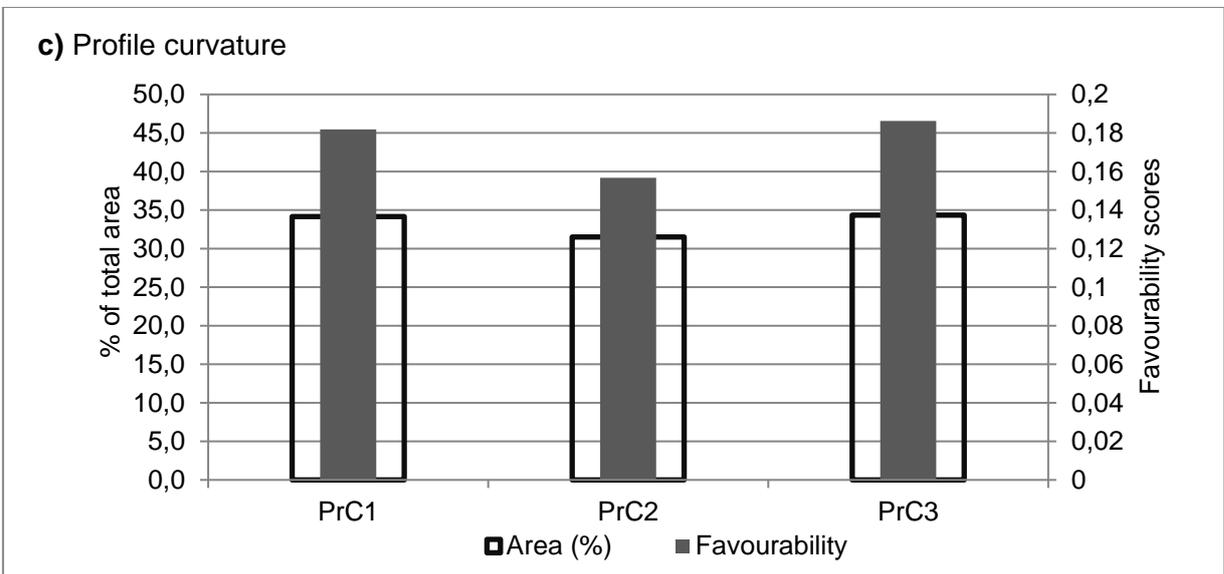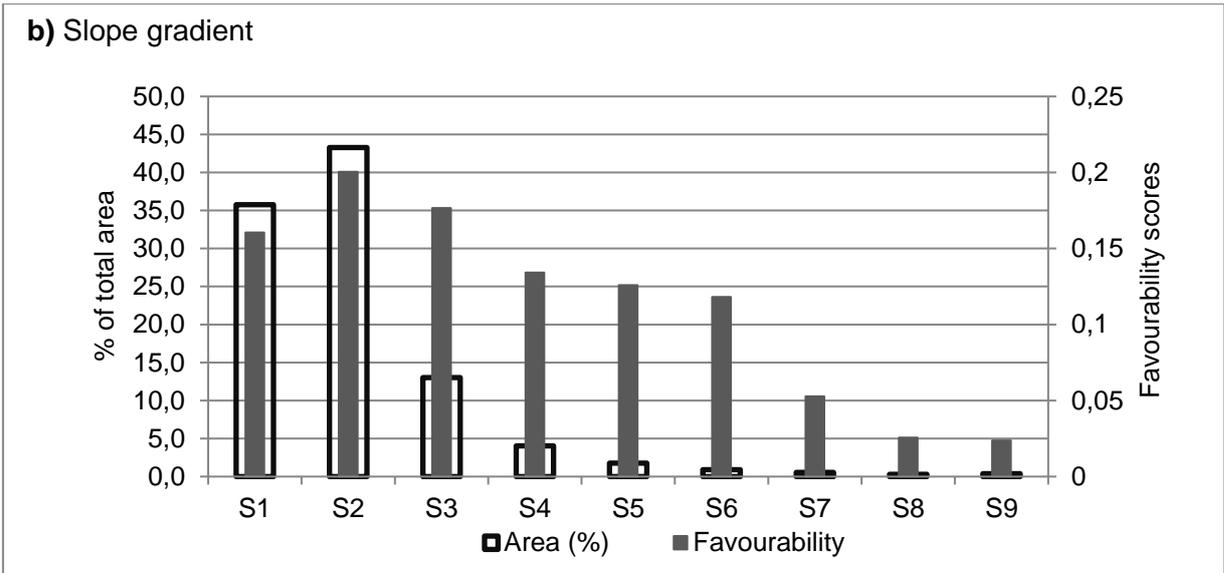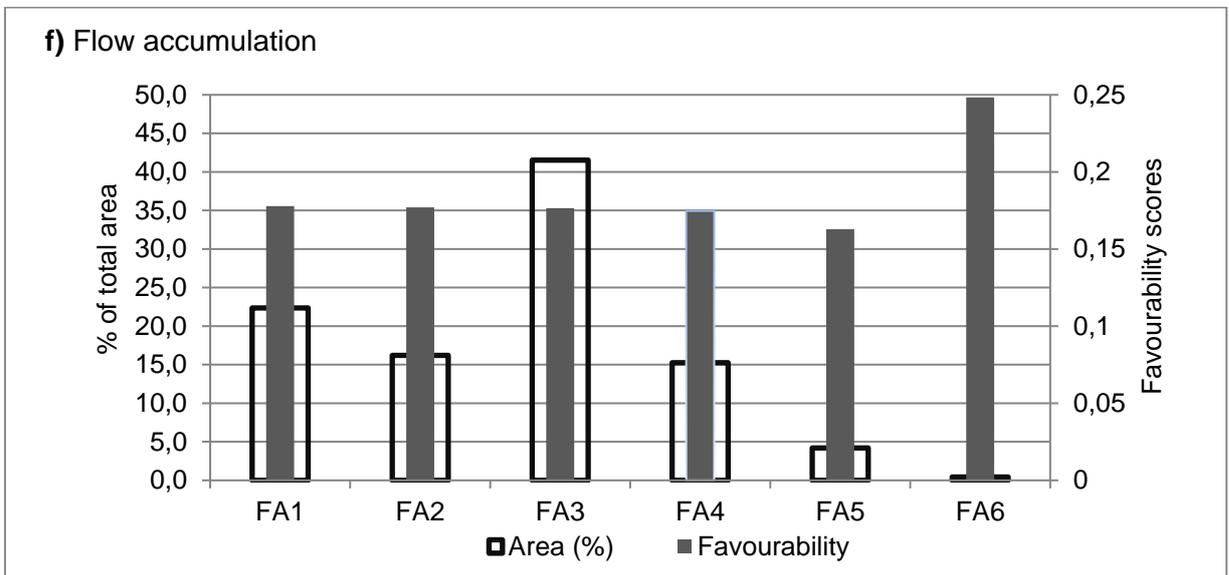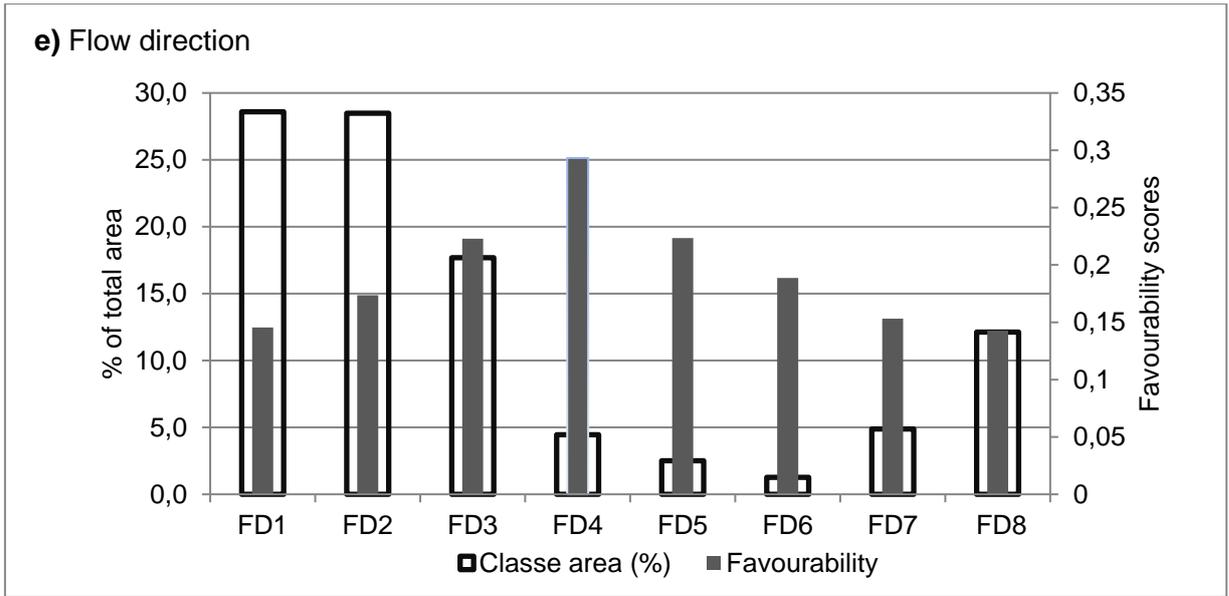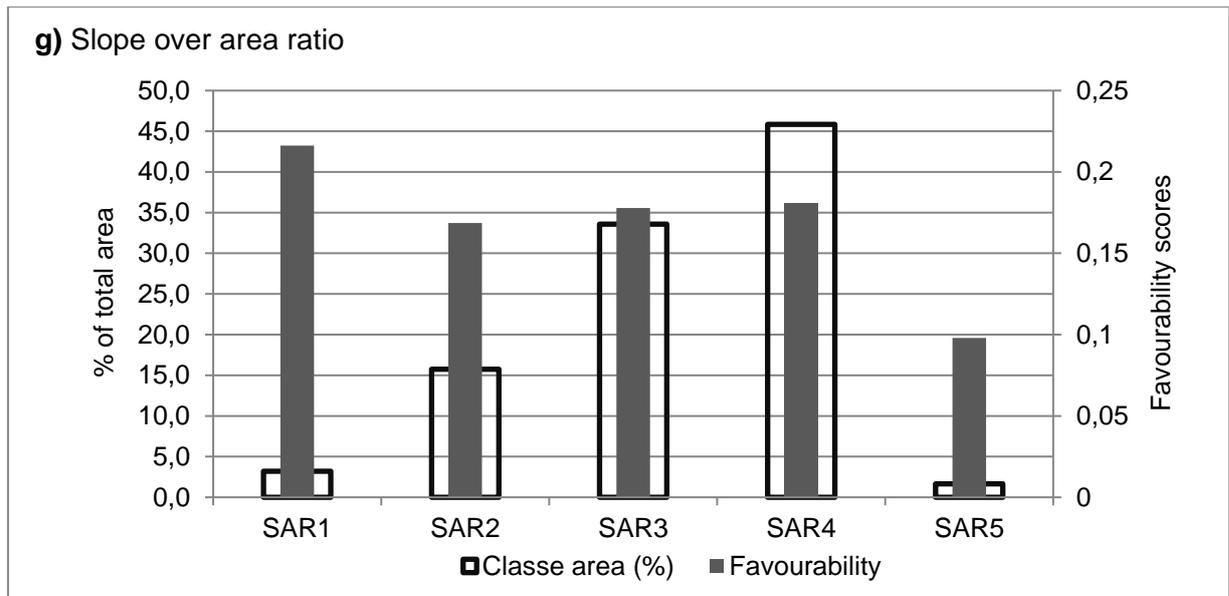
Figure 6.11 – Favourability and thematic layer class frequency of predisposing factors in Model 1, which uses the total area of MTDs; a) Elevation, b) Slope gradient, c) Profile curvature, d) Plan curvature, e) Flow direction, f) Flow accumulation and g) Slope over area ratio.

6.4.1.2. Model 2

Model 2 was prepared using 1/3 of the total length of the interpreted MTDs. The area covered by the MTDs reaches a total of 30.2 km^2 in Model 2 i.e., it was significantly reduced when compared to the total area. Using this smaller value constrains the modelling so that is closer to the rupture area of the MTDs (Chapter 3 for complete explanation). This way, the maximum and minimum favourability scores are better resolved, pointing out the areas where the MTDs were first triggered and their rupture zones. When modelling with this smaller inventory partition, some of the classes do not register pixels with MTDs.

The Elevation variable presents favourability scores for only 4 of the 7 classes. The highest score is recorded by class E6 (500-600 m) followed by class E4 (300-400 m), respectively at 0.095 and 0.072 (Figure 6.12a). Instead, the slope gradient variable presented favourability scores for all classes. Class S6 (0.9 % of total area) presents a score of 0.071 followed by S5 (1.8% of total area) with 0.071. Class S2 covers 43.3% of the area analysed and has a score of 0.046 (Figure 6.12b).

With regards to profile curvature, classes are uniformly distributed and their favourability is also uniform. However, class PrC3 shows the highest score, reaching a value of 0.047 (Figure

6.12c). For plan curvature, the highest favourability score is 0.046 in association with class PlC1 (Figure 6.12d).

The highest score for flow direction is observed by class FD3 (0.049), followed by FD2 (0.047) and FD8 (0.041). The classes that cover the largest area are FD1 (28.6%) and FD2 (28.5%) (Figure 6.12e). The highest favourability score for flow accumulation is observed at class FA6, the class covering the smallest area, and approaches 0.119. In parallel, class FA3 cover the largest area (41.5%) and has a favourability score of just 0.042 (Figure 6.12f).

The slope over area ratio has three classes with very similar favourability scores (Figure 6.12g). The highest score is recorded by class SAR2 with 0.042, and covers 15.7% of the analyses area. Class SAR4 covers 45.8% of the analysed area and has a favourability score of 0.039.

b) Slope gradient

c) Profile curvature

d) Plan curvature

e) Flow direction

f) Flow accumulation
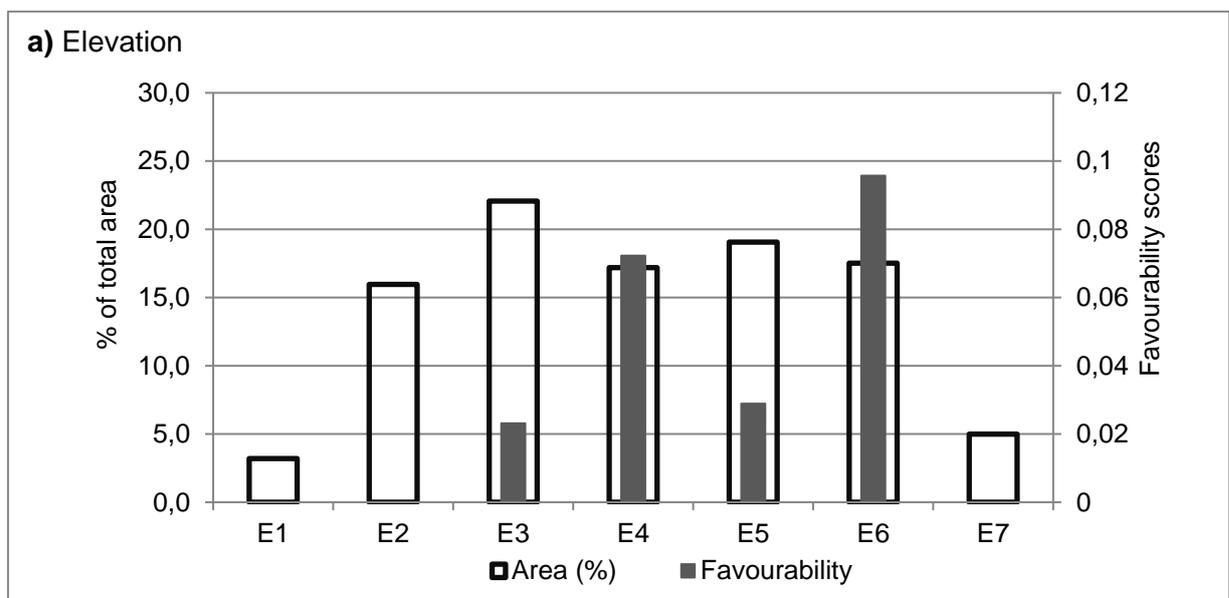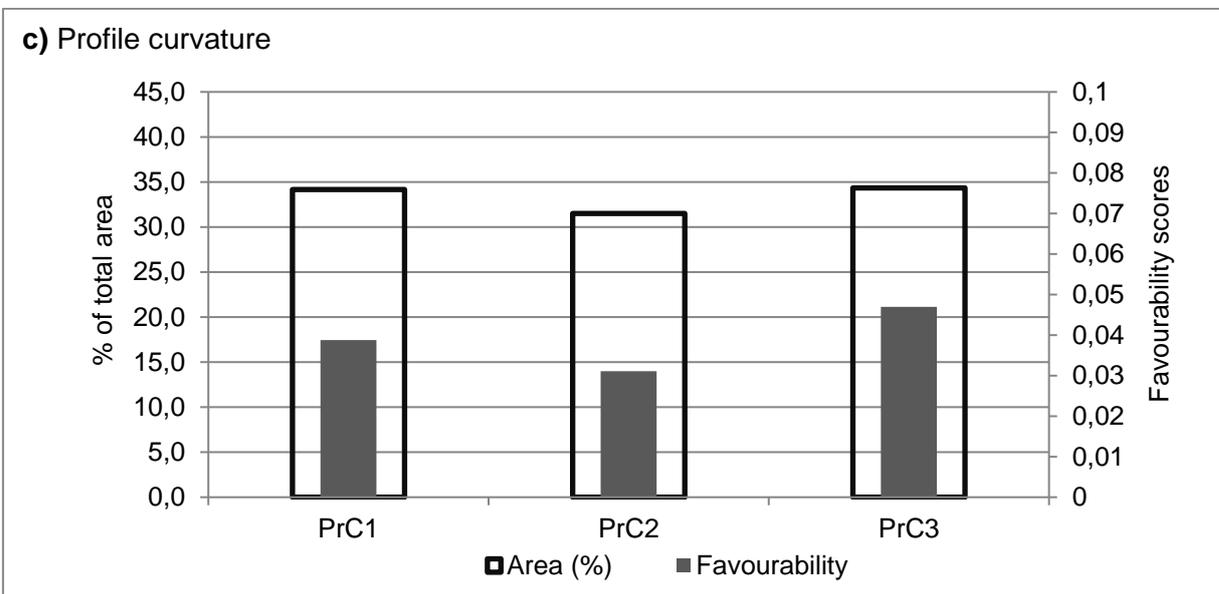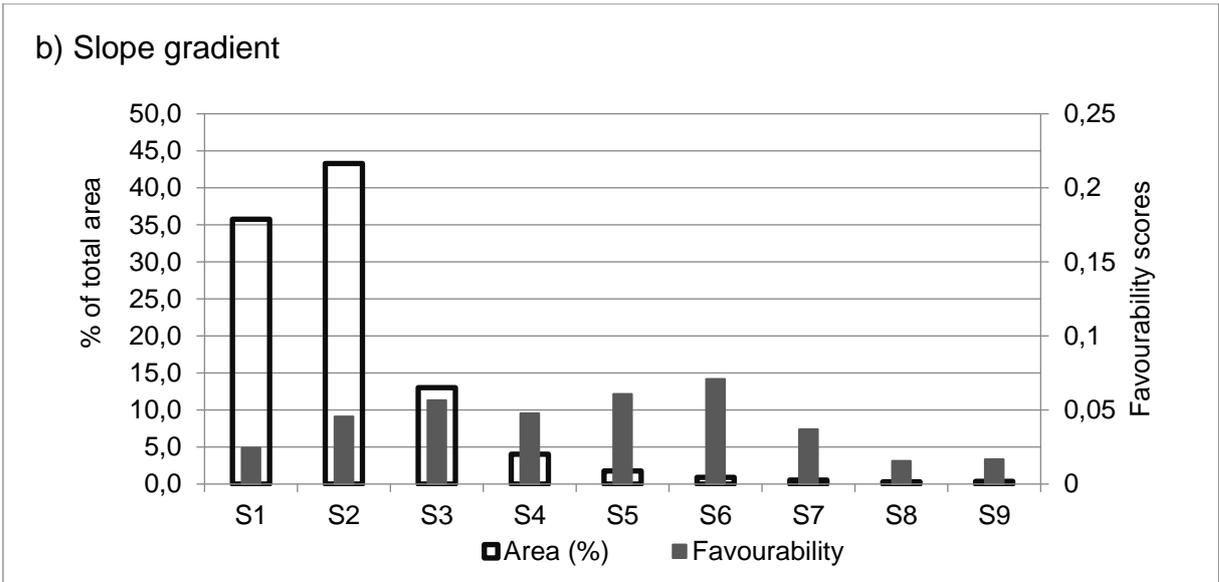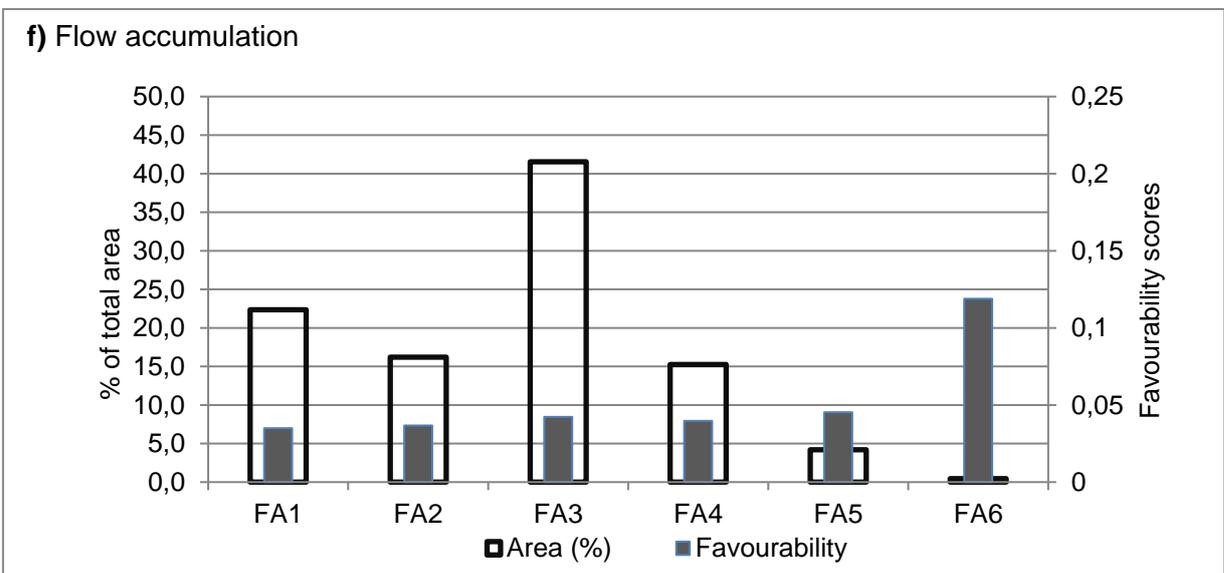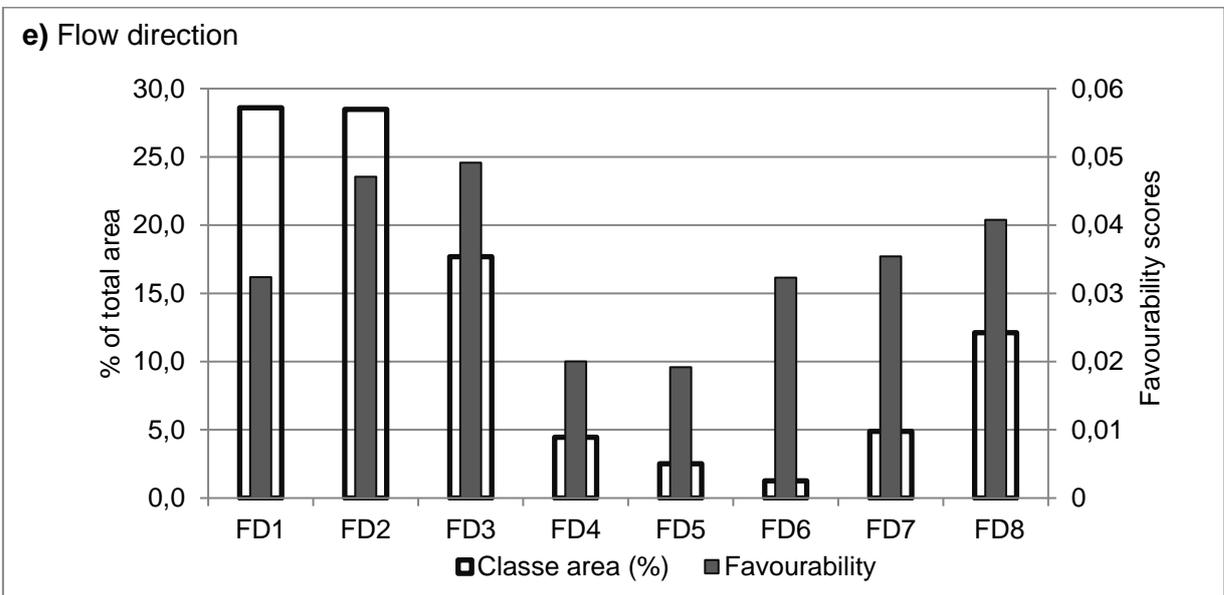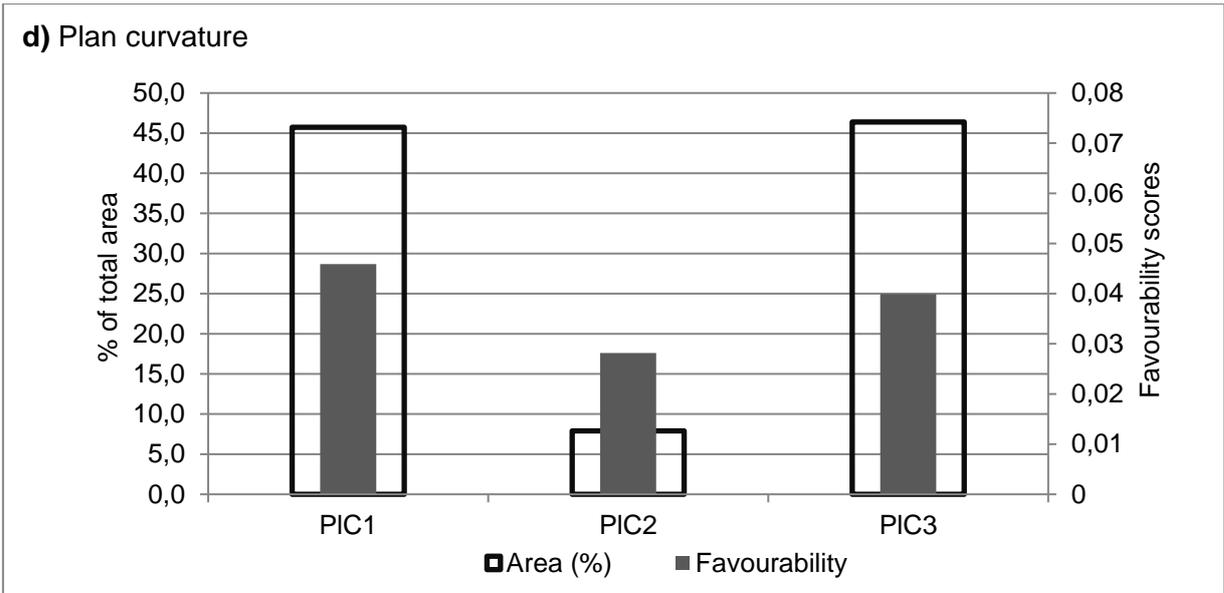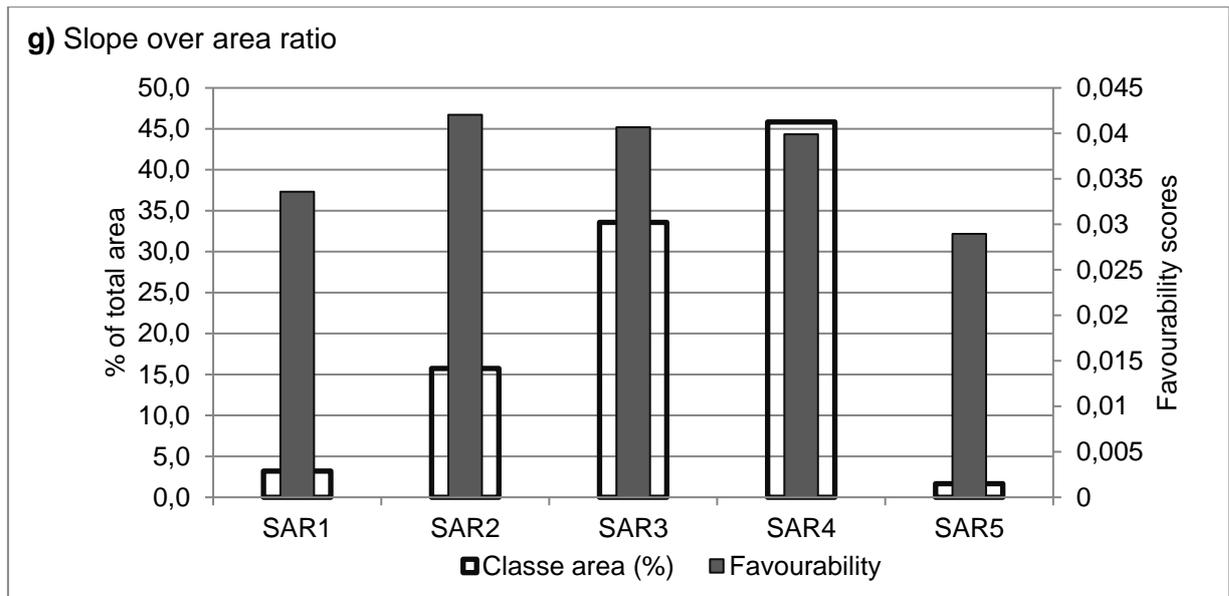
Figure 6.12 - Favourability and thematic layer class frequency of predisposing factors in Model 2, which uses 1/3 of the total area MTDs length; a) elevation, b) slope gradient, c) profile curvature, d) plan curvature, e) flow direction, f) flow accumulation and g) slope over area ratio.

6.4.1.3. Model 3

In order to better constrain the natural predisposing factors for MTDs in the study area, the inventory used in Model 2 was reduced in half to assemble Model 3.

Elevation has no pixels representing MTDs in 4 of the 7 classes (Figure 6.13a). Its highest favourability score is 0.047 in class E6 (5-6°), followed by class E4 with a favourability score of 0.035.

Slope gradient (Figure 6.13b) reveals the highest favourability score in class S6 (0.049). This same class covers only 0.9% of the total area analysed in Model 3. Class S6 is followed by the class S5, which shows a favourability score of 0.038 and covers 1.8% of the total area. The class covering the larger area is the S2 (43.3%) and its favourability score approaches 0.0146.

Similarly to Models 1 and 2, slope curvature shows a higher favourability score for PrC3 (0.090), due to local Profile curvature (Figure 6.13c). In addition, class PlC1 is the most important concerning Planform curvature evidencing the highest favourability score in the study area (0.118) (Figure 6.13d).

The highest favourability score for flow direction is recorded at class FD3 (0.022), which covers 28.5% of the study area (Figure 6.13e). Class FD3 is followed by class FD6 with a favourability score of 0.022 for an area of 1.3%. Again in similarity to Models 1 and 2, Flow accumulation shows a highest favourability (0.04) in the class FA6, which occupies only 0.45% of the total analysed area. Class FA3, comprising a larger area (41.5%), has a favourability score of 0.016 (Figure 6.13f).

The highest favourability score obtained for the Slope over area ratio theme is recorded by class SAR1 (0.023), which covers an area of 3.2%. This is followed by class SAR4 (0.016) which covers 45.8% of the total area (Figure 6.13g).

a) Elevation

b) Slope gradient

c) Profile curvature

d) Plan curvature

e) Flow direction

f) Flow accumulation

g) Slope over area ratio
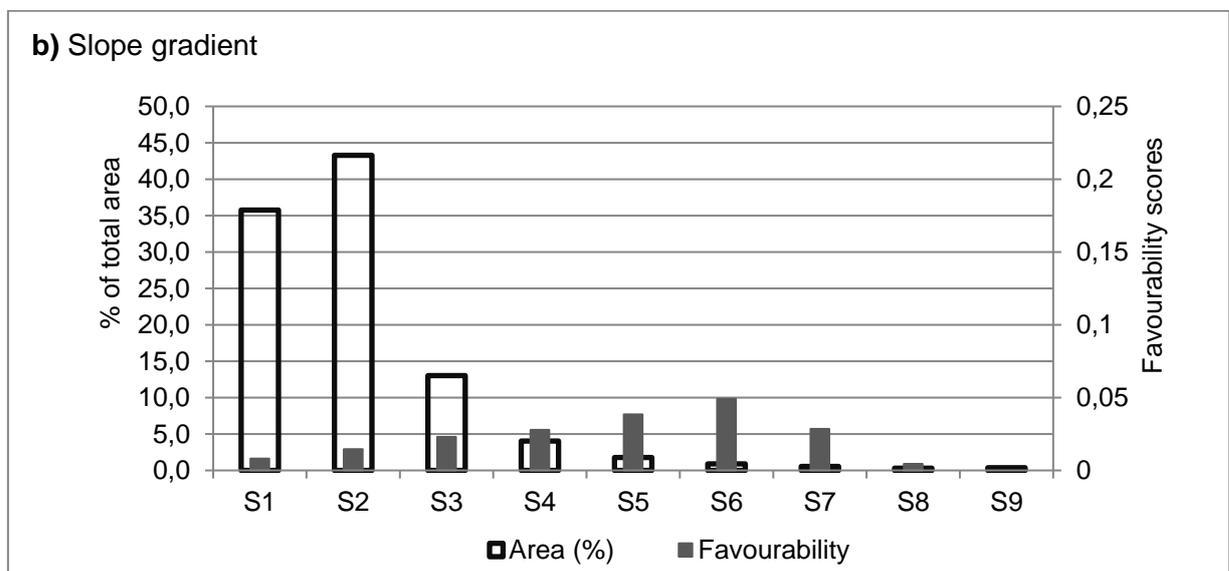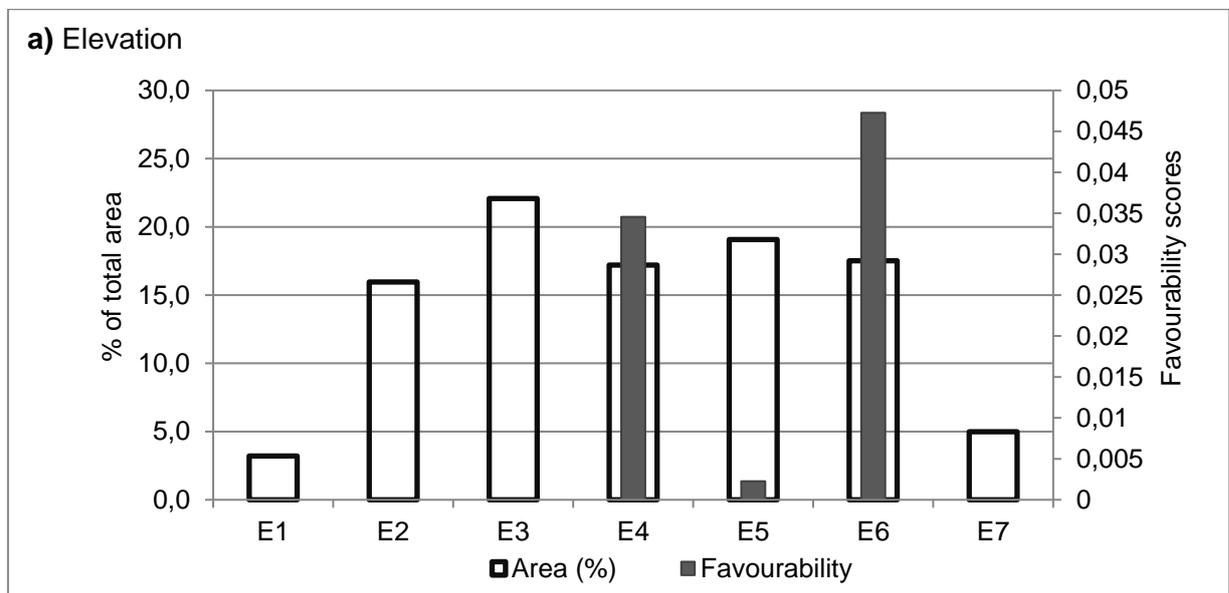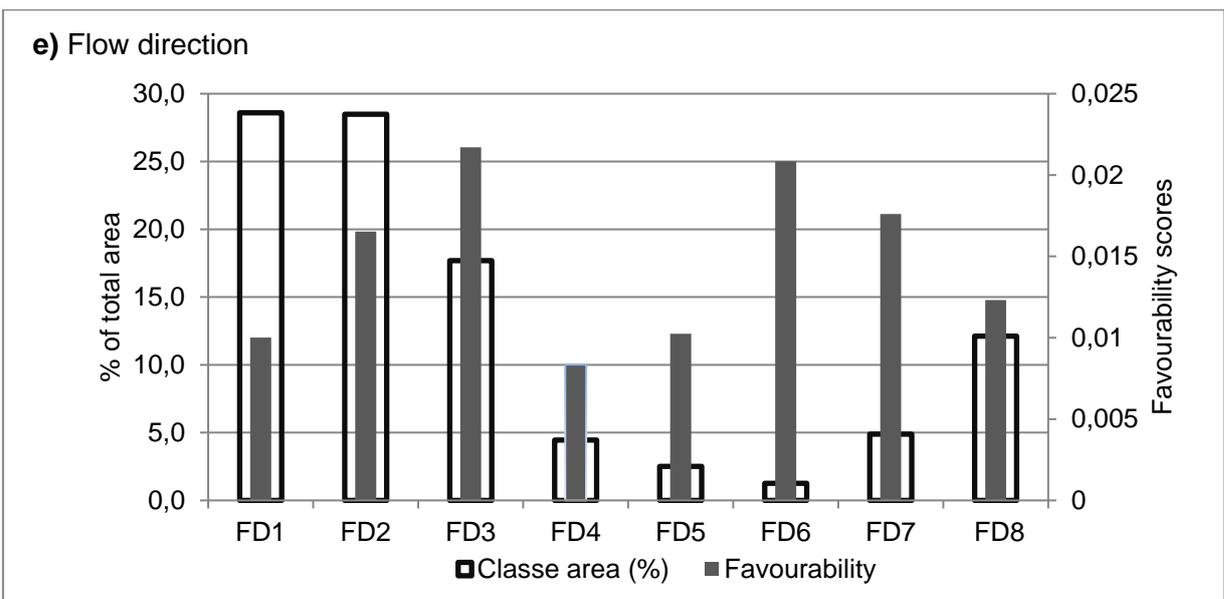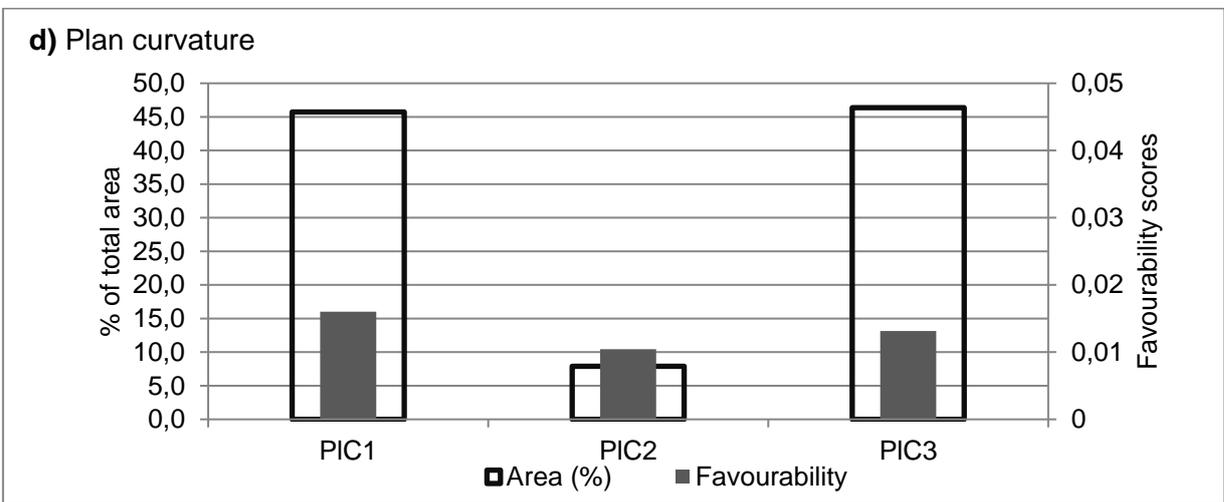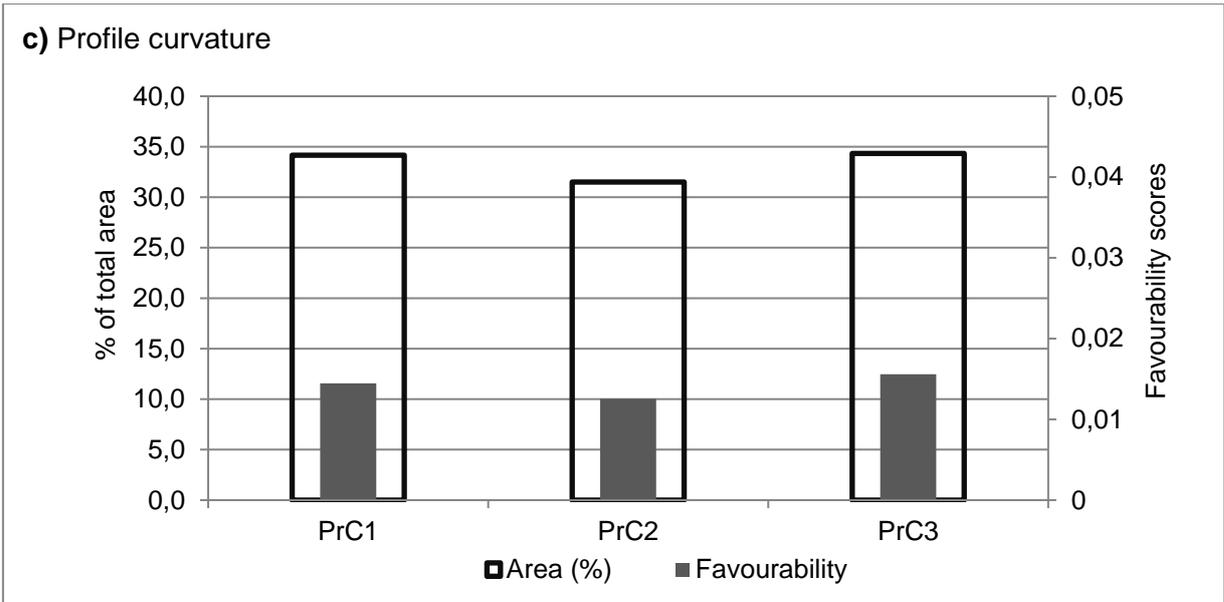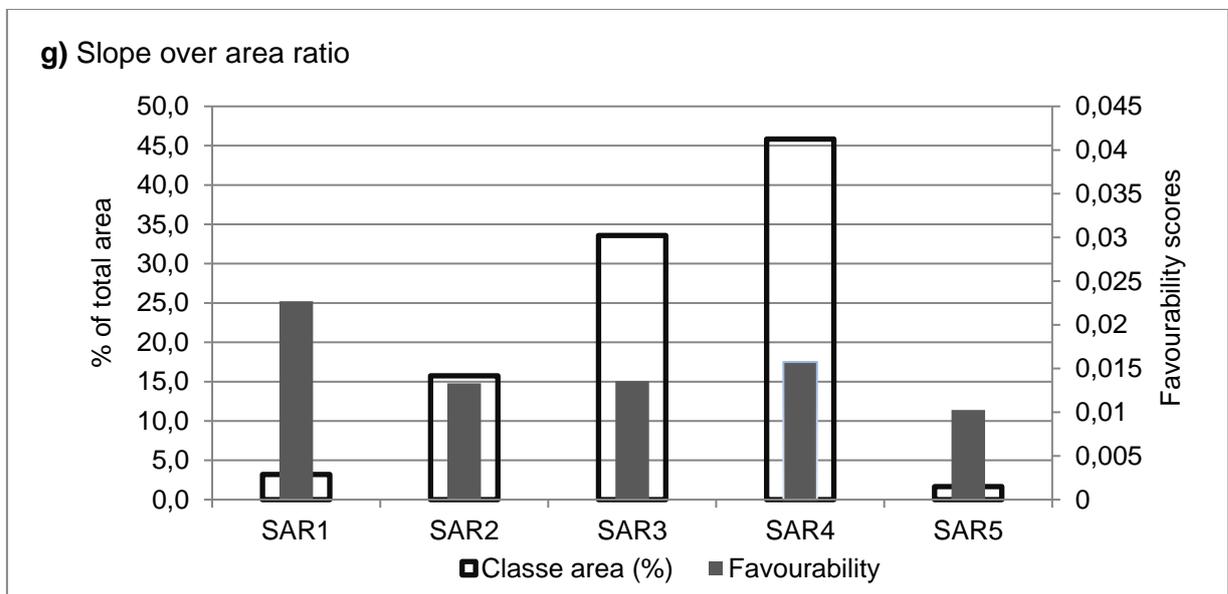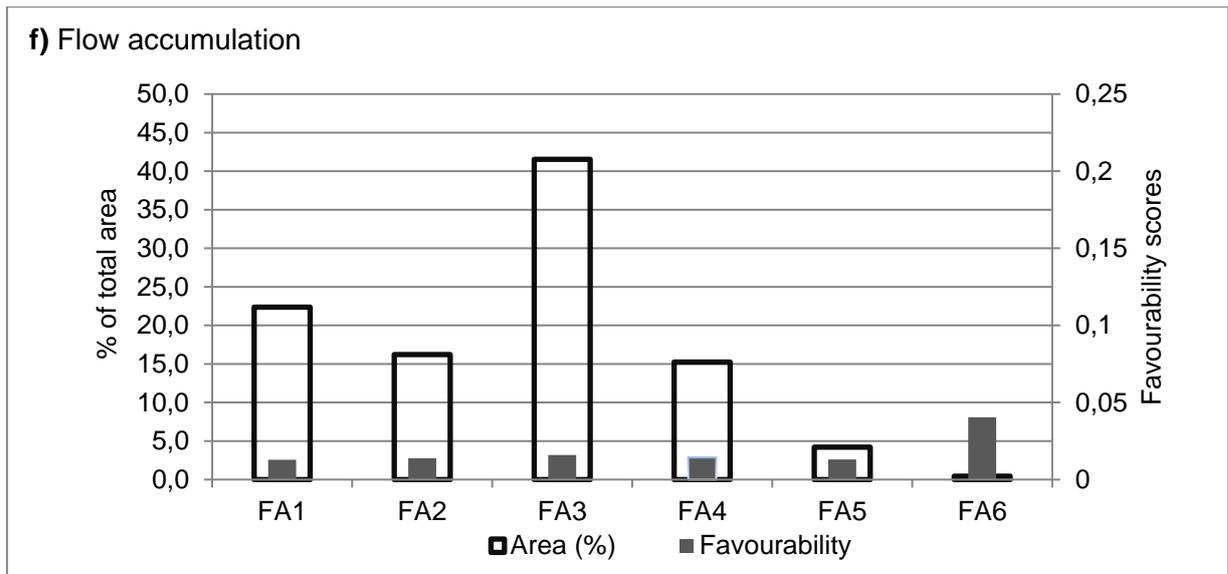
Figure 6.13 - Favourability and thematic layer class frequency of predisposing factors in Model 3, which uses half of 1/3 of the total MTDs length; a) Elevation, b) Slope gradient, c) Profile curvature, d) Plan curvature, e) Flow direction, f) Flow accumulation and g) Slope over area ratio.

6.4.2. **Informative Value Scores (IV)**

Informative Value scores obtained from the three susceptibility models (Models 1 to 3) are summarized in Table 6.4. In bold are highlighted the highest favourability scores for the occurrence of MTDs for each variable. The values in red are classes for which it was not possible to compute IV scores due the absence of MTDs pixels in that classes ($Si = 0$) due its logarithmic transformation (see previous section). To fill this data gap while modeling, the minimum IV score registered in all the variables for each model was given to these areas. This procedure does not interfere in the computation of the models. The classes with higher IV scores i.e., that contribute more for occurrence of MTDs in the study area, differ as a function of the total area considered in the three models performed (Models 1 to 3).

In Model 1 was considered the total length (and area) of MTDs in the study area and, based on the IV scores obtained, it is possible to state that the occurrence of MTDs was conditioned by local conditions. Local conditions of importance include an elevation between 100 – 300 m (namely elevation classes between 100 – 200 m), slope gradients between 1 and 2 degrees, and concave slope areas in both profile and plan curvature. Slopes that are most prone to the occurrence of MTDs are those flowing to SW, and secondarily to S and NW. In this model, the critical flow accumulation for the occurrence of MTDs occurs in the class >1000 and the most MTD prone slope over area ratio of ~0.

Model 2 was performed using 1/3 of the total MTDs length. Favourable conditions for the occurrence of MTDs occurrence change in Model 2 when compared with Model 1, as initially expected. In this case, the ideal conditions for the occurrence of MTDs are elevation ranging from 500 to 600 m and, to a lesser extent, elevation ranging between 300 and 400 m. Slope gradient ranges from 1 to 6 degrees, with the 5-6° class being the most favourable to the occurrence of MTDs. Concave slopes are prone to generate MTD, when considered the profile and plan curvature, as also recorded in Model 1. The critical flow direction is S and SE, although NE-dipping slopes also appear as favourable to the occurrence of MTDs. The flow accumulation most prone to the occurrence of MTDs is >1000 and, to a lesser extent, class

100 – 1000. Regarding slope over area ratio two classes are highlighted in Model 2: 0- 0.00001 and 0.00001 to 0.0001.

Model 3 used only half of the length of the MTDs considered in Model 2, but results show that preferential conditions for the occurrence of MTDs are similar to Model 2. In Model 3, perfect conditions for MTD occurrence are elevation between 500 and 600 m and to a less extent, elevation between 300 and 400 m. Slope gradient plays a major role in Model 2, particularly within the class ranging between 5 and 6°. However, slope gradients between 2 and 5º are also favourable. As with Models 1 and 2, slope curvatures most prone to MTD occurrence are concave and their flow directions are essentially S, NW, N and SE. Flow accumulation class >1000 is the most favourable, while the class 0 is the most favourable regarding the slope over area ratio.

Table 6.4 – Informative Value scores for each class of each variable for the three models proposed.

Variable	Class Code	Informative Value		
		Model 1	**Model 2**	**Model 3**
Elevation	E1	-2.527	-3.393	-1.868
	E2	**0.601**	-3.393	-1.868
	E3	**0.286**	-0.542	-1.868
	E4	-0.495	**0.596**	0.858
	E5	-0.118	-0.326	-1.868
	E6	-0.237	**0.877**	**1.171**
	E7	-2.527	-3.393	-1.868
Slope gradient	S1	-0.094	-0.488	-0.586
	S2	**0.128**	0.136	-0.004
	S3	0.002	**0.352**	**0.453**
	S4	-0.273	**0.182**	**0.643**
	S5	-0.337	**0.424**	**0.966**
	S6	-0.401	**0.577**	**1.209**
	S7	-1.208	-0.075	**0.664**
	S8	-1.929	-0.937	-1.191
	S9	-2.007	-0.869	-1.868
Profile curvature	PrC1	0.035	-0.01	0.015
	PrC2	-0.113	-0.231	-0.127
	PrC3	**0.059**	**0.182**	**0.090**
Plan curvature	PlC1	**0.038**	**0.095**	**0.118**
	PlC2	-0.258	-3.393	-0.376
	PlC3	0.0002	-0.044	-0.081

Flow direction	FD1	-0.192	-0.207	-0.381
	FD2	-0.015	**0.168**	**0.120**
	FD3	**0.234**	**0.211**	**0.393**
	FD4	**0.509**	-0.688	-0.562
	FD5	**0.237**	-0.731	-0.358
	FD6	**0.067**	-0.209	**0.352**
	FD7	-0.141	-0.117	**0.183**
	FD8	-0.219	**0.024**	-0.174
Flow accumulation	FA1	0.008	-0.130	-0.132
	FA2	0.004	-0.080	-0.065
	FA3	0.001	0.060	**0.088**
	FA4	-0.009	-0.004	-0.023
	FA5	-0.080	**0.129**	-0.117
	FA6	**0.342**	**1.094**	**1.014**
Slope over area ratio	SAR1	**0.196**	-0.175	**0.430**
	SAR2	-0.052	**0.049**	-0.103
	SAR3	0.001	**0.016**	-0.085
	SAR4	0.018	-0.003	0.065
	SAR5	-0.596	-0.324	-0.364

6.4.3. **Data integration and predictive maps**

Predictive maps are the final output derived from the integration of all steps previously described. Predictive maps represent the spatial distribution of the susceptibility of continental slopes for the occurrence of MTDs, considering the three models developed. The maps presented are computed based on the seven predisposing factors (variables) previously described: Slope gradient, Elevation, Profile curvature, Platform curvature, Flow direction, Flow accumulation and Slope over area ratio. Thus, Figure 6.14 was computed using the total area of MTDs, as considered in Model 1. Figure 6.15 was computed with inventory used in Model 2. Finally, Figure 6.16 is presented based on the outputs of Model 3. The three models show a non-classified legend, sorted in descending order of favourability values (Figure 6.14, Figure 6.15 and Figure 6.16). From a preliminary visual observation, there are clear differences between the three maps. Nevertheless, one can observe the prominent influence of the same variables - Elevation, Slope gradient, Profile curvature, Flow direction, Flow accumulation and Slope over ratio - in the three models.
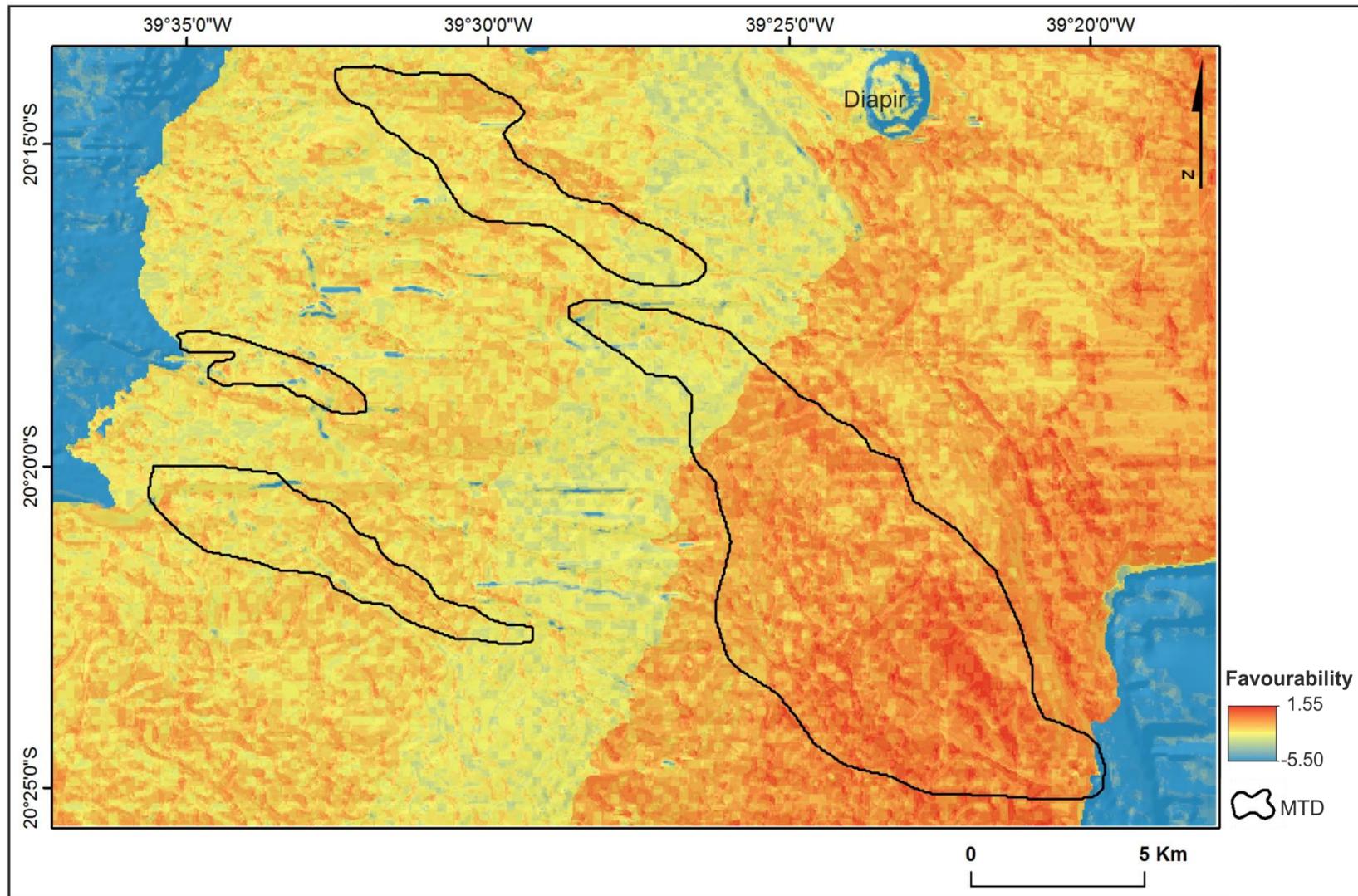
Figure 6.14 – Non-classified MTD predictive map for offshore Espírito Santo (SE Brazil), based on Model 1 (i.e. computed considering the total area of MTDs).
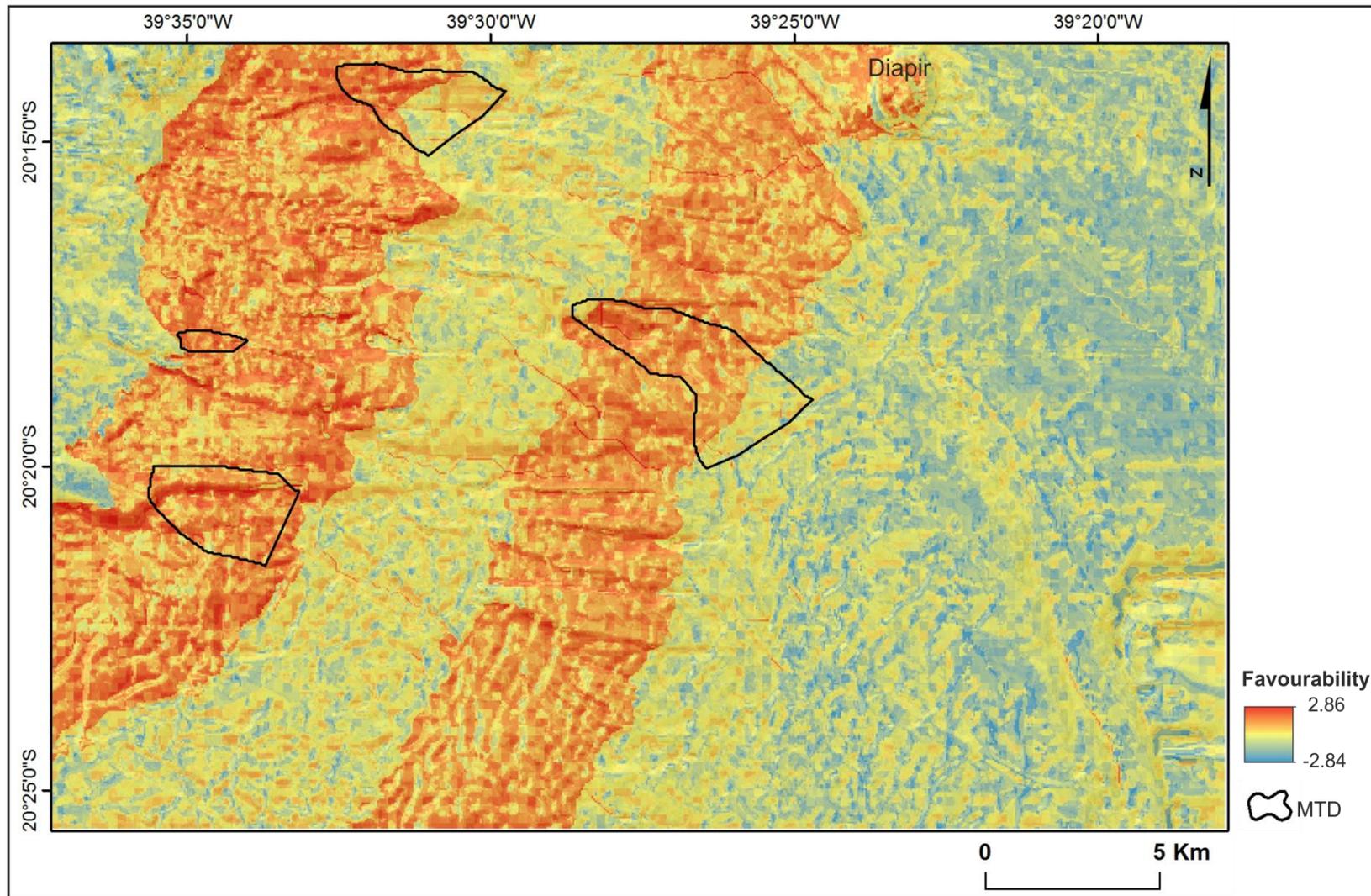
Figure 6.15 - Non-classified MTD predictive map for offshore Espírito Santo (SE Brazil), based on Model 2 (i.e. computed considering 1/3 of total MTDs length).
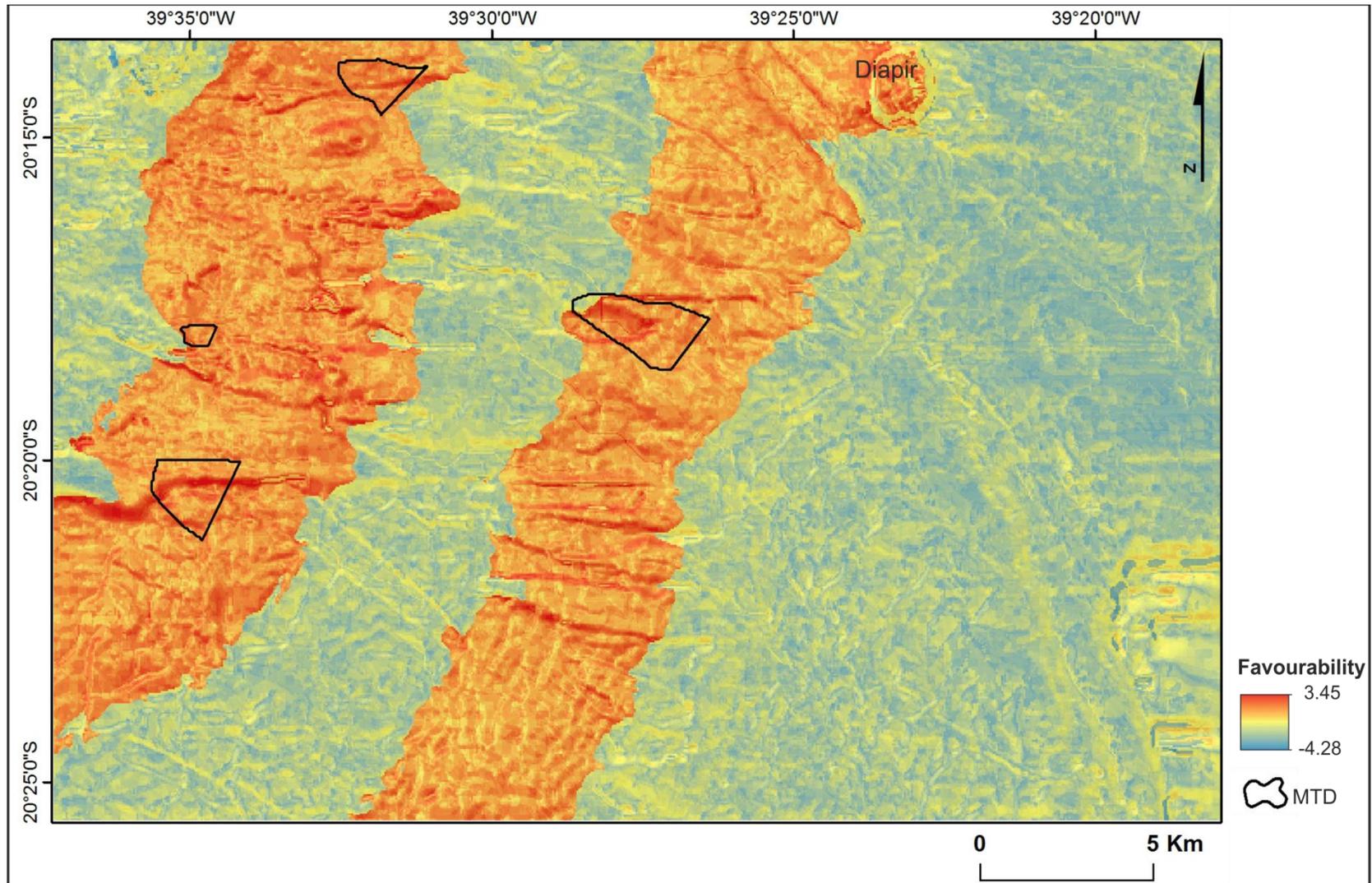
Figure 6.16 - Non-classified MTD predictive map for offshore Espírito Santo (SE Brazil), based on Model 3 MTDs group (computed with half of the area used before).

6.4.4. **Validation – Success-rates**

The AUC values range from 0-1, considering that the quality of the model increases towards a value of 1 Guzzetti (2005). Models showing an AUC of 0.75 are "acceptable", > 0.80 "very good" and >0.90 are considered "excellent".

The success-rate curves for Models 1 to 3 are displayed in Figure 6.17. As previously mentioned, the success-rate measures the goodness of fit assuming that the model is correct for the area analysed. Model 1 (dark blue line in Figure 6.17) was performed using the total area of the mapped MTDs and shows the lower goodness of fit. For Model 1, AUC is 0.657 (66%). In Model 1, 30% of the area classified as most favourable to the occurrence of MTD validates 50% of the MTDs. However, the curve loses gradient in Figure 6.17, to validate all the MTDs it is necessary 90% of the study area.

Regarding Model 2 (light blue line in Figure 6.17), AUC shows the model to perform better in comparison to Model 1. The goodness of fit for Model 2 is 0.747 (75%). Considering 50% of the area classified as most favourable to the occurrence of MTDs, Model 2 is valid for around 85% of the MTDs area. Yet, the totality of the MTD area is only validated when 90% of the study area is reached.

The Model 3 presents the highest goodness of fit, with an AUC of 0.862 (86%). The 30% of the area classified as most favourable to the occurrence of MTDs validates 90% of the MTD area, reaching the 100% with 55% of the total area.

Through the AUC's plots is observed Model 3 obtained the highest performance with 0.862 (Figure 6.17). Considering the classification of Guzzetti (2005), this value plots within the "very good" class. Model 2 obtained 0.747 of AUC, which can be classified as "acceptable", whereas Model 1 recorded an AUC of 0.657, which is below an acceptable class.
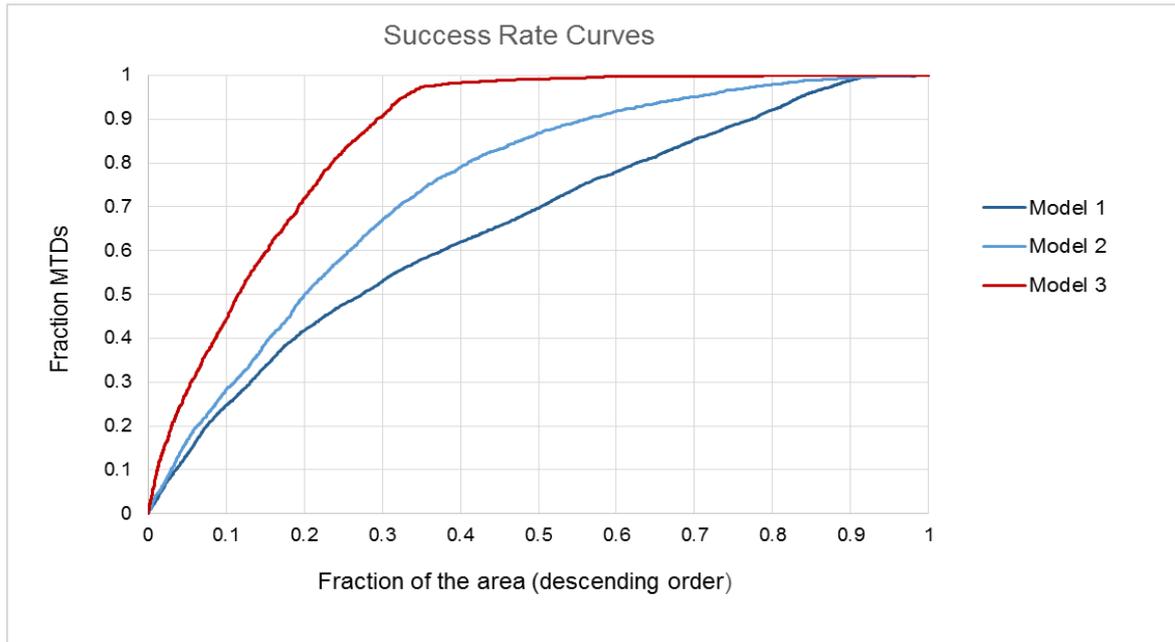
Figure 6.17 – Cumulative frequency diagram showing the cumulative MTDs occurrence (*y* axis) in the study area classified as susceptible in descending order. Success-rate curves of the final models are shown in the figure.

6.4.5. **Sensitivity analysis**

Sensitivity analysis allows us to outline which predisposing factors are key to explaining the spatial distribution of a dependent variable (e.g. the MTD). It assesses the weight of different MTD predisposing factors within a statistically-based model (more detail is given in Chapter 3). Therefore, Model 3 was chosen in this sub-section to run a sensitivity analysis, as it obtained the highest AUC value (0.862) from the three built models.

Table 6.5 – Hierarchy of predisposing factors for MTDs occurrences, according to success rate curves and AUC (Area Under the Curve).

Ranking	Variable	AUC
1	Elevation	0.832
2	Slope gradient	0.616
3	Flow direction	0.584
4	Plan curvature	0.542
5	Flow accumulation	0.537
6	Profile curvature	0.534
7	Slope over area ratio	0.493
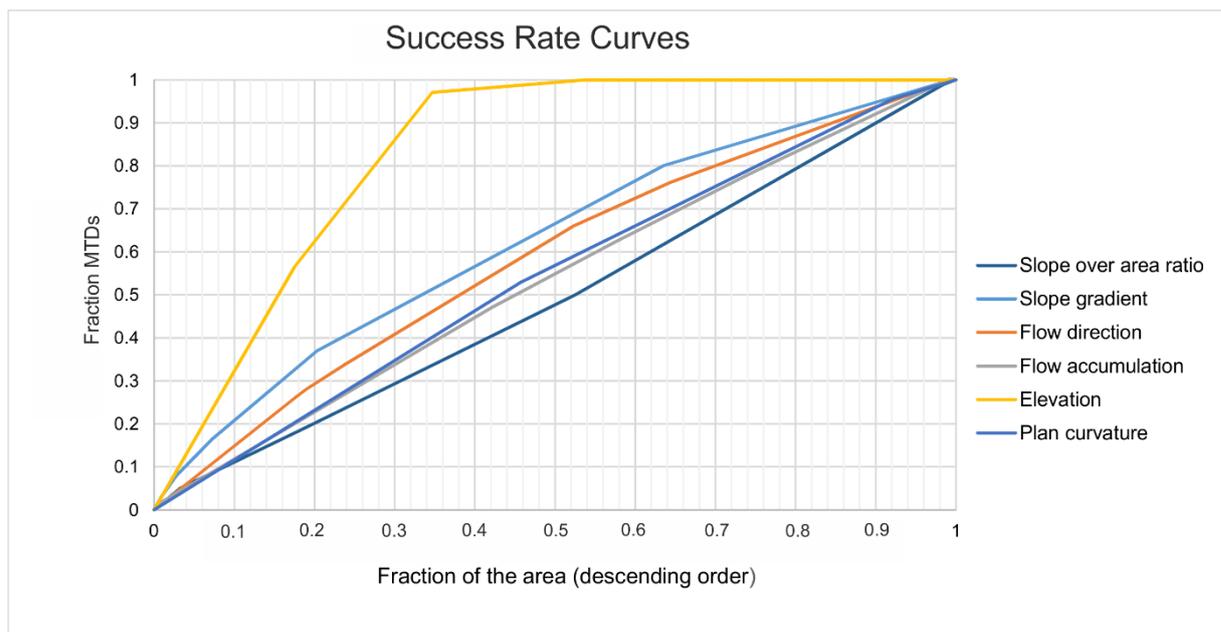
Figure 6.18 – Cumulative frequency diagram showing the success-rate curves of the seven predisposing factors used in the Model 3. The curves are showing how each variable correlates spatially with the MTD.

Table 6.5 shows the hierarchy of predisposing factors with the highest contribution to the occurrence of MTDs in the study area. The hierarchy is selected through the AUC values for success-rate which were ran independently for each predisposing factor. Through these analyses it is observed that elevation is the predisposing factor which most greatly influences Model 3, with 0.832 of AUC. It is followed by slope gradient, showing 0.616 of AUC and the flow direction with 0.584 (Table 6.5). At the bottom of the hierarchy appears slope over area ratio showing an AUC of 0.493.

The results obtained demonstrate that the independent variables considered do not correlate precisely with the distribution of MTDs, as it is demonstrated by the AUC range obtained from 0.493 (Slope over area ratio) to 0.832 (elevation). The ranking expressed in Table 6.5 was therefore used to define the relative importance of MTDs predisposing factors that support the model. Successive models were performed adding one additional variable to the model at each step following the raking previously archived. Results are summarized in Figure 6.19 and Table 6.6.

The quality of MTDs predictive model demonstrates a slight tendency to improve with an increment of variables, as shown by the AUC values on Table 6.6. This is particularly true until the model is run with 4 variables, from which moment a maximum AUC of 0.861 is achieved. After that, the increment of variable does not increase the predictive performance of the Model 3 (Table 6.6). Success curves represented in Figure 6.19 show that all models tend to behave very similar, whereby if we consider 30% of the area classified as most favourable to the occurrence of MTDs, the predicted result are similar in all models with the different set of variables (90%). This behaviour demonstrates the low sensibility of MTDs prediction to the increasing number of MTDs predisposing factors considered
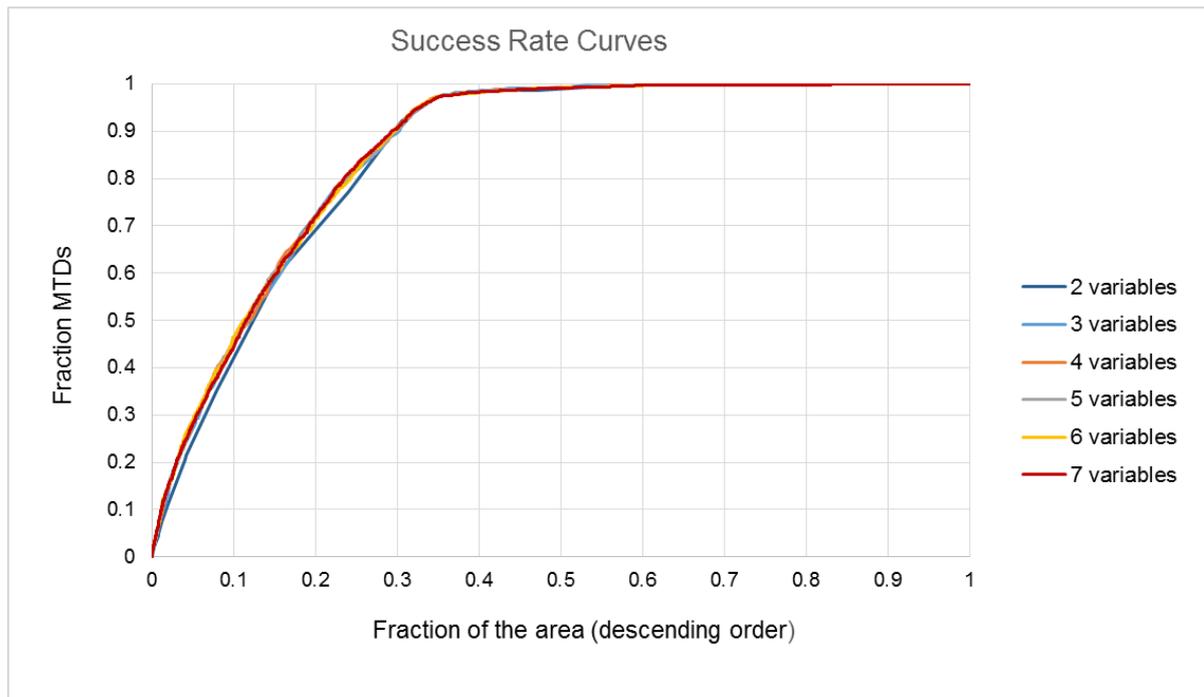
Figure 6.19 – Success rate curves corresponding to MTDs models obtained using 2 to 7 predisposing factors selected according the sensitivity analysis (2 variables = E+S; 3 variables = E+S+FD; 4 variables = E+S+FD+PlC; 5 variables = E+S+FD+PlC+FA; 6 variables = E+S+FD+PlC+FA+PrC; 7 variables= model 3)

Table 6.6 – Area under the curve (AUC) of success rate curves corresponding to the model 3 obtained using from 2 to 7 predisposing factors.

Variable	AUC
2 variables (Variable Id: E+S)	0.8543
3 variables (Variable Id: E+S+FD)	0.8603
4 variables (Variable Id: E+S+FD+PlC)	0.8619
5 variables (Variable Id: E+S+FD+PlC+FA)	0.8619
6 variables (Variable Id: E+S+FD+PlC+FA+PrC)	0.8616
7 variables (Variable Id: E+S+FD+PlC+FA+PrC+SAR)	0.8615

6.5. **Discussion**

6.5.1. **Depositional surface, predisposing factors and modelling**

The rationale for the work presented in this chapter is based on many studies for landslides susceptibility analyses onshore, which is part of the conceptual model of risk (e.g. van Westen et al., 1997, Guzzetti et al., 2006, Thiery et al., 2007, van Westen et al., 2008, Blahut et al., 2010, Guillard and Zezere, 2012, Pereira et al., 2012). Based on the conceptual model of risk, the existence of a topographic surface is crucial as a proxy of the Digital Terrain Model (DTM) from onshore studies, in order to compute a set of derived variables that could be used in GIS for that propose. Whereby, the follow step was to map a depositional surface which can be used to reproduce the topography and can be used as a DTM. This concept was previously applied to marine studies (e.g. Micallef, 2011).

The depositional surface mapped in this work was chosen based on two key aspects, already pointed out in the chapter 5. The first was the necessity of mapping a high-amplitude, regionally significant seismic reflection in the entire study area. Secondly, the possibility of mapping all the different MTD bodies immediately above the interpreted seismic reflection. Using a depositional surface mapped becomes crucial to the analysis in this chapter as it should represent the topography before the instability event occurs; in other words, it should not only reflect the slope instability morphology but the terrain attributes which were present before the occurrence of the MTDs. In onshore studies, a DTM is used to analyse the topographic features that are favourable to instability. In a previous work, Clerici et al. (2010) discussed a better approach for susceptibility studies, pointing out that some factors such slope angle, aspect or curvature may be modified by the occurrence of slope instability events, so the morphology present when the topographic/bathymetric/seismic survey is acquired can be substantially different from the pre-instability conditions. In such a case, some authors suggested and agreed that the factors values should be acquired in undisturbed areas, immediate surrounding the unstable areas (Clerici et al., 2002, Clerici et al., 2010) unless the morphometric parameters in those areas do not relate at all to the reality of pre-failure slope conditions.

In this work, the surface was used as a DTM and was integrated into a GIS software. Seven variables in raster format were computed to archive the predisposing factors that were present and more contributed to the occurrence of MTDs offshore Espírito Santo. The predisposing factors derive from the surface mapped and later integrated into the GIS software. The variables are precisely defined and comprehensively used in onshore studies (e.g. Soeters and Van Westen, 1996, van Westen et al., 1997, Cees J. van Westen, 2008, Zêzere et al., 2009, Piedade et al., 2010, Blahut et al., 2010, Pereira et al., 2012). However, similar offshore studies are scarce and lack terms of comparison between distinct continental slopes. Micallef et al. (2007) pointed out four morphometric maps used in the Storegga Slide using GIS terrain delivery attributes. They were slope gradient, slope aspect, profile curvature and plan curvature, apart from shaded relief. This work went beyond Micallef et al. (2007) to use seven morphometric variables, considered as predisposing factors to the occurrence of MTDs offshore Espírito Santo. The criteria to choose the variables to use into the bivariate is based on the mentioned studies that had proven to be capable to determinate area where the slope movement are more prone to occur. The variables are elevation, slope gradient, planform curvature, profile curvature, flow direction, flow accumulation and slope over area ratio. This work used data exclusively derived from the seismic volume interpreted - local information such as lithology were insufficient to interpolate and create a map containing its spatial distribution, due the insistence of data wells over the study area, which is a pitfall of this study.

The models were computed using three different areas of the same inventory. Clerici et al. (2010) pointed out that this kind of studies can identify the conditions under which the instability events are generated. This way, the favourability analyses have to be restricted to the areas from where the mass movement originated, i.e. the rupture zones. Other authors (Chung and Fabbri, 2005, Guillard and Zezere, 2012) stressed this same limitation, but concluded that modeling the favourability of slopes to the occurrence of mass movements using data from different areas does not affect the final results. To confirm this latter postulate, the model used three different MTD zones obtained from the same inventory. Based on this, the reason to model 3 different areas was to try getting close of what is believed to be the rupture zone and consequently to the area where the movement starts even without knowing exactly how much displacement it can present. The use of the total area (Model 1) is not considered as the most correct approach for most authors because the predisposing

factors are estimated also for the accumulation zone, which is affected by the arrival of depleted material from up-slope source areas. In this case, the conditions present in the accumulation zone are erroneously considered to be prone to sliding (Clerici et al., 2010).

Acknowledging the latter caveat, the data inventory was reduced to 1/3 of the total length in Model 2, getting close to excluding the depletion zones of the interpreted MTDs (Figure 6.1). This improved substantially the quality of Model 2 when compared to Model 1. However, the best performance was achieved by Model 3 by using half of the length of Model 2.

To understand how valid the models compiled in this work are, a validation was performed via the estimation of success-rates and corresponding Area Under the Curve (AUC) values (Fabbri et al., 2002, Zêzere et al., 2008, Vorpahl et al., 2012). The success-rate results obtained are considered very positive. As was expected, modelling using the total area (Model 1) obtained the poorest predictive capacity of 0.657 (66%) for the three models, followed by the model using 1/3 of the total length of MTD (Model 2) which improved success-rates to 0.747 (75%). Success-rates were even better when the study area was reduced to half of the previously length in Model 3, which showed an AUC of 0.862 (86%). The last two models are considered in Guzzetti (2005) classification, as "acceptable" and "very good", respectively. The models performed using an inventory collected with the area believed to be more closest to the rupture zone calculated the best predictive model.

Following the results of Models 1 to 3, it was decided that identifying what predisposing factors have more weight on the occurrence of MTDs offshore Espírito Santo Basin was important. As a result, a sensitivity analysis was undertaken crossing each variable (predisposing factors) individually with the inventory of MTDs used in Model 3 (which obtained the best predictive capacity), and the computation of success-rates and AUCs for each individual variable (Chung and Fabbri, 1999, Zêzere et al., 2008, Blahut et al., 2010, Pereira et al., 2012). The results obtained demonstrate that the independent variables considered do not contribute equally to explain the distribution MTDs in the study area, showing AUCs ranging from 0.493 to 0.832 (Table 6.4). Moreover, according to the AUC records, Elevation and Slope gradient are the variables that better correlate with the spatial occurrence of MTDs, showing AUCs of 0.832 and 0.616, respectively. Elevation is not often used as a predisposing factor; yet some authors have considered elevation as a predisposing

factor valid enough to be included in the models (e.g. Remondo et al., 2003, van Westen et al., 2008). In this analysis, elevation was included on all the modelling sets, and is revealed as the variable with higher prediction performance in Model 3. Slope gradient is generally the variable that most contributes to explaining slope instability (e. g. Remondo et al., 2003, Piedade et al., 2010, Pereira et al., 2012), but its recorded in this work as showing less predictive capacity when compared to Elevation (Table 6.4).

The ranking of variables was performed to understand which variables add more weight to the final model, but also to understand which are the best variable combinations. The capacity of the predictive models does not tend to improve with the increment on the number of variables within the model, as showed by the AUC distribution in Table 6. Thus, the models performed using four variables (Elevation, Slope gradient, Flow direction and Plan curvature) show the highest AUC (0.861). The results mean that the increment of variables in the MTD predictive models do not necessarily generate better success rates.

With this in mind, the results obtained by the validation exercise match the bibliography. The validation exercise in this chapter does not necessarily represent an improvement on the predictive capacity of the models, but success rates and AUC analyses help to discriminate the importance of each variable within the models considered in slope stability assessments undertaken using 3D seismic data.

As last and despite the good result, need to point out that due the small population of MTDs, the models presented in this chapter did not consider separately the different types of MTDs identified in the study area. In onshore studies, different types pf slope movements have been modelled separately based on the assumption that different slope movements are caused by different natural conditions (van Westen et al., 2008, Pereira et al., 2012). As it was identified in chapter 5, this work identified two types of MTDs, which in case of larger populations, need to be modelled separately in order to improve the predictive results.

6.5.2. **Applicability of the methodology to submarine slopes**

Theoretically and practically, the methodology proposed in this chapter has positive results on onshore studies, which has been extensively used and included in land management, urban planning and natural hazards prediction (Carrara et al., 1999, van Westen et al., 2003, Malamud et al., 2004, Pereira et al., 2012). Yet, the applicability of this method to submarine environments cannot simply be taken for granted. To apply statistical methods used on land to submarine environments, some assumptions have to be made when collecting and integrating basic morphological data. This work proposes the acquisition of topographic/morphological information through the mapping of palaeosurfaces represented as high-amplitude seismic reflections on 3D seismic data. The results confirm that the methodology adopted constitutes a valid approach; it nevertheless needs to take into account the resolution of the interpreted seismic volumes. Even when using high resolution seismic, topographic details can be partly lost by incorrect processing techniques and seismic artifacts (Marfurt and Alves, 2015) or simply by seismic vertical and horizontal resolution. The statistical bivariate analysis used in this chapter can be used in the assessment of offshore slopes and it may have better results if applied, for instance, to instability events at the seafloor mapped through bathymetry techniques such multibeam echosounders, sidescan sonars, interferometric sonars, seabed video systems, landers and sediment samples. Which are the sources of data of the most published studies (e.g. McAdoo et al., 2000, Urgeles et al., 2006, Mosher et al., 2010, Rodríguez-Ochoa et al., 2015, Moscardelli and Wood, 2015).

Submarine slopes have been comprehensively studied from multiple points of view. Mass movements have gained the attention of academia and industry, but most studies have focused on the sedimentary processes that result from slope instability, e.g. submarine landslides, MTDs, MTCs, slumps, debrites, etc. (e.g. Frey Martinez et al., 2005, Moscardelli et al., 2006, Moscardelli and Wood, 2008, Gamboa et al., 2010). Amongst these studies, Micallef et al. (2007) proposed the applicability of subaerial quantitative geomorphological techniques to submarine environments, opening an important research field in the direction of the rational and methodology presented in this chapter. It was by taking into consideration the know-how derived from onshore studies, namely knowledge associated with the compilation of predictive models to explained landslides susceptibility, that this work took a step further

by applying it to palaeo-MTDs offshore Espírito Santo, SE Brazil. The main advantage of the methodology presented in this chapter is the possibility of understanding which variables (or predisposing factors) are capable of better predicting the location of future slope instability events.

Geographic information Systems (GIS) are very suitable for indirect landslide hazard assessments, in which all possible terrain factors contributing to slope instability are combined within a landslide inventory map using data integration techniques (van Westen et al., 2003). In addition, Chung and Fabbri (1999) developed statistical procedures under the name of 'predictive modelling', applying favourability functions on individual parameters. Using this statistical methods, terrain units or grid cells can be adjusted to new values representing the degree of probability, certainty, belief or plausibility that the respective terrain units or grid cells may be subject to a particular type of landslide in the future. (van Westen et al., 2006) pointed out a number of drawbacks of this approach. One of these drawbacks is the fact that most methods simplify the factors that condition landslides by using only the variables that can be relatively easily mapped in an area, or derived from a DTM. Another problem also identified in the literature is related to the fact that each instability event (and type) will have its own set of predisposing factors and should be analysed individually. Different typologies need to be modelling separately. In this study, due the restriction of MTDs population (four), the models were computed not taking it into consideration, which can create more uncertainties to the final results. For the same reason, the models were validated through the success-rate (same inventory to model and to validate), which assess the goodness of fit of the MTD to the final model. In case of larger inventory, the predictive-rates that use a different inventory to model run and validation, the result are more accurate in predicting where MTDs will occur in the future, under the same geomorphologic conditions.

The bivariate statistical models, including the Informative Value presented in this thesis, still limited from geomorphological point of view, even when applied to onshore studies. Its expert dependency is very high because its good performance strongly depend from the inventory quality. When applied to offshore the uncertainties are even higher, because it still dependent of the expert knowledge about geomorphologic process but also from seismic resolution and expertise if the interpreter to produce a reliable mass movement inventory, which is crucial to model quality. This fact, is also important because statistical models are very sensitive to

the number of cells (pixels, in this case) that overlap the variables, once again responding to a quality of the inventory, which should have as must movements as possible and separated by typology.

6.6. **Conclusions**

The primary conclusion of this chapter is that the new methodology presented within this study can be positively applied to offshore slope instabilities, as the goodness of fit of the models was favourable. However, detailed observations about the best ways to apply this method need to be point out.

- The technique of mapping a depositional surface from a 3D seismic survey is a valid method and it can be used as topographic database. The horizon needs to be a relatively high-amplitude reflection and should be possible to follow throughout the entire study area.

- The data that can be extracted from a seismic volume have to be carefully considered. Most mapping techniques are unable to extract very detailed morphological features, due the limitations in seismic resolution.

- The bivariate statistic Informative Value (IV) method was revealed to be applicable to submarine environments. It was observed that models responds differently according the type and detail of MTD data provided to the model.

- The three models compiled were assessed via the analysis of success-rates and computing the Area Under the Curve (AUC). The assessment reveals that Model 3, which contains the MTDs area of which is believed to be the closest of the rupture zone, shows a highest AUC of 0.86. According (Guzzetti, 2005), this value can be classified as "Very good".

- The model performed using the set designed by Model 2 revels an AUC of 0.747, which following the classification above mentioned is on the lower threshold considering "acceptable". The model performed using the total MTD area (Model 1) reveals the poorest AUC (0.657). The results fit the expectations that modelling using the entire MTD body does not exactly reflect the predisposing factors at the rupture zone, where MTDs started.

201

- Sensitivity analysis performed to the model which obtained the highest AUC (Model 3), indicate that elevation and slope gradient are the most important variables in MTD initiation.

- Elevation is the variable that most contributes to the explanation of the MTDs in the study area, which is clear by marking the zonation of MTD occurrence in the predictive models (Figure 6.14, Figure 6.15 and Figure 6.16). This unusual result (considering onshore studies) will be under discussion in chapter 7.

DISCUSSION AND CONCLUSIONS

Chapter Seven

7.1. **Discussion**

The preceding chapters in this thesis have presented a new approach to the use of morphometric attributes in a sedimentary basin, the Espírito Santo Basin, using as base information high-resolution 3D seismic data.

In this section, the key scientific results from the three core result chapters (chapter 4, 5 and 6) are summarised and discussed to address the main research hypotheses in this thesis. The core result chapters are structured into two main themes. Chapter 4 addresses the last stage of deformation in areas with important halokinesis, highlighting the most significant structural deformation styles in tectonic raft and overlying stratigraphic units (Figure 7.2). It also describes how raft tectonics and halokinesis shape the seafloor and the Espírito Santo Basin *per se*, mainly through the formation (and reactivation) of faults. Chapters 5 and 6 presented a methodology to use seismic data into Geographic Information Systems (GIS), and later compute morphometric attributes for the analysis of mass-transport deposits (MTD). Chapter 5 identified two different types of MTDs and how local topography and bathymetric barriers can influence their movement and deposition on a Depositional surface. A combination of 3D seismic images, seismic attributes and GIS tools were used in chapter 5. The last data analysis chapter (chapter 6) proposed a new approach, using data acquired in the seismic environment into GIS and data integrated through a bivariate statistical method to obtain favourability scores to spatial occurrence of the MTDs. This step was achieved by using a set of variables related to the topography that were spatially related with location of MTDs.

The general limitations encountered during this project are highlighted, and future work is suggested at the end of this discussion.

7.1.1. **Summary of the results from technical chapters**

After the rationale of this thesis (chapter 1), three data analysis chapters were presented with novel data and analyses. Preceding these, the summarised chapters are introducing the main subjects of the discussion. In Figure 7.1 is presented a cross-session, which contains the actual configuration of the ESB, where the relative location of the interpreted geological bodies in the wider Espírito Santo Basin is highlighted.
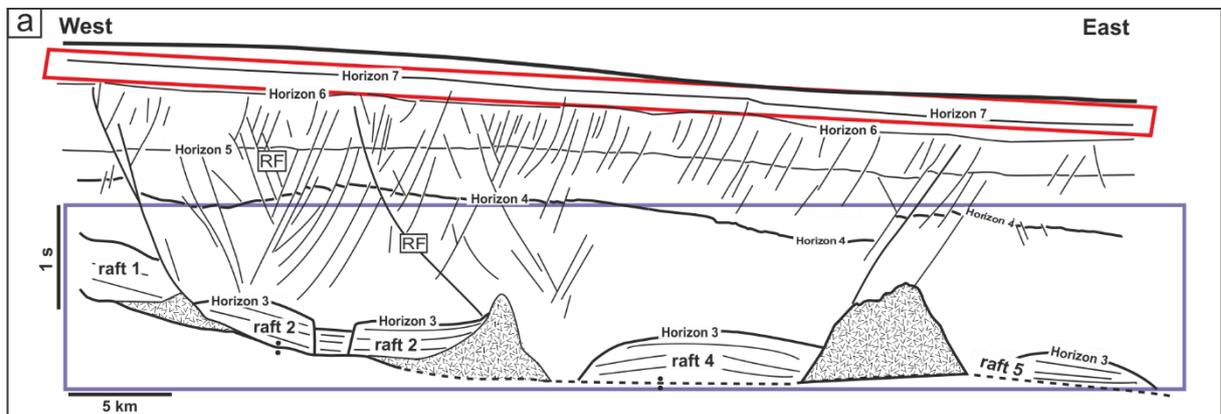
Figure 7.1 – Line cross-session representing the actual configuration of Espírito Santo Basin. The red and purple boxes are indicating where the main chapters of this thesis focus on relative to the cross-session. Purple box: chapter 4 and red box: chapter 5 and 6.

Chapter 4: Structural styles of Albian rafts recording tectonic reactivation and late halokinesis in offshore Espírito Santo Basin

Six rafts tectonics were identified through the mapping of high-amplitude seismic reflections corresponding to the base and top of tectonic rafts in the Espírito Santo Basin (Figure 7.2). The mapping of distinct horizons allowed the acquisition of structural data that was used later in chapter 4 to characterise the gliding and deformation styles of rafts vs. the thickness of post-raft overburden units in the Espírito Santo Basin. Raft tectonics are the last stage of deformation in regions with salt tectonics, and their evolution is usually prolonged in time (Alves, 2012). The extreme deformation observed resulted from prolonged salt withdrawal and fragmentation (and gliding) of tectonic rafts on an oversteepened continental slope. This fact resulted in the movement of rafts and generation of complex sets of faults - which were identified in section in the chapter. In addition, the study area records an important tectonic imbalance between overburden loading and slope gradient due to the multiple Andean tectonic phases that affected SE Brazil from the Cretaceous onwards. As a result, different types of raft deformation were identified in the study area. Stratigraphic units above were also influenced by deformation in underlying rafts. Methodologically, horizon mapping and structural measurements were the most important techniques applied in this chapter, and results show that the Albian rafts were deformed by withdraw of Aptian salt underneath - a phenomenon leading to the rafts' collapse and welding onto pre-salt units. This result is very important and enhanced connectivity between pre-salt and post-salt units. It also shaped the basin and influenced the post-raft overburden in depositional and stratigraphic points of view.

Chapter 4 - Raft tectonics in the Espírito Santo Basin (SE Brazil)

- Identification six raft tectonics in the study area and their styles of deformation.
- Identification different types of faults triggered by salt withdraw and rafts deformation.
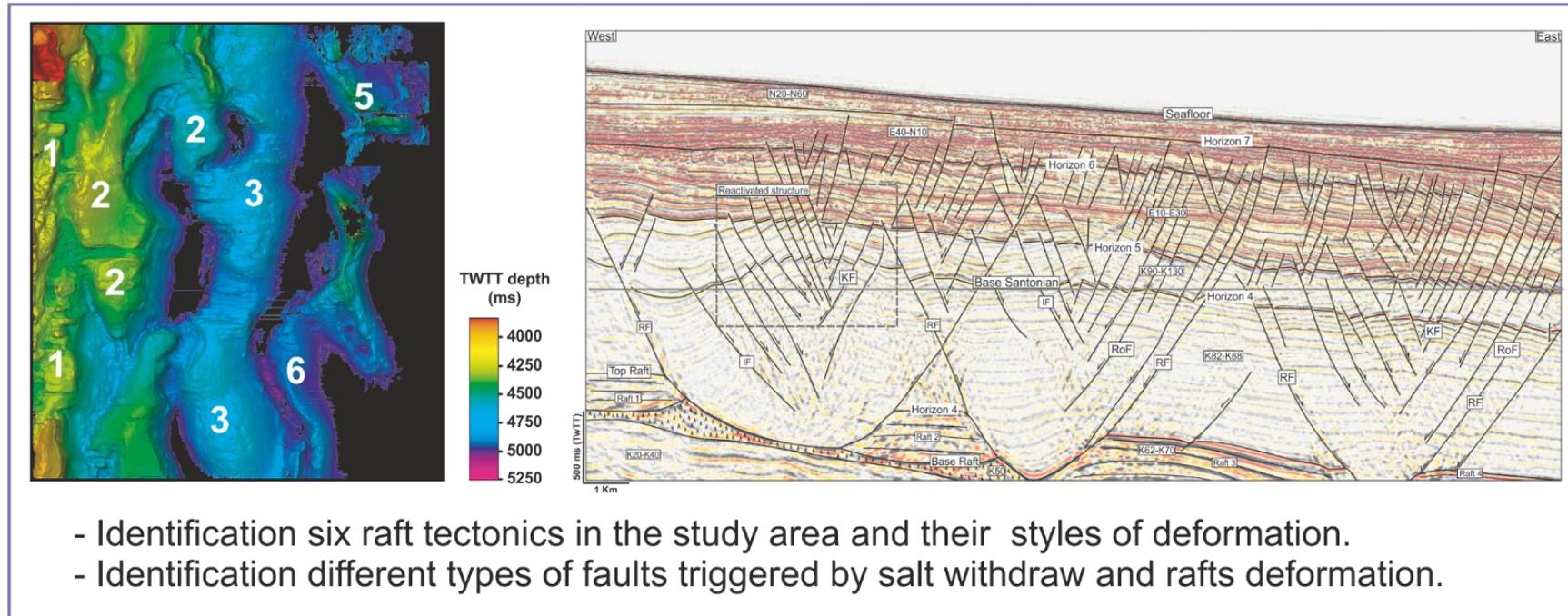
Figure 7.2 - Summary of the main findings and results from the technical chapter 4

Chapter 5: Palaeogeomorphological controls on mass-transport deposits (MTDs) offshore Espírito Santo Basin

Chapter 5 focused on the study of two types of MTDs. These MTDs were similar to submarine slope movements previously discussed in the literature (Frey-Martínez et al., 2006). The two MTDs are distinct in their dimensions, kinematic features and run-out distances on the Espírito Santo continental slope (Figure 7.3). The main contribution of this chapter relates to the identification of two different slope movements, which were markedly controlled by local topography where they occurred. In this thesis, the surface on which the MTDs were settled or reposed was named Depositional surface. The principal methods used in chapter 5 were the mapping of the basal and upper surfaces of interpreted MTDs, and of computation of the Depositional surface in a 3D seismic environment to be later imported into GIS. Both were the basis of the analysis and lead to computation of terrain morphometric attributes on from the Depositional surface as a raster file. The faults identified in the previous chapter were also brought to the discussion and pointed out as an important factor controlling the size and geometry of MTDs in the study area.

Two types of MTDs were identified in chapter 5. MTD A – Confined which show kinematic indicators that suggest topographic barriers confining its shape; and MTD B – Unconfined that appear larger than the previously type, with free translation downslope, without any apparent local topographic barriers.

Chapter 5 - Palaeogeomorphology controls on mass-transport deposits offshore ESB, (SE Brazil)
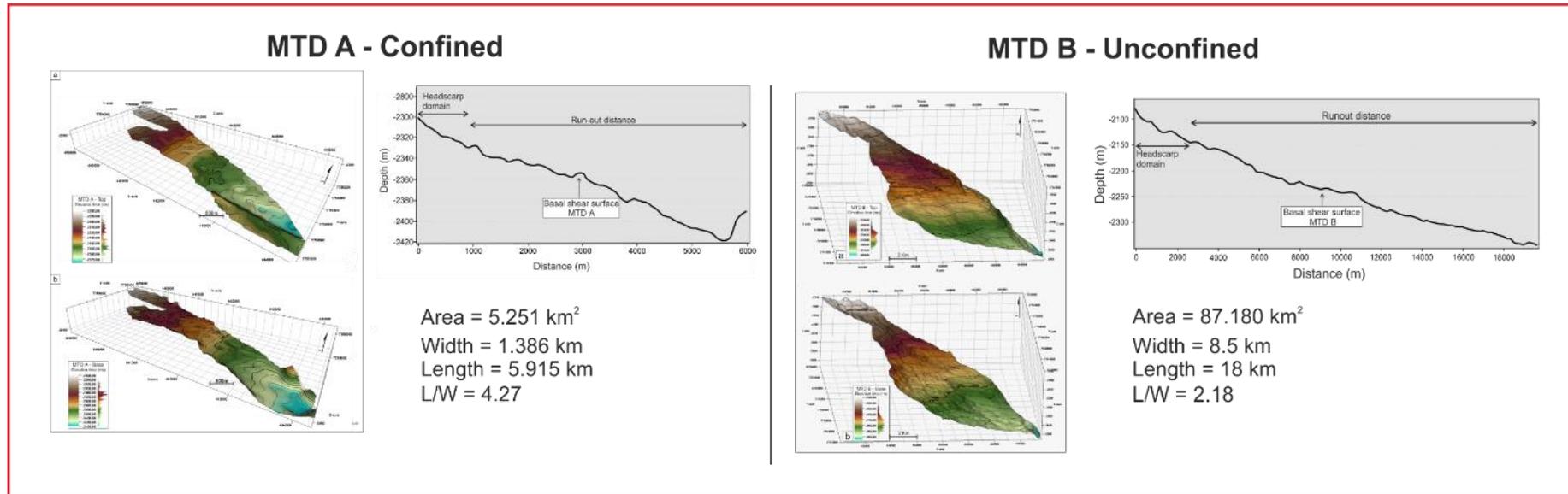
Figure 7.3 - Summary of the main findings and results from chapter 5.

Chapter 6: Favourability scores for the occurrence of mass-transport deposits (MTDs) offshore Espírito Santo

The aim of chapter 6 was to understand the natural conditions that are favourable to the occurrence of MTDs in the study area. Seven predisposing factors were computed from the topographic layer (Depositional surface) derived from chapter 5. Four MTDs were considered to the inventory, including the two types (MTDs A and B) previously identified (Figure 7.4). The spatial integration of the predisposing factors with the inventory was based on a statistics bivariate method (Informative Value), which assumes that the likelihood of and MTD to occur can be measured by a statistical relationship between past events and specified spatial datasets. In order to stress the scientific meaning of this method, the results were validated and the predisposing factors were ranked according to their contribution to explain the MTD spatial distribution, allowing for the computation of a sensitive analysis. The best Area Under the Curve (AUC) was recorded by model 3 (AUC = 0.862).

The top three predisposing factors that most contribute for the occurrence of MTDs in Espírito Santo Basin are elevation, slope gradient and flow direction, independently on the model considered.

Chapter 6 - Favourability scores for mass-transport for the occurrence of deposits occurence

Study area showing the MTDs inventory considered in the models.

Predictive map of Model 3 AUC of 0.86

Sensitive analysis of the 7 variables.
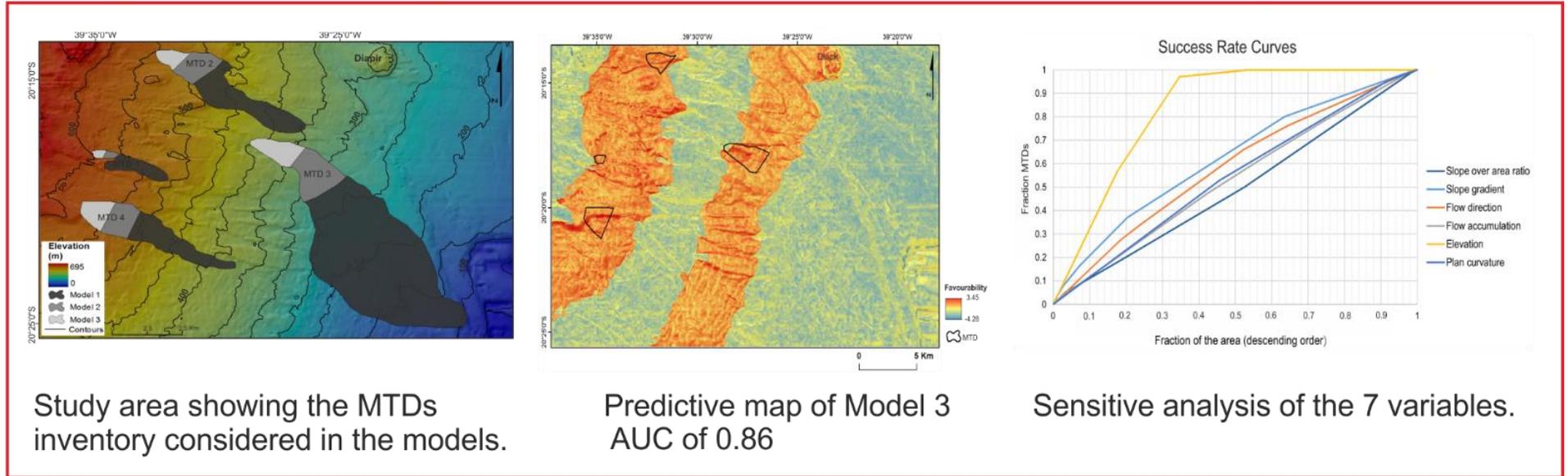
Figure 7.4 - Summary of the main findings and results from the technical chapter 6.

7.2. **Salt and raft tectonics influencing the deformation of overburden strata**

Regardless of the results obtained in chapter 4, the key additional finding in this thesis is that the long-term stratigraphic organisation of the upper slope area was influenced by salt withdrawal and raft tectonics. Both were capable of enhancing local sediment accommodation space, seafloor deformation and faulting. Controls on accommodation and fault patterns have a crucial impact on upper slope deposition patterns, as documented in areas of salt and raft tectonics offshore Angola (Anderson et al., 2000, Rouby et al., 2002, Fort et al., 2004, Olafiranye et al., 2013), Brazil (Demercian et al., 1993, Fiduk et al., 2004, Baudon and Cartwright, 2008, Alves et al., 2009, Alves, 2012, Garcia et al., 2012, Mohriak et al., 2012), Gulf of Mexico (Rowan et al., 1998, Rowan et al., 1999, Rowan et al., 2012, Rowan, 2014, Pilcher et al., 2014) and also in Northwest Europe (Penge et al., 1999).

The evolution of the Espírito Santo Basin was highlighted in chapter 4, which shows that accommodation space for overburden sediment was triggered by the reactivation and consequently salt withdraw and raft deformation.

7.2.1. **Faulting associated with raft tectonics in the Espírito Santo Basin**

Raft tectonics triggered a set of faults, which are documented in chapter 4 and in the literature focusing on the Espírito Santo Basin (Fiduk et al., 2004, Alves et al., 2009, Alves, 2012, Omosanya and Alves, 2014). Fiduk et al. (2004) stated that this additional element had a significant impact in shaping the architecture of the Espírito Santo Basin; in a first stage, due the deposition of Aptian-age salt and its later withdraw into rollers, diapirs and tongues during gravitational failure of the margin, it influenced the deposition of overlying and surrounding strata. At a later stage, due to further salt withdraw and raft deformation, it generated welds between Albian strata and pre-salt sequences. The details of raft deformation and compartmentalisation were presented and discussed in chapter 4. This discussion focus on the importance of deeper (raft-related) structures in controlling slope depositional systems,

and deformation of near-seafloor strata, which is believed to have triggered slope instability across the Espírito Santo Basin .

Faults near the palaeo-seafloor were triggered in discrete episodes throughout the Cenozoic (Omosanya, 2014). They are observed in different horizons, as shown in Figure 7.5. Faults propagated through the post-raft overburden, affecting and shaping it and interacting in slope movements, particularly above or adjacently to rising salt structures and rafts (Omosanya and Alves, 2014). Despite this latter fact, fault growth did not affect directly the MTDs documented in chapters 5 and 6. However, even if faults do not affect direct horizon 7 and MTDs interpreted in the study, they created extensional forced-folds at the base of the MTDs. In some areas, seabed topography beneath the MTD was also significantly changed due to the propagation of faults at depth, leading to local slope oversteepening (Figure 7.5).
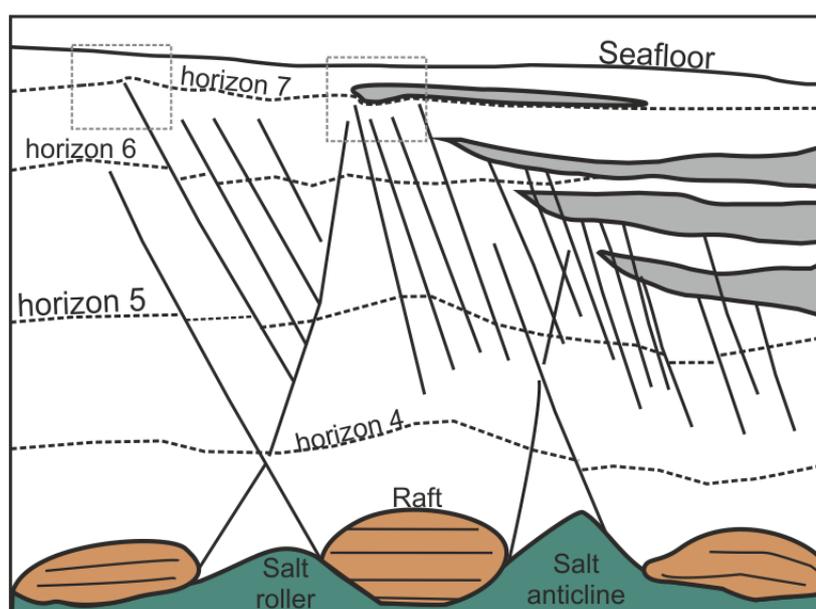
Figure 7.5 – Schematic representation of how the salt and raft tectonics controlled deformation in the post-raft overburden units. The MTDs in focus in this thesis are located right above horizon 7. Dashed lines in grey colour are highlighting the forced-folds created by the growth of underlying faults (modified from Omosanya and Alves, 2014).
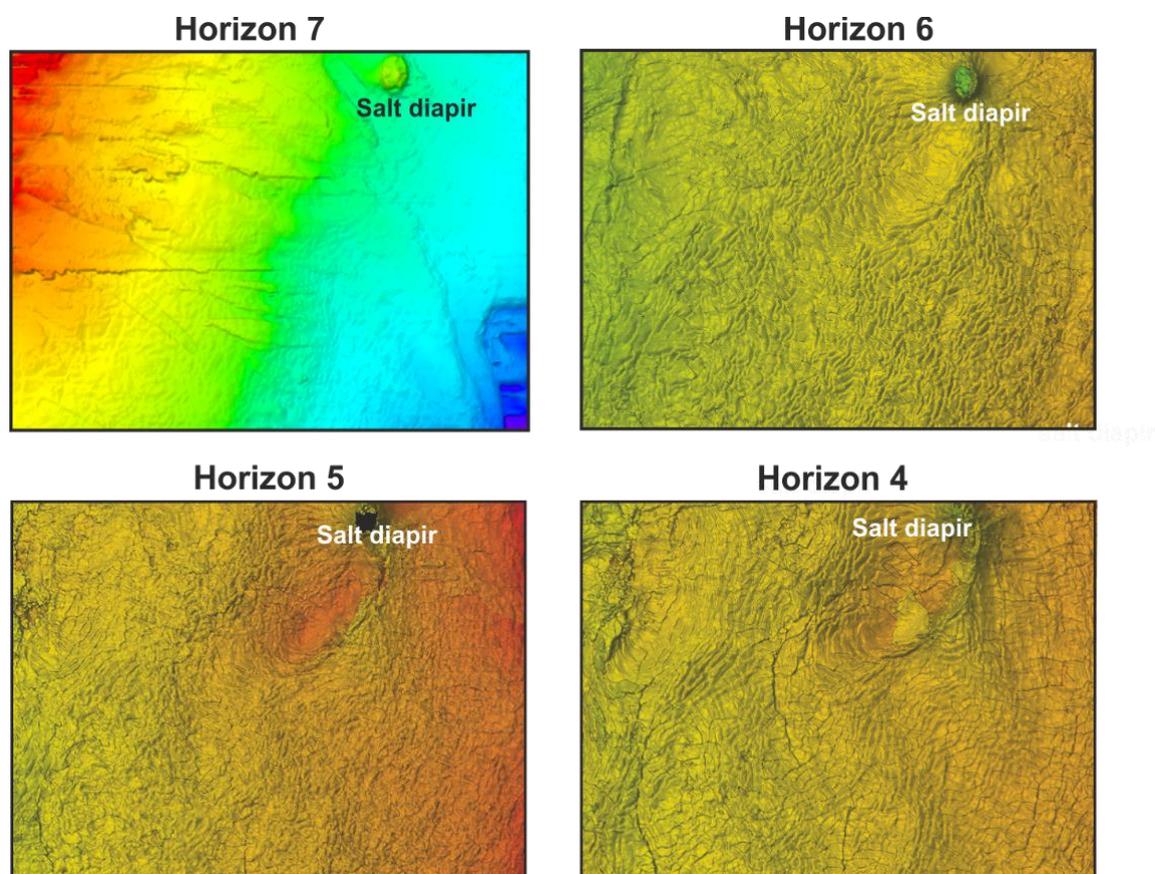
Figure 7.6 – Illustration of horizons above tectonic rafts and how faults rooted in Albian rafts propagated into the Cretaceous and Cenozoic overburden, up to horizon 7. Horizon 7 corresponds to the depositional surface used in chapters 5 and 6.

7.3. **Offshore slope instability**

Chapters 5 and 6 aimed at developing a set of methodologies to improve our understanding about submarine slope instability under a set of natural conditions. The starting point was the previous knowledge of submarine slope instability occurrences in the area, which show different aspects, different stratigraphic ages and are distributed in different areas within the Espírito Santo Basin (Alves, 2010, Gamboa et al., 2010, Omosanya and Alves, 2013a, Omosanya and Alves, 2013b, Omosanya and Alves, 2014). The fact that the Espírito Santo Basin is a well-documented area of slope instability was key to this study, which assumed that existing natural conditions were favourable to their occurrence.

7.3.1. **Three-dimensional (3D) seismic data as source of information to compute morphometric attributes**

A three-dimensional (3D) seismic volume was the main source of data for the new methodologies proposed in this thesis (chapter 2 – Data and Methods). Horizon mapping and their transformation into surfaces constitute a simple but crucial process during seismic interpretation, allowing the use of these same surfaces as a topographic indicator (i.e., a proxy to Digital Terrain Models), after being converted from time-depth (TWTT) to true depth (m).

The seismic volume used in this thesis (BES-100) comprises a high-resolution volume, which means it can be used in geomorphologic studies, not only on the seafloor, but also using mapped horizons of different ages and features, as undertaken in this study. The palaeo-horizon mapped and converted into a surface (depositional surface) turned out to be the most import dataset explored in this thesis.

Initial assessments of slope instability, in a given area, are often attained by documenting geomorphological features that indicate a slope has been affected by catastrophic events in the past (Locat and Lee, 2002). In this thesis, the computation of maps that document slope instability features on the seafloor has been used to document morphometric attributes and characterise multiple features, including slope movements that occurred previously, mostly on the seafloor (McAdoo et al., 2000, Micallef et al., 2007, Micallef, 2011, Haneberg et al., 2015), as well as topographic accidents on the modern or palaeo-seafloor.

215

In other words, the advantages of using a seismic dataset in this thesis included the acquisition of information that usually are only available for seafloor features, in offshore studies, and from Digital Terrain Models (DTM) from onshore studies. The information that was obtained included: i) topographic information from a seismic horizon across a given area on the continental slope, which was converted into raster format to compute morphometric parameters; and ii) an inventory of MTDs after mapping their basal surfaces, their upper surfaces, any kinematic indicators and sizes. These two elements constitute the crucial basis for the methods applied in chapter 5 and 6.

7.3.2. **Favourability scores for the occurrence of MTDs**

The method used to study the spatial distribution of MTDs was the Informative Value, which is based on the concept of favourability function (Chung and Fabbri, 1993, Fabbri et al., 2002). This concept assumes that the likelihood of a mass movement to occur can be measured by statistical relationships between past events and specified spatial data sets. This technique assumes that any slope movement occurs under particular conditions, and can be characterised by a set of spatial sets - the called independent predisposing factors (Zêzere et al., 2004).

The methodology proposed aims to understand which predisposing factors from the considered slope have the major influence on slope failure when specific trigger factors occur along the Espírito Santo Basin. The methodology is based on the assumption that the past is the key to the future.

7.3.3. **Validity of predisposing factors for the occurrence of MTDs**

It is common practice to distinguish between predisposing and trigger factors to understand the occurrence of MTDs (Zêzere et al., 1999, van Westen et al., 2008, Rodríguez-Ochoa et al., 2015). Therefore, a geodatabase containing MTDs predisposing factors was created in this work to allow the quantification of relationships between MTDs and the key geomorphological characteristics of the terrain (Carrara et al., 1982).

Spatial information that better represents topographic and geomorphological characteristics was computed for the entire study area. The predisposing factors that are normally used for

the kind of studies mostly depend on the typology of slope movements and the availability of existing data and resources (van Westen et al., 2008). Nevertheless, the digital representation of the topography is crucial for the models, because it constitutes the base to compute morphometric attributes. In this thesis, the mapped depositional surface was the only source of topographic information and was used as a DTM. The accuracy of the resulting DEM depended on the resolution of the seismic cube (vertical between 15.6 and 19.35 m and horizontal 12.5m, see chapter 3) and on the accuracy of the horizon mapping, which was done every 3 lines (inline and crossline), contributing for a very accurate output information. However, erosion in this same seismic horizon constituted the main problem controlling its accuracy at a local scale.

After obtaining the DTM, all the information was derived from the same elevation layer, following previously studies on onshore slope instability (Remondo et al., 2003, van Westen et al., 2006, van Westen et al., 2008, Thiery et al., 2007, Pereira et al., 2012), and from offshore studies (Micallef et al., 2007, Micallef, 2011, Baeten et al., 2013, Rovere et al., 2014). These studies used the topography of the seafloor as the base of their information. The use of seismic reflections to build a palaeo-topographic map that was used to study palaeo-slope movements is a novel method, where the terrain attributes, as derived from the DTM, are used as proxies for the natural factors present at the time of slope failure. By creating spatial representations of the predisposing factors as predictors for slope instability, the same maps could be (as morphometric attributes) integrated and used to compute favourability scores, resulting in final predictive maps.

7.3.4. **Predictive models for MTDs occurrence in the Espírito Santo Basin**

Favourability scores for the occurrence of MTDs were computed by integrating the data with a bivariate method, the Informative Value (Yan, 1988, Yin and Yan, 1988). In chapter 6, three models were ran to test the hypothesis that the increase of slope movement area used in a prediction model is not directly related to an increase in predictive rates (Blahut et al., 2010, Oliveira et al., 2015). The rationale was that due to their water content, slope movements achieve larger run-out areas in submarine environments than onshore (Blahut et al., 2010).

This means that the rupture zone may be a more accurate parameter for predictive models in submarine environments. This fact has already been tested in onshore analyses (e.g. Oliveira et al., 2015). In other words, the run-out area does not truly express the predisposing conditions responsible for the failure of MTDs in submarine environments.

Based on this rationale, three models were performed: Model 1 (for the MTDs total area) returned an Area Under the Curve (AUC) value of 0.657; Model 2 (for 1/3 of the total length of the MTDs) resulted in an AUC of 0.747; and Model 3 (half of the length of the Model 2) recorded an AUC of 0.862. Model 3 obtained the best predictive rates, which is classified as "good" following Guzzetti (2005) classification. MTD length and the area deemed unstable was reduced for which is believed to be the rupture zone (headscarp domain). Judging from AUC rate, this reduction in scale is proved correct and Model 3 reflects the accurate conditions for the occurrence of MTDs in the Espírito Santo Basin.

In chapter 5 the geomorphological approach led to the identification of the MTDs probable headscarp domain (or rupture zone), by using information from their basal topographic surface (Figure 7.7 and Figure 7.8). It means that by reducing the length, and consequently the area of the inventory, the favourability scores derived from Model 3 are more accurate in taking the natural slope conditions existing when the instabilities occur. It also demonstrates that the same types of slope movements were prone to fail in areas where the same conditions are present, i.e. an elevation between 500 - 600 m and 300 - 400m. Slope gradients also play an important role particularly within the class ranging between 5 and 6°. However, slope gradients between 2 and 5º are also favourable to the occurrence of MTDs. Slope curvatures that are most prone to MTD occurrence are concave and their flow directions are essentially S, SE, NW and N. Flow accumulation classes larger than 1000 are the most favourable, while class 0 is the most favourable regarding the slope over area ratio.
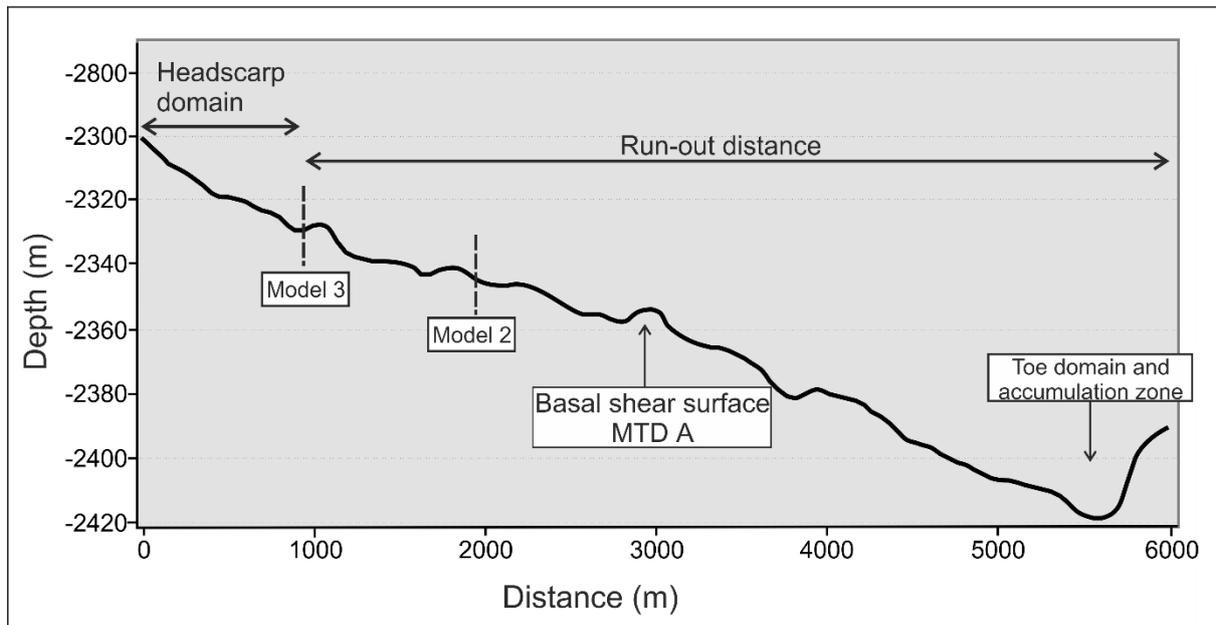
Figure 7.7 – Topographic profile of the basal surface of Confined MTD A, highlighting the length used the three models. Model 1, computed with total area; Model 2, computed with 1/3 of total length and; Model 3, half of the length of the model 2. In the figure is also identified the considered limits of headwall scarp domain and run-out.
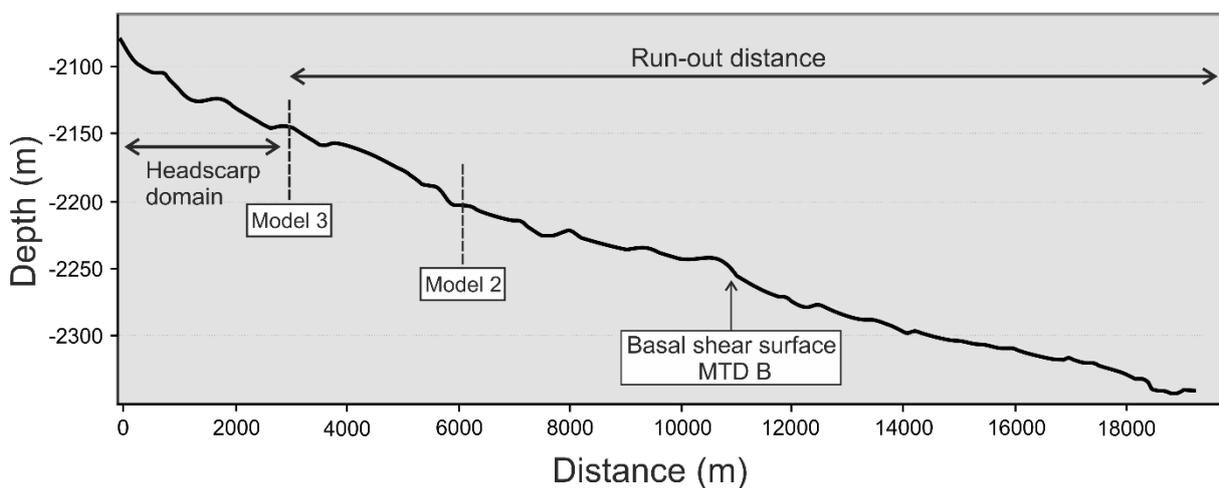
Figure 7.8 - Topographic profile of the basal surface of Unconfined MTD B, identifying the length used the three models. Model 1, computed with total area; Model 2, computed with 1/3 of total length and; Model 3, half of the length of the model 2. In the figure is also identified the considered limits of headwall scarp domain and run-out.

219

An important result of this thesis is that the quality of the prediction models does not automatically increase with an increase in the number of variables assumed as predisposing factors and included into the predictive model. This fact was demonstrated in chapter 6, where an increase in the number of variables did not increase the AUC values for Model 3. The model was applied individually for each variable of each model (Table 7.1) and computed success-rates where used to understand the behaviour and contribution of each variable within each model.

A sensitivity analyses was made to assess the weight of the different variables. They revealed elevation as the greater contributor for the model (0.832 AUC). Model 3 showed the best performance (0.862 AUC) overall, a result that is clearly visible in the predictive maps in chapter 6 showing the spatial distribution of favourability scores. Figure 7.9 shows the predictive map of Model 3, where the spatial distribution of the favourability score is marked by the elevation. The map shows that elevation is the key predisposing factor for the occurrence of MTDs.
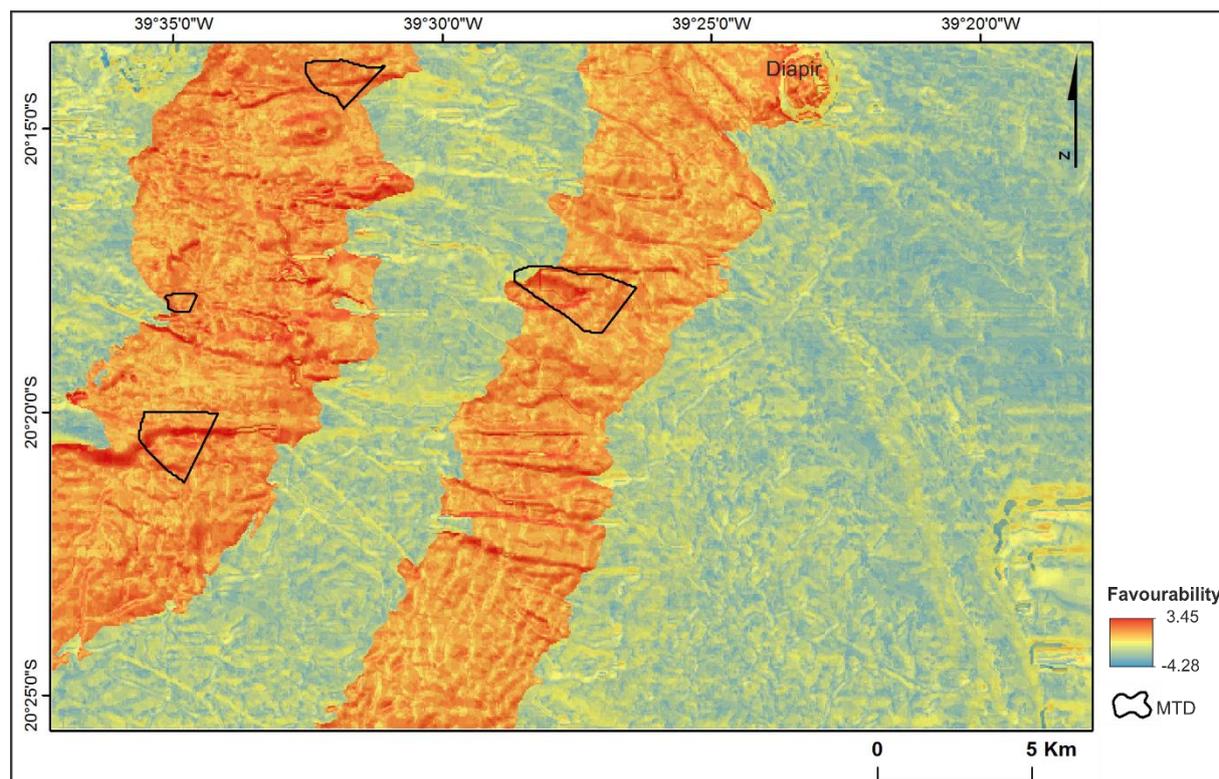
Figure 7.9 – Predictive Model 3 where is visually identifiable that elevation is the variable that most contribute for the computation of the predictive model, by it clear denotation of given highest favourability band on the predictive image.

A similar trend is observed in the other two models, Models 1 and 2 (chapter 6). Elevation is the variable that contributes more for the occurrence of MTDs in Models 1 and 2, and it is clearly independent on the inventory used to run the models. Elevation by itself is not often an important parameter for occurrence of slope movements, or can even seldom be considered in this type of exercise, simply because it can be represented by the input of other variables in the models. The fact that elevation is the variable that most contributes to the models can be related to multiple factors such as local geology - different lithological facies that can be present in different elevations to favour to the occurrence of MTDs, which cannot be proved due to missing detailed lithological data. Salt tectonics is another important phenomenon playing an important role in shaping the Espírito Santo Basin. Overburden accommodation space is responsible by the sediment remobilisation and deposition, which can be more frequent in specific elevation sets due the location of the fault or week sedimentological layers.

221

Another reason that can explain the results obtained for the elevation variable is the influx of sediments coming from the shelf edge, acting as an 'external' force on the slope or constituting a weak layer prone to glide when triggered by an external factor. Hühnerbach and Masson (2004) documented, in the western Canary Islands, that the greatest number of submarine landslide headwalls occurs on the mid-slope, with a peak at 1000 – 1300 m water depth, rather than at the shelf edge or upper slope as one might be expect. The results of predictive models obtained in this thesis for the Espírito Santo Basin are in line with Hühnerbach and Masson (2004) findings - the headscarp of the interpreted MTDs are located roughly at the same depth (Figure 7.9). The last explanation that can be pointed out is related to a marked structural control of the salt and raft tectonics, as mentioned in chapter 4.

In onshore, slope gradient exerts a significant influence on mass movement's distribution. Indeed slope gradient or slope angle has been proved to be the predisposing factor that more contribute to the occurrence of mass movements onshore (Zêzere et al., 2008, Piedade et al., 2010, Pereira et al., 2012, Guillard and Zezere, 2012). In the three models developed in the thesis, Slope gradient is the second variable that contributes more to the predictive models (Table 7.1). Compared to elevation, the AUC of Slope gradient is significantly reduced. Nevertheless, in the literature slope gradient is not the factor considered the most important for the occurrence of MTDs in offshore environments. Masson et al. (2006) refer that the largest submarine landslides occur in areas where specific aspects of the local geology and morphology are placed together to trigger slope failure. Continental slopes on which mass movements occur are typically of low gradients (1° to 5°) and gentle topography (Wilson et al., 2004, Hühnerbach and Masson, 2004, Masson et al., 2006). In the models presented in chapter 6, the slope gradient where most MTDs occur varies between 1° to 6°, and can be considered of low gradient. Model 3 achieved the best goodness of fit (Table 6.4), in which the headwall scarp domain of the MTD has a slope angle of 6°. However, when the others two models are considered the favourability scores for slope gradient are extended to areas of lower slope gradients. This is explained by the fact that the models with larger area and length (Models 1 and 2) are already modelling part of the run-out areas of the MTDs (Model 2) or even the total area of run-out (Model 1).

Flow direction appears in third as a key parameter in the three models. Considering Table 6.6, the flow direction variable increases the predictive capacity of the models (Model 3 in the

Table 6.6.). However, adding more variables to the models does not increase its predictive rate, meaning that the set of variables including elevation, slope gradient and flow direction is the most appropriate to assess the spatial distribution of MTDs in the study area.

The other variables used in the model are showing a very little contribution for the final prediction values. The Figure 7.10a illustrates how this contribution is given. Figure 7.10b shows the variables of Model 3. It still clear that Elevation provides the greater contribution by the curve trend. The slope over ratio does not give any contribution to the model, been the worse variable within Model 3.

Table 7.1 – Area under the curve (AUC) corresponding to each variable in Model 1, Model 2 and Model 3. The scores in bold are the three highest ones for each model.

Variable	Model 1 - AUC	Model 2 - AUC	Model 3 - AUC
Elevation	**0.636**	**0.737**	**0.832**
Slope gradient	**0.537**	**0.584**	**0.616**
Flow direction	**0.555**	**0.559**	**0.584**
Plan curvature	0.514	0.528	0.542
Profile curvature	0.335	0.531	0.534
Flow accumulation	0.504	0.526	0.537
Slope over area ratio	0.512	0.495	0.493
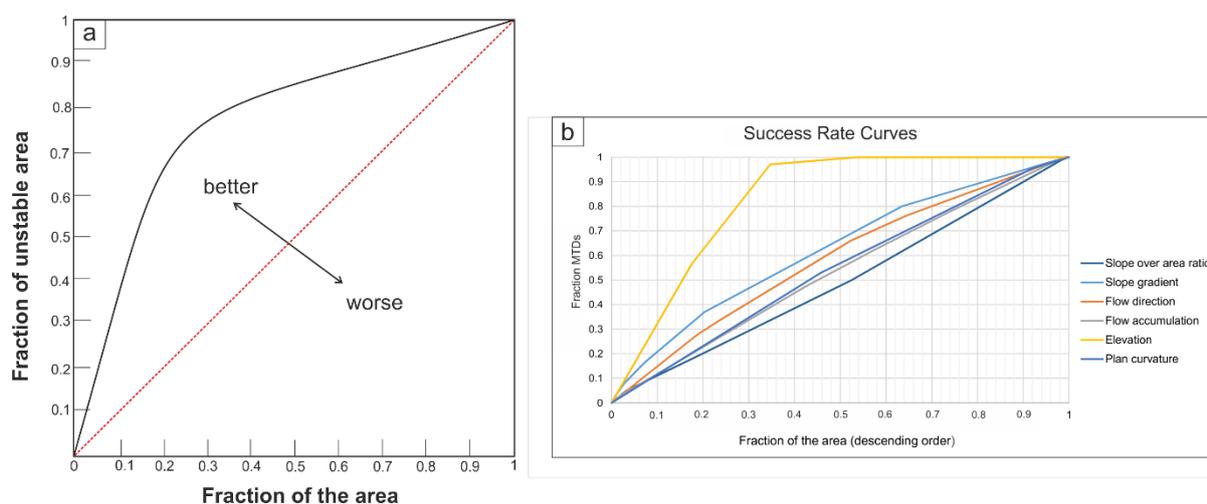
Figure 7.10 – a) conceptual representation of the success curve-rate. The red line represent the AUC of 0.50; b) representation of the success rates obtained for each variable for used to compute Model 3.

7.3.5. **Triggering factors**

Neither chapter 5 or 6 the triggering factors where brought into the analyses of predisposing factors for the occurrence of MTDs. In hazard assessment, there is clear and evident separation between the predisposing factors (the natural conditions of a given area that favours the event occurrence) and the triggering factors, which are actually, the latter factor that initiate the slope movement in a last instance. Nevertheless, even if they were not considered in the models (chapter 6) the literature has pointed out some of the most common triggering factors affecting continental slopes worldwide. Emphasising the importance of local triggers (e.g. Sultan et al., 2004), the most common triggering factors were pointed out in chapter 1and are summarized in Figure 7.11.

The reduction of effective stress and resulting seafloor strength are crucial factors in slope instability (Masson et al, 2012). As described in chapter 1, predisposing factors are the long-term slope natural conditions and the triggering factors are relatively short events that destabilize the submarine slope. Rodríguez-Ochoa et al. (2015) stated that, depending on the environment of the slope, the trigger has little importance if the predisposing factors are ruling the stability of the slope. The trigger is considered an external stimulus that initiates the slope instability process (Sultan et al., 2004).

224

The main challenge for a complete understanding of submarine slope failure is the incorporation of triggering factors into the models of hazard assessment, which was not addressed in this thesis. Firstly, because in a given phenomenon of trigger it is very difficult to find features reflecting past triggers, or even record the trigger events themselves. Even more difficult is to spatially represent the triggers over affected areas, assessing their frequency and intensity.
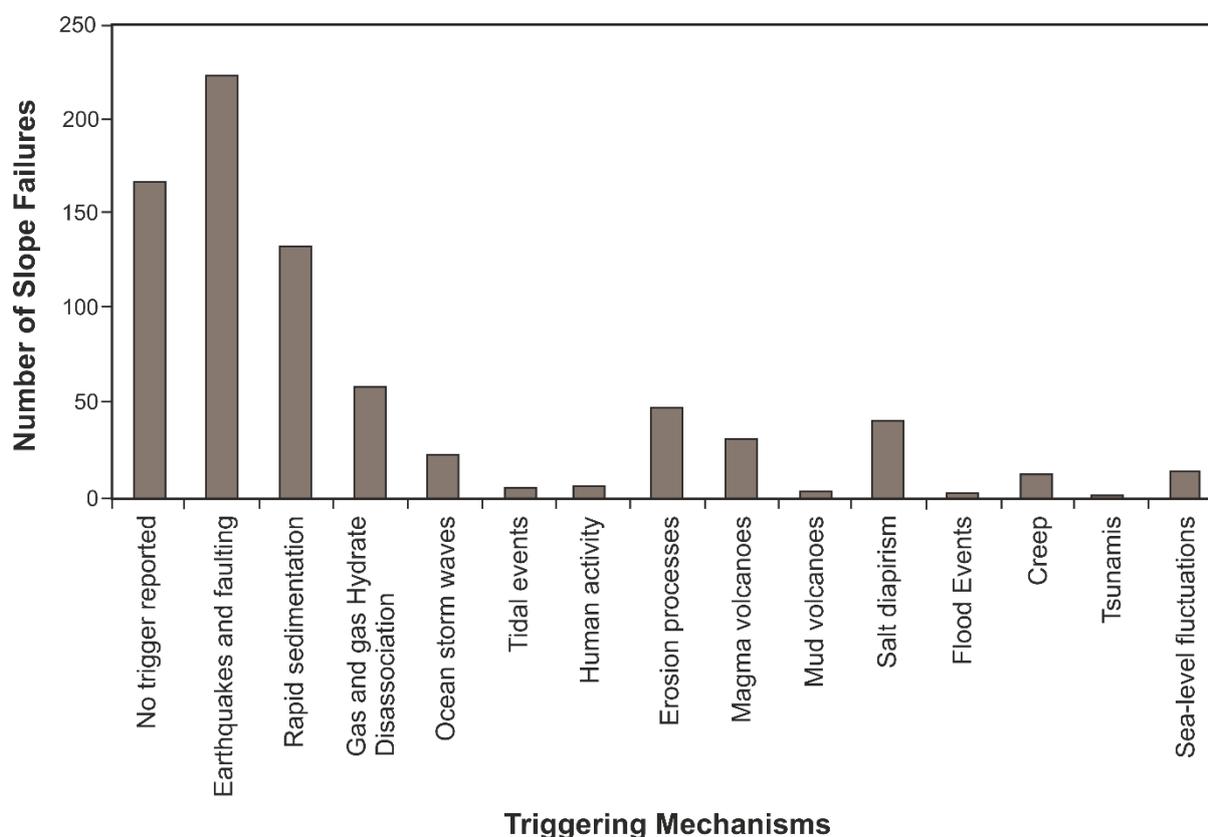
Figure 7.11 – Frequency of slope failures triggering mechanisms on continental margins worldwide based on the literature. See Hance (2003).

7.3.6. **Are future submarine slope events possible to predict?**

The workflow for hazard assessment is very complex even when applied to onshore mass movements. It is particularly challenging to reduce the uncertainties of the vast methodologies that have been used to achieve it (van Westen et al., 2006). Nevertheless, the consideration of offshore hazard assessment has started to take consistent steps, even if started less than a decade ago. There is a wide range of methods and contributions to offshore hazard assessment that have significantly improved risk analyses on submarine slopes (Nadim and Locat, 2005, Nadim, 2006, Hough et al., 2011, Gilbert et al., 2013, Dan et al., Rodríguez-Ochoa et al., 2015, Haneberg et al., 2015). Mostly of these studies were developed due to the necessity of predicting hazards associated to offshore exploration, and were later applied to assess seafloor instabilities.

The main questions raised about submarine hazards are the same as for onshore studies: i) where did the mass movement occur and where will it occur in the future? ii) How frequently will the mass movements occur?; (iii) What are the triggering mechanism(s) of the mass movements? (iv) What is the influence of the present and past mass movements on future instabilities? and (v) Can a previous failure be reactivated? (Locat and Lee, 2002, Nadim, 2006). These questions are transversal to onshore hazard assessments, where even actual knowledge is far from what has been recorded offshore. During the last decade, background knowledge on offshore slope instabilities significantly improved following the development of techniques for submarine data acquisition. Great effort has also been done to improve hazard assessment on submarine slopes. Nadim (2006) pointed out a state-of-the-art methodology to understand submarine slides and identified a long list of applications with the ultimate aim of keeping the focus of research on the development of new techniques and methods. Since then, important steps have been taken, mainly in data acquisition, submarine slope characterisation and slope movement characterisation (e.g. Posamentier and Kolla, 2003, Moscardelli and Wood, 2008, Alves and Cartwright, 2009, Mosher et al., 2010, Vanneste et al., 2014, O'Brien et al., 2015, Moscardelli and Wood, 2015, Pope et al., 2015).

The work presented in this thesis did not intend to complete a hazard assessment for offshore Espírito Brazil (see conceptual model of risk assessment in chapter 1). However, the methodology tested in chapter 6 was successfully applied to offshore environments,

providing an important tool for the practical application of risk assessment workflows. According to this methodology, favourability scores and their respective predictive maps can be used as a susceptibility map in offshore risk analyses. The bivariate statistic Informative Value integrated a set of data, and allowed for the computation of predictive maps. These maps provide *per se* an answer for the first question highlighted above: where did mass movement occur in the past and where will they occur in the next future? The use of an inventory with the precise location of submarine mass movements correlated with reliable topographic information (DTM) can greatly contribute for the improvement of offshore risk assessment. Thus, this thesis proves that statistic methods together with spatial analysis can be applied and used as reliable tools in slope susceptibility analyses, which constitute one of the first steps for the risk assessment workflow.

To provide an answer for the further question the triggering factors for MTDs occurrence need to be incorporate in the models (e.g. Dai et al., 2002, Glade and Crozier, 2005, Cees J. van Westen, 2008, van Westen et al., 2008).

7.4. **Conclusions**

The main conclusion from this thesis are provided below:

Chapter 4 - Structural styles of Albian rafts recording tectonic reactivation and late halokinesis in offshore Espírito Santo Basin, (SE Brazil).

- Six tectonic rafts recorded late deformation in the Espírito Santo Basin. Raft were imaged in 3D and described considering their relationship with the salt layer below and overburden strata above.

- Aptian salt was withdraw below the Albian rafts in parts of the study area. This promoted a series of salt welds between rafts and pre-salt units. Salt accumulated into salt pillows and rollers.

- Raft deformation and compartmentalisation included the following:

- (i) Rolling-over and internal strata growth in rafts that were displaced in the Albian-Cenomanian; (ii) Fragmentation in the form of sub-tabular rafts whenever they were 'passively' translated on the continental slope; (ii) Collapse of rafts' flanks due to salt withdrawal from beneath them; (iv) Tilting and fragmentation of raft on the flanks of growing salt rollers.

- In contrast to previous literature, the post-raft overburden thickness does not show influence on raft deformation.

- Salt withdraw and raft tectonics reactivation/deformation triggered a set of fault families developed above the Aptian salt and Albian rafts (roller, rollover, keystone, reactivated and concentric faults), which affect the post-raft overburden units.

Chapter 5 - Palaeogeomorphology as a control on mass-transport deposits offshore Espírito Santo Basin (SE Brazil).

- Two types of MTDs were identified: Confined (MTD A) and Unconfined (MTD B), within the same stratigraphic package (Sequences N20 to N60 - Early Miocene to Holocene). Their differences are expressed in the form of distinct kinematic indicators and dimensions.

- MTDs morphology and run-out distances in these two examples were controlled by the local geomorphology of the Depositional surface underneath the MTDs. The slope gradient are very low across the entire Depositional surface, nevertheless where kinematic indicators such as headscarp are located, the slope gradient is higher.

- Despite visible differences in the MTDs morphology that were acquired though mapping and GIS techniques, there is some lack of information in this study related to sedimentation and erosion patterns, together with local geology. Detailed geological information is not available for this study as well as seismological data from nearby stations.

Chapter 6: Favourability scores for Mass-Transport deposits (MTD) occurrence, offshore Espírito Santo Basin, (SE Brazil).

- A bivariate statistic method was revealed to be applicable to the study area.

- Using the same MTDs inventory, three models were performed with different MTDs areas. The best predictive model performance was recorded with the reduced inventory (Model 3), which obtained an AUC of 0.862. Elevation appear as the predisposing factor with higher predictive capacity.

- The models were validated using the success-rate (the same inventory was used to model and to validate). Although with good validation results, the success-rate curve was not able to validate the favourability maps as a susceptibility assessment. The AUC measures the goodness of fit assuming the model is correct, based on the comparison the prediction map and the dataset used to build the model.

General conclusions:

- Three-dimensional (3D) seismic reflection data was used as a source of information and imported into Geographic Information Systems (GIS). It proved to be a valid tool to study the morphometric attributes of submarine slope movements and surrounding areas.

- The identification of two types of MTDs, Confined and Unconfined was complemented by the exploitation of extensive literature, which pointed out kinematic indicators that were observed in this study. Nevertheless, to relate their morphology to the local topography is a

valid contribution that needs to be further exploited when studying submarine slope movements.

- The application of statistic bivariate models to return favourability models to slope instability occurrence has proven to be a valid methodology. The predictive maps as outputs constitute an initial step that can be incorporated in risk assessment in offshore environments.

- Despite the good results from this academic exercise, this piece of information must be considered in geohazards analysis and integrated in future drilling plan activities, in order to understand where continental slopes are prone to fail.

7.5. **Data limitations**

Three-dimensional (3D) seismic interpretations can provide information on palaeogeographic settings which were not possible to analyse using another technique, providing palaeogeologic information about the stratigraphic and morphological expression of geologic bodies.

This thesis has benefited from a set of high resolution 3D seismic data, which made possible the methodological application presented in this thesis.

Despite the high quality of the seismic volume, the validity of the seismic attributes and its valid combination with GIS, there is still a large set of uncertainties, due the process of converting the data source suitable to GIS analysis.

The first limitation relates to the absence of well data to calibrate the seismic data and to constrain the geology. For this thesis, well data from ODP Site 516 (located in the Santos Basin) was used and information extrapolated into Espírito Santo Basin. That calibration was done with a high degree of confidence. Nevertheless, in operations related to volume calculation and depth-time to true time, further well data was needed for the study area. Another limitation related to the seismic data was related to the base of the salt and raft were not visible thought out the entire area. This fact, did not allow to full characterise raft 5 and 6 (chapter 4)

Specifically to chapter 5 and 6, the mainly limitations are related to the degree of detail of the seismic data. Even with a high resolution, one should consider that some important geomorphologic details can be beyond the resolution of seismic resolution data. The inexistence of horizontal lithological information was another limitation for the models.

França et al. (2007) presented information about the regional stratigraphy (chapter 2). Nevertheless, information from one well was not enough to create spatial information about lithology in the study area. For that reason, only topographic information was used into the model, which could be computed from the topographic information created from seismic mapping (Depositional surface). The information on accurate lithology and geology needs to be considered in further analyses. Statistic models applied in chapter 6 will certainly gain accuracy if lithological and geological data can be considered. The results showed in chapter 5 also can be improved with well data because the lithological data is crucial do understand slope movement fail and run-out distances.

Another data limitation of this work is related to the inventory of MTDs used in chapter 6. The population of four (4) MTDs is consistent enough to be uses in the models. Nevertheless, it is not big enough for data partition whereby the same inventory was used to modelling and to validation. In case of a larger population of MTDs, one can use one part of the dataset for modelling and another part for the independent validation of the models by computing predictive-curves. The computation of the predictive-rate curve is the key strategic element to interpret the MTD prediction on ESB and to advanced further on hazard studies.

As last, due the small population of MTD, the models in chapter 6 did not consider separately the different types of MTDs identified in the study area. In onshore studies, different types pf slope movements have been modelled separately based on the assumption that different slope movements are caused by different natural conditions . As it was identified in chapter 5, this work identified two types of MTDs, which in future works, and with larger populations, need to be modelled separately in order to improve the predictive results.

7.6. **Future work**

The work developed in this thesis provided a number of new techniques that are novel in their applicability to offshore instabilities. The study of buried surfaces and MTDs into the methodology presented in the chapter 5 and 6 in future will benefit from data that was not available for this thesis. In this sense, the future work proposed is related to the integration of new dataset, which can provide detailed information and its integration in the models, such as, lithology, viscosity, more accurate velocity values for depth conversation, etc. The aim is two introduce variables into the models that are known as good predictors while studding slope instabilities and at the same time, reducing the uncertainties by the introduction of geological layers and data that are more accurate. As a future work is proposed the input of a range of new dataset that can be spatial represented in raster format, testing new variables and decrease the importance of layers exclusive originated from the DTM.

The question how the water pressure is acting as a slope instability trigger comes as an aim to answer in the future work. Is know that overpressure sediments and slope inclination lead to increased likelihood of instability at the seabed and at depth, but how acts in the Espírito Santo Basin concerning slope instability is not yet pointed out in the literature. It could be very interesting to understand how thickness of water column can trigger slope movements in the seafloor and even at depth, whereby needs to be also considered the overburden strata.

Looking further, the application of the presented methodology to a seafloor dataset promise to archive great results, using high accurate bathymetric data will add detail describing kinematic features of the mass-movements but also introducing new predisposing factors. The combination of bathymetric seismic profiles and lithology data, constitute a robust piece of information that can improve considerable the models. Doing so, the susceptibility models of offshore natural hazards can be considered into coastal management or offshore exploration risk assessment as a valid and accurate tool.

The availability of a larger population of mass movements will also increase the quality of the models, whereby in a future work the use of a dataset contain a larger population of mass movements will be an asset to archive higher scientific validation for the obtained results.

This thesis provided great advance for risk assessment of submarine slope movements and the application of this methodology to other geologic settings, such as convergent margin or even lakes, will be interesting and useful. Nevertheless, in the future it requires identification and analysis if relevant failure scenarios, understanding the slope natural condition to fail (predisposing factors) but going a bit further to understand triggering sources and related failures consequences for a step further in the risk assessment direction in submarine environments.

References

ALFARO, E. & HOLZ, M. 2014. Seismic geomorphological analysis of deepwater gravity-driven deposits on a slope system of the southern Colombian Caribbean margin. *Marine and Petroleum Geology,* 57**,** 294-311.

ALVES, T. M. 2010. 3D Seismic examples of differential compaction in mass-transport deposits and their effect on post-failure strata. *Marine Geology,* 271**,** 212 - 224.

ALVES, T. M. 2012. Scale-relationships and geometry of normal faults reactivated during gravitational gliding of Albian rafts (Espírito Santo Basin, SE Brazil). *Earth and Planetary Science Letters***,** 80-86.

ALVES, T. M., CARTWRIGHT, J. & DAVIES, R. J. 2009. Faulting of salt-withdrawal basins during early halokinesis: effects on the Paleogene Rio Doce Canyon system (Espírito Santo Basin, Brazil). *AAPG bulletin,* 93**,** 617-652.

ALVES, T. M. & CARTWRIGHT, J. A. 2009. Volume balance of a submarine landslide in the Espírito Santo Basin, offshore Brazil: Quantifying seafloor erosion, sediment accumulation and depletion. *Earth and Planetary Science Letters,* 288**,** 572-580.

ANDERSON, J. E., CARTWRIGHT, J., DRYSDALL, S. J. & VIVIAN, N. 2000. Controls on turbidite sand deposition during gravity-driven extension of a passive margin: examples from Miocene sediments in Block 4, Angola. *Marine and Petroleum Geology,* 17**,** 1165-1203.

BACON, M., SIMM, R. & REDSHAW, T. 2003. 3-D Seismic Interpretation. Cambridge University Press. ISBN 0 521 79203 7. *Geological Magazine,* 141**,** 245-246.

BAETEN, N. J., LABERG, J. S., FORWICK, M., VORREN, T. O., VANNESTE, M., FORSBERG, C. F., KVALSTAD, T. J. & IVANOV, M. 2013. Morphology and origin of smaller-scale mass movements on the continental slope off northern Norway. *Geomorphology,* 187**,** 122-134.

BARKER, P. F., BUFFER, R. T. & GOMBÔA, L. A. 1993. A seismic reflection study of the Rio Grande Rise. *Barker, P. F., Carlson, R. L., Hohnson, D. A. (Eds.), Initial Reports of the Deep Sea Drilling Program. Government Printing Office, Washington, D. C.* **,** 953 - 976.

BAUDON, C. & CARTWRIGHT, J. 2008. The kinematics of reactivation of normal faults using high resolution throw mapping. *Journal of Structural Geology,* 30**,** 1072-1084.

BI, J. & BENNETT, K. P. Regression Error Characteristic Curves. Proceedings of the 20th International Conference on Machine Learning (ICML-03), 2003. 43-50.

BLAHUT, J., VAN WESTEN, C. J. & STERLACCHINI, S. 2010. Analysis of landslide inventories for accurate prediction of debris-flow source areas. *Geomorphology,* 119**,** 36-51.

BROWN, A. R. 2004. *Interpretation of three-dimensional seismic data*, American Association of Petroleum Geologists, Tulsa.

BRUHN, C. H. L. & WALKER, R. G. 1997. Internal architecture and sedimentary evolution of coarse-grained, turbidite channel-levee complexes, Early Eocene Regência Canyon, Espírito Santo Basin, Brazil. *Sedimentology,* 44**,** 17-46.

BRUN, J.-P. & FORT, X. 2011. Salt tectonics at passive margins: Geology versus models. *Marine and Petroleum Geology,* 28**,** 1123-1145.

BRUN, J.-P. & MAUDUIT, T. P. O. 2008. Rollovers in salt tectonics: The inadequacy of the listric fault model. *Tectonophysics,* 457**,** 1-11.

BRUN, J.-P. & MAUDUIT, T. P. O. 2009. Salt rollers: Structure and kinematics from analogue modelling. *Marine and Petroleum Geology,* 26**,** 249-258.

BRYN, P., BERG, K., LIEN, R. & SOLHEIM, A. 2005. Submarine slides on the Mid-Norwegian Continental Margin—A challenge to the oil industry. *In:* BJØRN T.G WANDÅS, J. P. N. E. E. & FELIX, G. (eds.) *Norwegian Petroleum Society Special Publications.* Elsevier.

BULL, S., CARTWRIGHT, J. & HUUSE, M. 2009. A review of kinematic indicators from mass-transport complexes using 3D seismic data. *Marine and Petroleum Geology,* 26**,** 1132-1151.

CAMERLENGHI, A., URGELES, R. & FANTONI, L. 2010. A Database on Submarine Landslides of the Mediterranean Sea. *In:* MOSHER, D., SHIPP, R. C., MOSCARDELLI, L., CHAYTOR, J., BAXTER, C. P., LEE, H. & URGELES, R. (eds.) *Submarine Mass Movements and Their Consequences.* Springer Netherlands.

CARRARA, A., GUZZETTI, F., CARDINALI, M. & REICHENBACH, P. 1999. Use of GIS Technology in the Prediction and Monitoring of Landslide Hazard. *Natural Hazards,* 20**,** 117-135.

CARRARA, A., SORRISO-VALVO, M. & REALI, C. 1982. Analysis of landslide form and incidence by statistical techniques, Southern Italy. *Catena,* 9**,** 35-62.

CARTWRIGHT, J. & HUUSE, M. 2005. 3D seismic technology: the geological 'Hubble'. *Basin Research,* 17**,** 1-20.

CEES J. VAN WESTEN, E. C., SEKHAR L. KURIAKOSE 2008. Spatial data for landslide susceptibility, hazard, and vulnerability assessment: An overview. *Engineering Geology,* 112 - 131.

CHANG, H. K., KOWSMANN, R. O., FIGUEIREDO, A. M. F. & BENDER, A. A. 1992. Tectonics and stratigraphy of the East Brazil Rift system: an overview. *Tectonophysics,* 213**,** 97 - 138.

CHANG, Y.-S. & PARK, H.-D. 2004. Development of a web-based Geographic Information System for the management of borehole and geological data. *Computers & Geosciences,* 30**,** 887-897.

CHOPRA, S. & MARFURT, K. J. 2005. Seismic attributes — A historical perspective. *Geophysics,* 70**,** 3SO-28SO.

CHUNG, C.-J. & FABBRI, A. 1993. The representation of geoscience information for data integration. *Nonrenewable Resources,* 2**,** 122-139.

CHUNG, C.-J. & FABBRI, A. 2003. Validation of Spatial Prediction Models for Landslide Hazard Mapping. *Natural Hazards,* 30**,** 451-472.

CHUNG, C.-J. & FABBRI, A. G. 1999. Probabilistic prediction models for landslide hazard mapping. *Photogrammetric Engineering and Remote Sensing,* 65-12**,** 1389-1399.

CHUNG, C.-J. F. & FABBRI, A. G. 2005. Systematic Procedures of Landslide Hazard Mapping for Risk Assessment Using Spatial Prediction Models. *Landslide Hazard and Risk.* John Wiley & Sons, Ltd.

CHUNG, C. & MOON, W. 1991. Combination rules of spatial geoscience data for mineral exploration. *Geoinformatics,* 2**,** 159-169.

CLERICI, A., PEREGO, S., TELLINI, C. & VESCOVI, P. 2002. A procedure for landslide susceptibility zonation by the conditional analysis method. *Geomorphology,* 48, 349-364.

CLERICI, A., PEREGO, S., TELLINI, C. & VESCOVI, P. 2010. Landslide failure and runout susceptibility in the upper T. Ceno valley (Northern Apennines, Italy). *Natural Hazards,* 52, 1-29.

COBBOLD, P. R., MEISLING, K. E. & MOUNT, V. S. 2001. Reactivation of an obliquely rifted margin, Campos and Santos basins, southeastern Brazil. *AAPG bulletin,* 85, 1925-1944.

COROMINAS, J., WESTEN, C., FRATTINI, P., CASCINI, L., MALET, J. P., FOTOPOULOU, S., CATANI, F., EECKHAUT, M., MAVROULI, O., AGLIARDI, F., PITILAKIS, K., WINTER, M. G., PASTOR, M., FERLISI, S., TOFANI, V., HERVÁS, J. & SMITH, J. T. 2013. Recommendations for the quantitative analysis of landslide risk. *Bulletin of Engineering Geology and the Environment,* 1-55.

DAI, F. C., LEE, C. F. & NGAI, Y. Y. 2002. Landslide risk assessment and management: an overview. *Engineering Geology,* 64, 65-87.

DALLA VALLE, G., GAMBERI, F., ROCCHINI, P., MINISINI, D., ERRERA, A., BAGLIONI, L. & TRINCARDI, F. 2013. 3D seismic geomorphology of mass transport complexes in a foredeep basin: Examples from the Pleistocene of the Central Adriatic Basin (Mediterranean Sea). *Sedimentary Geology,* 294, 127-141.

DAN, G., CAUQUIL, E. & BOUROULLEC, J.-L. 2014. 3D Seismic and AUV Data Integration for Deepwater Geohazard Assessment: Application to Offshore Northwest Borneo, Brunei. Offshore Technology Conference.

DAVISON, I. 2007. Geology and tectonics of the South Atlantic Brazilian salt basins. *Geological Society, London, Special Publications,* 272, 345-359.

DEMERCIAN, S., SZATMARI, P. & COBBOLD, P. R. 1993. Style and pattern of salt diapirs due to thin-skinned gravitational gliding, Campos and Santos basins, offshore Brazil. *Tectonophysics,* 228, 393-433.

DEN EECKHAUT, M. V., MARRE, A. & POESEN, J. 2010. Comparison of two landslide susceptibility assessments in the Champagne–Ardenne region (France). *Geomorphology,* 115, 141-155.

DIAS, J. L. 2005. Tectônica, estratigrafia e sedimentação no Andar Aptiano da margem leste brasileira. *B. Geoci. Petrobras, Rio de Janeiro,* v. 13, n. 1, 27 - 25.

DUVAL, B., CRAMEZ, C. & JACKSON, M. P. A. 1992. Raft tectonics in the Kwanza Basin, Angola. *Marine and Petroleum Geology,* 9, 389-404.

FABBRI, A., CHUNG, C., NAPOLITANO, P., REMONDO, J. & ZÊZERE, J. 2002. Prediction rate functions of landslide susceptibility applied in the Iberian Peninsula. *Risk analysis III, series: management information systems,* 5, 703-718.

FIDUK, J. C., BRUSH, E. R., ANDERSON, L. E., GIBBS, P. B. & ROWAN, M. G. 2004. Salt deformation, magmatism, and hydrocarbon prospectivity in the Espirito Santo Basin, offshore Brazil.

FORT, X., BRUN, J.-P. & CHAUVEL, F. 2004. Salt tectonics on the Angolan margin, synsedimentary deformation processes. *AAPG Bulletin,* 88, 1523-1544.

FRANÇA, R. L., DEL REY, A. C., TAGLIARI, C. V., BRANDÃO, J. R. & FONTANELLI, P. R. 2007. Bacia do Espírito Santo. *Bol. Geocienc. Petrobras,* 15, 501 - 509.

FREY-MARTÍNEZ, J., CARTWRIGHT, J. & JAMES, D. 2006. Frontally confined versus frontally emergent submarine landslides: A 3D seismic characterisation. *Marine and Petroleum Geology,* 23, 585-604.

FREY MARTINEZ, J., CARTWRIGHT, J. & HALL, B. 2005. 3D seismic interpretation of slump complexes: examples from the continental margin of Israel. *Basin Research,* 17, 83-108.

GAMBOA, D., ALVES, T. & CARTWRIGHT, J. 2011. Distribution and characterization of failed (mega)blocks along salt ridges, southeast Brazil: Implications for vertical fluid flow on continental margins. *Journal of Geophysical Research: Solid Earth,* 116, B08103.

GAMBOA, D., ALVES, T., CARTWRIGHT, J. & TERRINHA, P. 2010. MTD distribution on a 'passive' continental margin: The Espírito Santo Basin (SE Brazil) during the Palaeogene. *Marine and Petroleum Geology,* 27, 1311-1324.

GAMBOA, D., ALVES, T. M. & CARTWRIGHT, J. 2012. A submarine channel confluence classification for topographically confined slopes. *Marine and Petroleum Geology,* 35, 176-189.

GAMBOA, D. A. 2011. *An integrated seismic-scale analysis of reservoir compartmentalisation on continental margins: the Espirito Santo Basin, SE Brazil.* Doctor of Philosophy, Cardiff University.

GARCIA, S. F. D. M., LETOUZEY, J., RUDKIEWICZ, J.-L., DANDERFER FILHO, A. & FRIZON DE LAMOTTE, D. 2012. Structural modeling based on sequential restoration of gravitational salt deformation in the Santos Basin (Brazil). *Marine and Petroleum Geology,* 35, 337-353.

GARZIGLIA, S., MIGEON, S., DUCASSOU, E., LONCKE, L. & MASCLE, J. 2008. Mass-transport deposits on the Rosetta province (NW Nile deep-sea turbidite system, Egyptian margin): Characteristics, distribution, and potential causal processes. *Marine Geology,* 250, 180-198.

GAULLIER, V., BRUN, J. P., GUE´RIN, G. & LECANU, H. 1993. Raft tectonics: the effects of residual topography below a salt de´collement. *Tectonophysics,* 228, 363-381.

GEE, M. J. R. & GAWTHORPE, R. L. 2006. Submarine channels controlled by salt tectonics: Examples from 3D seismic data offshore Angola. *Marine and Petroleum Geology,* 23, 443-458.

GEE, M. J. R., GAWTHORPE, R. L. & FRIEDMANN, J. S. 2005. Giant striations at the base of a submarine landslide. *Marine Geology,* 214, 287-294.

GEE, M. J. R., GAWTHORPE, R. L. & FRIEDMANN, S. J. 2006. Triggering and Evolution of a Giant Submarine Landslide, Offshore Angola, Revealed by 3D Seismic Stratigraphy and Geomorphology. *Journal of Sedimentary Research,* 76, 9-19.

GILBERT, R. B., LACASSE, S. & NADIM, F. 2013. Advances in geotechnical risk and reliability for offshore applications. *Geotechnical Safety and Risk IV.* CRC Press.

GLADE, T. & CROZIER, M. J. 2005. A Review of Scale Dependency in Landslide Hazard and Risk Analysis. *Landslide Hazard and Risk.* John Wiley & Sons, Ltd.

GONG, C., WANG, Y., HODGSON, D. M., ZHU, W., LI, W., XU, Q. & LI, D. 2014. Origin and anatomy of two different types of mass–transport complexes: A 3D seismic case study from the northern South China Sea margin. *Marine and Petroleum Geology,* 54, 198-215.

GREGORY-WODZICKI, K. M. 2000. Uplift history of the Central and Northern Andes: A review. *Geological Society of America Bulletin,* 112**,** 1091-1105.

GROHMANN, C., SMITH, M. & RICCOMINI, C. 2009. Surface roughness of topography: A multi-scale analysis of landform elements in midland valley, Scotland. *Proceedings of geomorphometry,* 140148.

GUILLARD, C. & ZEZERE, J. 2012. Landslide Susceptibility Assessment and Validation in the Framework of Municipal Planning in Portugal: The Case of Loures Municipality. *Environmental Management,* 50**,** 721-735.

GUZZETTI, F. 2005. Landslide hazard and risk assessment – concepts, methods and tools for the detection and mapping of landslides, for landslides susceptibility zonation and hazard assessment, and for landslide risk evaluation. *PhD Thesis. Mathematchinaturwissenschaftlichen Fakultät da Rheinischen Friedrich-Wilhelms, University of Bonn.*

GUZZETTI, F., CARRARA, A., CARDINALI, M. & REICHENBACH, P. 1999. Landslide hazard evaluation: a review of current techniques and their application in a multi-scale study, Central Italy. *Geomorphology,* 31**,** 181-216.

GUZZETTI, F., REICHENBACH, P., ARDIZZONE, F., CARDINALI, M. & GALLI, M. 2006. Estimating the quality of landslide susceptibility models. *Geomorphology,* 81**,** 166-184.

HAMPTON, M. A., LEE, H. J. & LOCAT, J. 1996. Submarine landslides. *Reviews of Geophysics,* 34**,** 33-59.

HANCE, J. 2003. *Development of a database and assessment of seafloor slope stability based on published literature*, Faculty of the Graduate School, University of Texas at Austin.

HANEBERG, W. C., KELLY, J. T., GRAVES, H. L. & DAN, G. 2015. A GIS-based decision-support approach to deepwater drilling-hazard maps. *The Leading Edge,* 34**,** 398-404.

HANSEN, A. 1984. Landslide hazard analysis. *En: D. Brundsen and D. B. Prior (Editors), Slope Stability. John Wiley and Sons***,** 523-602.

HARISHIDAYAT, D., OMOSANYA, K. D. O. & JOHANSEN, S. E. 2015. 3D seismic interpretation of the depositional morphology of the Middle to Late Triassic fluvial system in Eastern Hammerfest Basin, Barents Sea. *Marine and Petroleum Geology.*

HART, B. S. 1999. Definition of subsurface stratigraphy, structure and rock properties from 3-D seismic data. *Earth-Science Reviews,* 47**,** 189-218.

HOUGH, G., GREEN, J., FISH, P., MILLS, A. & MOORE, R. 2011. A geomorphological mapping approach for the assessment of seabed geohazards and risk. *Marine Geophysical Research,* 32**,** 151-162.

HUDEC, M. R. & JACKSON, M. P. 2007. Terra infirma: understanding salt tectonics. *Earth-Science Reviews,* 82**,** 1-28.

HÜHNERBACH, V. & MASSON, D. G. 2004. Landslides in the North Atlantic and its adjacent seas: an analysis of their morphology, setting and behaviour. *Marine Geology,* 213**,** 343-362.

IOUALALEN, M., MIGEON, S. & SARDOUX, O. 2010. Landslide tsunami vulnerability in the Ligurian Sea: case study of the 1979 October 16 Nice international airport submarine landslide and of identified geological mass failures. *Geophysical Journal International,* 181**,** 724-740.

ISACKS, B. L. 1988. Uplift of the Central Andean Plateau and bending of the Bolivian Orocline. *Journal of Geophysical Research: Solid Earth,* 93, 3211-3231.

JACKSON, C. A. L., JACKSON, M. P. A., HUDEC, M. R. & RODRIGUEZ, C. R. 2015. Enigmatic structures within salt walls of the Santos Basin—Part 1: Geometry and kinematics from 3D seismic reflection and well data. *Journal of Structural Geology,* 75, 135-162.

JACKSON, M. & TALBOT, C. J. 1991. *A glossary of salt tectonics*, Bureau of Economic Geology, University of Texas at Austin.

JEAN-PIERRE BRUN, X. F. 2011. Salt tectonics at passive margins: Geology versus models. *Marine and Petroleum Geology,* 28, 1123 - 1145.

KEAREY, P., BROOKS, M. & HILL, I. 2009. An introduction to geophysical exploration. *John Wiley & Sons*

KUMAR, N., GAMBOA, L., SCHREIBER, B. & MASCLE, J. 1977. Geologic history and origin of Sao Paulo Plateau (Southeastern Brazilian Margin), comparison with the Angolan margin and the early evolution of the Northern South Atlantic. *Initial Reports of the Deep Sea Drilling Program,* 39, 927-945.

KVALSTAD, T. J., ANDRESEN, L., FORSBERG, C. F., BERG, K., BRYN, P. & WANGEN, M. 2005. The Storegga slide: evaluation of triggering sources and slide mechanics. *Marine and Petroleum Geology,* 22, 245-256.

LI, C., WU, S., ZHU, Z. & BAO, X. 2014. The assessment of submarine slope instability in Baiyun Sag using gray clustering method. *Natural Hazards*, 1-12.

LIMA, C. 2003. Ongoing compression across South American plate: observations, numerical modelling and some implications for petroleum geology. *Geological Society, London, Special Publications,* 209, 87-100.

LOCAT, J. & LEE, H. J. 2002. Submarine landslides: advances and challenges. *Canadian Geotechnical Journal,* 39, 193-212.

MALAMUD, B. D., TURCOTTE, D. L., GUZZETTI, F. & REICHENBACH, P. 2004. Landslide inventories and their statistical properties. *Earth Surface Processes and Landforms,* 29, 687-711.

MARFURT, K. J. & ALVES, T. M. 2015. Pitfalls and limitations in seismic attribute interpretation of tectonic features. *Interpretation,* 3, SB5-SB15.

MASSON, D. G., HARBITZ, C. B., WYNN, R. B., PEDERSEN, G. & LØVHOLT, F. 2006. Submarine landslides: Processes, triggers and hazard prediction. *Philosophical Transactions of the Royal Society A: Mathematical, Physical and Engineering Sciences,* 364, 2009-2039.

MAUDUIT, T., GUERIN, G., BRUN, J. P. & LECANU, H. 1997. Raft tectonics: the effects of basal slope angle and sedimentation rate on progressive extension. *Journal of Structural Geology,* 19, 1219-1230.

MCADOO, B. G. 2000. Mapping Submarine Slope Failures. *Marine and Coastal Geographical Information Systems, London: Taylor and Francis*, 189-204.

MCADOO, B. G., PRATSON, L. F. & ORANGE, D. L. 2000. Submarine landslide geomorphology, US continental slope. *Marine Geology,* 169, 103-136.

MCKEE, E. H. & NOBLE, D. C. 1982. Miocene volcanism and deformation in the western Cordillera and high plateaus of south-central Peru. *Geological Society of America Bulletin,* 93, 657-662.

MÉGARD, F. 1984. The Andean orogenic period and its major structures in central and northern Peru. *Journal of the Geological Society,* 141, 893-900.

MÉGARD, F., NOBLE, D. C., MCKEE, E. H. & BELLON, H. 1984. Multiple pulses of Neogene compressive deformation in the Ayacucho intermontane basin, Andes of central Peru. *Geological Society of America Bulletin,* 95, 1108-1117.

MEISLING, K. E., COBBOLD, P. R. & MOUNT, V. S. 2001. Segmentation of an obliquely rifted margin, Campos and Santos basins, southeastern Brazil. *AAPG bulletin,* 85, 1903-1924.

MENNO-JAN, K. 2013. Map use: reading, analysis, interpretation. *Cartography and Geographic Information Science,* 40, 53-54.

MICALLEF, A. 2011. Marine Geomorphology: Geomorphological Mapping and the Study of Submarine Landslides. *Geomorphological Mapping: Methods and Applications,* 15, 377.

MICALLEF, A., BERNDT, C., MASSON, D. G. & STOW, D. A. V. 2007. A technique for the morphological characterization of submarine landscapes as exemplified by debris flows of the Storegga Slide. *Journal of Geophysical Research: Earth Surface,* 112, F02001.

MIENERT, J., BERNDT, C., LABERG, J. S. & VORREN, T. O. 2003. Slope Instability of Continental Margins. *In:* WEFER, G., BILLETT, D., HEBBELN, D., JØRGENSEN, B., SCHLÜTER, M. & VAN WEERING, T. E. (eds.) *Ocean Margin Systems.* Springer Berlin Heidelberg.

MOERNAUT, J. & DE BATIST, M. 2011. Frontal emplacement and mobility of sublacustrine landslides: Results from morphometric and seismostratigraphic analysis. *Marine Geology,* 285, 29-45.

MOHRIAK, W., NEMČOK, M. & ENCISO, G. 2008. South Atlantic divergent margin evolution: rift-border uplift and salt tectonics in the basins of SE Brazil. *Geological Society, London, Special Publications,* 294, 365-398.

MOHRIAK, W. U. 2003. Bacias Sedimentares da Margen Continental Brasileira. *Geologia, Tectônica e Recursos Minerais do Brasil, CPRM, São Paulo, Capítulo III* In: Bizzi, L. A., SCHOBBENHAUS, C., VIDOTTI, R. M. & GONÇALVES, J. H. (eds), 87 - 165.

MOHRIAK, W. U. 2005. Interpretação geológica e geofísica da Bacia do Espírito Santo e da região de Ambrolhos: Petrografia, datação radiométrica e visualização sísmica das rochas vulcânicas. . *Bol. Geocien. ,* Petrobras 14, 73 - 87.

MOHRIAK, W. U., SZATMARI, P. & ANJOS, S. 2012. Salt: geology and tectonics of selected Brazilian basins in their global context. *Geological Society, London, Special Publications 2012,* 363.

MOSCARDELLI, L. & WOOD, L. 2008. New classification system for mass transport complexes in offshore Trinidad. *Basin Research,* 20, 73-98.

MOSCARDELLI, L. & WOOD, L. 2015. Morphometry of mass-transport deposits as a predictive tool. *Geological Society of America Bulletin*.

MOSCARDELLI, L., WOOD, L. & MANN, P. 2006. Mass-transport complexes and associated processes in the offshore area of Trinidad and Venezuela. *AAPG bulletin,* 90, 1059-1088.

MOSHER, D. C., MOSCARDELLI, L., BAXTER, C. D. P., URGELES, R., SHIPP, R. C., CHAYTOR, J. D., LEE, H. J., CAMERLENGHI, A., URGELES, R. & FANTONI, L. 2010. A Database on Submarine Landslides of the Mediterranean Sea Submarine Mass Movements and Their Consequences. Springer Netherlands.

NADIM, F. 2006. Challenges to geo-scientists in risk assessment for sub-marine slides. *Norsk Geologisk Tidsskrift,* 86**,** 351-362.

NADIM, F. & LOCAT, J. Risk assessment for submarine slides. International Conference for Landslide Risk Management. AA Balkema, Vancouver, BC, Canada, 2005. 321-334.

O'BRIEN, P. E., SMITH, J., STARK, J. S., JOHNSTONE, G., RIDDLE, M. & FRANKLIN, D. 2015. Submarine geomorphology and sea floor processes along the coast of Vestfold Hills, East Antarctica, from multibeam bathymetry and video data. *Antarctic Science,* FirstView**,** 1-21.

OJEDA, H. A. O. 1982. Structural framework, stratigraphy, and evolution of Brazilian marginal basins. *AAPG Bulletin,* 66**,** 732-749.

OLAFIRANYE, K., JACKSON, C. A. L. & HODGSON, D. M. 2013. The role of tectonics and mass-transport complex emplacement on upper slope stratigraphic evolution: A 3D seismic case study from offshore Angola. *Marine and Petroleum Geology,* 44**,** 196-216.

OLIVEIRA, S. C., ZÊZERE, J. L. & GARCIA, R. A. C. 2015. Structure and Characteristics of Landslide Input Data and Consequences on Landslide Susceptibility Assessment and Prediction Capability. *In:* LOLLINO, G., GIORDAN, D., CROSTA, B. G., COROMINAS, J., AZZAM, R., WASOWSKI, J. & SCIARRA, N. (eds.) *Engineering Geology for Society and Territory - Volume 2: Landslide Processes.* Cham: Springer International Publishing.

OMERU, T. & CARTWRIGHT, J. A. 2015. Multistage, progressive slope failure in the Pleistocene pro-deltaic slope of the West Nile Delta (Eastern Mediterranean). *Marine Geology,* 362**,** 76-92.

OMOSANYA, K. D. O. & ALVES, T. M. 2013a. Ramps and flats of mass-transport deposits (MTDs) as markers of seafloor strain on the flanks of rising diapirs (Espírito Santo Basin, SE Brazil). *Marine Geology,* 340**,** 82-97.

OMOSANYA, K. D. O. & ALVES, T. M. 2014. Mass-transport deposits controlling fault propagation, reactivation and structural decoupling on continental margins (Espírito Santo Basin, SE Brazil). *Tectonophysics,* 628**,** 158-171.

OMOSANYA, K. O. 2014. Seismic character and interactions of of intrabasinal mass-transport deposit in deep-water contimental margins (Espírito Santo Basin, SE Brazil). Cardiff University.

OMOSANYA, K. O. & ALVES, T. M. 2013b. A 3-dimensional seismic method to assess the provenance of Mass-Transport Deposits (MTDs) on salt-rich continental slopes (Espírito Santo Basin, SE Brazil). *Marine and Petroleum Geology*.

PENGE, J., MUNNS, J. W., TAYLOR, B. & WINDLE, T. M. F. 1999. Rift–raft tectonics: examples of gravitational tectonics from the Zechstein basins of northwest Europe. *Geological Society, London, Petroleum Geology Conference series,* 5**,** 201-213.

PEREIRA, S., ZÊZERE, J. L. & BATEIRA, C. 2012. Technical Note: Assessing predictive capacity and conditional independence of landslide predisposing factors for shallow landslide susceptibility models. *Nat. Hazards Earth Syst. Sci.,* 12**,** 979-988.

PIEDADE, A., ZÊZERE, J. L., ANTÓNIO TENEDÓRIO, J., GARCIA, R. A., OLIVEIRA, S. C. & ROCHA, J. Generalization of landslide susceptibility models in geologic-

geomorphologic similar context. EGU General Assembly Conference Abstracts, 2010. 3666.

PILCHER, R. S., MURPHY, R. T. & CIOSEK, J. M. 2014. Jurassic raft tectonics in the northeastern Gulf of Mexico. *Interpretation, 2,* SM39-SM55.

POPE, E. L., TALLING, P. J., URLAUB, M., HUNT, J. E., CLARE, M. A. & CHALLENOR, P. 2015. Are large submarine landslides temporally random or do uncertainties in available age constraints make it impossible to tell? *Marine Geology, 369,* 19-33.

POSAMENTIER, H., MARTINSEN, O., SHIP, R., WEIMER, P. & POSAMENTIER, H. 2011. The character and genesis of submarine mass-transport deposits: insights from outcrop and 3D seismic data. *Mass-transport deposits in deepwater settings.* SEPM Tulsa.

POSAMENTIER, H. W. & KOLLA, V. 2003. Seismic geomorphology and stratigraphy of depositional elements in deep-water settings. *Journal of Sedimentary Research, 73,* 367-388.

PRIOR, D. B., BORNHOLD, B. D. & JOHNS, M. W. 1984. Depositional Characteristics of a Submarine Debris Flow. *The Journal of Geology, 92,* 707-727.

REMONDO, J., GONZÁLEZ-DÍEZ, A., DE TERÁN, J. & CENDRERO, A. 2003. Landslide Susceptibility Models Utilising Spatial Data Analysis Techniques. A Case Study from the Lower Deba Valley, Guipuzcoa (Spain). *Natural Hazards, 30,* 267-279.

RODRÍGUEZ-OCHOA, R., NADIM, F., CEPEDA, J. M., HICKS, M. A. & LIU, Z. 2015. Hazard analysis of seismic submarine slope instability. *Georisk: Assessment and Management of Risk for Engineered Systems and Geohazards, 9,* 128-147.

ROUBY, D., RAILLARD, S., GUILLOCHEAU, F., BOUROULLEC, R. & NALPAS, T. 2002. Kinematics of a growth fault/raft system on the West African margin using 3-D restoration. *Journal of Structural Geology, 24,* 783-796.

ROVERE, M., GAMBERI, F., MERCORELLA, A. & LEIDI, E. 2014. Geomorphometry of a submarine mass-transport complex and relationships with active faults in a rapidly uplifting margin (Gioia Basin, NE Sicily margin). *Marine Geology, 356,* 31-43.

ROWAN, M. G. 2014. Passive-margin salt basins: hyperextension, evaporite deposition, and salt tectonics. *Basin Research, 26,* 154-182.

ROWAN, M. G., HART, B. S., NELSON, S., FLEMINGS, P. B. & TRUDGILL, B. D. 1998. Three-dimensional geometry and evolution of a salt-related growth-fault array: Eugene Island 330 field, offshore Louisiana, Gulf of Mexico. *Marine and Petroleum Geology, 15,* 309-328.

ROWAN, M. G., JACKSON, M. P. A. & TRUDGILL, B. D. 1999. Salt-related fault families and fault welds in the northern Gulf of Mexico. *AAPG Bulletin, 83,* 1454-1484.

ROWAN, M. G., PEEL, F. J., VENDEVILLE, B. C. & GAULLIER, V. 2012. Salt tectonics at passive margins: Geology versus models – Discussion. *Marine and Petroleum Geology, 37,* 184-194.

SCHEUBER, E., BOGDANIC, T., JENSEN, A. & REUTTER, K.-J. 1994. Tectonic Development of the North Chilean Andes in Relation to Plate Convergence and Magmatism Since the Jurassic. *In:* REUTTER, K.-J., SCHEUBER, E. & WIGGER, P. (eds.) *Tectonics of the Southern Central Andes.* Springer Berlin Heidelberg.

SCHOLZ, N. A., RIEDEL, M., BAHK, J. J., YOO, D. G. & RYU, B. J. 2012. Mass transport deposits and gas hydrate occurrences in the Ulleung Basin, East Sea – Part 1:

Mapping sedimentation patterns using seismic coherency. *Marine and Petroleum Geology,* 35**,** 91-104.

SHERIFF, R. E. & GELDART., L. P. 1995. *Exploration Seismology*, Cambridge University Press.

SOETERS, R. & VAN WESTEN, C. J. 1996. Slope instability recognition, analysis, and zonation. *Special Report - National Research Council, Transportation Research Board,* 247**,** 129-177.

STERLACCHINI, S., BALLABIO, C., BLAHUT, J., MASETTI, M. & SORICHETTA, A. 2011. Spatial agreement of predicted patterns in landslide susceptibility maps. *Geomorphology,* 125**,** 51-61.

SULTAN, N., COCHONAT, P., CANALS, M., CATTANEO, A., DENNIELOU, B., HAFLIDASON, H., LABERG, J. S., LONG, D., MIENERT, J., TRINCARDI, F., URGELES, R., VORREN, T. O. & WILSON, C. 2004. Triggering mechanisms of slope instability processes and sediment failures on continental margins: a geotechnical approach. *Marine Geology,* 213**,** 291-321.

TALLING, P. J., WYNN, R. B., MASSON, D. G., FRENZ, M., CRONIN, B. T., SCHIEBEL, R., AKHMETZHANOV, A. M., DALLMEIER-TIESSEN, S., BENETTI, S., WEAVER, P. P. E., GEORGIOPOULOU, A., ZUHLSDORFF, C. & AMY, L. A. 2007. Onset of submarine debris flow deposition far from original giant landslide. *Nature,* 450**,** 541-544.

THIERY, Y., MALET, J. P., STERLACCHINI, S., PUISSANT, A. & MAQUAIRE, O. 2007. Landslide susceptibility assessment by bivariate methods at large scales: Application to a complex mountainous environment. *Geomorphology,* 92**,** 38-59.

TRINCARDI, F. & ARGNANI, A. 1990. Gela submarine slide: A major basin-wide event in the plio-quaternary foredeep of Sicily. *Geo-Marine Letters,* 10**,** 13-21.

URGELES, R., LEYNAUD, D., LASTRAS, G., CANALS, M. & MIENERT, J. 2006. Back-analysis and failure mechanisms of a large submarine slide on the ebro slope, NW Mediterranean. *Marine Geology,* 226**,** 185-206.

URGELES, R., MASSON, D. G., CANALS, M., WATTS, A. B. & LE BAS, T. 1999. Recurrent large-scale landsliding on the west flank of La Palma, Canary Islands. *Journal of Geophysical Research: Solid Earth,* 104**,** 25331-25348.

VAN WESTEN, C. J., CASTELLANOS, E. & KURIAKOSE, S. L. 2008. Spatial data for landslide susceptibility, hazard, and vulnerability assessment: An overview. *Engineering Geology,* 102**,** 112-131.

VAN WESTEN, C. J., RENGERS, N. & SOETERS, R. 2003. Use of Geomorphological Information in Indirect Landslide Susceptibility Assessment. *Natural Hazards,* 30**,** 399-419.

VAN WESTEN, C. J., RENGERS, N., TERLIEN, M. T. J. & SOETERS, R. 1997. Prediction of the occurrence of slope instability phenomenal through GIS-based hazard zonation. *Geologische Rundschau,* 86**,** 404-414.

VAN WESTEN, C. J., VAN ASCH, T. W. J. & SOETERS, R. 2006. Landslide hazard and risk zonation—why is it still so difficult? *Bulletin of Engineering Geology and the Environment,* 65**,** 167-184.

VANNESTE, M., SULTAN, N., GARZIGLIA, S., FORSBERG, C. F. & L'HEUREUX, J.-S. 2014. Seafloor instabilities and sediment deformation processes: the need for integrated, multi-disciplinary investigations. *Marine Geology*.

VARNES, D. J. 1978. Slope movement types and processes. *Transportation Research Board Special Report*.

VENDEVILLE, B. C. 2005. Salt tectonics driven by sediment progradation: Part I—Mechanics and kinematics. *AAPG Bulletin,* 89**,** 1071-1079.

VENDEVILLE, B. C. & JACKSON, M. P. A. 1992a. The fall of diapirs during thin-skinned extension. *Marine and Petroleum Geology,* 9**,** 354-371.

VENDEVILLE, B. C. & JACKSON, M. P. A. 1992b. The rise of diapirs during thin-skinned extension. *Marine and Petroleum Geology,* 9**,** 331-354.

VIEIRA, P. E., BRUHN, C. H. L., SANTOS, C. F., DEL REY, A. C. & ALVES, R. G. 2007. Golfinho Field-Discovery, Development, and Future Prospects. Offshore Technology Conference.

VORPAHL, P., ELSENBEER, H., MÄRKER, M. & SCHRÖDER, B. 2012. How can statistical models help to determine driving factors of landslides? *Ecological Modelling,* 239**,** 27-39.

WELBON, A. I. F., BROCKBANK, P. J., BRUNSDEN, D. & OLSEN, T. S. 2007. Characterizing and producing from reservoirs in landslides: challenges and opportunities. *Geological Society, London, Special Publications,* 292**,** 49-74.

WILSON, C. K., LONG, D. & BULAT, J. 2004. The morphology, setting and processes of the Afen Slide. *Marine Geology,* 213**,** 149-167.

YAN, T. Z. 1988. Recent advances of quatitative prognoses of landslides in China *in* Bonnard, C. (Ed.) *Landslides*. Proceeding of the 5th ISL, Lausanne. Vol. 2. Balkema, Rotterdam: 1263 - 1268.

YILMAZ, Ö. 2001. *Seismic data analysis*, Investigations in Geophysics No. 10. Society of Exploration Geophysicists.

YIN, K. L. & YAN, T. Z. 1988. Statistical prediction models for slope instability of metamorphosed rocks *in* Bonnard, C. (Ed.) *Landslides.* Proceeding of the 5th ISL, Lausane. Vol. 2. Balkema, Rotterdam: 1269 - 1272.

ZÊZERE, J., HENRIQUES, C., GARCIA, R., OLIVEIRA, S., PIEDADE, A. & NEVES, M. 2009. Effects of landslide inventories uncertainty on landslide susceptibility modelling. *Mallet, J.-P.; Remaitre, A.; Boggard, T. (Eds.), Landslide Processes: From Geomorphologic Mapping to Dynamic Modelling. CERG Editions, Strasbourg*, 81-86.

ZÊZERE, J. L., OLIVEIRA, S. C., GARCIA, R. A. C. & REIS, E. 2008. Weighting predisposing factors for shallow slides susceptibility assessment on the regional scale. *Landslides and Engineered Slopes. From the Past to the Future, Two Volumes + CD-ROM.* CRC Press.

ZÊZERE, J. L., REIS, E., GARCIA, R., OLIVEIRA, S., RODRIGUES, M. L., VIEIRA, G. & FERREIRA, A. B. 2004. Integration of spatial and temporal data for the definition of different landslide hazard scenarios in the area north of Lisbon (Portugal). *Nat. Hazards Earth Syst. Sci.,* 4**,** 133-146.

ZÊZERE, J. L. S., DE BRUM FERREIRA, A. & RODRIGUES, M. L. S. 1999. The role of conditioning and triggering factors in the occurrence of landslides: a case study in the area north of Lisbon (Portugal). *Geomorphology,* 30**,** 133-146.

Appendix I:

Seismic acquisition and processing parameters of BES-100 survey

Acquisition parameters

Vessel: CGG Harmattan

Source: Airgun Dual

Shotpoint Interval: 25m flip-flop

CMP xline: 25 metres

Group spacing: 12.5 m

Streamers: 6 x 5700 m

Record length: 8.0 sec

Sample interval: 2ms

Processing Sequence

Reformat from SEGD

Navigation/seismic merge

Resample from 2ms to 4ms with anti-alias filter

Spherical divergence correction

"SPARN" – signal preserving attenuation of random noise and swell noise

Zero phase conversion using modeller far field signature

Q phase only compensation (referenced to water bottom)

FX shotpoint interpolation and radon multiple attenuation

3D Kirchhoff Bin centring DMO

3D V (c) pre-stack time migration using Stolt algorithm

0.5 km grid Final velocity analysis

Full offset stack

Post stack demigration

Crossline FX trace interpolation

Zhimming Li Steep dip one pass 3D time migration

Final Product

Raw stack in SEGY format

Raw migration in SEGY format

Final stacking velocities in VelTape format

Final migration velocities in VelTape format

Migrated bin centre position in UKOOA P1/90 format

Final report

Appendix II:

Informative value method calculations

Calculations of Informative Value Method of Model 1, Model 2 and Model 3 in support to chapter 6

Model 1

Slope gradient

Slope Class Code	Unstable area		Total area		Total unstable area		Total area		Si/Ni	S/N	Si/Ni	S/N	VIVar	VI
	Si		Ni		S		N							
	#pixels	m²	#pixels	m²	#pixels	m²	#pixels	m²	#pixels		m²			
0 - 1	17426	43565000	108560	271400000	53525	133812500	303524	758810000	0.16052	0.176345198	0.16052	0.176345	0.910257	-0.09403
1 - 2	26337	65842500	131386	328465000	53525	133812500	303524	758810000	0.200455	0.176345198	0.200455	0.176345	1.13672	0.128147
2 - 3	6982	17455000	39530	98825000	53525	133812500	303524	758810000	0.176625	0.176345198	0.176625	0.176345	1.001589	0.001587
3 - 4	1641	4102500	12232	30580000	53525	133812500	303524	758810000	0.134156	0.176345198	0.134156	0.176345	0.76076	-0.27344
4 - 5	677	1692500	5377	13442500	53525	133812500	303524	758810000	0.125907	0.176345198	0.125907	0.176345	0.713978	-0.3369
5 - 6	325	812500	2751	6877500	53525	133812500	303524	758810000	0.118139	0.176345198	0.118139	0.176345	0.66993	-0.40058
6 - 7	87	217500	1651	4127500	53525	133812500	303524	758810000	0.052695	0.176345198	0.052695	0.176345	0.298819	-1.20792
7 -8	23	57500	898	2245000	53525	133812500	303524	758810000	0.025612	0.176345198	0.025612	0.176345	0.145241	-1.92936
> 8	27	67500	1139	2847500	53525	133812500	303524	758810000	0.023705	0.176345198	0.023705	0.176345	0.134424	-2.00676
	53525	133812500	303524	758810000										

Flow accumulation

Flow Accumulation Class	Unstable area		Total area		Total unstable area		Total area		Si/Ni	S/N	Si/Ni	S/N	VIVar	VI
	Si		Ni		S		N							
	#pixels	m²	#pixels	m²	#pixels	m²	#pixels	m²	#pixels		m²			
0	12069	30172500	67875	169687500	53525	133812500	303524	758810000	0.177812	0.176345	0.177812	0.176345	1.008319	0.008284
1	8711	21777500	49210	123025000	53525	133812500	303524	758810000	0.177017	0.176345	0.177017	0.176345	1.003809	0.003802
1 - 10	22254	55635000	126086	315215000	53525	133812500	303524	758810000	0.176499	0.176345	0.176499	0.176345	1.00087	0.000869
10 - 100	8085	20212500	46277	115692500	53525	133812500	303524	758810000	0.174709	0.176345	0.174709	0.176345	0.990721	-0.00932
100 - 1000	2074	5185000	12739	31847500	53525	133812500	303524	758810000	0.162807	0.176345	0.162807	0.176345	0.92323	-0.07988
< 1000	332	830000	1337	3342500	53525	133812500	303524	758810000	0.248317	0.176345	0.248317	0.176345	1.408131	0.342263
	53525	133812500	303524	758810000										

Profile curvature

Profile Curvature Class	Unstable area		Total area		Total unstable area		Total area		Si/Ni	S/N	Si/Ni	S/N	VIVar	VI
	Si		Ni		S		N							
	#pixels	m²	#pixels	m²	#pixels	m²	#pixels	m²	#pixels		m²			
Convex	755	47187500	4151	259437500	2132	133250000	12150	759375000	0.181884	0.175473	0.181884	0.175473251	1.036533	0.035882
Flat	600	37500000	3827	239187500	2132	133250000	12150	759375000	0.156781	0.175473	0.156781	0.175473251	0.893474	-0.11264
Concave	777	48562500	4172	260750000	2132	133250000	12150	759375000	0.186242	0.175473	0.186242	0.175473251	1.061368	0.059558
	2132	133250000	12150	759375000										

Plan curvature

Plan Curvature Class	Unstable area		Total area		Total unstable area		Total area		Si/Ni	S/N	Si/Ni	S/N	VIVar	VI
	Si		Ni		S		N		#pixels		m²			
	#pixels	m²	#pixels	m²	#pixels	m²	#pixels	m²						
Concave	1013	63312500	5556	347250000	2132	133250000	12150	759375000	0.182325	0.175473	0.182325	0.175473	1.03905	0.038
Flat	130	8125000	959	59937500	2132	133250000	12150	759375000	0.135558	0.175473	0.135558	0.175473	0.772527	-0.258
Convex	989	61812500	5635	352187500	2132	133250000	12150	759375000	0.17551	0.175473	0.17551	0.175473	1.000211	0.0002
	2132	133250000	12150	759375000										

Elevation

Elevation Class (m)	Unstable area		Total area		Total unstable area		Total area		Si/Ni	S/N	Si/Ni	S/N	VIVar	VI
	Si		Ni		S		N		#pixels		m²			
	#pixels	m²	#pixels	m²	#pixels	m²	#pixels	m²						
0 - 100	137	342500	9721	24302500	53525	133812500	303524	758810000	0.014093	0.176345	0.0140932	0.176345198	0.079918	-2.527
100 - 200	15581	38952500	48435	121087500	53525	133812500	303524	758810000	0.321689	0.176345	0.3216889	0.176345198	1.8242	0.601
200 - 300	15722	39305000	66999	167497500	53525	133812500	303524	758810000	0.23466	0.176345	0.2346602	0.176345198	1.330687	0.286
300 - 400	5612	14030000	52189	130472500	53525	133812500	303524	758810000	0.107532	0.176345	0.1075322	0.176345198	0.609783	-0.495
400 - 500	9073	22682500	57874	144685000	53525	133812500	303524	758810000	0.156772	0.176345	0.1567716	0.176345198	0.889004	-0.118
500 - 600	7400	18500000	53176	132940000	53525	133812500	303524	758810000	0.139161	0.176345	0.1391605	0.176345198	0.789137	-0.237
600 - 700	0	0	15130	37825000	53525	133812500	303524	758810000	0	0.176345	0	0.176345198	0	#NUM!
	53525	133812500	303524	758810000										

Flow direction

Flow Direction Class	Unstable area		Total area		Total unstable area		Total area		Si/Ni	S/N	Si/Ni	S/N	VIVar	VI
	Si		Ni		S		N							
	#pixels	m²	#pixels	m²	#pixels	m²	#pixels	m²	m²		#pixels	m²		
FD1	12632	31580000	86791	216977500	53525	303524	758810000		0.145545	0.176345	0.145545	0.176345	0.825342	-0.19196
FD2	15015	37537500	86456	216140000	53525	303524	758810000		0.173672	0.176345	0.173672	0.176345	0.984842	-0.01527
FD3	11964	29910000	53672	134180000	53525	303524	758810000		0.22291	0.176345	0.22291	0.176345	1.264052	0.234323
FD4	3968	9920000	13530	33825000	53525	303524	758810000		0.293274	0.176345	0.293274	0.176345	1.663069	0.508665
FD5	1701	4252500	7613	19032500	53525	303524	758810000		0.223434	0.176345	0.223434	0.176345	1.267024	0.236671
FD6	724	1810000	3839	9597500	53525	303524	758810000		0.188591	0.176345	0.188591	0.176345	1.069441	0.067136
FD7	2271	5677500	14827	37067500	53525	303524	758810000		0.153167	0.176345	0.153167	0.176345	0.868561	-0.14092
FD8	5250	13125000	36796	91990000	53525	303524	758810000		0.142679	0.176345	0.142679	0.176345	0.809087	-0.21185
	53525	133812500	303524	758810000										

Slope over area ratio

Slope Area Ration Class	Unstable area		Total area		Total unstable area		Total area		Si/Ni	S/N	Si/Ni	S/N	VIVar	VI
	Si		Ni		S		N							
	#pixels	m²	#pixels	m²	#pixels	m²	#pixels	m²	#pixels		m²			
SAR1	2086	5215000	9648	24120000	53525	133812500	301278	753195000	0.216211	0.17766	0.216211	0.17766	1.22	0.196382
SAR2	7991	19977500	47399	118497500	53525	133812500	301278	753195000	0.16859	0.17766	0.16859	0.17766	0.95	-0.0524
SAR3	17987	44967500	101146	252865000	53525	133812500	301278	753195000	0.177832	0.17766	0.177832	0.17766	1.00	0.000969
SAR4	24974	62435000	138112	345280000	53525	133812500	301278	753195000	0.180824	0.17766	0.180824	0.17766	1.02	0.017655
SAR5	487	1217500	4973	12432500	53525	133812500	301278	753195000	0.097929	0.17766	0.097929	0.17766	0.55	-0.59563
	53525	133812500	301278	753195000										

Model 2

Slope gradient

Slope Class Code	Unstable area		Total area		Total unstable area		Total area		Si/Ni	S/N	Si/Ni	S/N	VIVar	VI
	Si		Ni		S		N							
	#pixels	m²	#pixels	m²	#pixels	m²	#pixels	m²	#pixels		m²			
0 - 1	2653	6632500	108560	271400000	12085	30212500	303524	758810000	0.024438	0.0398156	0.024438	0.039816	0.613782	-0.48812
1 - 2	5994	14985000	131386	328465000	12085	30212500	303524	758810000	0.045621	0.0398156	0.045621	0.039816	1.145814	0.136115
2 - 3	2238	5595000	39530	98825000	12085	30212500	303524	758810000	0.056615	0.0398156	0.056615	0.039816	1.421935	0.352018
3 - 4	584	1460000	12232	30580000	12085	30212500	303524	758810000	0.047744	0.0398156	0.047744	0.039816	1.199118	0.181586
4 - 5	327	817500	5377	13442500	12085	30212500	303524	758810000	0.060815	0.0398156	0.060815	0.039816	1.527405	0.42357
5 - 6	195	487500	2751	6877500	12085	30212500	303524	758810000	0.070883	0.0398156	0.070883	0.039816	1.780289	0.576775
6 - 7	61	152500	1651	4127500	12085	30212500	303524	758810000	0.036947	0.0398156	0.036947	0.039816	0.92796	-0.07477
7 -8	14	35000	898	2245000	12085	30212500	303524	758810000	0.01559	0.0398156	0.01559	0.039816	0.39156	-0.93762
> 8	19	47500	1139	2847500	12085	30212500	303524	758810000	0.016681	0.0398156	0.016681	0.039816	0.418964	-0.86997
	12085	30212500	303524	758810000										

Flow accumulation

Flow Accumulation Class	Unstable area		Total area		Total unstable area		Total area		Si/Ni	S/N	Si/Ni	S/N	VIVar	VI
	Si		Ni		S		N		#pixels		m²			
	#pixels	m²	#pixels	m²	#pixels	m²	#pixels	m²						
0	2373	5932500	67875	169687500	12085	30212500	303524	758810000	0.034961	0.039816	0.034961	0.039816	0.87808	-0.13002
1	1808	4520000	49210	123025000	12085	30212500	303524	758810000	0.03674	0.039816	0.03674	0.039816	0.922766	-0.08038
1 - 10	5332	13330000	126086	315215000	12085	30212500	303524	758810000	0.042289	0.039816	0.042289	0.039816	1.06211	0.060258
10 - 100	1836	4590000	46277	115692500	12085	30212500	303524	758810000	0.039674	0.039816	0.039674	0.039816	0.996446	-0.00356
100 - 1000	577	1442500	12739	31847500	12085	30212500	303524	758810000	0.045294	0.039816	0.045294	0.039816	1.137593	0.128915
> 1000	159	397500	1337	3342500	12085	30212500	303524	758810000	0.118923	0.039816	0.118923	0.039816	2.986841	1.094216
	12085	30212500	303524	758810000										

Profile curvature

Profile Curvature Class	Unstable area		Total area		Total unstable area		Total area		Si/Ni	S/N	Si/Ni	S/N	VIVar	VI
	Si		Ni		S		N		#pixels		m²			
	#pixels	m²	#pixels	m²	#pixels	m²	#pixels	m²						
Convex	161	10062500	4151	259437500	476	29750000	12150	759375000	0.038786	0.039177	0.038786	0.039176955	0.990017	-0.01003
Flat	119	7437500	3827	239187500	476	29750000	12150	759375000	0.031095	0.039177	0.031095	0.039176955	0.793703	-0.23105
Concave	196	12250000	4172	260750000	476	29750000	12150	759375000	0.04698	0.039177	0.04698	0.039176955	1.199171	0.18163
	476	29750000	12150	759375000										

Plan curvature

| Plan | Unstable area | Total area | Total unstable area | Total area | |
| | | | | | |

Curvature Class	Si		Ni		S		N		Si/Ni	S/N	Si/Ni	S/N	VIVar	VI
	#pixels	m²	#pixels	m²	#pixels	m²	#pixels	m²	#pixels		m²			
Concave	255	15937500	5556	347250000	507	31687500	12150	759375000	0.045896	0.041728	0.045896	0.041728	1.099882	0.0952033
Flat	27	1687500	959	59937500	507	31687500	12150	759375000	0.028154	0.041728	0.028154	0.041728	0.674704	-0.393481
Convex	225	14062500	5635	352187500	507	31687500	12150	759375000	0.039929	0.041728	0.039929	0.041728	0.956879	-0.044079
	507	31687500	12150	759375000										

Elevation

Elevation Class (m)	Unstable area		Total area		Total unstable area		Total area							
	Si		Ni		S		N		Si/Ni	S/N	Si/Ni	S/N	VIVar	VI
	#pixels	m²	#pixels	m²	#pixels	m²	#pixels	m²	#pixels		m²			
0 - 100	0	0	9721	24302500	12085	30212500	303524	758810000	0	0.039816	0	0.039815632	0	#NUM!
100 - 200	0	0	48435	121087500	12085	30212500	303524	758810000	0	0.039816	0	0.039815632	0	#NUM!
200 - 300	1551	3877500	66999	167497500	12085	30212500	303524	758810000	0.02315	0.039816	0.0231496	0.039815632	0.58142	-0.54228
300 - 400	3772	9430000	52189	130472500	12085	30212500	303524	758810000	0.072276	0.039816	0.0722758	0.039815632	1.815261	0.596229
400 - 500	1672	4180000	57874	144685000	12085	30212500	303524	758810000	0.02889	0.039816	0.0288903	0.039815632	0.725603	-0.32075
500 - 600	5090	12725000	53176	132940000	12085	30212500	303524	758810000	0.09572	0.039816	0.0957199	0.039815632	2.404078	0.877166
600 - 700	0	0	15130	37825000	12085	30212500	303524	758810000	0	0.039816	0	0.039815632	0	#NUM!
	12085	30212500	303524	758810000										

Flow direction

Flow Direction Class	Unstable area		Total area		Total unstable area	Total area							
	Si		Ni		S	N		Si/Ni	S/N	Si/Ni	S/N	VIVar	VI
	#pixels	m²	#pixels	m²	#pixels	m²	#pixels	m²		#pixels			
FD1	2809	7022500	86791	216977500	12085	303524	758810000	0.032365	0.039816	0.032365	0.039816	0.812874	-0.20718
FD2	4072	10180000	86456	216140000	12085	303524	758810000	0.047099	0.039816	0.047099	0.039816	1.18293	0.167994
FD3	2638	6595000	53672	134180000	12085	303524	758810000	0.04915	0.039816	0.04915	0.039816	1.23445	0.210625
FD4	271	677500	13530	33825000	12085	303524	758810000	0.02003	0.039816	0.02003	0.039816	0.503058	-0.68705
FD5	146	365000	7613	19032500	12085	303524	758810000	0.019178	0.039816	0.019178	0.039816	0.481663	-0.73051
FD6	124	310000	3839	9597500	12085	303524	758810000	0.0323	0.039816	0.0323	0.039816	0.811241	-0.20919
FD7	525	1312500	14827	37067500	12085	303524	758810000	0.035408	0.039816	0.035408	0.039816	0.889308	-0.11731
FD8	1500	3750000	36796	91990000	12085	303524	758810000	0.040765	0.039816	0.040765	0.039816	1.023852	0.023572
	12085	30212500	303524	758810000									

Slope over area ratio

Slope Area Ration Class	Unstable area		Total area		Total unstable area		Total area		Si/Ni	S/N	Si/Ni	S/N	VIVar	VI
	Si		Ni		S		N							
	#pixels	m²	#pixels	m²	#pixels	m²	#pixels	m²	#pixels		m²			
SAR1	324	810000	9648	24120000	12058	30145000	301278	753195000	0.033582	0.040023	0.033582	0.040023	0.84	-0.17546
SAR2	1993	4982500	47399	118497500	12058	30145000	301278	753195000	0.042047	0.040023	0.042047	0.040023	1.05	0.049345
SAR3	4114	10285000	101146	252865000	12058	30145000	301278	753195000	0.040674	0.040023	0.040674	0.040023	1.02	0.016136
SAR4	5510	13775000	138112	345280000	12058	30145000	301278	753195000	0.039895	0.040023	0.039895	0.040023	1.00	-0.0032
SAR5	144	360000	4973	12432500	12058	30145000	301278	753195000	0.028956	0.040023	0.028956	0.040023	0.72	-0.32366
	12085	30212500	301278	753195000										

Model 3

Slope gradient

Slope Gradient Class	Unstable area		Total area		Total unstable area		Total area		Si/Ni	S/N	Si/Ni	S/N	VIVar	VI
	Si		Ni		S		N							
	#pixels	m²	#pixels	m²	#pixels	m²	#pixels	m²	#pixels		m²			
0 - 1	885	2212500	108560	271400000	4448	11120000	303524	758810000	0.008152	0.0146545	0.008152	0.014655	0.556291	-0.58646
1 - 2	1918	4795000	131386	328465000	4448	11120000	303524	758810000	0.014598	0.0146545	0.014598	0.014655	0.996157	-0.00385
2 - 3	911	2277500	39530	98825000	4448	11120000	303524	758810000	0.023046	0.0146545	0.023046	0.014655	1.572606	0.452734
3 - 4	341	852500	12232	30580000	4448	11120000	303524	758810000	0.027878	0.0146545	0.027878	0.014655	1.902327	0.643078
4 - 5	207	517500	5377	13442500	4448	11120000	303524	758810000	0.038497	0.0146545	0.038497	0.014655	2.626991	0.965839
5 - 6	135	337500	2751	6877500	4448	11120000	303524	758810000	0.049073	0.0146545	0.049073	0.014655	3.348663	1.208561
6 - 7	47	117500	1651	4127500	4448	11120000	303524	758810000	0.028468	0.0146545	0.028468	0.014655	1.942581	0.664017
7 -8	4	10000	898	2245000	4448	11120000	303524	758810000	0.004454	0.0146545	0.004454	0.014655	0.303957	-1.19087
> 8	0		1139	2847500	4448	11120000	303524	758810000	0	0.0146545	0	0.014655	0	#NUM!
	4448	11120000	303524	758810000										

Flow accumulation

Flow Accumulation Class	Unstable area		Total area		Total unstable area		Total area		Si/Ni	S/N	Si/Ni	S/N	VIVar	VI
	Si		Ni		S		N		Si/Ni	S/N	Si/Ni	S/N	VIVar	VI
	#pixels	m²	#pixels	m²	#pixels	m²	#pixels	m²	#pixels		m²			
0	872	2180000	67875	169687500	4448	11120000	303524	758810000	0.012847	0.014655	0.012847	0.014655	0.876667	-0.13163
1	676	1690000	49210	123025000	4448	11120000	303524	758810000	0.013737	0.014655	0.013737	0.014655	0.937393	-0.06465
1 - 10	2017	5042500	126086	315215000	4448	11120000	303524	758810000	0.015997	0.014655	0.015997	0.014655	1.091609	0.087653
10 - 100	663	1657500	46277	115692500	4448	11120000	303524	758810000	0.014327	0.014655	0.014327	0.014655	0.977635	-0.02262
100 - 1000	166	415000	12739	31847500	4448	11120000	303524	758810000	0.013031	0.014655	0.013031	0.014655	0.889203	-0.11743
> 1000	54	135000	1337	3342500	4448	11120000	303524	758810000	0.040389	0.014655	0.040389	0.014655	2.756072	1.013807
	4448	11120000	303524	758810000										

Profile curvature

Profile Curvature Class	Unstable area		Total area		Total unstable area		Total area		Si/Ni	S/N	Si/Ni	S/N	VIVar	VI
	Si		Ni		S		N		Si/Ni	S/N	Si/Ni	S/N	VIVar	VI
	#pixels	m²	#pixels	m²	#pixels	m²	#pixels	m²	#pixels		m²			
Convex	60	3750000	4151	259437500	173	10812500	12150	759375000	0.014454	0.014239	0.014454	0.014238683	1.015146	0.015033
Flat	48	3000000	3827	239187500	173	10812500	12150	759375000	0.012542	0.014239	0.012542	0.014238683	0.880872	-0.12684
Concave	65	4062500	4172	260750000	173	10812500	12150	759375000	0.01558	0.014239	0.01558	0.014238683	1.094206	0.090029

	173	10812500	12150	759375000				

Plan curvature

Plan Curvature Class	Unstable area		Total area		Total unstable area		Total area		Si/Ni	S/N	Si/Ni	S/N	VIVar	VI
	Si		Ni		S		N							
	#pixels	m²	#pixels	m²	#pixels	m²	#pixels	m²	#pixels		m²			
Concave	89	5562500	5556	347250000	173	10812500	12150	759375000	0.016019	0.014239	0.016019	0.014239	1.125014	0.1177955
Flat	10	625000	959	59937500	173	10812500	12150	759375000	0.010428	0.014239	0.010428	0.014239	0.732338	-0.311513
Convex	74	4625000	5635	352187500	173	10812500	12150	759375000	0.013132	0.014239	0.013132	0.014239	0.922291	-0.080894
	173	10812500	12150	759375000										

Elevation

Elevation Class (m)	Unstable area		Total area		Total unstable area		Total area		Si/Ni	S/N	Si/Ni	S/N	VIVar	VI
	Si		Ni		S		N							
	#pixels	m²	#pixels	m²	#pixels	m²	#pixels	m²	#pixels		m²			
0 - 100	0	0	9721	24302500	4448	11120000	303524	758810000	0	0.014655	0	0.014654525	0	#NUM!
100 - 200	0	0	48435	121087500	4448	11120000	303524	758810000	0	0.014655	0	0.014654525	0	#NUM!
200 - 300	0	0	66999	167497500	4448	11120000	303524	758810000	0	0.014655	0	0.014654525	0	#NUM!
300 - 400	1803	4507500	52189	130472500	4448	11120000	303524	758810000	0.034548	0.014655	0.0345475	0.014654525	2.357464	0.857586
400 - 500	131	327500	57874	144685000	4448	11120000	303524	758810000	0.002264	0.014655	0.0022635	0.014654525	0.15446	-1.86782
500 - 600	2514	6285000	53176	132940000	4448	11120000	303524	758810000	0.047277	0.014655	0.047277	0.014654525	3.2261	1.171274
600 - 700	0	0	15130	37825000	4448	11120000	303524	758810000	0	0.014655	0	0.014654525	0	#NUM!
	4448	11120000	303524	758810000										

Flow direction

Flow Direction Class	Unstable area Si		Total area Ni		Total unstable area S		Total area N		Si/Ni	Si	Ni	S	N	Si/Ni
	#pixels	m²	#pixels	m²	#pixels	m²	#pixels	m²	#pixels		m²			
FD1	869	2172500	86791	216977500	4448	11120000	303524	758810000	0.010013	0.014655	0.010013	0.014655	0.68324	-0.38091
FD2	1429	3572500	86456	216140000	4448	11120000	303524	758810000	0.016529	0.014655	0.016529	0.014655	1.127886	0.120345
FD3	1165	2912500	53672	134180000	4448	11120000	303524	758810000	0.021706	0.014655	0.021706	0.014655	1.481175	0.392836
FD4	113	282500	13530	33825000	4448	11120000	303524	758810000	0.008352	0.014655	0.008352	0.014655	0.569913	-0.56227
FD5	78	195000	7613	19032500	4448	11120000	303524	758810000	0.010246	0.014655	0.010246	0.014655	0.699145	-0.3579
FD6	80	200000	3839	9597500	4448	11120000	303524	758810000	0.020839	0.014655	0.020839	0.014655	1.422002	0.352066
FD7	261	652500	14827	37067500	4448	11120000	303524	758810000	0.017603	0.014655	0.017603	0.014655	1.2012	0.183321
FD8	453	1132500	36796	91990000	4448	11120000	303524	758810000	0.012311	0.014655	0.012311	0.014655	0.84009	-0.17425
	4448	11120000	303524	758810000										

Slope over area ratio

Slope Area Ration Class (m)	Unstable area Si		Total area Ni		Total unstable area S		Total area N		Si/Ni	S/N	Si/Ni	S/N	VIVar	VI
	#pixels	m²	#pixels	m²	#pixels	m²	#pixels	m²	#pixels		m²			
SAR1	219	547500	9648	24120000	4448	11120000	301278	753195000	0.022699	0.014764	0.022699	0.014764	1.54	0.430145
SAR2	631	1577500	47399	118497500	4448	11120000	301278	753195000	0.013313	0.014764	0.013313	0.014764	0.90	-0.10347
SAR3	1372	3430000	101146	252865000	4448	11120000	301278	753195000	0.013565	0.014764	0.013565	0.014764	0.92	-0.08472
SAR4	2175	5437500	138112	345280000	4448	11120000	301278	753195000	0.015748	0.014764	0.015748	0.014764	1.07	0.064543
SAR5	51	127500	4973	12432500	4448	11120000	301278	753195000	0.010255	0.014764	0.010255	0.014764	0.69	-0.36437
	4448	11120000	301278	753195000										